STUDY OF PCDTBT:PC$_{71}$BM NANOCOMPOSITE VIA TEMPLATE-ASSISTED METHOD FOR HUMIDITY SENSING APPLICATION

NOR ASMALIZA BINTI BAKAR

FACULTY OF SCIENCE
UNIVERSITY OF MALAYA
KUALA LUMPUR

2018

STUDY OF PCDTBT:PC$_{71}$BM NANOCOMPOSITE VIA TEMPLATE-ASSISTED METHOD FOR HUMIDITY SENSING APPLICATION

NOR ASMALIZA BINTI BAKAR

THESIS SUBMITTED IN FULFILMENT OF THE REQUIREMENTS FOR THE DEGREE OF DOCTOR OF PHILOSOPHY

DEPARTMENT OF PHYSICS
FACULTY OF SCIENCE
UNIVERSITY OF MALAYA
KUALA LUMPUR

2018

UNIVERSITY OF MALAYA

ORIGINAL LITERARY WORK DECLARATION

Name of Candidate: **NOR ASMALIZA BINTI BAKAR**

Registration/Matric No: **SHC130079**

Name of Degree: **DOCTOR OF PHILOSOPHY**

Title of Thesis ("this Work"): **STUDY OF PCDTBT:PC$_{71}$BM NANOCOMPOSITE VIA TEMPLATE-ASSISTED METHOD FOR HUMIDITY SENSING APPLICATION**

Field of Study: **EXPERIMENTAL PHYSICS**

I do solemnly and sincerely declare that:

(1) I am the sole author/writer of this Work;
(2) This Work is original;
(3) Any use of any work in which copyright exists was done by way of fair dealing and for permitted purposes and any excerpt or extract from, or reference to or reproduction of any copyright work has been disclosed expressly and sufficiently and the title of the Work and its authorship have been acknowledged in this Work;
(4) I do not have any actual knowledge nor do I ought reasonably to know that the making of this work constitutes an infringement of any copyright work;
(5) I hereby assign all and every rights in the copyright to this Work to the University of Malaya ("UM"), who henceforth shall be owner of the copyright in this Work and that any reproduction or use in any form or by any means whatsoever is prohibited without the written consent of UM having been first had and obtained;
(6) I am fully aware that if in the course of making this Work I have infringed any copyright whether intentionally or otherwise, I may be subject to legal action or any other action as may be determined by UM.

Candidate's Signature Date: 12/6/2018

Subscribed and solemnly declared before,

Witness's Signature Date: 12/6/2018

Name:

Designation:

STUDY OF PCDTBT:PC$_{71}$BM NANOCOMPOSITE VIA TEMPLATE-ASSISTED METHOD FOR HUMIDITY SENSING APPLICATION

ABSTRACT

The quest for materials with molecular scale properties has led to the development of one-dimensional (1D) nanostructures. Both solution and melt-assisted template provides a simple and cost-effective method for fabrication of 1D nanostructures. This method has been used to fabricate various types of nanostructures with different morphological, optical and structural properties. However, the parameters and principles that govern the final properties still remain ambiguous. This research aims to investigate the involved parameters and infiltration techniques and develop an understanding of the nanostructure formation mechanism. The effect of spinning rate, polymer solution concentration and temperature have also been evaluated. In the first phase, Poly [N-9′-heptadecanyl- 2,7- carbazole- alt- 5, 5- (4′, 7′- di- 2- thienyl- 2′, 1′, 3′-benzothiadiazole)] (PCDTBT) nanostructures are formed via the porous alumina template of three different infiltration techniques; spin coating, immersion and combination of drop casting & annealing technique. Different solution concentrations of 5, 10 and 15 mg/ml have been evaluated for all the three techniques. For spin coating technique, PCDTBT was deposited onto the alumina template using 1000, 2000 and 3000 rpm spinning rate. PCDTBT nanotubes were successfully grown by immersing the porous alumina template (immersion technique) into 5, 10 and 15 mg/ml PCDTBT solution for 2, 12 and 24 hours followed by annealing at 50 and 150°C. In the combination of drop casting and annealing technique, PCDTBT nanostructures were prepared via porous alumina template by varying the solution concentrations (5, 10 and 15 mg/ml) and annealing temperatures (300, 350 and 400 °C) which are above the PCDTBT melting point. Changes in morphological, optical and structural properties among nanostructures at different concentrations, spinning rate, infiltration time and annealing temperature have been studied using Field Emission Scanning Electron

Microscope (FESEM), Ultraviolet-visible (UV–vis), Photoluminescence (PL) and Raman spectroscopy. The correlation between the parameters involved was also investigated. PCDTBT nanostructures that produced at optimum processing parameters demonstrated more enhanced morphological, structural and optical properties. In the second phase, several selected parameters from the first phase were used to synthesise the *p-n* junction composite of [N-90-hepta-decanyl-2, 7-carbazole-alt-5, 5-(40, 70-di-2-thie-nyl 20, 10,30benzothiadiazole)] (PCDTBT): [6, 6]-phenyl C$_{71}$-butyric acid methyl ester (PC$_{71}$BM). PCDTBT nanostructures were first produced followed by the infiltration of PC$_{71}$BM. Formation of *p-n* junction composite was elaborated in which its morphological, optical and structural properties were compared over its *p*-type counterparts. In the third phase, PCDTBT:PC$_{71}$BM composite nanostructures was used as an active layer in the capacitive type humidity sensor (Al/PCDTBT:PC$_{71}$BM/Al). The humidity sensing characteristics of the sensor were investigated by exposing the organic active layer to a wide range relative humidity (%*RH*) levels at room temperature. Different morphological properties exhibited by each of the nanostructures from different techniques contributed to different abilities of the sensors. PCDTBT:PC$_{71}$BM composite nanostructures produced from immersion technique showed significantly higher sensitivity ~62.34 pF/ %*RH* as compared to the spin coating and combination of drop casting & annealing technique. The ideal capacitive sensors showed the desirable reproducibility, acceptable hysteresis (~11 %), faster response (10 s) and recovery (5 s) time.

Keywords: PCDTBT; PC$_{71}$BM; 1-D Nanostructures; Alumina template; Infiltration; Humidity Sensor

KAJIAN KE ATAS PCDTBT:PC$_{71}$BM NANOKOMPOSIT MELALUI KAEDAH BANTUAN TEMPLAT UNTUK APLIKASI PENGESAN KELEMBAPAN

ABSTRAK

Pencarian bahan yang mempunyai ciri-ciri skala molekul telah membawa kepada pembangunan nanostruktur satu-dimensi (1D). Kedua-dua kaedah menggunakan bantuan templat untuk fabrikasi 1D nanostruktur samaada melalui larutan mahupun cairan adalah mudah dan menjimatkan. Kaedah ini telah digunakan untuk menghasilkan pelbagai jenis nanostruktur dengan ciri-ciri morfologi, optik dan struktur yang berbeza. Walau bagaimanapun, parameter dan teknik yang mengawal sifat akhir masih tetap samar-samar. Penyelidikan ini bertujuan untuk menyiasat parameter dan teknik penyusupan yang terlibat selain mengembangkan pemahaman tentang mekanisma pembentukan nanostruktur. Kesan kadar putaran, kepekatan larutan polimer dan suhu juga telah dinilai. Pada fasa pertama, nanostruktur PCDTBT dibentuk melalui tiga teknik penyusupan yang berlainan menggunakan templat alumina berpori; putaran salutan, rendaman dan kombinasi titisan jatuhan & teknik penyepuhlindapan. Kedua-dua teknik putaran salutan dan rendaman menjalani mekanisma larutan polimer pembasahan manakala teknik titisan jatuhan & penyepuhlindapan menggunakan mekanisma cairan polimer pembasahan. Kepekatan larutan yang berbeza 5, 10 dan 15 mg / ml telah dinilai untuk ketiga-tiga teknik. Untuk teknik putaran salutan, PCDTBT telah didepositkan ke templat alumina menggunakan kadar putaran 1000, 2000 dan 3000 rpm. Nanotiub PCDTBT berjaya dihasilkan dengan merendamkan templat alumina (teknik rendaman) ke dalam 5, 10 dan 15 mg / ml larutan PCDTBT selama 2, 12 dan 24 jam yang kemudian disepuh lindap pada 50 dan 150 °C. Dalam kombinasi titisan jatuhan dan teknik penyepuhlindapan, nanostruktur PCDTBT dihasilkan melalui liang templat alumina dengan mengubah kepekatan larutan (5, 10 dan 15 mg / ml) dan suhu penyepuhlindapan (300, 350 dan 400 °C) yang melebihi titik pencairan PCDTBT.

Perubahan sifat morfologi, optik dan struktur di antara nanostruktur dengan kepekatan, kadar putaran, masa penyusupan dan suhu penyepuh yang berbeza telah dikaji melalui FESEM, spektra UV-vis, PL dan Raman. Hubungan antara parameter yang terlibat juga diperhatikan. Nanostruktur PCDTBT yang dihasilkan pada gabungan parameter yang optimum menunjukkan ciri morfologi, struktur dan optik yang lebih baik. Dalam fasa kedua, beberapa parameter terpilih dari fasa pertama akan digunakan untuk mensintesis komposit simpang *p-n* [N-90-hepta-decanyl-2, 7-carbazole-alt-5, 5- (40, 2-thie-nyl 20, 10,30benzothiadiazole)] (PCDTBT): [6, 6] -phenyl C71-butyric metil ester ($PC_{71}BM$). Nanostruktur PCDTBT dihasilkan pada permulaan diikuti dengan penyusupan $PC_{71}BM$. Pembentukan simpang *p-n* diuraikan di mana sifat-sifat morfologi, optik dan struktur dibandingkan dengan rakan-rakan *p*-jenisnya. Dalam fasa ketiga, komposit nanostruktur PCDTBT:$PC_{71}BM$ digunakan sebagai lapisan aktif dalam sensor kelembapan jenis kapasitif (Al/PCDTBT: $PC_{71}BM$/Al). Ciri-ciri pengesan kelembapan telah disiasat dengan mendedahkan lapisan aktif organik ke pelbagai tahap kelembapan relatif (*%RH*) pada suhu bilik. Ciri-ciri morfologi yang dipamerkan oleh nanostruktur masing-masing yang berbeza menyumbang kepada keupayaan pengesan yang berlainan. Komposit nanostruktur PCDTBT: $PC_{71}BM$ yang dihasilkan daripada teknik rendaman menunjukkan sensitiviti yang lebih tinggi ~ 62.34 pF /*%RH* berbanding dengan putaran salutan dan gabungan titisan jatuhan dan penyepuhlindapan. Sensor kapasitif yang ideal menunjukkan kebolehan semula jadi, histeresis yang boleh diterima (~ 11 %), tindak balas (10 s) dan masa pemulihan (5 s) yang lebih cepat.

Keywords: PCDTBT; $PC_{71}BM$; 1-D Nanostruktur; Templat Alumina; Penyusupan; Pengesan kelembapan

ACKNOWLEDGEMENTS

All praises and glory to Almighty Allah (swt) for giving countless blessings, including physical and mental strength in me, which helped me in completing this thesis. I humbly offer salutations upon all Prophets, the source of guidance and knowledge to all mankind. The work presented in this thesis would not have been possible without my close association with many people. I take this opportunity to extend my sincere gratitude and appreciation to all those who made the completion of this PhD journey possible.

I would like to express my deepest gratitude towards my research advisors, Dr. Azzuliani Binti Supangat and Associate Prof. Dr. Khaulah @ Che Som Binti Sulaiman. I extend my heartfelt respect for their persistent encouragement and diligent supervision. Their understanding towards my weakness and determination in helping me to overcome them really impress me enough. Their co-operative and friendly nature is indeed exemplary. Thank you also for the chances and trust they gave to me. I could not have imagined having a better advisor and mentor for my PhD study.

Special thanks to my fellow lab mates Adilah, Azlinda, Haziq, Zharfan, Saipul, Doris, Farhanah, Aishah, Yanti, Najwa, Najiha, Ain, Karwan, Izzat, Shahino and all the LDMRC members who made my PhD journey a delightful and inspiring experience. They have been so supportive and always there when I am in need. No research is possible without infrastructure and requisite materials and resource. For this I extend thanks to Department of Physics, Faculty of Science, University of Malaya for providing me with the requisite institutional facilities throughout my research tenure.

Special thanks to the University of Malaya for the project funding under the University Malaya Postgraduate Research Grant (PG093-2014A), the University of

Malaya High Impact Research Grant UM-MoE (UM.S/625/3/HIR/MoE/SC/26), Fundamental Research Grant Scheme (FP002-2013A) and Ministry of Education Malaysia for financially supporting my study.

I am also grateful and highly indebted to my beloved husband Arif Asyraf bin Yaacob, for the sleepless night we have together, for helping` me in taking care of our two little girls and the household chores as well, for always around at times where I thought it is almost impossible to continue, for always be patience in handling my stress, helped me to keep things in perspective, etc. Not to forget my father, Bakar bin Ibrahim and my younger brother, Abdullah bin Bakar who living under one roof and always tried to understand my situations. I consider myself the luckiest in the world to have a lovely family, standing beside me with their love and unconditional support. For my littles cuties (Hasanah and Sakinah), I would like to apologize for the time that has been borrowed from you both for the sake of this PhD journey completion.

As always it is impossible to mention everybody who had an impact to this work. I feel a deep sense of gratitude for my uncles, aunties, relatives, all friends and family members. Their infallible love and support has always been my strength. Last but not the least, thanks to everyone, who is not, mentioned here, for his/her contribution, direct or indirect during the completion of my research work. Thank You!

TABLE OF CONTENTS

LIST OF FIGURES

LIST OF TABLES

LIST OF SYMBOLS AND ABBREVIATIONS

1D	:	One dimensional
BHJ	:	Bulk-heterojunction
CPs	:	Conjugated polymers
CVD	:	Chemical Vapour Deposition
Cz	:	Carbazole
DI	:	Deionized
D / A	:	Donor / Acceptor
FESEM	:	Field Emission Scanning Electron Microscope
HRTEM	:	High Resolution Transmission Electron Microscope
HOMO	:	Highest occupied molecular orbital
kHz	:	Kilohertz
LUMO	:	Lowest unoccupied molecular orbital
NNI	:	National Nanotechnology Initiative
N_2	:	Nitrogen
PL	:	Photoluminescence
PVD	:	Physical vapour deposition
PA	:	Polyacetylene
PT	:	Polythiophene
PAn/PANi	:	Polyaniline
PPy	:	Polypyrrole
PPV	:	Poly(p-phenylene vinylene)
PPP	:	Poly(p-phenylene)
PF	:	Polyfluorene
$PC_{61}BM$	:	Phenyl-C_{61}-butyric acid methyl ester

$PC_{71}BM$	:	Phenyl-C_{71}-butyric acid methyl ester
pF	:	Pico Farad
PCDTBT	:	Poly[N-9′-heptadecanyl-2,7-carbazole-alt-5,5-(4′,7′-di-2-thienyl-2′,1′,3′-benzothiadiazole)]
rpm	:	Revolutions per minute
RH	:	Relative Humidity
THF	:	Tetrahydrofuran
UV-vis	:	Ultraviolet-visible
wt%	:	Weight percentage

CHAPTER 1: INTRODUCTION

1.1 Introduction

The interest in nanomaterials increased considerably after the launch of National Nanotechnology Initiative (NNI) in 2001. Since then, nanomaterials have been used in numerous applications including energy storage (Zhang et al., 2013), electrical devices (Leonard & Talin, 2011) and sensors (Holzinger et al., 2014). Everything from industrial technology (Corti et al., 2002) to even cosmetics used (Raj et al., 2012) has some sort of nanotechnology being used inside. Moreover, ‘nano’ term has been overly used in many products as a marketing tool.

Materials can be categorised into several types, which are organic, inorganic, metallic or composite. Up to now, inorganic- and metallic-based nanotechnology are the the main choices for commercialisation due to their strong chemical bonding nature that holds their molecules or ions together. The strong ionic bonds in inorganic nanomaterials allow control over the dimensions of uniform nanostructures to be fabricated via techniques such as chemical vapour deposition (CVD). Meanwhile, van der walls forces or weak hydrogen bonding that hold organic molecules together has caused many attempts to grow ‘homogenous’ 1D nanostructures such as nanowires via CVD to fail. However, the hazardous impact due to the inorganic nanomaterials towards environment and human health (Kumar et al., 2014) has opened up the room for organic-based nanotechnology to be intensively investigated.

Not all the methods used for fabricating inorganic nanostructures are applicable for the fabrication of organic nanostructures. Several methods with special approach such as vapour deposition (Liu et al., 2003), self-assembly from aqueous solutions (Ryu et al., 2008) and reprecipitation-based method (Al-Kaysi et al., 2005) have been successful in synthesising the organic nanostructures made from selected materials. There are some other methods that can be used to fabricate organic 1D nanostructures, however, most of these do not provide high yielding results and cost a fortune. Hence, the template-assisted method is favoured due to it cost effective and mass-scale production capability.

The introduction of organic polymer into humidity sensing active layer is initiated since the last four decades (Chen & Lu, 2005). Despite being less efficient as compared to ceramic or metal oxide-based devices, organic polymer-based humidity sensors offer special advantages such as economic, highly flexible, effortless processing and environmentally friendly (Ahmad et al., 2013; Li et al., 2008). Owing to these features, research involving organic polymer-based humidity sensors has shown a tremendous progress since then.

The presence of humidity or water vapour in our surrounding air can affect human comfort and influence various physical, chemical and biological processes either in industries or in our daily life. Hence, humidity sensing is very crucial in environmental monitoring purposes as well as industrial process since it can affect the production cost, health and safety of the personnel. However, there are many aspects to be considered and intensively investigated in order to produce organic-based humidity sensor that can meet the standard of practical purpose. One of the important factors that affect humidity sensor performance is the degree of porosity of the sensing film (Azmer et al., 2016; Farahani et al., 2014). Both pores and its traits such as size, distributions, volume and dimensions is vital to initiate any changes in the sensing film properties either physically or chemically (Aziz et al., 2012).

1.2 Motivation

PCDTBT is an auspicious *p*-type conjugated polymer that holds outstanding electrical conductivity and optical properties (Burgues-Ceballos et al., 2015; Kannappan et al., 2012; Moon et al., 2012; Yang et al., 2011). Due to these superior properties, PCDTBT have been utilised as an active layer in the form of thin film in light harvesting-based devices such as photovoltaic devices (Boland et al., 2010; Murugesan et al., 2015; Wang et al., 2012) and rarely been exploited in other field of applications. To the best of my knowledge, so far only one research (PCDTBT nanofibers) on modification of PCDTBT thin film into 1D nanostructures is available in literature (Kim et al., 2014).

From previous reports, the combination of electron donating-conjugated polymer and electron accepting-fullerene in a composite form has been demonstrated to exhibit remarkable properties such as high collection efficiency which results from a bicontinuous network of internal donor-acceptor heterojunctions in solar cells devices (Blouin et al., 2007; Park et al., 2009; Yu et al., 1995). Furthermore, enhancement in the electrical properties of the composite structures compared to its separated materials has also been observed (Kumar et al., 2015). However, the investigation towards other applications for these promising composite properties has not been exploiting yet.

In recent years, 1D nanostructures have attracted a great amount of attention because of its distinctive properties that differ and unique from their constituent atoms or the bulk materials (Gleiter, 2000). One of the most generally used methods in preparing 1D polymer nanostructure is the template-assisted method due to its cost effective, versatility and simplicity (Ahmad Makinudin et al., 2015; Al-Kaysi et al., 2009; Bakar et al., 2015). Although different types of 1D nanostructures can be prepared through template-assisted method, the relationship between the preparation condition such as parameters, infiltration technique and combination of the parameters involved with the resultant properties (morphological, optical and structural) of the nanostructures has not fully understood.

Superior physical, mechanical and thermal properties owns by the ceramic-based humidity sensor allow them to dominate the market as compared to the other types of hygrometers devices. However, laborious effort is needed in order to produce highly porous surface structure during the fabrication of ceramic-based humidity sensor (Jain et al., 1999). Due to these matters, the intensive research in other types of humidity sensor such as organic polymer is always substantial. The degree of porosity on the sensing surface layer is one of the crucial factors in determining the final performance of the sensors (Azmer et al., 2016; Salehi & Jamshidi Kalantari, 2007). Although organic polymer-based sensor has lower sensitivity, there are always room for improvement since it offers simplicity in modification during the fabrication process. Hence, the influencing factor such as porosity could be easily altered and improved.

Therefore, the motivation and aim of this works is to explore PCDTBT:PC_{71}BM composite *p-n* junction in another field of applications other than light harvesting-based devices based on the superior properties it possess. PCDTBT has been reported to exhibit the longest operating lifetime up to 7 years at ambient conditions in solar cells applications (Peters et al., 2011; Wang et al., 2012). This indicates PCDTBT has high stability which is worth to be explored in various other research fields and applications. It is believed that the great properties offered by 1D nanostructures will enhance the properties of PCDTBT:PC_{71}BM composite material. Due to the simplicity and versatility as well as cost effectiveness, the template-assisted method is chosen with the aim to further clarify the interrelating factors in the formation of polymer nanostructures. Since the template-assisted method offers an easy way to manipulate the morphological and optical properties of the produced 1D nanostructures, high porosity of the nanostructure film can be obtained which is very beneficial in humidity sensing applications.

1.3 Research Objectives

The objective of this research is to develop a fundamental understanding of the mechanism of the nanostructures formation through the solution or melt alumina template wetting and to relate their morphological, optical and structural properties using different infiltration techniques and parameters. Investigation of the produced nanostructures in terms of humidity sensing applications was also been conducted. The objectives of this research work can be summarised as follows:

- To fabricate various PCDTBT and PCDTBT:$PC_{71}BM$ composite nanostructures using different infiltration techniques of template-assisted method.
- To determine the mechanism of nanostructures formation during template wetting for different parameters.
- To determine the effect of critical parameters involved in the formation of PCDTBT and PCDTBT:$PC_{71}BM$ composite nanostructures on their properties (morphological, optical and structural properties).
- To identify the relationship between the morphological characteristics of the sensing layer and the electrical properties of the fabricated sensors.

1.4 Thesis Frameworks

Chapter 2 provides the theory and literature review to present an overview of the latest progress made in the field of organic polymer nanostructures formation using template-assisted method focusing on PCDTBT and PCDTBT:$PC_{71}BM$ composite. The theory and underlying principles related to the topic are further explained in this chapter. The working mechanisms of humidity sensors are also presented. Extensive background information on previous studies and recent finding related to the research topics have been further elaborated.

Chapter 3 outlines the materials used and experimental methods as well as characterisations procedures that have been carried out throughout the present research works.

In chapter 4, results, discussion and analysis related to the formation mechanism of PCDTBT nanostructures using three different infiltration techniques, which are spin coating, immersion and combination of drop casting & annealing techniques are provided. Both solution and melt wetting were utilised within these three techniques. The relationship between the produced nanostructures at varied parameters and the resultings properties (morphological, optical and structural) of the nanostructures have also been discussed in this chapter. The optimum combination of parameters was selected for the fabrication of PCDTBT:$PC_{71}BM$ composite nanostructures.

Chapter 5 discusses the effect of infiltration of $PC_{71}BM$ on the properties of the PCDTBT nanostructures. The mechanisms of the infiltration of $PC_{71}BM$ into the infiltrated PCDTBT have been elaborated. The morphological, optical and structural properties between PCDTBT:$PC_{71}BM$ composite and PCDTBT nanostructures were compared and carefully discussed in this chapter.

The fabrication and electrical characterisation of the capacitive humidity sensor have been reported in Chapter 6. Discussion and analysis of the results that obtained from the measurement of the humidity sensing behaviour of PCDTBT:$PC_{71}BM$ composite-based device have been presented. Relationships between the novel morphological structures of the active sensing layer and the sensing performance of the device have been discussed thoroughly.

Finally, the research work reported in this study was summarised in Chapter 7. Author’s point of view on the future research directions has been given in the second section of this chapter.

CHAPTER 2: THEORY AND LITERATURE

This chapter details the literature review and theory related to the field of organic polymer nanostructures formation using template-assisted method with focus on the polycarbazoles derivative of PCDTBT and its composite of PCDTBT:$PC_{71}BM$. The theory and underlying principles are the explained in this chapter. The working mechanisms and principles of humidity sensors are also presented. Extensive background information on previous studies and recent findings related to the research topics are further elaborated.

2.1 Wettability

Various industries such as printing, painting and textile utilised wetting phenomena in most of their products. Hence, wettability has become the main concern in most research areas. Once a liquid and a surface come into a contact between each other, the surface will get wet by a liquid and this phenomenon is known as wettability. How the liquid wets the surface depends on the interactions that occur between them, in which, different liquids will have a different wetting mechanism on a particular surface. For instance, a material with good adhesion properties may wet a surface by increasing the interactions between itself and the surface by forming either a chemical or electrostatic bond, or by increasing the intermolecular forces among them.

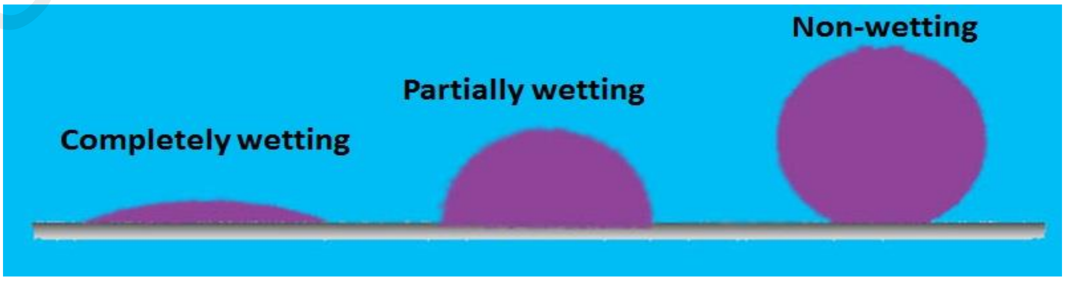

Figure 2.1: Wetting category of completely wetting, partial wetting and non-wetting.

Surface can be either wet partially (partial wetting) or completely (complete wetting) as well as cannot (non-wetting) be wet by a particular liquid as illustrated in Figure 2.1. Wetting can be affected by surface's roughness (Huh & Mason, 1977; Prabhu et al., 2009), chemical heterogeneity or surface contamination (Yuan & Lee, 2013) and molecular re-structuring (Zheng et al., 2009), briefly described as follows:

2.1.1 Molecular Interactions

Wettability involved molecular interactions between a liquid and a surface. Most of the interfacial phenomena and interactions that occur at the surfaces are governed by the van der Waals forces which originate from the atomic and molecular levels interactions (Bonn et al., 2009; Luanphaisarnnont, 2009). Van der Walls forces can be divided into three types which are Keesom interactions (permanent dipole-permanent dipole), Debye interactions (permanent dipole-induced dipole) and London interactions (induced dipole-induced dipole) (Luanphaisarnnont, 2009). The latter forces are commonly present in the molecules and are very important in many aspects including adhesion, physical adsorption, and surface tension in both the biological and non-biological polymer molecules. The properties of liquids, gases and solids are also partly contributed to these forces. Meanwhile, London forces which are also known as dispersion forces are repulsive over a long distance unlike the previously mentioned forces (Keesom and Debye interactions) that are always attractive. Different types of interactions may occur among the molecules depending on the functional group and type of charge they possess. Various types of interactions that occur at a material's interface contribute to the surface energy of the interface.

2.1.2 Surface Energy

Surface energy results from the intermolecular forces where molecules at the surface are exposed to unbalanced forces and having extra energy compared to the molecules in the bulk. The surface energy strength depends on the number of broken bonds associated with the surface and nature of the broken bonds (Fraunhofer, 2012). New surfaces can be created either by increasing the surface area or by stretching the pre-existing surface with a static number of atoms which then modifying its strain. Therefore, the surface energy of a solid is the reversible work required per unit area to form a new surface, while its surface tension is defined as the work needed per unit area to elastically stretch a pre-existing surface (Bonn et al., 2009; Fraunhofer, 2012).

Meanwhile, surface energy of a liquid involves the internal force, which tends to reduce the surface area to minimum. This additional energy can be described using a specific term “surface tension”, since atoms in a liquid can diffuse rapidly to accommodate any variations in the surface energy (Navascues, 1979). Furthermore, a liquid cannot withstand any shear stress. Surface energy and interfacial energy are well correlated with each other which is the work per unit area to form a new interface/surface at constant temperature and pressure (Holm & Storp, 1980; Jacobasch, 1993). These energies play an important part especially in wetting phenomena.

2.2 Conjugated Polymers (CPs)

A lot of new research regarding conjugated polymers (CPs) that emerged within a short period has been very useful for the future research development in the field. Before mid-1970s, CPs did not draw significant research attention until the discovery of free standing thin films of polyacetylene that could be doped to exhibit high electrical conductivity (Chiang et al., 1977). Since then, new fields of polymer chemistry and physics have emerged (Pethrick, 1994). CPs are polymers with spatially extended π-bonding system that exhibit good electrochemical activity, high conductivities, unique optical properties and biocompatibility. Due to these superior traits, CPs are considered as the promising candidates in many areas including nanotechnology and nanoscience.

Conjugated molecular structure in the polymer main chain is one of the exclusive features of the CPs where π-electrons delocalize over the whole polymer chain. Several main chain structures of representatives CPs including polyacetylene (PA), polythiophene (PT), polyaniline (PAn or PANi), polypyrrole (PPy), poly(p-phenylene vinylene) (PPV), poly(p-phenylene) (PPP), polycarbazole (Cz) and polyfluorene (PF) are shown in the Figure 2.2.

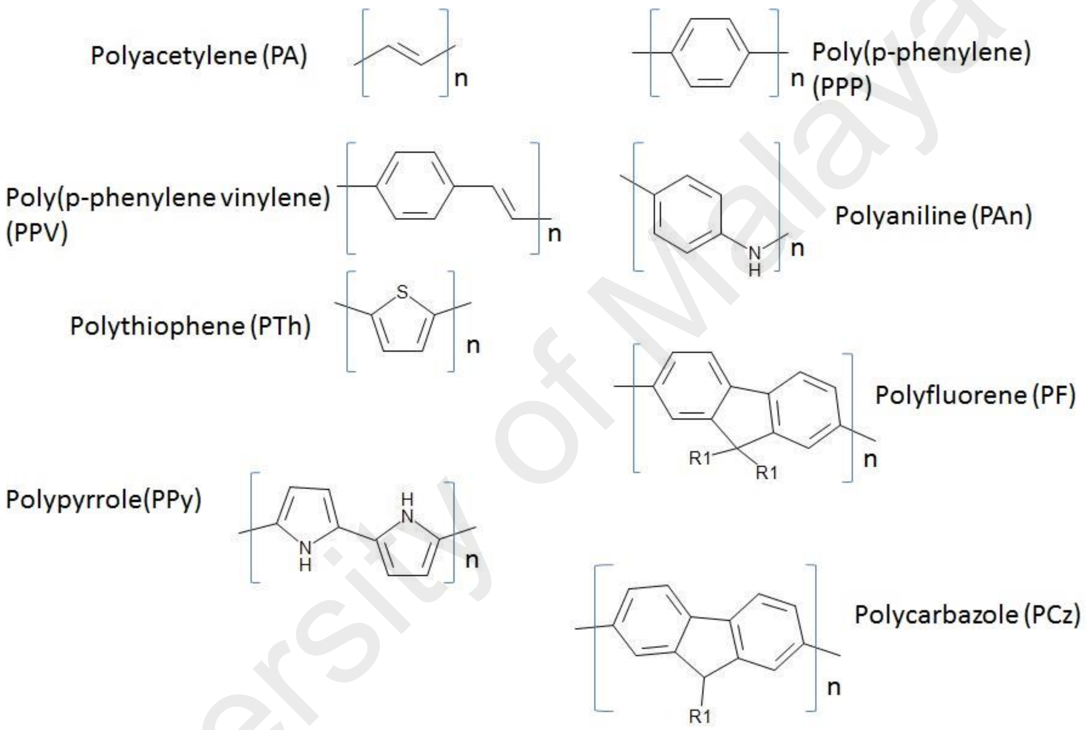

Figure 2.2: Main chain structures of several representative conjugated polymers.

2.2.1 Polycarbazoles

Carbazole is a tricyclic fused aromatic hydrocarbon consisting of two benzene rings fused to a pyrrole ring and polycarbazoles is a carbazole-based polymeric materials. Among the other conjugated polymer, polycarbazole is very fascinating for the following reasons (Boudreault et al., 2010; Morin et al., 2005; Souharce et al., 2009):

- Low cost starting material (9H- carbazole).
- Good chemical and environmental stability provided by its fully aromatic ring.
- The chemical, optical and electrical properties can be easily tuned by substituting nitrogen atoms with any functional group.
- The carbazole unit can be easily substituted at the 3- and 6- positions or 2- and 7-positions to provide polycarbazole derivatives, with different properties and potential applications.
- It consists of bridged biphenyl unit which produces materials with a lower band gap.

Due to these features, polycarbazole and its derivatives have become the best candidates for applications in several fields especially in light harvesting devices and molecular electronic (Bovill et al., 2014; Burgues-Ceballos et al., 2015). However, polycarbazole have poor processing abilities due to the π-π electron system along their backbone. Hence, it is essential to prepare mechanically resistant polycarbazole films for practical applications. In order to further improve their thermal, electrical and several other properties, numerous materials have been derived from polycarbazole (Abthagir & Saraswathi, 2004; Burgues-Ceballos et al., 2015; Clarke et al., 2012).

2.2.1.1 Structural Properties

Carbazole is isoelectronic with fluorine (Figure 2.3), however the presence of the electron rich nitrogen provides carbazoles a higher HOMO energy, which makes it, better hole acceptor than fluorine. Other than that, the presence of the ortho-/para-directing activating nitrogen also contributes to the difference of chemistry between carbazoles and fluorine. Up to date, there are four types of polycarbazole, which are 3, 6- 1, 8-, 2, 7- and 3,9-substituted carbazoles.

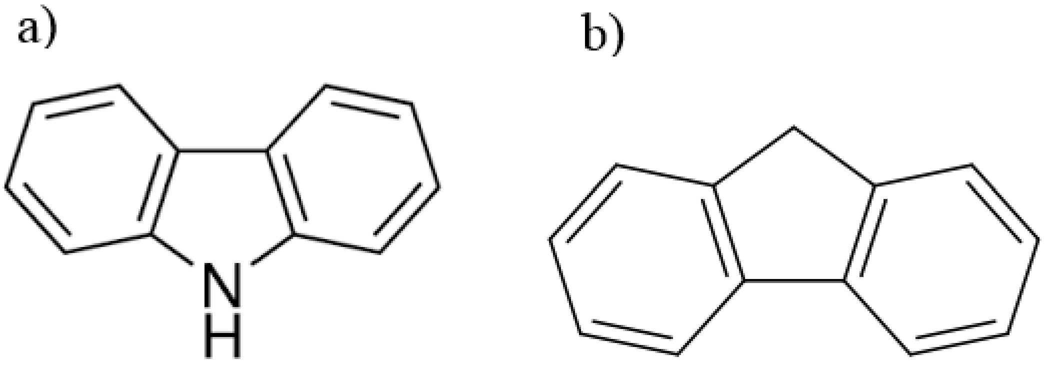

Figure 2.3: Chemical structure of carbazoles (a) and fluorine (b).

Polymerization of carbazole monomer can occur by linking to each other either at 3,6-position or 2,7-position to form poly(3,6-carbazole) or poly(2,7-carbazole), respectively (Cheng et al., 2009). However, meta-linkages of phenylene in poly (3, 6-carbazole) have limited conjugation compared to para linkage present in poly (2, 7-carbazole) which possess longer conjugation length (Cheng et al., 2009; Tan & Sarjadi, 2016). The development to produce a better carbazole unit has continued where in year 2009, poly (1, 8-carbazole) is successfully synthesised (Michinobu et al., 2009). This study also found that poly (2, 7-carbazole) have more efficient connectivity compared to the other two poly (3, 6-carbazole) and poly (1, 8-carbazole). Poly (2, 7-carbazole) also was discovered to be the most suitable donor moieties in photon harvesting devices than the other polycarbazole type (Cheng et al., 2009). This is due to the good hole mobility and better charge diffusion along the 2, 7-linked conjugated carbazole backbones than other linkage carbazole. Raj et al have studied the structural properties of polycarbazoles through FTIR. Various band assignments are summarized and shown in Figure 2.4 (Raj et al., 2010).

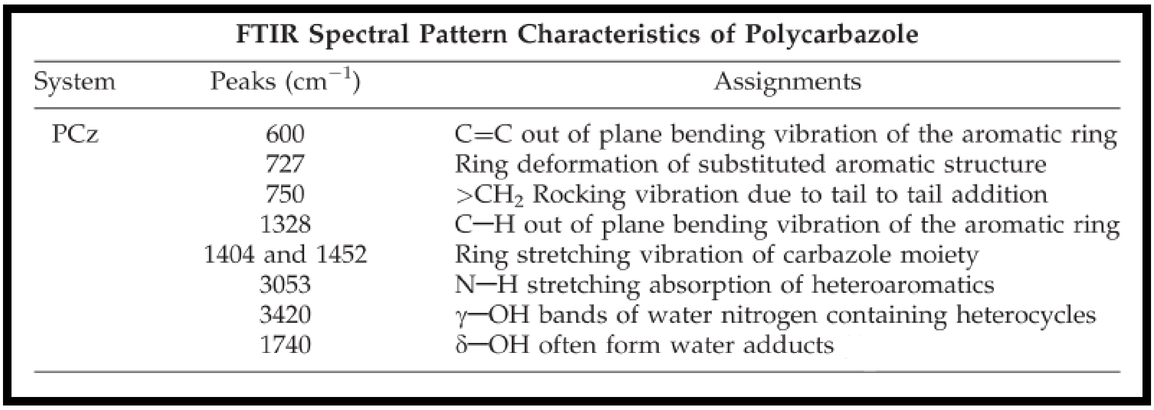

FTIR Spectral Pattern Characteristics of Polycarbazole

System	Peaks (cm^{-1})	Assignments
PCz	600	C=C out of plane bending vibration of the aromatic ring
	727	Ring deformation of substituted aromatic structure
	750	$>CH_2$ Rocking vibration due to tail to tail addition
	1328	C—H out of plane bending vibration of the aromatic ring
	1404 and 1452	Ring stretching vibration of carbazole moiety
	3053	N—H stretching absorption of heteroaromatics
	3420	γ—OH bands of water nitrogen containing heterocycles
	1740	δ—OH often form water adducts

Figure 2.4: FTIR Spectral Pattern Characteristics of Polyarbazole (Raj et al., 2010).

2.2.1.2 Optical Properties

Steady state photoabsorption and fluorescence spectra of polycarbazoles has been analysed by Yasutani et al, which suggest that poly (2, 7-carbazole) has the longest effective conjugation length as compared to poly(3,6-carbazole) (Yasutani et al., 2012). The conjugation break may occur due to the discontinuities in the overlapping of π-orbital between adjacent carbazole units. Poly (3,6-carbazole) shown a red shift and wider fluorescence spectra in chloroform but not in THF. Their study also demonstrated the change in the fluorescence of the copolymer from blue to green once irradiated with UV light, which also occur only in the chloroform but not with THF and toluene. Continuous irradiation of UV at 365 nm causes the fluorescence intensity of the copolymer to gradually decrease with the emerging of new peak at 496 nm. The oxidation of poly(3,6-carbazole) is said to be the dominant factors that contribute to the green fluorescence in chloroform solutions.

In the other study (Fu & Bo, 2005), it is found that effective conjugation length of polycarbazoles could be decrease either with the introduction of alkyl chains onto the carbazole rings or polymerisation with 3,6-linked monomers. Alkyl chains on a carbazole rings are claimed to increase the dihedral angles between the carbazoles rings.

The absorption band of polymer in solid films is broader and longer wavelength compared to its solution spectrum, which is attributed to the aggregation or interactions of the polymer chains in the solid state.

2.2.1.3 Conductivity

The mechanism of conducting polymers has been comprehensively explained by Brédas and Street (Bredas & Street, 1985). The intrinsic electronic properties of the material are determined by its band gap, which is the difference in energy between valence and conduction band (π-π* transition). In the nature of the semiconducting or conjugated polymers, π electrons can be simply removed from or added to the polymer backbone without disturbing the σ bonds. A mobile charge carrier that formed on the polymer backbone known as a polaron is formed due to the removal of π electron from the polymer chain. This polaron (with a spin) is a kind of radical cation that delocalized over several monomer unit (Skotheim & Reynolds, 2006). Meanwhile, bipolaron is formed when the second electron at the polaron's site is removed. The formations of this dicationic with no electron spin enable the further relaxation in polymer geometry as well as tune the band gap of the material. The position and transition between these polaron and bipolaron energy levels plays important part in the absorption present in the UV-vis spectrum of a polymer. Only one absorption band at ca. 330 nm exhibits by a fully reduced polymer which represent benzenoid π–π* transition which is the promotion of electrons from the valence band into the conducting band. Fully oxidized conducting polymers also exhibits a similar transition (π–π* transition) but with additional lower energy absorption bands (polaron–π^*) at ca. 430 nm. Meanwhile, absorbance that are greater than 800 nm usually referred as a free carrier tail (Xia et al., 1995) which attributed by intraband transitions within half-filled polaron and bipolarons bands. The steps such as substituting the hydrobic alkyl chains into the monomer or careful choice of polymerization dopant may be used to alter the properties of the polymer (wettability) (Chang & Hunter, 2011; Darmanin & Guittard, 2014; Sohn et al., 2011).

The electrical conductivity of conducting polymers depends on various factors such as nature and chemical reactivity of the dopant, the process of doping, doping level and polymer crystallinity. Abthagir and Saraswathi have conducted a research on charge transport and thermal properties of polycarbazoles (Abthagir & Saraswathi, 2004). Conductivity in polycarbazole could be loss through the elimination of the dopant, loss in conjugation length and structural reorganization due to heat treatment at certain temperature. The conductivity of polycarbazole gradually increases with the increase in temperature up to 413 K, and decreases rapidly beyond 413 K. Several model theories could be used to explain the conductivity-temperature dependent; one of it is Arrhenius equation of conductivity (Equation 2.1).

$$\sigma = \sigma_0 \exp\left(-\frac{E_a}{kT}\right) \tag{2.1}$$

Where E_a is the activation energy, σ is the temperature dependant quantity (in general), σ_o is the temperature independent quantity, T is the temperature in Kelvin and k is the Boltzmann constant. Arrhenius equation usually applicable around room temperature indicating the interaction of nearest neighbouring charge carriers (Abthagir & Saraswathi, 2004). Practically, higher conductivity film displays thermal activation behaviour with very low activation energy. Hence, higher activation energy indicates that deficient charge carriers at room temperature results in low conductivity of polycarbazole.

2.2.1.4 Wettability and Surface Energy

Polymer wetting properties has been a vital part of surface science for decades. However, researches related to factors affecting the conjugated or conducting polymer wettability are still relatively few. The emergence of various applications where control of wettability is crucial, has contributed to the increase in the research interest. Wetting properties of the polycarbazoles could be explained through basic theory of conducting polymers wetting properties. Once polymer is exposed to a different environment, polymer chains at the surfaces will enables the group rearrangement to occur. This reorientation may lead to spreading of the drop on the surface in order to minimise the interfacial energy between two materials (Andrade et al., 1985; Zhang et al., 1997).

Many initial studies demonstrated the importance of the substrate in prevailing the polymer wetting properties (Geoghegan & Krausch, 2003). A research regarding effect of polymer oxidation state on wettability has also been performed. Research done by Lee et al. has found that the force between liquid and polymer is increased upon doping due to the increased in interaction between water and oxidized polymer and vice versa (Lee, 1998). Meanwhile, Wang et al. found that wetting ability of poly-3-hexylthiophene (P3HT) is strongly related to their oxidation state where P3HT is more hydrophilic in the oxidized state as compared to the poly(3,4-ethylenedioxythiophene) (PEDOT) which is less hydrophilic in their oxidized state (Wang et al., 2006). Wettability is also found to be affected by the polymer oxidation and polymer reduction that doped with different materials (Darmanin & Guittard, 2014). Hence, it is indicated that counter ion plays an important part in determining the wettability of the polymer.

The interactions that occur in conducting or conjugated polymer such as acid base interactions (Kraus et al., 2017), hydrophobic interactions and hydrogen bonding (Darmanin & Guittard, 2014; Zha et al., 2015) has been relate to the surface energy interpretation of various conducting polymers. The dispersive component of surface energy is increase with doping level. Most the studies have shown a strong relationship between oxidation state of polymer with surface energy and wettability.

2.2.2 Polycarbazole Derivatives

During the past few decades, incorporation of various kinds of carbazole derivatives with various types of acceptor units has been intensively studied. Figure 2.5 shows the carbazole-based polymers where X as an acceptor unit which could be thienopyrazine, benzoxadizole, benzothiadiazole, pyrido [3,4-b]pyrazine, quinoxaline and etc (Blouin et al., 2007)

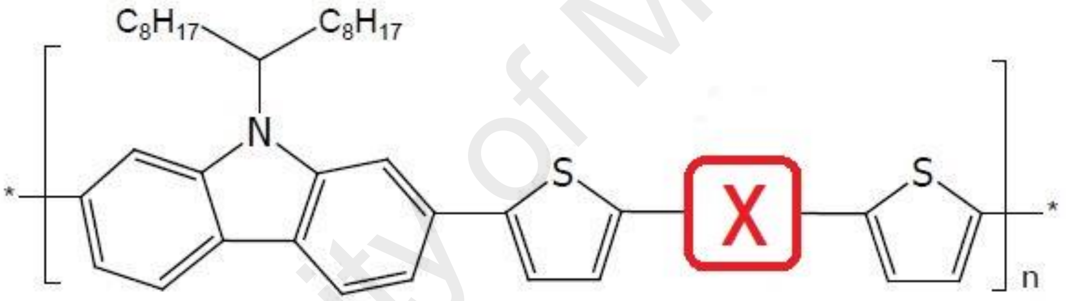

Figure 2.5: Carbazole-based polymers where X as an acceptor unit.

Among these numerous acceptor moieties, 2, 1, 3- benzothiadiazole (BTD) has been intensively investigated and it has established itself as a favourable building block for D-A polymer derivatives (Neo et al., 2015; Wang & Michinobu, 2016). One of the D-A derivatives polymer is poly [N-9′-heptadecanyl 2, 7-carbazole-alt-5, 5-(4′,7′-di-2-thienyl-2′,1′,3′-benzothiadiazole)] (PCDTBT) where utilised 2, 1, 3- benzothiadiazole (BTD) as an acceptor moiety.

2.2.2.1 Poly [N-9′-heptadecanyl 2, 7-carbazole-alt-5, 5-(4′,7′-di-2-thienyl-2′,1′,3′-benzothiadiazole)] (PCDTBT)

PCDTBT is a low band gap polymer made up from carbazole, benzothiadiazole and thiophene unit with alkyl side chain as shown by its constituent molecular structures in Figure 2.6(a-d). PCDTBT is discovered to be a promising donor material which having incredible stability and low HOMO level (Burgues-Ceballos et al., 2015; Cho et al., 2010; Wang et al., 2012). The main properties of PCDTBT such as its optoelectronic properties and solubility are primarily determined by the choice of the conjugated backbone and the position, length and makeup of the alkyl side chains.

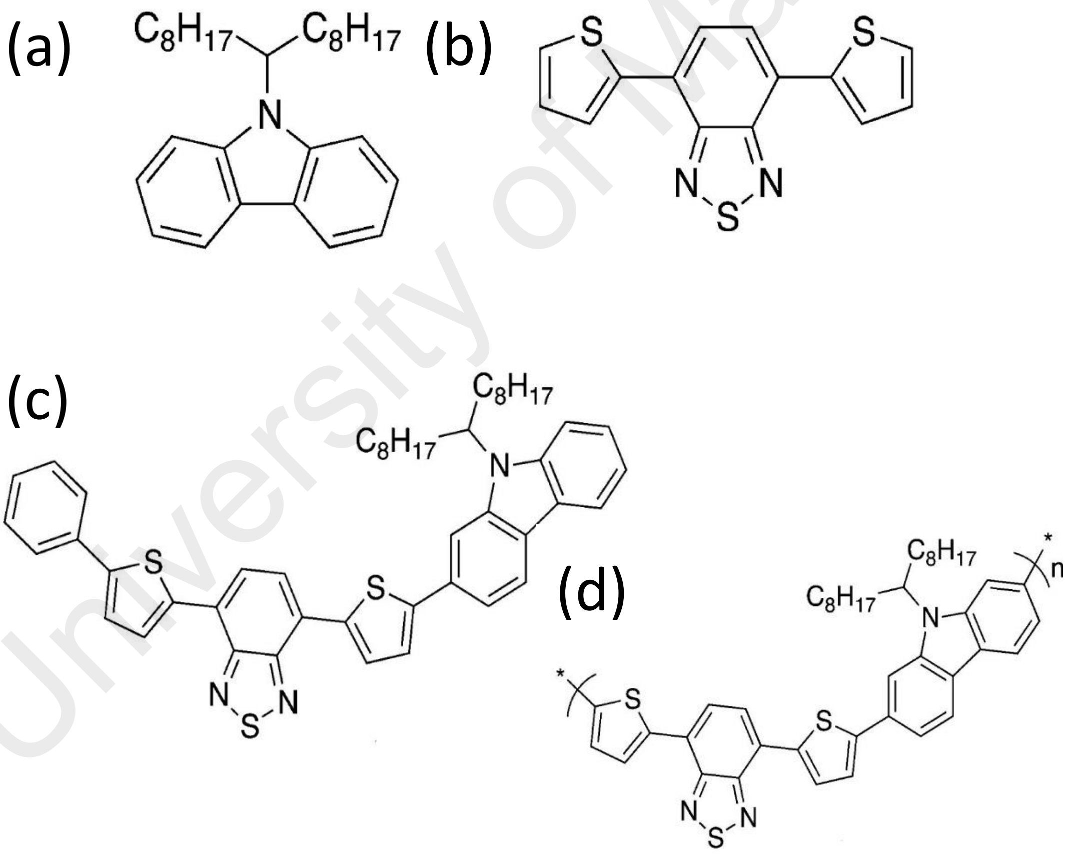

Figure 2.6: Molecular structure of the PCDTBT constituent compounds of (a) carbazole (b) dithienylbenzothiadiazole (DTBT) (c) isolated repeat unit of PCDTBT (CDTBT) and (d) PCDTBT.

The device efficiency and its molecular packing structure (π–π distance and polymer orientation) are well affected by the polymer backbone and the alkyl side chains (Cho et al., 2010; Lu et al., 2012). Large bulky alkyl chains or aryl groups on the carbazole nitrogen atom seem to be important in increasing the solubility and molecular weight of PCDTBT (Blouin et al., 2007). A pure PCDTBT thin film shows "camel back" of two broad absorption bands which represent donor carbazole (Cz) and acceptor dithienylbenzothiadiazole (DTBT) (Banerji et al., 2012) as shown in Figure 2.7. The 'camel back' curves seen from the partial DTBT charge transfer character in the dominant transitions of PCDTBT mainly contribute to the absorption spectrum. According to Banerji et al, these two bands which situated in the visible region are dominated by only one transition where involved partial charge transfer character and some delocalization in the excited state that more significant in the second band. Absorption at shorter wavelength is attributed to π–π* transition, whereas absorption at longer wavelength is known to be due to a intramolecular charge transfer from donor Cz unit to acceptor DTBT unit (Kim et al., 2012; Kim, et al., 2014; Tan & Sarjadi, 2016).

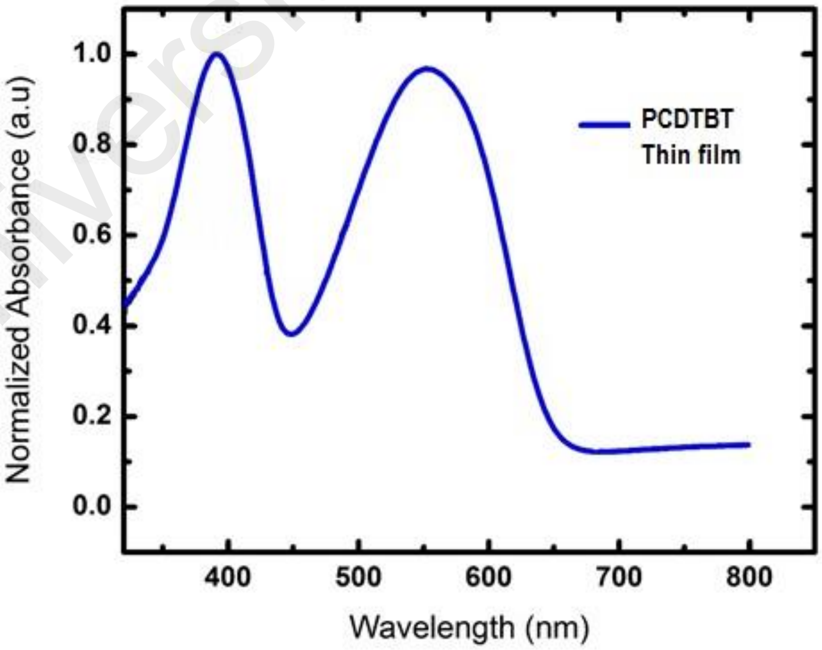

Figure 2.7: UV-vis absorption spectrum of PCDTBT thin film.

2.3 Composite

Conductive polymeric materials have attracted considerable interest in both industrial and academic world for various type of applications such as biosensors (Gerard et al., 2002), humidity sensor (Cai et al., 2013) and optoelectronic devices (Stegamat & So, 2004). However, the electrical performance of conducting polymer often poor due to its low mechanical properties and processability (Kaur et al., 2015). This has led to more current attention being focused towards polymeric composites materials. Past research has also shown that, polymer composite possess a better electrical properties as compared to its individual component (Kumar et al., 2015; Nalwa, 1997). A composite material is made up of two or more constituent materials with considerably dissimilar in physical or chemical properties that produced another new properties when combined (Reviews, 2016). Up to now, fullerene is the best material to be incorporated with the PCDTBT due to its outstanding acceptor component features such as superior ability to transport charge and its high electron affinity (Mi et al., 2014). Fullerene is composed of entirely carbon. Buckyball structure of the fullerene (C60) is a combination of 12 pentagonal and 20 hexagonal rings forming a spheroid shape as shown in Figure 2.8.

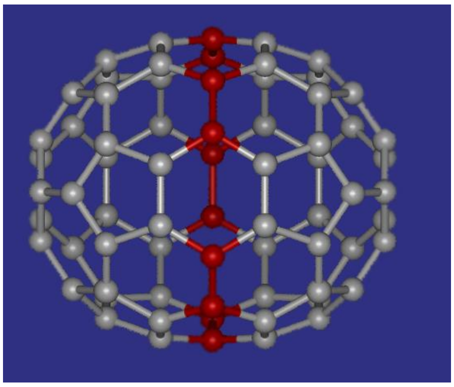

Figure 2.8: Structure of C_{70} molecule where red atoms indicate addition of another five hexagons to the C_{60} molecule.

The most commonly used fullerene derivatives are Phenyl-C61- Butyric-Acid-Methyl-Ester ([60]PCBM) and Phenyl-C_{71}- Butyric-Acid-Methyl-Ester ([70]PCBM).

[70]PCBM have shown some enhanced features compared to [60]PCBM in certain condition such as having higher optical absorption in the visible region (Hare et al., 1991; Huang et al., 2009; Zang, 2011). [70]PCBM have also shown a higher stability compared to [60]PCBM (Kronholm & Hummelen, 2007). Other than that, [70]PCBM is easily to be dissolved in most common solvent. The highly efficient photoluminescence quenching due to the ultrafast photoinduced charge transfer from PCDTBT to PCBM has been reported in previous works (Blouin et al., 2007; Clarke et al., 2012; Provencher et al., 2014). By considering the amazing characteristics of these two materials (PCDTBT and $PC_{71}BM$), the incorporation between this two materials worth to be investigated.

2.4 Polymeric 1D Nanostructures

In recent years, one-dimensional (1D) nanostructures have attracted many researchers to intensively investigate their nature with its fascinated characteristics. Their one dimensionality have produced very interesting chemical, mechanical, electrical and optical properties which pulled-in a lot of consideration for proficient charge transport (Burda et al., 2005; Xia et al., 2003). However, 1D nanostructures have been utilised in the large number of scientific area including optoelectronic, nanoelectronic, diagnostics and sensing. The combination of low dimensionality and organic semiconductor give an excellent complement towards inorganic conductors' due to their desirable characteristics such as an easily tuneable band gap, high mechanical flexibility and greater biocompatibility than many inorganic materials. Other than that, organic nanomaterials can be obtained through inexpensive and readily available synthesis technique.

1D nanostructures of conducting polymers are first reported in the late 1970s by Shirakawa et al. where the formation of films of polyacetylene nanofibers have been observed (MacDiarmid, 2001; Shirakawa et al., 1977) through the polymerisation of acetylene using an Al/Ti catalyst. This area of research has kept on developing as the extensive number of studies have recently revealed an excellent device performance of 1D conducting polymer nanostructures over the bulk conducting polymers (Huang et al., 2003; Tran et al., 2009).

2.4.1 Template-assisted Method (Alumina Template)

Up to now, various methods have been developed in fabricating the 1D nanostructures, i.e. vapour-phase deposition, solvothermal, photochemical and hydrothermal methods, with or without the assistance of template (Ahmad Makinudin et al., 2015; Baruah & Dutta, 2009; Szilágyi & Nagy, 2014). Among the numerous synthesis methods, template-assisted method is a widely used method to obtain 1D nanostructures in a convenient way. Besides being cost effective, template-assisted method is able to produce a large scale of nanostructures in one time fabrication (Lee & Park, 2014). In this template-assisted method, various deposition techniques (spin coating, dip coating, drop casting etc.) with easy tuneable parameters (concentrations, spinning rate, immersion time etc.) could be utilised. Formations of nanostructures by template-assisted method are generally involved three steps, which are preparation of template (in this work, commercially available templates were used), infiltration process (various techniques) and template removal process. Template removal process has to be chosen and conducted in a proper way so that the physical and chemicals properties of the final product are not affected. Template-assisted method is usually divided into two categories of hard and soft template. The different between soft and hard template is summarised in Table 2.1.

Table 2.1: Comparison between soft and hard template.

Soft template	Hard template
Does not have fixed structure.	Rigid material, fixed structure.
Morphology control of your target products is hard to obtain.	Dimensions and specifications of target production can be precisely controlled.
Based on action of the micelle, which forms organic-inorganic phase between surfactant, high polymer, biopolymer and target production.	Used previously prepared template material such as AAO template, mesoporous carbon and polymer microsphere.
Formed within the reaction.	Prepared before reaction.
Easy to eliminate.	Challenging removal process.

The choice of templates is crucial depending on the desired final product and the applications involved. Among these, hard template has very enormous advantages for the synthesis of 1D nanostructures since it has adjustable pore structure and morphology. The samples produced from this method usually have simple process, good dispersion, uniform pore size and simple operation. One of the potential hard templates is Anodic Aluminium Oxide (AAO) or alumina template.

2.4.2 Porous Alumina Template

Porous alumina template has pores that evenly distributed. As reported in the literature, the pore size can be modified in the range of 50 to 200 nm with the density is between 1×10^9 to 1×10^{12} cm^{-2} (Jie et al., 2008; Kai et al., 2010). Conductive polymer, semiconductor and metal has been successfully deposited on the template's pore surface to produce the desired nanostructures for various applications (Xie et al., 2016). Figure 2.9 shows a schematic cross section of alumina template honey-comb structures (Stępniowski & Salerno, 2014). Several geometrical factors such as pore diameter (D_p), interpore distance, diameter of the circle enclosing the hexagonal cell with the pore in its centre (D_c), thickness of the grown oxide (H), thickness of the barrier layer at the pores bottoms (B) and pore density (n) are considered for alumina template features classification.

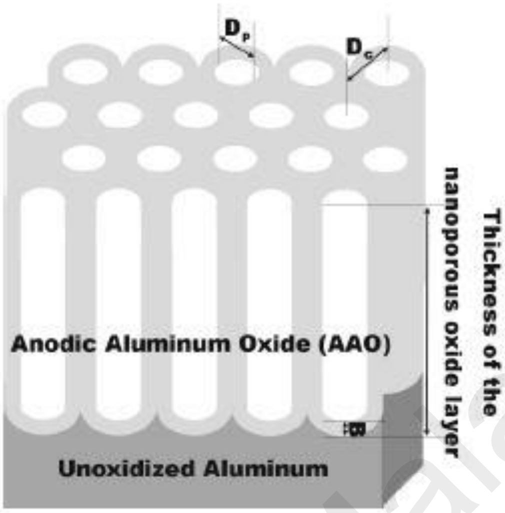

Figure 2.9: Ideal structure of porous alumina template (Stępniowski & Salerno, 2014).

2.4.3 Fabrication of Porous Alumina Template

Usually high purity aluminium is placed into an acidic solution and electrolysis by the anodic oxidation to produce the alumina template. The aluminium is first annealed at ~600 °C in vacuum condition, then thoroughly degreased and electro-polished. Changing the anode voltage, composition and concentration of the electrolyte can control the size and pore’s distribution. Four basic stages are involved in the growth formation of alumina template as shown in Figure 2.10 (Parkhutik & Shershulsky, 1992). It starts with the formation of barrier oxide layer on the electro-polished aluminium in the stage 1 and followed by the crack of barrier oxide layer (stage 2). Then, the pores nucleation process will occur in the stage 3, which leads to the formation of steady state growth of the nanopores (stage 4).

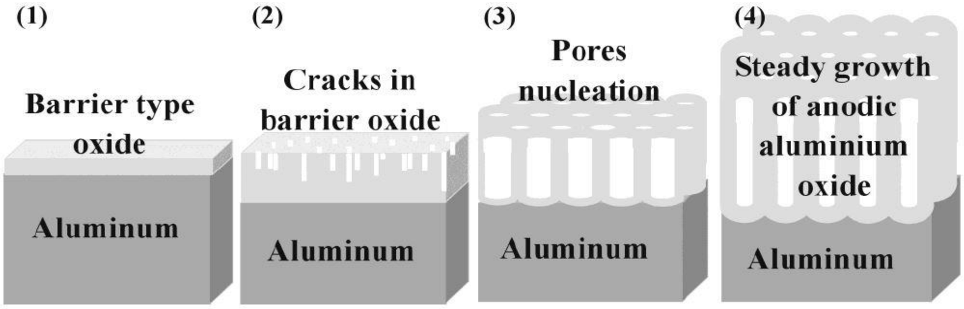

Figure 2.10: Schematic cross section of growth formation of porous alumina template (Parkhutik & Shershulsky, 1992).

However, best ordering pores only occurred at the pores bottom. In order to obtain a highly ordered template's pores, second anodization need to be done (Stępniowski et al., 2011) as illustrated in Figure 2.11. Alumina template that was formed from the first anodization will be removed by chemical etching and left the aluminium surface with concaves with degree of order and uniformity proportional to the first anodization. These concaves will serve as a nucleation sites for the second anodization, which then will result in a highly ordered alumina template.

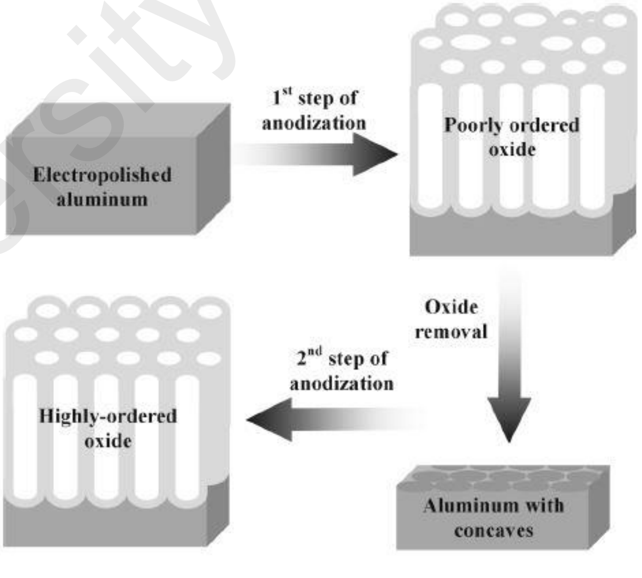

Figure 2.11: Schematic of self-organized pre-patterning of aluminium for the formation of highly ordered AAO (Stępniowski & Salerno, 2014).

2.4.4 Alumina Template Wetting Technique

As the polymer solution passes through the alumina template’s pore, capillary action will take place and cause the solution to spread evenly on the template’s pores surface. The layer of the polymer will be deposited on the template’s surface once the solution evaporates. Attempts to fabricate polymer nanostructures by wetting the porous alumina template have been achieved by several researchers where materials such as poly (vinylidene fluoride), poly (methyl methacrylate), poly (2, 6- dimethyl-1, 4-phenylene oxide), polystyrene, poly (lactic acid) and poly (bisphenol A carbonate) were exploited (Al-Kaysi et al., 2009). The polymer solution will replicate the porous alumina template which then will produce 1D nanostructures either nanotubes (Ahmad Makinudin et al., 2015) or nanorods/wires (Fakir et al., 2014b) depends on the materials, parameters and templating technique involved. Different wetting mechanism based on the concept of capillary action has also applied to each of the produced nanostructures. Two wetting techniques, which are solution and molten-based have been used to produce 1D nanostructures.

2.4.4.1 Melting-Recrystallization Template Wetting Method

One of the routes for fabricating the 1D nanostructure is to melt the polymer and let its molten to wet the template’s pore surface. Complete filling of the nanopore is usually prohibited in this polymer melt method due to the strong adhesive forces between the template’s pore surface and the polymer. The adhesive force between the polymer molecules themselves is much stronger than the cohesive forces. Main factor that influence the flow of polymer melt is the viscosity. Low viscosity indicates that the forces between the polymers melt molecules and template’s surfaces are weak and vice versa. The flow ability of polymer melt or any liquid can be control through viscosity (Fakir et al., 2016). Low surface energy of polymer melt can easily wet the high-energy template’s pore surface either with partial or complete wetting regime. The wetting driven force p from high-energy surface can be described by the Laplace equation shown below (Equation 2.2).

$$p=2\gamma\cos\theta/R \tag{2.2}$$

Where γ is surface tension of polymer melts on alumina surface, θ is contact angle, R is hydraulic radius and equal to half of the radius of a nanochannel. Specifically, the contact angle θ is provided by the solid-gas γ_{SG}, solid-liquid γ_{SL}, and liquid-gas γ_{SG} interfacial tensions as shown in Figure 2.12.

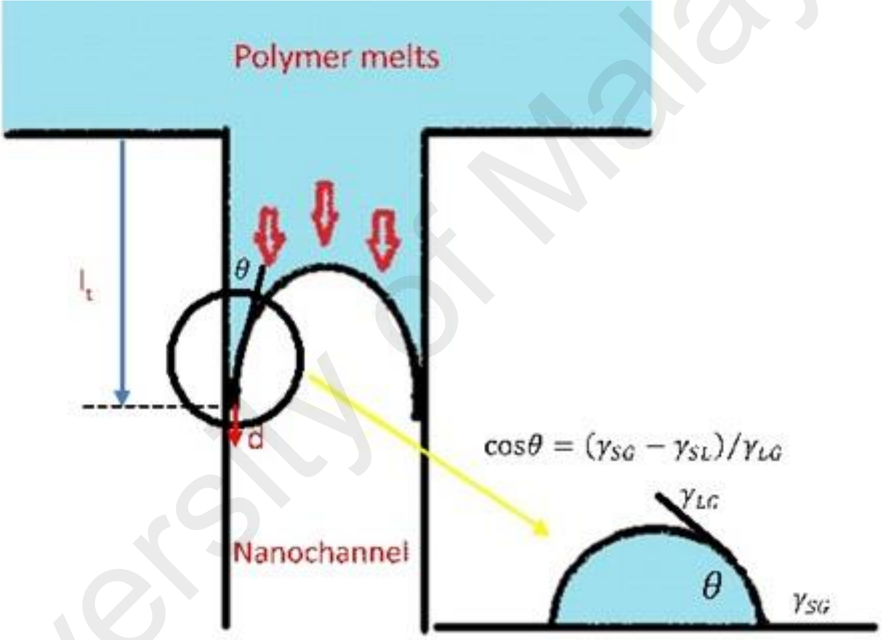

Figure 2.12: Dynamic flow parameters of polymer melt in nanochannels.

Yung et al. have successfully fabricated polyethylene nanofibers with high aspect ratio using alumina template. It is revealed, once the temperature of the polymer melts is higher than the melting point of the materials, the melts will speedily wet and flow inside the channel. The higher flow displacement can be achieved at wetting temperature higher than 160 °C because of the reduction in viscosity of melts with the rise of temperature (Yung et al., 2007). It shows that the polymer melts can wet the alumina nanopores' inner walls with high-energy surface when the majority of polymer materials are melted with the temperature far above the $T_{m.}$ Apart from temperature, the pore size, surface properties, viscosity and pore diameter are some of the parameters that determine the flow of liquid or melt inside the nanochannel (Ali et al., 2015). Another alternative way to fabricate 1D nanostructures is by solution-based template wetting method.

2.4.4.2 Solution-Based Template Wetting Method

When porous alumina template is dip in a polymer solution, the capillary action that takes place will soak up the alumina template rapidly. Strong surface energy of the template’s pore surface compared to the low intermolecular forces within the polymer molecules allows the polymer solution to wet the pore surface. Attempts to fabricate 1D nanostructures using this polymer solution-based approach, is progress rapidly since several years ago using various techniques (Ahmad Makinudin et al., 2015; Bearden et al., 2011; Fakir et al., 2014a).

Doris et al. (Doris et al., 2017) have conducted the special technique under the solution-based wetting in order to expedite the infiltration process. In this technique, centrifugal force is used to assist the infiltration of polymer solution into the porous alumina template. Different infiltration forces are obtained by manipulating rotational speeds that will produce the various forms of nanostructures such as nanotubes and nanorods/wires. Other than that, effect of different solvent on the properties of resulting nanostructures has also been studied via the solution-based method (Bearden et al., 2011).

Both polymer solution and melt template wetting approaches have been conducted by Dougherty et al. in fabricating the 1D nanostructure core-shell (PLLA-PMMA) polymer nanorods (Dougherty & Liang, 2009a). Two steps are involved during the formation of the core-shell nanostructures where outer shell is formed through solution-based approach followed by the infiltration of polymer melt for the core. The shell thickness has been found to be increased as the concentration, viscosity of polymer solution and melt is increased. These approaches could be further explored in a numerous way to enhance the outcomes of nanostructured materials properties. The infiltration techniques that utilise these approaches still do not extensively explore and room for further improvement is always there.

2.5 Applications: Humidity Sensors

In order for the hygrometric sensor to detect any changes in the humidity level at ambient condition, the physical and electrical properties of the sensing materials need to be altered. Different quantity of moisture that absorb and desorb from the surrounding by the sensing materials influenced its properties. One of the important features for efficient absorption and desorption process is the presence of porosity on the sensing film surface (Farahani et al., 2014; Tripathy et al., 2016). Higher porosity of the sensing film has become the main factor for the improved in the humidity sensor sensitivity that has been demonstrated by several past researches (Ahmad et al., 2008; Li et al., 2017). Previously, high performance device of ceramic-based humidity sensor has been related to its high porous structure, which improved the water vapours absorption (Chou et al., 1999; Gusmano et al., 1993). Polymer-based humidity sensors were then develop with the principles analogous to the ceramic-based humidity sensors (Farahani et al., 2014).

2.5.1 Humidity Measurements

The amount of water vapours that pervade the environment can be measured by using several units of measurement such as Relative Humidity (*RH*) and Absolute Humidity (AB) depending on the techniques used. *RH* sensors are commonly applied in our daily life as well as in the research field due to its simplicity and cheaper evaluating mechanism compared to AB sensors. *RH* can be expressed through Equation 2.3.

$$RH\% = \frac{P_V}{P_S} X100 \tag{2.3}$$

Where P_v represents measured partial pressure of moisture in the air and P_s denotes the saturated pressure of the humid air at given temperature. In another word, *RH* can be defined as the ratio of vapour amount in the atmosphere to that of maximum content that can be hold at fixed level of temperature and pressure of the air. It is considered as relative measurement due to its dependent upon magnitude such as temperature.

2.5.2 Sensing Mechanism

The condensation of water occurs throughout the opening capillary pores of the sensing layer during the exposure to high humidity environment (Hong-Tao et al., 1989). Dimensions, density and sizes of the pores give a big influence to the water absorption ability (Banerjee & Sengupta, 2002; Korotcenkov, 2016). Hence, the appropriate manipulation of these characteristics needs to be considered for the enhancement of humidity device. Azmer et al. have reported the fabrication of solution-processed capacitive humidity sensor based on Poly[2-methoxy-5-(2-3 ethylhexyloxy)-1,4-phenylenevinylene]:Polyvinylpyrrolidone (MEH-PPV:PVP) (Azmer et al., 2016). The porous and coarse surface of the sensing layer is believed to be a reason for the sensing parameters improvement. It has been argued that smaller pore radius provides a better condensation of water at lower temperature (Rezlescu et al., 2004).

Once the sensing film gets exposed to humidity, chemisorption process takes place where the first few vapours get condensed on the sensing film surface through chemical adsorptions. During the reactions between the sensing layer and water molecules, free moving hydroxyl groups are produced. These free moving hydroxyl groups will then get attached to metal cations that already permeate the sensing layer. Moreover, immobile secondary layer will take place as the water molecules accumulate on the sensing surface. Rigidity of the first physically absorbed layer is gained from the double hydrogen bonding with the prior formed chemisorbed layer. During this early phase, electron tunnelling that occur between the donor water sites become the main contributor for the electrical conductions (Khanna & Nahar, 1986).

Proton conduction is then initiated by the condensed water vapours on the sensing surface where proton acts as a dominant carrier. Reactions caused by the surrounding water vapours on the sensing surface contribute to the success of the dissociations of condensed H_2O molecules into their ionic components of H^+ and OH^-. Consequently, the increase in conductivity and dielectric constant has caused to the decrease in resistivity.

At low humidity level, only the minimum condensed layers will cover the film surface. However, the continuous aquatic layer that formed at higher humidity is owing to the enormous amount of water vapours. Due to the disordered secondary physisorbed hydroxyl multilayers, proton (H^+) is allowed to move freely in a large degree, which results in substantial conductivity. Diffusion of proton occurs among the nearby OH^- ions. As the humidity is increased, the intensification of water (H_2O) molecules will draw the liberated H^+ to hop between them to produce hydronium ions, H_3O^+. The cycles to produce hydronium ions continue as resulting previous hydronium ions release proton and react with the nearby water molecules. The proton hopping process is illustrated in Figure 2.13.

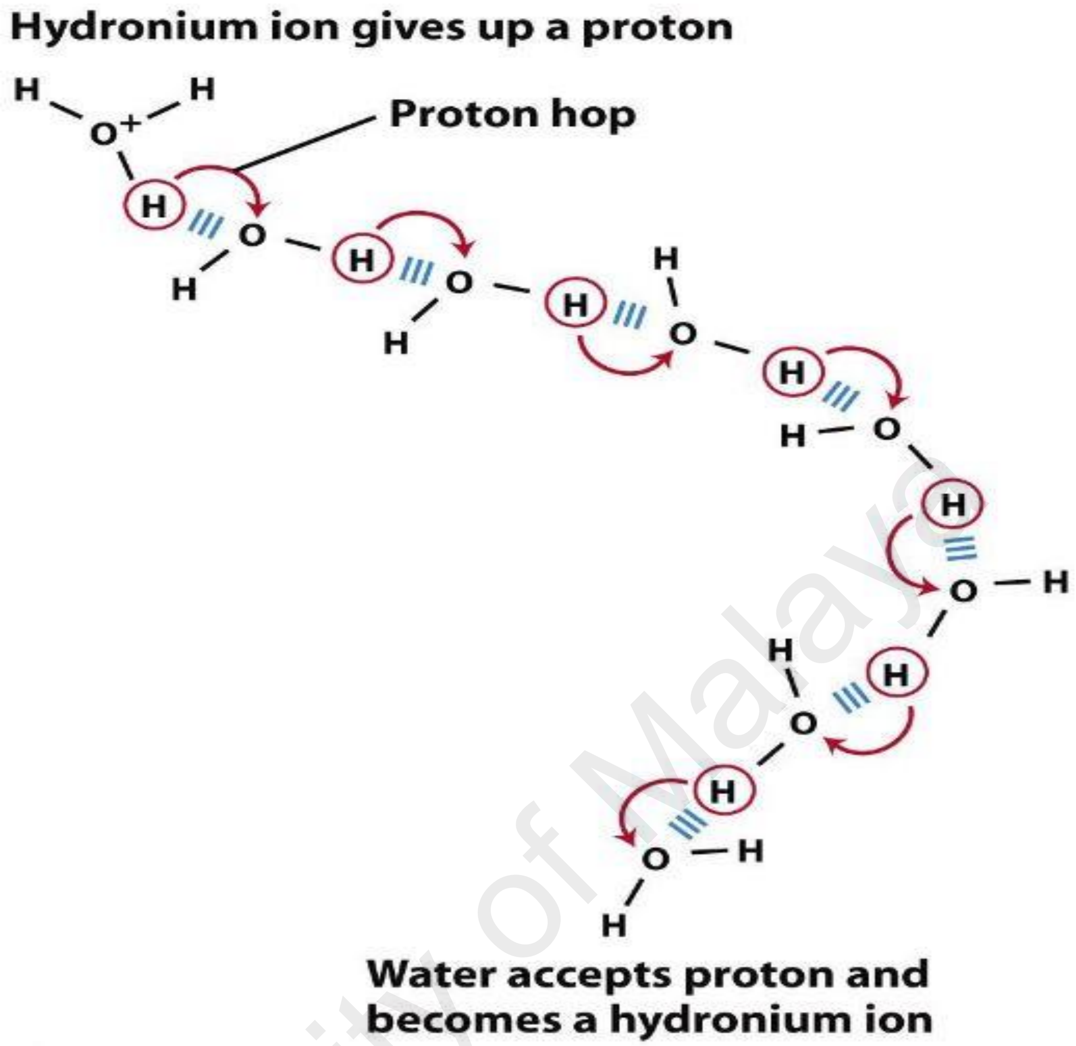

Figure 2.13: Illustration of proton hopping phenomenon (Boyle, 2005).

For sensing mechanism at low humidity level, electronic conduction resulting from electron tunnelling plays a role, while the responsible is take place by ionic conduction from proton diffusion at higher humidity level. During the transitional phase, which is formation of first and second physisorbed layers, dominative transition between electronic and ionic conduction is occurred. Changes in environment humidity level that trigger such changes in electrical properties are one of the common sensing mechanisms in hygrometer device.

2.5.3 Ceramic-Based Humidity Sensors

Metal oxide or ceramic-based humidity sensor mostly exploited in the market compared to the other sensors types owing to their superior traits of highly durable, mechanically stable, chemically potent and high thermal tolerance. However, rigorous fabrication process usually conducted for the denser porous structure of ceramic film to be realised, either through conventional (Jain et al., 1999) or most recent methods (Hu et al., 2008).

Ceramic sensor types can be divided into two categories of capacitive and resistive type that utilise change in dielectric permittivity of the ceramic film and conduction mechanism of the film for vapour detection, respectively. Efficient vapour permeability could be obtained through condensation and following diffusion of water molecules inside the opening pores by manipulating the microstructures of the ceramic grainy surface. The frequent distributions, dimensions and surface area are some of the important factors to be considered which affect the condensation rate (Rezlescu et al., 2004) and vapour diffusion. Ceramic materials that possess unique properties can be optimised, which enable it to form an ideal active layer for humidity sensing applications.

As detailed in the aforementioned section, conduction mechanism of ceramic-based humidity sensor rely on physisorption and chemisorption rate of water vapour that occur on the ceramic film surface which then altered their electrical properties through protonic conduction (Nitta & Hayakawa, 1980). Capacitive humidity sensor of perovskite structured ceramic film is investigated by Smit et al (Smit et al., 2013). This type of ceramic humidity sensor utilised electronic conduction mechanism through electron donation as its main charge carrier and work remarkably fine at higher temperature (Wang & Virkar, 2004).

The sensing range of ceramic humidity is commonly found to be as low as 8 %*RH* to as high as greater than 97 %*RH* which is very practical for commercial application (Bauskar et al., 2012; Jingbo et al., 2001; Upadhyay, 2008). Zhu et al. has demonstrated a silica SBA-15 based humidity sensor with widest sensing range of 1-100 % relative humidity that have the highest sensitivity around 11-97.6 *%RH*. Apart from having widest sensing range, this type of sensor has also reported to exhibit good stability, short response-recovery time, well reproducibility and narrow hysteresis (Zhu et al., 2010).

Metal oxide is one of the promising ceramic humidity-based sensors due to their intriguing mechanical and chemical properties (Tripathy et al., 2016). Physical vapour deposition (PVD) or chemical vapour deposition (CVD) is some of the techniques used in device fabrication. However, CVD is more favourable since it offers better micro-structural control of the film, synthesis of contamination free sensing and possibility of sensor miniaturization (D'apuzzo et al., 2000; Montesperelli et al., 1995). Recently, Tripathy et al. has developed Ca,Mg,Fe,Ti-Oxide (CMFTO)-based electro-ceramics with perovskite structures synthesized by solid-state step-sintering. It is claimed that the technique used helps in maintaining the desired morphology structure as well as providing enhanced water physisorption behaviour. It shows the higher sensitivity up to 3000 % compared to other materials even at low frequency. Other than that, the fabricated sensor also holds the short response-recovery time and low hysteresis value (Tripathy et al., 2016). However, difficulties in ensuring the desired active film surface morphology in ceramic-based humidity sensor and to escape from frequent need of heating in order to eliminate contamination on the film surface (Kulwicki, 1991), the alternative organic-based humidity sensors are actively investigated.

2.5.4 Organic-Based Humidity Sensor

Up to now, there are three types of available humidity sensors, which are organic polymer-based sensor, metal oxide-based sensor and organic-inorganic hybrid sensor. All these three categories are fabricated based on *RH* measurement and normally have the same sensing mechanism. In this research work, polymer organic-based sensors are the main categories that will be explored.

In organic-based humidity sensors, the interactions between the condensed vapours and the active element of the organic sensing layer will trigger a change in electrical properties. Due to the low intrinsic conductivity of the organic polymer, enhancement in the conduction mechanism is vital for the humidity-sensing characteristic to be realised. As the interaction between organic sensing layer and water molecules takes place, free protons are released through protonation phenomenon, which the further interact with the conjugated polymer matrix. Electron hopping process will then triggered throughout the sensing surface structure. There are three basic types of humidity sensor, which are capacitive, resistive and thermal. Resistive and capacitive-based sensors react with surrounding humidity by facilitating changes in its conductivity and polarizability, respectively. This work focuses on capacitive-based sensor due to its simplicity, stable at high or low temperature and suitable for vast majority of humidity measurement applications compared to the other types.

2.5.4.1 Capacitive Type Polymeric Sensors

Capacitive type polymeric sensor often fabricated with a planar structure where the dielectric film deposited between two electrodes on each side, and sandwich structure either with two adjacent side electrodes or inter-digitated comb designed electrode. Capacitive sensor with a sandwich configuration known as ‘Humicape’ is first invented by a Vaisala, one of the Finnish companies that has been engaged in radio probing application henceforth. Mechanism of the capacitive sensor is influenced by the proportional dielectric permittivity changes of the hygroscopic layer to changing surrounding humidity level.

Other than have the capability to operate at higher temperature of up to 200 °C within ambient condition, capacitive sensors also have better recovery from heavy condensation at higher *%RH* level. This type of sensor conquered more than 70 % of transducer in the market due to its superior sensitivity and linearity (Dongfeng et al., 2009; Mahboob et al., 2016). Vitally, capacitive sensors depend on the total dielectric constant of the sensing film and the ability of its surface to hold water cluster (Farahani et al., 2014). Hence, the optimisation of this sensor typically based on these criteria in order to fully exploit the hygroscopic properties of the sensing material efficiently (Sakai et al., 1996).

2.5.5 Composite-Based Humidity Sensors

In general, there are three types of composite nanomaterials systems namely organic/organic, polymer/inorganic (hybrid) and inorganic/inorganic composite. Inorganic-based humidity sensors are recognised for having higher sensitivity and decent physical while organic especially polymeric sensor usually cheaper, flexible and more environmental friendly. Due to these matters, the incorporation between these two materials (inorganic and organic) into composite has attracted many researchers and has shown favourable results since several years ago (Ahmad et al., 2013; Farahani et al., 2014).

Lu et al. have observed the significantly improved humidity sensing performance of TiO_2/LiCl composite nanofiber humidity sensor as compared to the individual component of pure TiO_2 nanofibers (Lu et al., 2009). The reported TiO_2/LiCl composite humidity sensor exhibits good reproducibility, linearity and stability.

Meanwhile, Su and Tsai have used composite material of nano-sized SiO_2 and poly(2-acrylamido-2-methylpropane sulfonate) (poly(AMPS)) to make a humidity sensor (Su & Tsai, 2004). The sensor shows a good linearity but depends on the applied frequency. The amount of SiO_2 content is proportional to the stability of the sensor in highly humid air. In another recent study, TiO_2:WO_3 composites humidity sensors doped withV_2O_5 are prepared by Faia et al. This research has confirmed that doping is one of the approach that can change overall electrical response (Faia et al., 2016). The presence of doping by 3 wt% has improved the sensor sensitivity within the range of 30-100 % as compared to the non-doped sensor.

Sensing mechanism for all types of composite materials is still in the concept of manipulating changes in both electrical and physical properties in reaction to varying ambient humidity level. Usually, the tussle is always in maximising the detection sensitivity of the sensor (Banerjee & Sengupta, 2002; Chen & Lu, 2005; Farahani et al., 2014; Hong-Tao et al., 1989) where the efficient adsorption-desorption process is needed. The combination between organic/inorganic materials into composite provides excellent properties due to the early mentioned reason. However, the environmental issues become an unsolved problem since the inorganic materials still played a role in the applications. The incorporation between organic/organic materials into composite has shown a promising materials enhancement as well as could produce good device performances (Azmer et al., 2016). This could provide an alternative way in reducing the issues arise from the utilisation of inorganic materials. However, the research conducted on organic composite (organic/organic) for humidity sensing applications is still limited and rare as compared to the inorganic and hybrid composite. Hence, the future application of this organic composite in humidity sensing area is crucial to be discovered.

CHAPTER 3: MATERIALS, EXPERIMENTAL METHODS AND PROCEDURES

The physical and chemical properties of alumina template and organic materials employed throughout this research have been presented herein. Procedures involved during the fabrication of nanostructures and development of devices (organic humidity sensors) have been explained in detail. Morphological, optical and structural characterisation techniques of the produced nanostructures including Field Emission Scanning Electron Microscope (FESEM), High Resolution Transmission Electron Microscope (HRTEM), UV-visible spectroscope, photoluminescence (PL) spectroscope, Raman spectroscope and humidity sensing characterisation are also discussed.

3.1 Materials

3.1.1 Alumina Template

Nanoporous Anodic Aluminium Oxide (AAO) or commonly called as alumina template is a self-organised material with honeycomb-like structure consists of high density arrays of parallel nanopores that penetrate through its entire thickness which can be varied from few tens of nanometres to few hundred micrometres. The diameters of the nanopores can be tuned from 5 nm to several hundred nanometres.

Besides being simple and easy to use for nanostructure fabrication process, alumina template is also optically transparent, electrically insulating, thermally and mechanically strong as well as chemically inert (Schmidt, 2013). In the present work, the commercial available alumina template was purchased from Whatman Anodisc (Sigma-Aldrich, St. Louis, USA). This work utilised an alumina template of 20 nm (for the first top 2 µm) and ~200 nm for the rest of inner pore diameter with 60 µm thickness (Figure 3.1(a) & (b)). Alumina template exhibits Y-branched nanopore as shown in Figure 3.1(c).

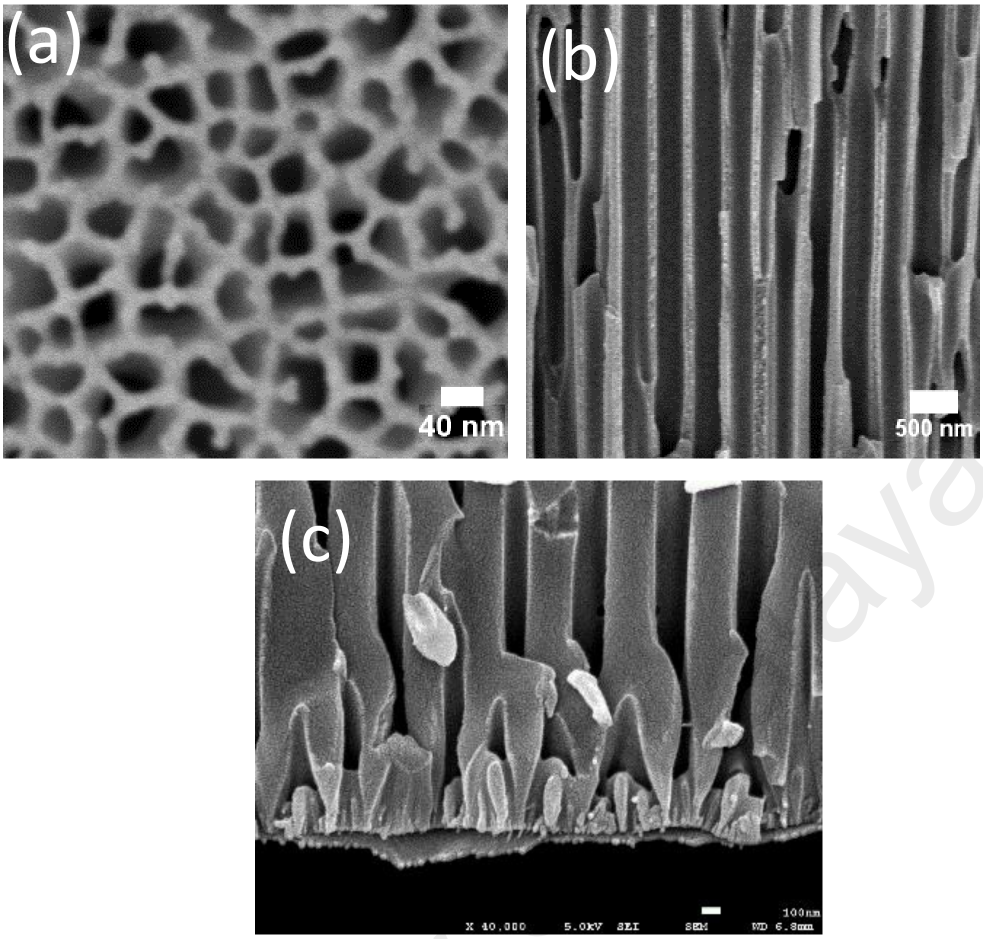

Figure 3.1: (a) Top surface, (b) cross-sectional and (c) Y-branched FESEM images of alumina template.

3.1.2 Poly[N-9′-heptadecanyl-2,7-carbazole-alt-5,5-(4′,7′-di-2-thienyl-2′,1′,3′-benzothiadiazole)] (PCDTBT)

PCDTBT is a low band-gap semiconductor with *p*-type hole mobility of ~ 6 × 10^{-5} $cm^2/V \cdot s$, melting point of 270-300 °C, transition temperature $T_m > 400$ °C and average molecular weight M_w of 20,000~100,000. Its absorption spectrum exhibits two maxima; the absorption band at smaller wavelengths is attributed to carbazole (Cz) segment while the other peak at a longer wavelength referred to DTBT unit (Jha et al., 2013). In the present work, commercially available PCDTBT from Luminescence Technology Corp. is used without further purification. PCDTBT is readily soluble in several organic solvents such as chloroform, chlorobenzene and dichlorobenzene. Figure 3.2 represents the chemical structure of PCDTBT.

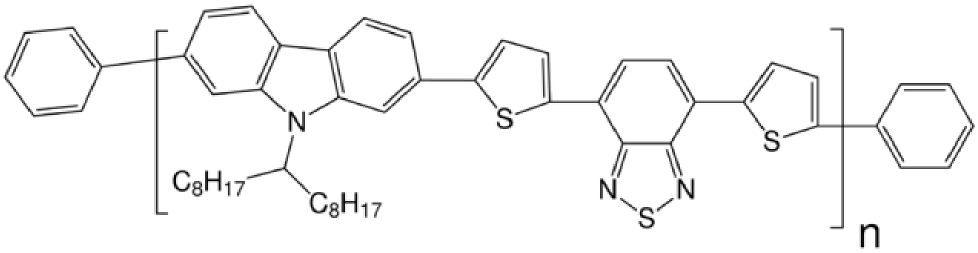

Figure 3.2: The chemical structure of PCDTBT.

3.1.3 Phenyl-C_{71}-Butyric-Acid-Methyl Ester ($PC_{71}BM$)

In this research, 99 % pure $PC_{71}BM$ (empirical formula $C_{82}H_{14}O_2$) is purchased from Luminescence Technology Corp. (Taiwan). $PC_{71}BM$ is a fullerene derivative of the C_{70} buckyball. It appears black in colour and its molecular weight is 1030.93 g/mole. $PC_{71}BM$ is an electron acceptor material and is often used in plastic solar cells or flexible electronics in conjunction with electron donor materials such as PCDTBT or other polymers. Molecular structure of $PC_{71}BM$ is depicted in Figure 3.3.

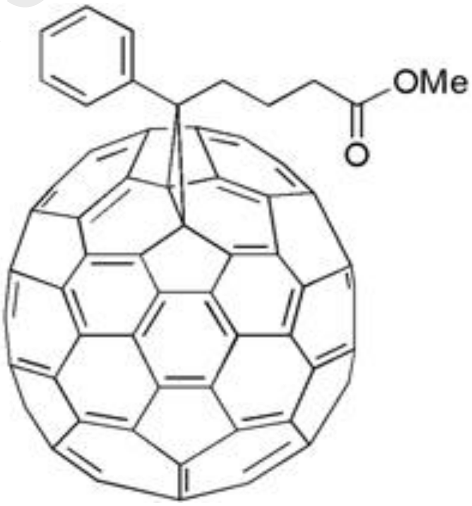

Figure 3.3: Molecular structure of $PC_{71}BM$.

3.1.4 Chloroform ($CHCl_3$)

Chloroform is one of the organic compounds that have been used, as a major solvent throughout this study with a chemical formula of $CHCl_3$. Chloroform is a highly volatile transparent compound, which is commonly used as a solvent in both laboratory and industry. Its chemical structure shown in Figure 3.4 indicates that hydrogen is attached to the carbon chain through hydrogen bonding.

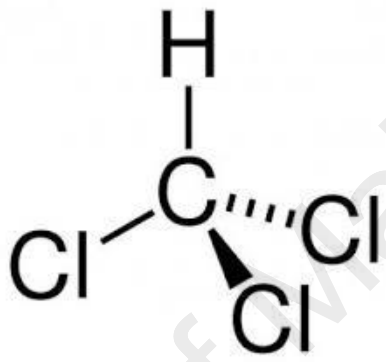

Figure 3.4: Molecular structure of chloroform.

3.2 Experimental Methods

3.2.1 Glass Substrate Preparation

In this work, microscope glass slide has been purchased and used as a substrate (Figure 3.5) for the fabrication of nanostructures and sensors. Glass is chosen due to its low cost, excellent transparency as well as simple cleaning process. The substrate surfaces must be clean, smooth and dry before any fabrication process is undertaken in order to avoid contamination that may cause adhesion problem. Thermo-6D ultrasonic bath was used in the substrate cleaning process. In cleaning the substrate, some protocols need to be followed:

- Sonication of glass substrate in soap water for 15 minutes to remove dust particles.
- Rinsing of substrates in deionized (DI) water.
- Rinsing of substrates in acetone.
- Rinsing of substrates in isopropyl alcohol.
- Rinsing of substrates in DI water.
- Drying of the substrates by nitrogen gas.

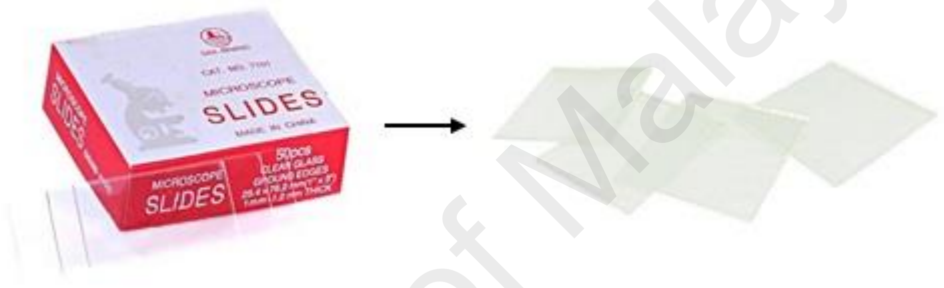

Figure 3.5: Preparation of glass substrates.

3.2.2 Alumina Template Cleaning Protocol

Before being used in nanostructure fabrication, alumina template needs to undergo several cleaning processes to remove dirt or any contaminant on its pore surface as well as to clear the pore from any clogging. Contaminant on the surface will cause adhesion problem during the wetting process meanwhile clogging will affect the density of produced nanostructures. Cleaning of the porous alumina template could be done by sonicating it in the acetone, ethanol and deionized water for 15 minutes each, prior to oven drying at 60 °C for 30 min.

3.2.3 Infiltration of Polymers and Fullerenes into Alumina Template: Processes and Techniques

In this research, three different techniques have been used to infiltrate polymer (PCDTBT) and fullerene ($PC_{71}BM$) solution into the alumina template. The techniques involved are as follows:

3.2.3.1 Spin Coating (Formation of PCDTBT nanostructures)

Spin coating is a process in which solution is spread evenly over a surface using centripetal force. It has been used in semiconductor industry for decades to create a uniform thin film on substrates. The solutions will be deposited first onto the substrate primarily on the centre which then spin at a preferred rate (in this research, 1000, 2000 and 3000 rpm are used) and spread over a substrate (alumina template) within a specified time (30 s). The solution will infiltrate into the alumina template in a different way based on the selected parameters such as spinning rate, drying time, concentration of the solution and choice of solvent. Figure 3.6 depicts the Laurell WS-650Mz-23NPP spin coater used in this work.

Figure 3.6: Laurell WS-650Mz-23NPP spin coater.

The 5, 10 and 15 mg/ ml of PCDTBT solution were prepared in chloroform. The templates were cleaned prior to use by sonicating in water and acetone for 15 min. 5, 10 and 15 mg/ml of PCDTBT solution was dropped into a cleaned template followed by spin coating at 1000, 2000 and 3000 rpm for 30 s. Prior to the dissolution, the template that has been spin-coated with solution was stuck upside down on the copper tape. The coated template is stick upside down due to the more constructive PCDTBT film deposited at the upper side of coated template. The role of the copper tape is to hold the nanostructures from collapse during the dissolution. It can also ease the characterisation of FESEM since the copper tape is conductive. After the template's dissolution, nanostructures were rinsed with distilled water. PCDTBT nanostructures were characterised by Field Emission Scanning Electron Microscope (FESEM-EDX) (QuantaFEG450), Transmission Electron Microscope (TEM) (TecnaiG2FEI), UV–vis spectroscope (Shimadzu UV-3101PC), and Raman and Photoluminescence spectroscope (RENISHAW).

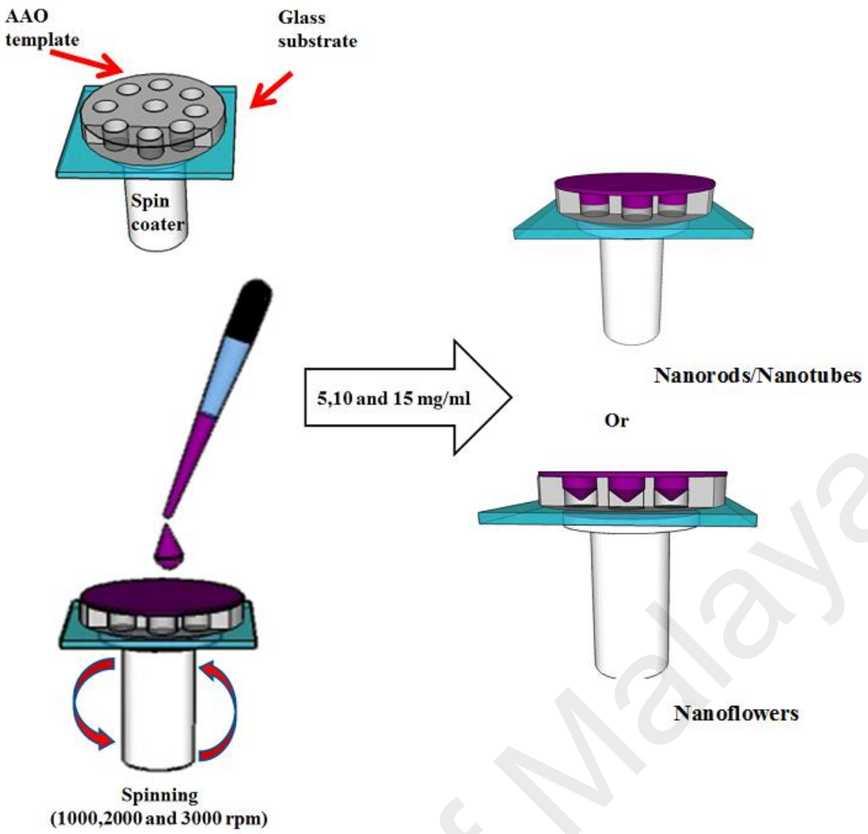

Figure 3.7: **Schematic illustrations depicting the steps involved in formation of PCDTBT nanostructure by spin coating technique.**

3.2.3.2 Immersion (Formation of PCDTBT nanostructures)

Immersion is one of the techniques employed to infiltrate the PCDTBT solution into the alumina template. Immersing the alumina template into the solution for a certain time of period does this technique. Immersion technique utilised solution-wetting mechanism for the solution to adhere onto the template's pore surface. Properties of the produced nanostructures are defined by several parameters such as immersion time, solution concentration and the cleanliness of the alumina template. Experimental Procedures

The 5, 10 and 15 mg/ml of PCDTBT solution concentration were prepared in chloroform. The cleaned template was then immersed in PCDTBT solution for 2, 12 and 24 hours prior to the annealing at 50 and 150 °C (1 min). The template that has been immersed in PCDTBT solution needs to be dissolved in 4 M sodium hydroxide for 24 hours to obtain the nanostructures. PCDTBT nanostructures were characterised by field emission scanning electron microscope (FESEM) (JSM 7600-F, JEOL Ltd., Tokyo, Japan), high-resolution transmission electron microscope (HRTEM) (JEM 2100-F, JEOL Ltd., Tokyo, Japan), UV-vis spectroscope (Jasco V-750, JASCO, Tokyo, Japan), photoluminescence spectroscope (PL) (Renishaw, Gloucestershire, UK), and Raman spectroscope. Figure 3.8 illustrates the experimental steps involved.

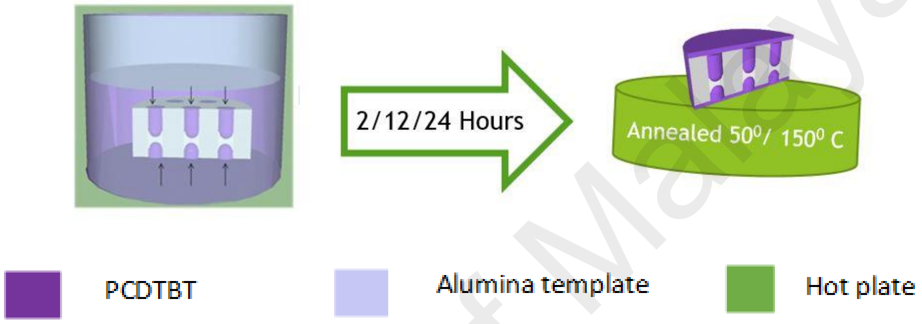

Figure 3.8: Schematic illustration of experimental steps involved in immersion technique.

3.2.3.3 Combination of Drop Casting at Room Temperature & Annealing Above Melting Point (Formation of PCDTBT nanostructures)

If spin coating and immersion techniques utilised solution-wetting mechanism, this technique is a combination between solutions and melt wetting mechanism. Two approaches are combined namely drop casting followed by annealing above the melting point. Once the PCDTBT solution wet the alumina template's pore surface via drop cast approach, it will then let to melt (melt wetting) once being annealed above the PCDTBT melting point. Combination between these techniques is believed to improve the properties of the produced nanostructure.

PCDTBT (M_w = 20664, M_n = 3984, PDI = 5.19) was dissolved in 1 mL of chloroform to form solution in three different concentrations of 5, 10 and 15 mg/ml.

Porous alumina templates (Whatman Anodisc) and glass substrates were used in the preparation of PCDTBT nanostructures. The glass substrates (Sail Brand, China) and porous alumina templates were cleaned by sonicating them in acetone, ethanol and deionized water for 15 minutes prior to oven drying and nitrogen blowing. PCDTBT nanostructures were synthesised using the solution wetting followed by melt wetting techniques. A 25 µL of each concentration (5, 10 and 15 mg/ml) was first drop casted onto glass substrate and the alumina template was immediately placed on top of the drop casted solution. The nanochannels of the template were immediately filled with the PCDTBT solution, which were subjected to solvent evaporation at ambient condition for 5 minutes. These neat samples were designated as PT5 (5 mg/ml), PT10 (10 mg/ml) and PT15 (15mg/ml). After the further analysis was done, only the dried infiltrated alumina templates of PT5 and PT10 were chosen and placed into the furnace before being heated above their melting point (melting point 270-300 °C) at 300, 350 and 400 °C for 1 hour. Consequently, a total of six annealed samples (three samples of PT5 and PT10 each), were prepared which were named as follows: PT5 annealed at 300, 350 and 400 ºC were given the names as PT5-1, PT5-2 and PT5-3, respectively, while the annealed samples of PT10 were designated as PT10-1, PT10-2 and PT10-3. Afterwards, all the samples were dried at room temperature prior to the dissolution process. Template dissolution was conducted for 12 hours by immersing each template in 4 M sodium hydroxide (NaOH). The morphological, structural and optical properties were investigated by field emission scanning electron microscope (FESEM) (JSM 7600-F, JEOL Ltd., Tokyo, Japan), transmission electron microscope (TEM) (Hitachi HT7700, Japan) and UV-vis spectroscope (Lambda 750, Perkin Elmer, Waltham, USA). Photoluminescence and Raman characterisation were carried out using Renishaw in Via Raman microscope using He-Cd laser.

3.2.3.4 Formation of PCDTBT: $PC_{71}BM$ composite nanostructures

PCDTBT and $PC_{71}BM$ were separately dissolved in chloroform for the solution concentration of 5 mg/ml, 10 mg/ml and 15 mg/ml. Porous alumina templates (Whatman Anodisc) were used in synthesising the *p-n* junction composite nanostructures. The porous alumina template was cleaned by sonicating in acetone, ethanol and deionized water for 15 minutes prior to oven drying. 5, 10 and 15 mg/ml of PCDTBT solution was first infiltrated into the alumina pores using the spin coating, immersion technique and combination of drop casting & annealing technique as previously mentioned followed by the spin coated of 5, 10 and 15 mg/ml of $PC_{71}BM$ solution at 1000 rpm. Afterwards, these samples were dried at room temperature prior to the dissolution process. Template dissolution was conducted for 12 hours by immersing the template in 4 M sodium hydroxide (NaOH). Characterisations of their morphological, structural and optical properties were carried out by field emission scanning electron microscope (FESEM) (JSM 7600-F, JEOL Ltd., Tokyo, Japan), high resolution transmission electron microscope (HRTEM) (Hitachi HT7700, Japan), UV-vis spectroscope (Lambda 750, Perkin Elmer, Waltham, USA), photoluminescence spectroscope (Renishaw, Gloucestershire, UK) and Raman spectroscope.

3.2.4 Humidity sensor

PCDTBT and $PC_{71}BM$ were purchased from Luminescence Technology Corp. (Taiwan) and Sigma Aldrich (St. Louis, USA), respectively, and used without further purification. PCDTBT and $PC_{71}BM$ were separately dissolved in chloroform for the solution concentration of 5 and 15 mg/ml. Porous alumina templates (Whatman Anodisc, St. Louis, USA) were used in synthesising the *p-n* junction composite nanostructures. The porous alumina templates were cleaned by sonicating in acetone, ethanol and deionized water for 15 minutes prior to oven drying.

PCDTBT solution was first infiltrated into the alumina template’s pores with several selected parameters of spin coating (5 mg/ml, 1000 rpm), immersion (15 mg/ml, 50 ^{0}C, 24 hours) and drop casting & annealing combination techniques (5 mg/ml, 300 ^{0}C) as mentioned in Chapter 4. Then, PC$_{71}$BM solution was spun-coated at 1000 rpm. The infiltrated template that placed on top of the glass substrate was then dissolved in 4 M sodium hydroxide (NaOH) in order to extract the confined nanostructures. The dissolution process was closely and carefully observed. Once the infiltrated template was dissolved, NaOH was sucked away and followed by cleaning process using deionized water (DI) for several times. The extracted nanostructures on top of the glass substrate have been dried at room temperature overnight.

For the device fabrication, a thin film of aluminium (thickness of ~120 nm) was deposited on the glass substrate which consists of a layer of PCDTBT: PC$_{71}$BM nanostructure through a shadow mask by an Edward Auto 306 thermal evaporator (pressure ~10^{-5} mbar, deposition rate 0.2 nm/s). A pair of rectangular aluminium electrodes separated by 40 micron gap was obtained on the PCDTBT: PC$_{71}$BM nanostructures layer. Figure 3.9 shows the schematic illustration of cross-sectional view of Al/PCDTBT: PC$_{71}$BM/Al humidity sensor.

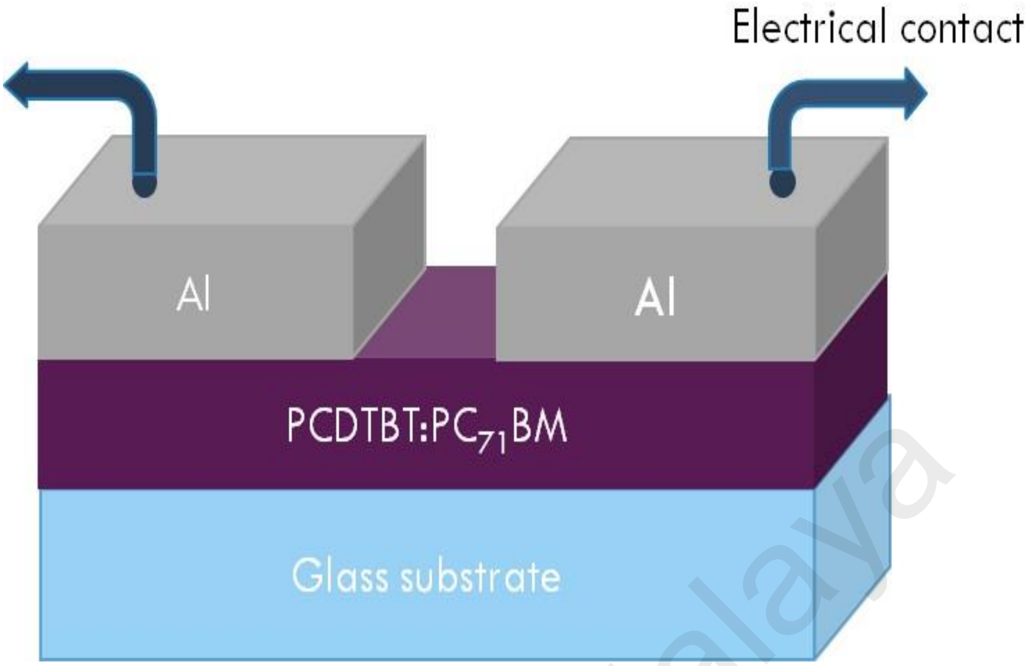

Figure 3.9: Schematic illustration of cross-sectional view of Al/PCDTBT: PC$_{71}$BM/Al humidity sensor.

3.2.5 Physical Vapour Deposition (PVD)

PVD techniques have been employed for aluminium electrode deposition process using an auto Edward 306 deposition system. Before being placed inside the deposition chamber, a few pieces of 99.9 % pure aluminium are attached on a tungsten filament coil. The pressure inside the chamber has been set to be ~ 1.5 x 10^{-5} mbar prior to the deposition process. After the electrical current passing through the filament coil, it will slowly heat up. The increasing current that passing through the filament, will cause to the collisions between electrons and tungsten atoms. The collisions energy will be dissipated as heat. Constant heating at 20 amperes applied current has caused the aluminium attached around the tungsten filament coil to melt, which then evaporated upwards coating the glass substrate. The shuttle that covered the glass substrate was then removed for deposition of the glass substrate to occur.

3.3 Characterisation Techniques

3.3.1 Analysis of Morphological Properties

3.3.1.1 Field Emission Scanning Electron Microscope (FESEM)

In this research, FESEM (JSM 7600-F, JEOL Ltd., Tokyo, Japan) is one of the instrumentations that used in analysing the morphological properties of nanostructures. The morphological properties of the produced nanostructures that were analysed through FESEM are important to be studied in order to suit the properties of the devices. For the nanostructures to be observed under FESEM, the template that has been infiltrated and coated with PCDTBT needs to be dissolved away in order to extract the nanostructure. The collapse of nanostructures can be prevented after dissolution by sticking the infiltrated template upside down on the copper tape.

High vacuum environment with a tightly sealed condition is needed for the images probing. Electron emitted by the field emission source will conduct the scanning mechanism, which is afterwards being accelerated by the induced electric field gradient. Subsequently, the accelerated primary electrons pass through electromagnetic lenses before get deflected which then produce a narrow scan beam through continues bombardment of the sample. This will generate secondary electrons emissions from the sample, which at the end get detected by a photo-sensor. Resultantly, the information obtained from the sensor enables construction of topological surface imaging of the films surface. The cross-sectional image of FESEM is shown in Figure 3.10.

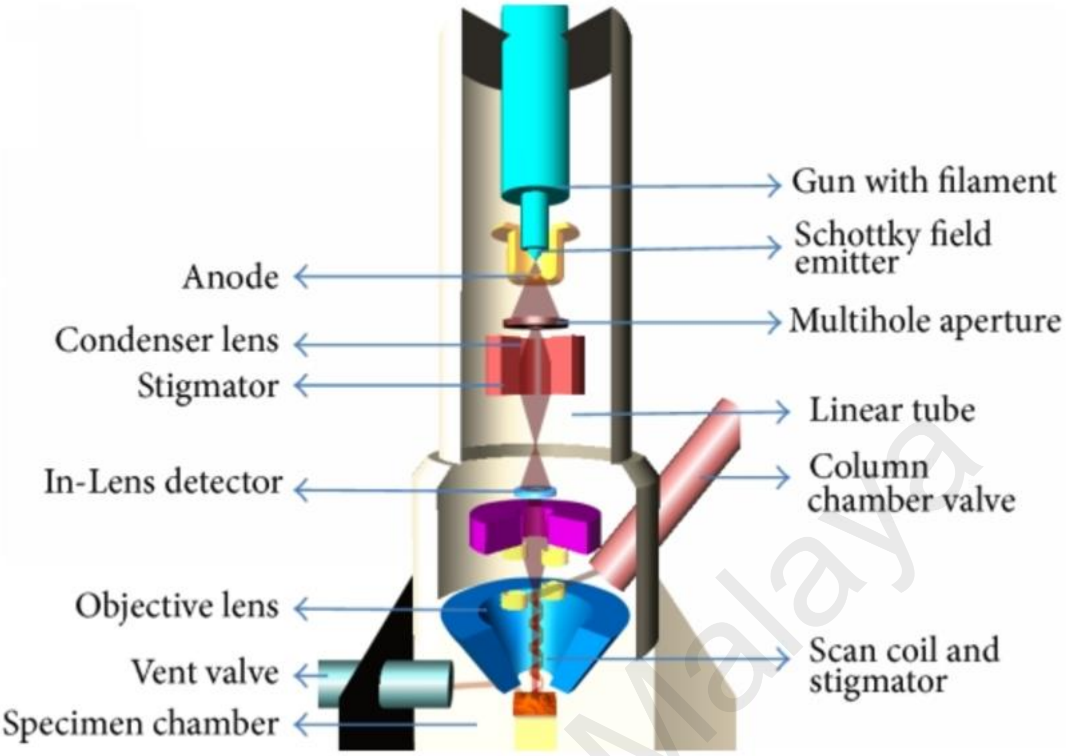

Figure 3.10: Cross sectional image of FESEM (Jusman et al., 2014).

3.3.1.2 High Resolution Transmission Electron Microscope (HRTEM)

HRTEM is an imaging mode of the transmission electron microscope (TEM). It is one of the powerful tools to study the properties of the materials at the atomic scale. In this work, the morphological analyses that done through FESEM can be deeply studied and further confirmed using HRTEM. The type of structure produced either hollow or solid, the diameter, size and any distinctive occurrence can be further confirmed through HRTEM. Several differences between FESEM and HRTEM are tabulated in Table 3.1.

Table 3.1: Comparison between FESEM and HRTEM.

FESEM	HRTEM
Produce images of the surfaces of sample (nanostructures). Used for studying surface morphology of the samples.	Used to study the ultra-structure of the samples and its components. Provides details about internal composition.
Electron beam scans over the surface of the sample.	Electron beam pass through the sample.
Images are produced by detecting secondary electrons that emit from the surface cause by the excitation of the primary electron beam (based on scattered electrons).	Primary electrons transmitted from the samples are detected to produce images (based on the transmitted electron).
Comparatively low resolution.	High resolution.
Specimen contrast by electron adsorption.	Specimen contrast by electron scattering.
Easy sample preparation.	Need a proper technique based on the type of sample.
Similarities	
Both use electron as source of radiation.	
Use high vacuum as a medium.	
Focusing current in the objective lens coil.	
Magnification adjustment using current in the projector lens coil.	

3.3.2 Analysis of Photophysical Properties

3.3.2.1 UV-vis Spectroscope

In the present study, Perkin Elmer Lambda 750 UV-vis spectrometer has been employed to study the visible wavelength absorption profile of the PCDTBT and PCDTBT:$PC_{71}BM$ nanostructures. The instrument parameters have been controlled by UV Winlab version 6 software. The amount of ultraviolet and visible light absorbed by the obtained nanostructures can be measured by ultraviolet-visible spectrophotometer. The electronic structure of certain chemical species will provide a unique absorption UV-vis profile. The amount of the light absorb by the chemical species is directly proportional to the amount of them. UV-vis also can be used to study any changes occurred in their electronic structure for a certain chemical species. Hence, absorption spectrophotometry is an effective tool for identification (qualitative analysis) and estimation (quantitative analysis) measurements. The image of Perkin Elmer Lambda

750 UV-vis spectrometer and its technical specifications are shown in Figure 3.11 and Table 3.2, respectively.

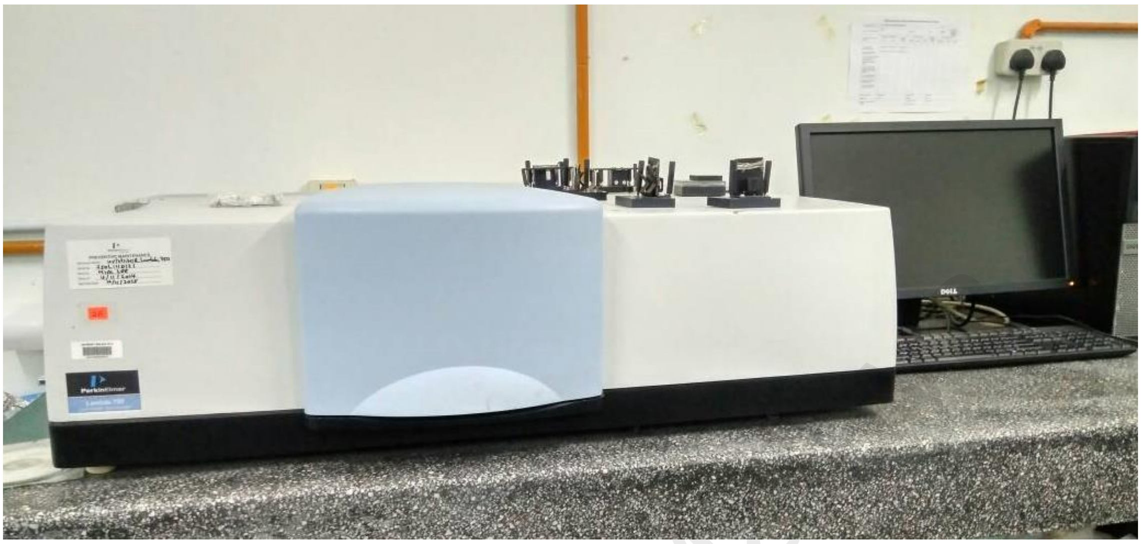

Figure 3.11: Perkin Elmer Lambda 750 UV-vis spectrometer.

Table 3.2: Key technical specifications of PerkiN Elmer Lambda 750 UV-vis spectrometer.

Wavelength range	190 nm – 3300 nm
Wavelength accuracy	± 0.15 nm UV/vis ± 0.5 nm NIR
Wavelength reproducibility	UV/vis ≤ 0.06 nm
Light source	Tungsten-Halogen (vis) and Deuterium (UV)
Light detector	Photomultiplier R955

3.3.2.2 Photoluminescence (PL) Spectroscope

PL spectroscope is a non-destructive and contactless method of probing the electronic structure of materials. Photo-excitation occurs when light is directed onto a sample, being absorbed and imparts excess energy into the material. One of the ways sample can dissipate this excess energy is through the emission of light or luminescence. This luminescence is called photoluminescence (in the case of photo-excitation). Electrons within a material will move into permissible excited state during photo-excitation. When these electrons return to their equilibrium states, excess energy will be released and may also include the emission of light. The differences in energy levels between excited and equilibrium states during transition linked to the energy of the photoluminescence (emitted light). Interfacial interactions of the donor-acceptor at microscopic scale can be further investigated through PL spectrum. Donor-acceptor could be the interaction within the PCDTBT polymer itself (Cz-DTBT) or in a PCDTBT:PC$_{71}$BM composite junction. Upon absorption of light, the dissociation of photogenerated excitons in the donor phase occurred at the D/A interface. Two distinct interfacial processes may occur due to the dissociation process. (i) The energy transfer process of HOMO/LUMO levels where light is emitted (photoluminescence phenomenon) or (ii) the charge transfer process where hole mainly get localized in donor phase and electrons in acceptor phase. The quenching phenomena occur during charge transfer process, indicate that PL can be one of the rough indicators on how well exciton can lead to efficient charge transfer at the D/A interface. In present study, PL spectroscope (Renishaw, Gloucestershire, UK) assists in investigating the optical properties of the PCDTBT and PCDTBT:PC$_{71}$BM nanostructures. The blue and red shift of the PL spectrum as well as correlation with the UV-vis spectrum is also considered in this study. In Rayleigh scattering, photon will be emitted from a material with the same energy and frequency as the incident but with a change in the direction of propagation. The electronic state of the material does not change during this scattering. However, in Raman scattering, a molecule in the material absorbs the energy of the incident photon, which then excite to a virtual electronic level.

3.3.3 Raman Spectroscope

Rayleigh scattering (elastically) and Raman scattering (in-elastically) occur when the incident photon propagates into a material. In Rayleigh scattering, photon will be emitted with the same energy and frequency as its incident when passes through a material but with a change in a direction of propagation. The material’s electronic state also remains the same. However, in Raman scattering, molecule in a material absorbs the energy of the passing photon, which then excite to a virtual electronic level. Another photon is emitted after the molecule relaxes back to a lower energy level (Stokes) or excite to higher energy level (Anti-stokes). Usually the emitted photon will have less energy than the incident photon. In Raman spectroscope, the interaction between monochromatic light from a several range types of laser (UV/visible/NR) and molecular vibration system will cause a shifting in laser photon, which then will provide information about vibrational modes in the system. Figure 3.12(a) & (b) shows Renishaw inVia Raman microscope that is used in present work and Jablonski diagram for the Rayleigh and Raman scattering, respectively.

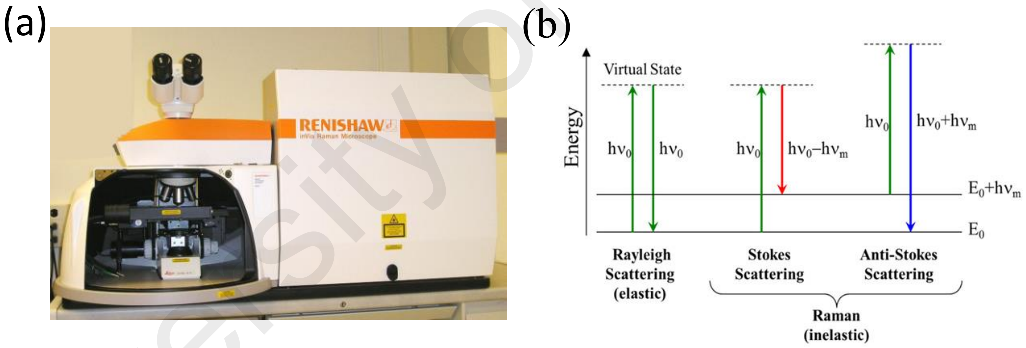

Figure 3.12: (a) Renishaw inVia Raman microscope and (b) Jablonski diagram representing quantum energy transition for Rayleigh and Raman scattering.

3.3.4 Humidity Sensing Characterisation

Fabricated devices, which are humidity sensor, are characterised inside a humidity chamber where the *RH* level can be manipulated preferably. The electrical characterisation was performed in a closed chamber (dimensions of ~ 40 cm x 60 cm) with inlet and outlet valves were used for the flowing of humid air and dry nitrogen gas, respectively. In order to increase the *%RH* level in the chamber, the commercially available Rossmax NB80 humidifier was utilised to supply the humid air into the chamber through the inlet valve. Similarly, to decrease the humidity level, humid air is allowed to escape through an outlet valve, while nitrogen gas is channelled into the chamber through an inlet valve. A Mastech MS 6503 humidity meter (humidity sensitivity ± 2.5 *%RH*, temperature sensitivity ± 0.7 ºC) was used in monitoring the variations in humidity level inside the chamber, whereas a GW Instek LCR-829 meter was used to provide the capacitance of the fabricated sensor at varied humidity level. Figure 3.13 depicts the general layout of the characterisation setup utilised in the calibration of humidity sensor at various *%RH* levels. For the comparison purposes, a commercial alumina template without any infiltrated PCDTBT was used as a control by applying the same fabrication and characterization method of the polymeric sensor device.

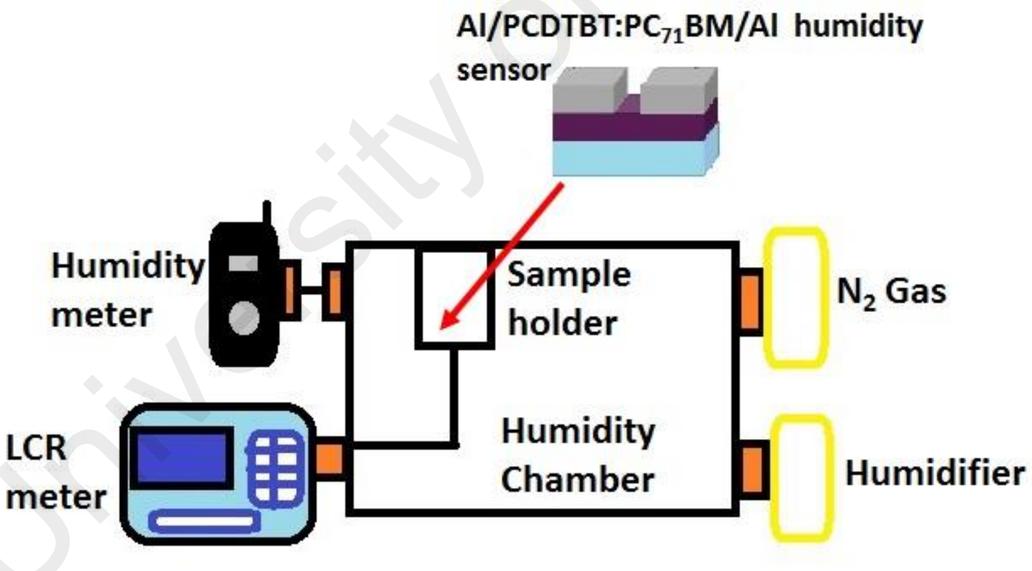

Figure 3.13: Characterisation setup used for calibration of humidity sensor.

Figure 3.14 and Table 3.3 shows the experimental setup and its descriptions, respectively, which consist of the following instruments;

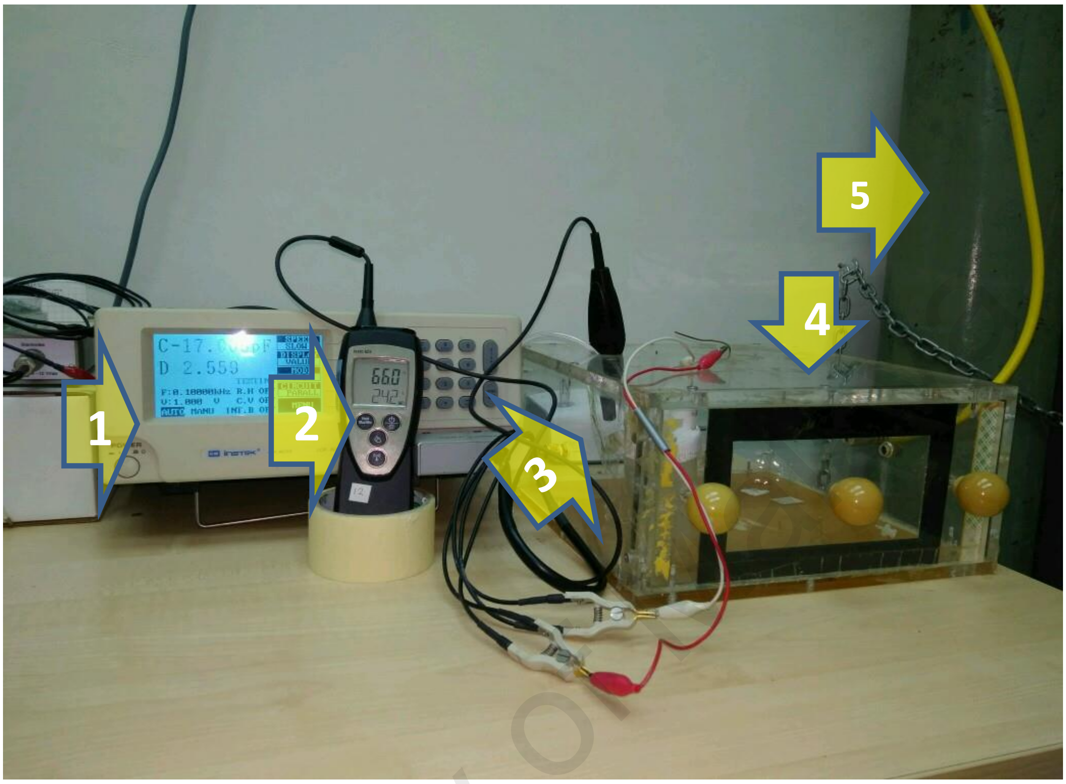

Figure 3.14: Experimental setup for humidity sensing measurement.

Table 3.3: Descriptions of experimental setup as shown in Figure 3.10.

Components	**Functions**
1-LCR Meter	Measurements of sensing outputs
2-Hygrometer	Measurement of *RH* level
3-Humidifier	Supplying vapours source
4-Humidity Chamber	Sample placing
5-Nitrogen Gas	Removing water vapours

CHAPTER 4: FORMATION OF PCDTBT NANOSTRUCTURES BY TEMPLATE WETTING

Recently, rigorous efforts have been focused on the facile synthesis routes to fabricate polymer nanostructures for investigation and application purposes. A simple, common and cost effective technique, that extensively used for the fabrication of polymer nanostructures, is the template-assisted method (Al-Kaysi et al., 2009). In this method, polymer melt or solution is allowed to infiltrate inside the porous alumina templates to form nanostructures (Dougherty & Liang, 2009b; Zhang et al., 2006). By varying templating techniques and parameters such as the infiltration time, spin coating rate and polymer concentration; the optical, structural properties and polymer chain packing of PCDTBT nanostructures can be favourably altered. In this study, three templating techniques have been explored as mentioned in the earlier section, which are spin coating, immersion and combination of drop casting & annealing (above PCDTBT melting point) techniques.

Spin coating is one of the most common techniques for deposition of thin films onto substrates. However, this simple technique rarely be applied in infiltrating the solution into alumina template even it has been used in a wide variety of industries and technology sectors. The ability of the spin coating to quickly produce uniform films from a few nanometres to a few microns in thickness would have some benefit in producing the desired nanostructures for the template-assisted method. Varying the time and spinning rate of the spin coater can control the degree of infiltration controlled according to the desired aspect ratio of the nanostructure.

In order to understand the effect of infiltration time on the growth mechanism of polymeric nanostructures, immersion technique has been employed. Immersion technique is conducted by varying the immersion time at 2, 12 and 24 hours which then further annealed at 50 and 150 °C. In templating method, immersion technique is a common technique utilised by most researchers (Chen et al., 2014; Feng et al., 2011; Wei et al., 2013), however, to the best of our knowledge no studies on the effect of further annealing treatment after immersion has been reported. In the present work, any enhancement in the morphological as well as its optical properties provide by the annealing treatment after immersion would be further investigated.

In particular, nanorods or nanotubes are produced by wetting the templates with polymer solution or melts, respectively (Ali et al., 2015). The nanostructures produced by polymer solution wetting can be transformed into different nanostructures by further processes of annealing (Chen et al., 2007; Schlitt et al., 2008). The wetting of porous templates with polymer melts is a highly effective way to produce nanotubes (Schlitt et al., 2008), which result from wetting with melts of high molecular weight polymers (Steinhart et al., 2004; Steinhart et al., 2002; Steinhart et al., 2003). To obtain the proper flow of polymer melts in the nanochannels of the templates, it is essential to have deep insight of the wetting phenomenon of liquid on a high-energy surface (Saritha et al., 2006; Xu et al., 2004). Owing to nanochannels employing high surface energy materials, low surface energy polymer melts can effectively wet and penetrate well into nanochannels due to wetting behaviour. Polymer solution and melt wetting techniques are the common technique exploited by the researchers in templating method. Usually, these techniques are used individually. Here, we report the combination of polymer solution (drop cast) and melt (annealing above melting point) technique in producing PCDTBT nanostructures.

This chapter divided into three parts which are spin coating (part I), immersion (part II) and combination of drop casting & annealing (above PCDTBT melting point) (part III) techniques. For spin coating technique, three different spinning rates of 1000, 2000 and 3000 rpm are used for each 5, 10 and 15 mg/ml PCDTBT solution concentration. Several distinct nanostructures have portrayed the dissimilarity in their morphological and optical properties. Immersion technique is conducted by immersing the porous alumina template into 5, 10 and 15 mg/ml of PCDTBT solution concentration for 2, 12 and 24 hours then annealed at 50 and 150 °C. The correlation between the parameters involved is also studied. In the combination of drop casting & annealing technique, the PCDTBT solution is first drop casted onto the alumina template before being annealed above its melting point at 300, 350 and 400 °C for 1 hour. All changes in morphological (FESEM and HRTEM), optical (UV-vis and PL spectroscope) and structural properties (Raman spectroscope) of nanostructures of different infiltration techniques are observed and discussed in this chapter.

4.1 Part I: Spin Coating Technique

4.1.1 Results & Discussion

4.1.1.1 Morphological Properties

Different spinning rates (1000, 2000 and 3000 rpm) with the combination of different concentration of 5, 10 and 15 mg/ml have produced numerous types of 1D nanostructures, which are nanorods, nanotubes and nanoflowers. Aligned growth of 1D nanostructures were expected to occur after the dissolution of infiltrated template, however, the nanostructures formed have collapsed into bundle. The collapse of 1D nanostructures into bundle could be due to the attractive force between the nanostructures. Fundamentally, the attractive force is related to the phenomena of van der Waals (attractive intermolecular forces) interactions. Different spinning rate give a significant different of morphological properties of produced nanostructures.

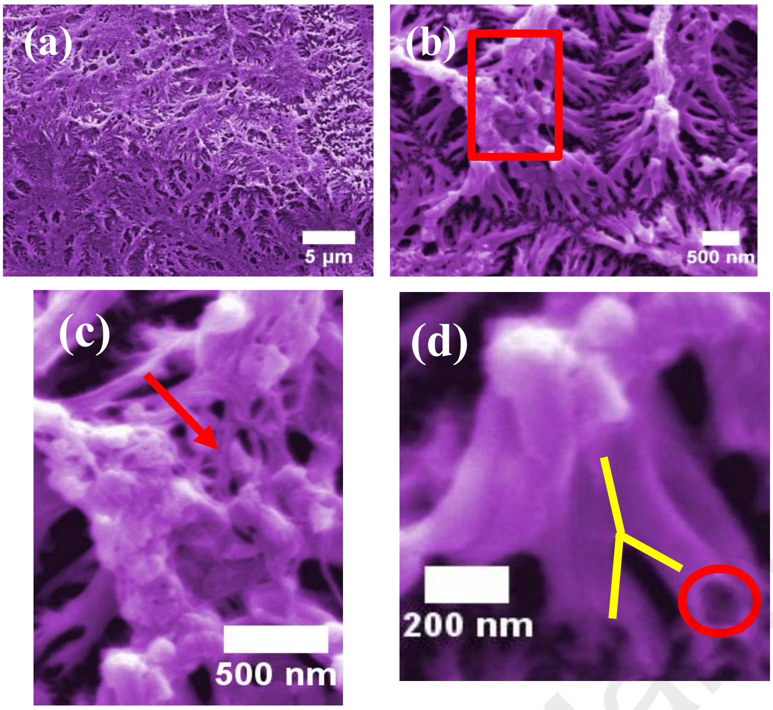

Figure 4.1: (a-d) FESEM images of nanotubes produced from 5 mg/ml PCDTBT solution spin coated at 1000 rpm.

Once the polymer solution is placed on a substrate of high surface energy, it will spread to form a thin film at the initial stage of wetting. The stronger adhesive forces as compared to the cohesive forces cause the wall wetting and complete filling to occur at a different time. The latter is prevented by a solvent evaporation which preserve nanotube structure (Steinhart et al., 2004). Figure 4.1(a) shows an overview of nanotubes produced from 1000 rpm spinning rate. Collapse structure can be seen from a closer view of the nanotube's top part as shown in Figure 4.1(b). Magnified view of the red box in Figure 4.1(b) is presented in Figure 4.1(c), where individual collapse and entangle nanotubes indicated by the red arrow. Collapse of the nanotube's top part could be the main reason for the shorter nanostructure as can be seen in Figure 4.1(c). The distance from the top part to the branched structure indicates how long the solution has infiltrated and the occurrence of any collapse to the structure, which is marked by the yellow Y-shaped line shown in Figure 4.1(d). Red circle in Figure 4.1(d) shows broken part, which confirm the present of hollow structure (nanotubes) instead of solid form.

Slower rate of 1000 rpm compared to 2000 and 3000 rpm cause a less amount of solution to splash at the start of spinning. This will provide quite large amount of solution to infiltrate deeper compared to the other spinning rates (2000 and 3000 rpm). Low evaporation rate of 1000 rpm also allow the PCDTBT solution to infiltrate deeper before dried up. The longer the solution infiltrates, the thinner the wall of the nanotubes. Although only less solution is splashed away, yet is still not enough PCDTBT to produce a thicker and stable wall. In order to produce a thicker and stable wall with low concentration, once the PCDTBT solution is infiltrate to the bottom of the alumina pore, there should be another PCDTBT flowing from the top to make another layer of wall. This process should be repeated to produce a thicker wall, which illustrated in schematic diagram in Figure 4.2.

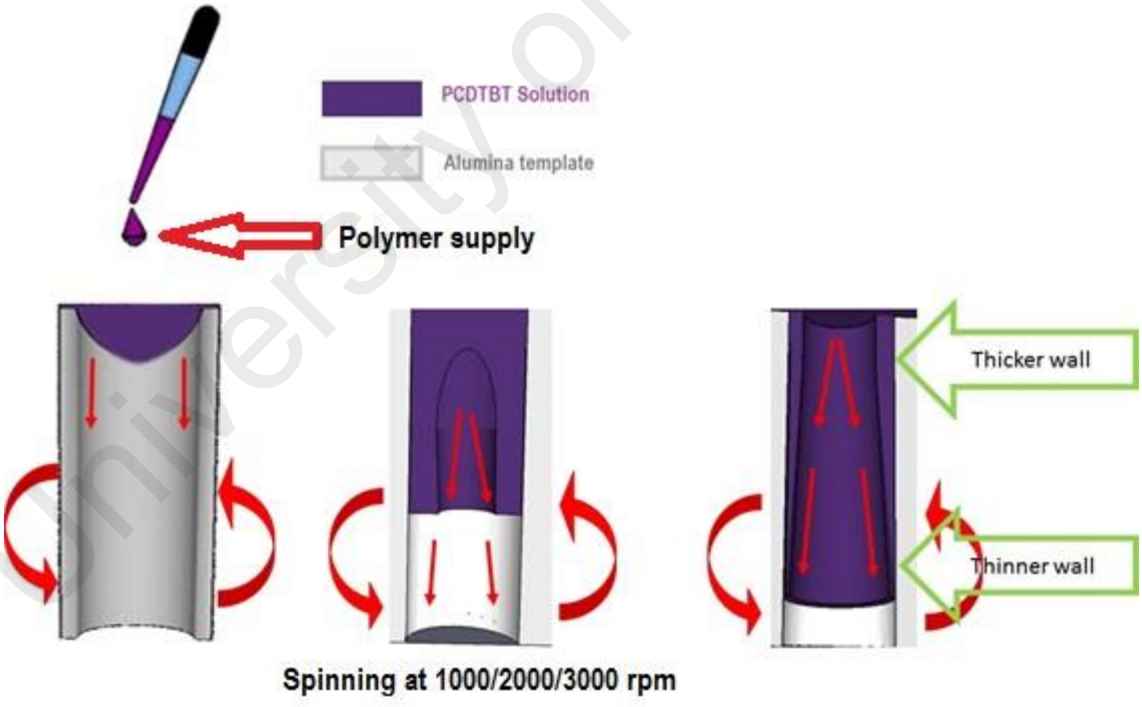

Figure 4.2: Wall thinning process in polymer solution wetting.

However, the combination between low spinning rate (1000 rpm) with low concentration of 5 mg/ml gives a large contribution to the very thin wall of nanotubes compared to the other concentrations (10 and 15 mg/ml). These very thin wall nanotubes will collapse in a large degree during the dissolution process.

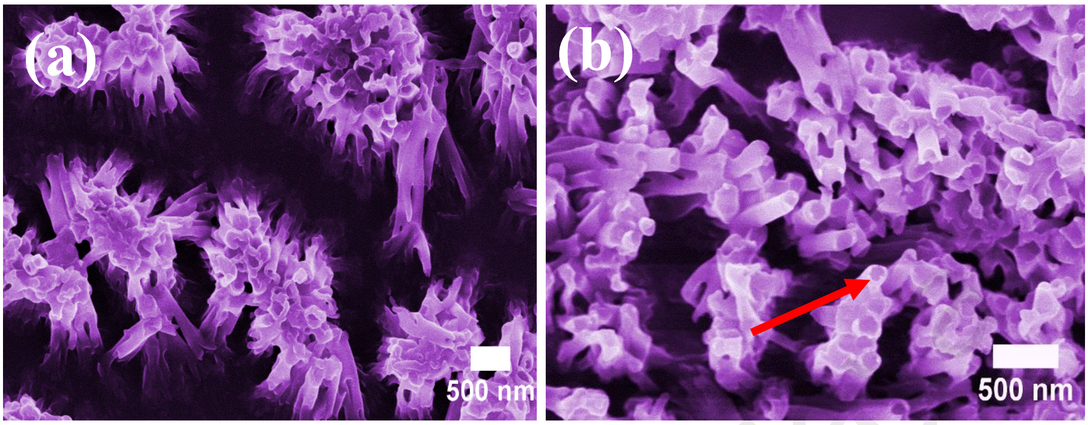

Figure 4.3: (a&b) FESEM images of nanotubes produced from 5 mg/ml PCDTBT solution spin coated at 2000 rpm.

Meanwhile, 2000 rpm spinning rate has produced nanotubes with less collapse and entanglement compared to 1000 rpm of the same concentration (5 mg/ml) which can be seen in Figure 4.3(a) & (b). No entanglement and collapse structures nanotubes can be seen from the top surface of nanotubes as shown by the red arrow in Figure 4.3(b). This indicates that the nanotubes possess a slightly thicker wall compared to the nanotubes produces by 1000 rpm. Higher spinning rate (2000 rpm) cause a larger amount of low concentration of 5 mg/ml PCDTBT solution to splash away at the start of spinning and leave a small amount of PCDTBT solution to infiltrate through. Higher evaporation rate at 2000 rpm compared to 1000 rpm, cause the low concentration of 5 mg/ml PCDTBT solution to dried up faster and stop flowing which then prevent further wall's thinning process to occur which can be one of the reason for slightly thicker nanotube's wall and less entanglement at the top surface.

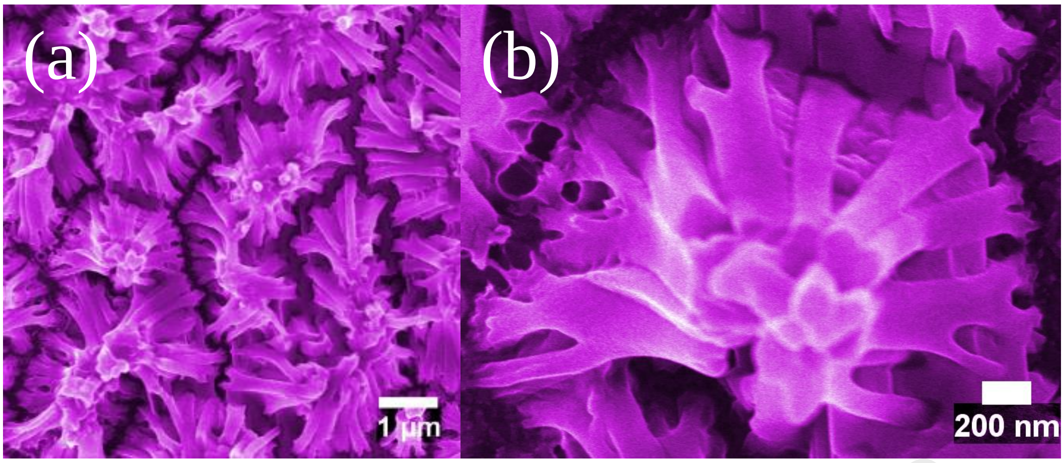

Figure 4.4: (a&b) FESEM images of nanotubes produced from 5 mg/ml PCDTBT solution spin coated at 3000 rpm.

Instead of hollow structure (nanotubes), solid structure (nanorods) was formed when 5 mg/ml PCDTBT solution was spin coated at 3000 rpm as shown in Figure 4.4(a) & (b). Higher spinning rate at 3000 rpm cause a larger amount of polymer supply (PCDTBT solution) to splash away at the start of the spin compared to 1000 and 2000 rpm. The solution is dried up rapidly at 3000 rpm (high evaporation rate) has caused the infiltration to stop before forming a tube wall and produce nanorods instead of nanotubes. The low viscosity solution that spin coated at high spinning rate (3000 rpm) also flows rapidly through the porous and causes the saturation at the end of the flow. This 'end' is referred to the tip of nanorod, which has additional stress than in the bottom part. There is no broken part that can be seen from the FESEM images of nanorods, which indicate the higher stability compared to the nanotubes produce from 1000 and 2000 rpm. The stability of the nanorods also provide by its solid form structure. Other than that, nanorods also possess smoother surface which indicate that the structure does not disturb by the dissolution process due to its solid form structure unlike the other two structures of 5 mg/ml (1000 and 2000 rpm). The joining tips shown by nanorods are due to the low viscosity behaviour of solution during infiltration.

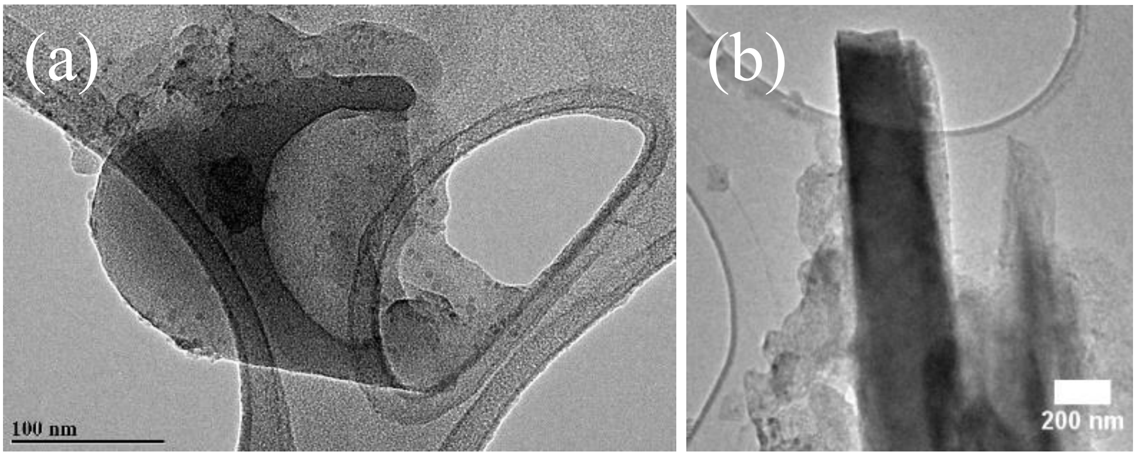

Figure 4.5: HRTEM images of 5 mg/ml PCDTBT nanotubes (a) and PCDTBT nanorods (b).

Figure 4.5(a) showing the meniscus cap of the hollow nanotubes structure that cannot be seen from FESEM images especially for 5 mg/ml at 1000 rpm due to the higher degree of collapse and broken structures. The HRTEM image of the individual nanorod is shown in Figure 4.5(b). The flat tip can be seen at the end of the nanorod with diameter of ~200 nm which replicated the template’s inner porous diameter and also correlated well with the flat tip shown in FESEM images (Figure 4.4(b)).

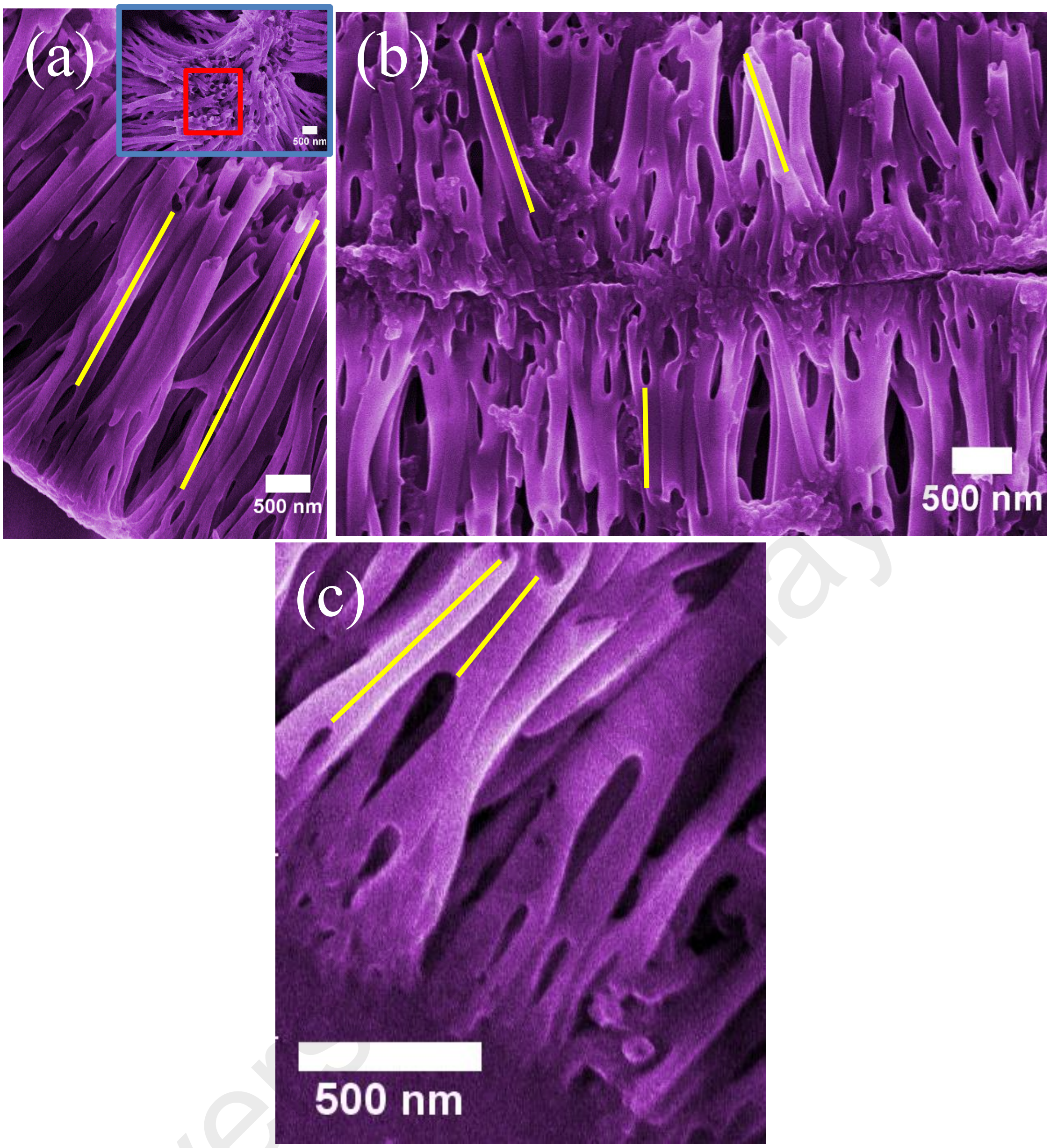

Figure 4.6: FESEM images of nanotubes produced from 10 mg/ml PCDTBT solution spin coated at (a) 1000 rpm, (b) 2000 rpm and (c) 3000 rpm.

Higher concentration of 10 mg/ml produces hollow structures (nanotubes) for all spinning rates (1000, 2000 and 3000 rpm) as shown in Figure 4.6. Higher concentration of 10 mg/ml causes the nanotube's wall to be more stable and thicker though the PCDTBT solution penetrate deeper which can be observed from 1000 rpm PCDTBT nanotubes in inset of Figure 4.6(a), no entangle of collapse structure observed from the top where hollow structure can be clearly seen as enclosed in the red box. Longer nanotubes of higher aspect ratio could be seen for 1000 rpm followed by 2000 (Figure

4.6(b)) and 3000 rpm (Figure 4.6(c)), which are well correlated with 5 mg/ml concentration as tabulated in Table 4.1. The average length of PCDTBT nanotubes decreases approximately half, as the spinning rate increases from 1000, 2000 and 3000 rpm, which are 2.4, 1 and 0.5 µm, respectively. This can be measured from the Y-branched to the top of the nanotubes as indicated by the yellow line in Figure 4.6(a), (b) & (c). As explained earlier in 5 mg/ml section, higher spinning rate of 2000 and 3000 rpm cause PCDTBT solution to splash in a large amount before infiltrate, hence will produce less amount of polymer supply to infiltrate through and cause a shorter nanostructure. 10 mg/ml PCDTBT nanotubes of 1000 rpm also possess a smoother surface structure as compared to 2000 and 3000 rpm PCDTBT nanotubes.

Table 4.1: Average length for 10 mg/ml nanotubes produced from 1000, 2000 and 3000 rpm.

Spinning rate (rpm)	Average length (µm)
1000	2.4
2000	1
3000	0.5

Figure 4.7 (a&b), (c&d) and (e&f) showed the FESEM images of nanotubes produced from 15 mg/ml PCDTBT solution spin coated at 1000, 2000 and 3000 rpm, respectively. Figure 4.7(a) shows an island of nanotubes for 15 mg/ml spin coated at 1000 rpm which is clearly isolated and much smaller if compared to lower concentration of 5 mg/ml that spin coated at the same spinning rate (Figure 4.1(a) & (b)). It is seen that 15 mg/ml (1000 rpm) shown less collapse and entanglement compared to 5 mg/ml (1000 rpm). However, the entanglement still occurs as can be seen in the red box of Figure 4.7(b). Low spinning rate of 1000 rpm (30s) provide not enough assistance to help the higher concentration of 15 mg/ml to infiltrate deeper.

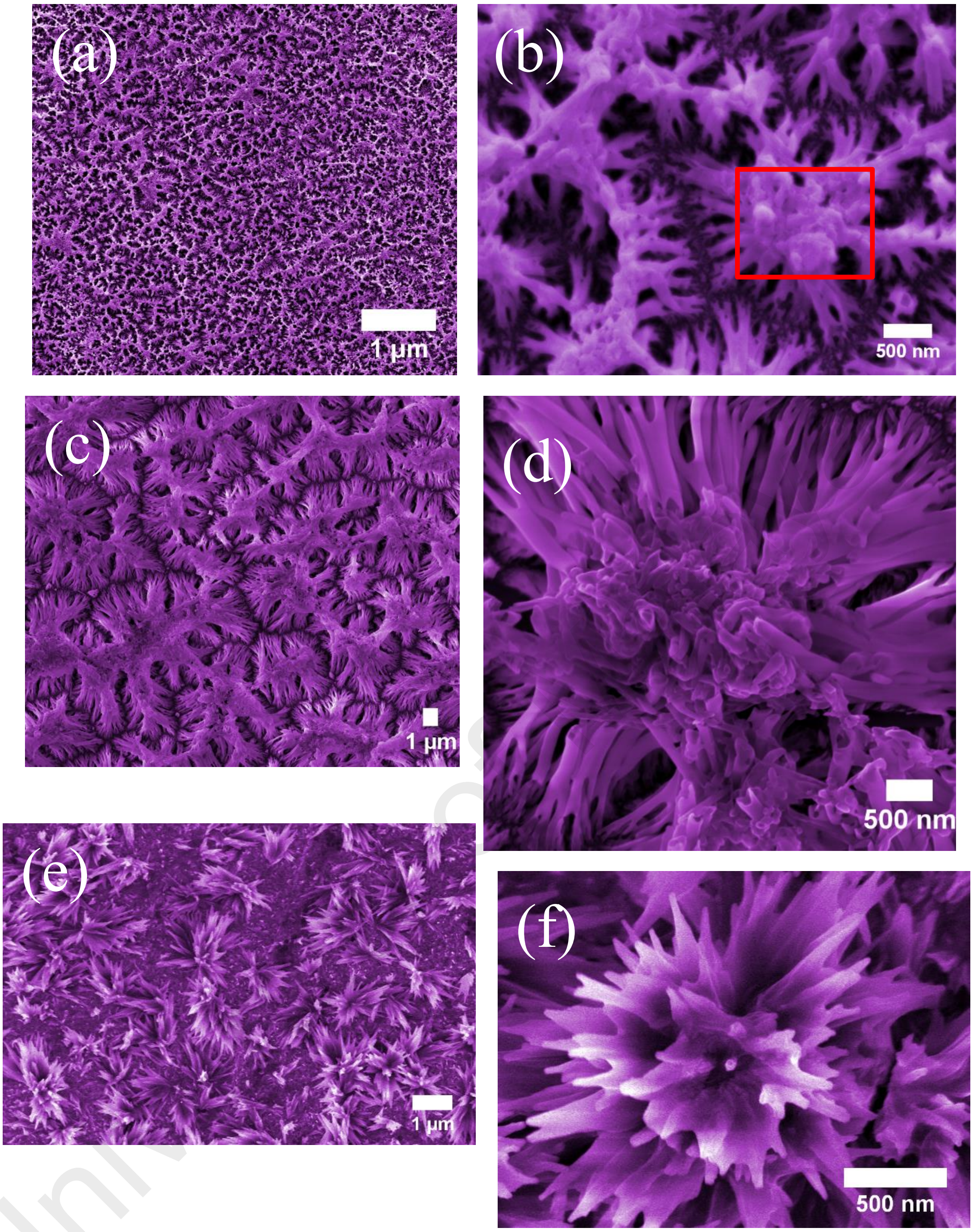

Figure 4.7: FESEM images of nanotubes produced from 15 mg/ml PCDTBT solution spin coated at (a&b) 1000 rpm, (c&d) 2000 rpm and (e&f) 3000 rpm.

Some high concentrated solution may stick at the top surface of template; some may infiltrate through and create a thin wall that will collapse during dissolution process. Furthermore, high concentration of 15 mg/ml owns a slower evaporation rate since the water molecules not easily escape as the surface tension of solution is increased. As the concentration increases, the intermolecular forces are also increase due to the increase in the number of molecules which cause the molecule to be attracted in many directions as well as decrease in the distance between the molecules. Thus, higher energy is needed for the water molecule to escape, which then slower the evaporation rate as illustrated in Figure 4.8.

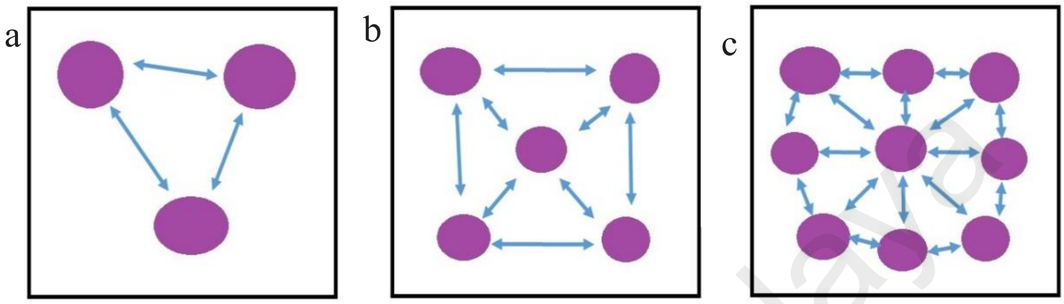

Figure 4.8: Schematic illustration of different intermolecular forces for different concentration (a) 5 mg/ml, (b) 10 mg/ml and (c) 15 mg/ml.

Low spinning rate of 1000 rpm contributes to the low evaporation rate. This low evaporation rate allows the solution to infiltrate deeper before dried up and continue the wall thinning process. Nanostructures for 5 mg/ml (1000 rpm) and 15 mg/ml (1000 rpm) have almost the same characteristics, which are shorter and collapse in a quite large degree but infiltrate in different way where concentration plays a vital role. Conversely, for 10 mg/ml (1000 rpm), less degree of collapsing and entanglement can be seen where intermediate concentration of 10 mg/ml is able to flow and create a thicker and stable nanotube's wall. As the spinning rate increases to 2000 rpm for 15 mg/ml, the nanostructures become more stable and able to create some thicker wall, however, less amount of collapsing is occurred at the end of the flowing as shown in Figure 4.7(c) & (d).

Surprisingly, when the spinning rate is increased to 3000 rpm (15 mg/ml), flower-like structure was formed instead of nanorods or nanotubes. The magnified view of PCDTBT nanoflowers demonstrates the highly dense ensemble if compared with nanorods or nanotubes. Most of the individual nanoflower tends to merge with several of its species (neighbours) and forms a circular petal of sharp-end. Unlike the individual nanorod or nanotubes, which meet up at the tip, the nanoflowers arose from the basal and pointed outward. By tuning the solution concentration (15 mg/ml) and spinning rate (3000 rpm), distinct behaviours of polymer may have been presence, both for before and after template's dissolution. For the nanoflowers, the stress is accumulating at the bottom rather than at the top. High solution viscosity of 15 mg/ml has triggered to decelerate the solution motion. Rather than accelerating rapidly to the end, high viscous solution tends to enhance stress at the basal. Flowing of high concentration solution with high spinning rate through a small channel cause some separation in the solution viscosity (viscosity gradient) (Pasquali et al., 2011). Higher viscosity at the start of flow tends to enhance stress at the basal, while high spinning rate of 3000 rpm cause the low viscous part to accelerate and cause a sharp end. Due to this behaviour, nanoflowers that comprised of petals can easily be assembled.

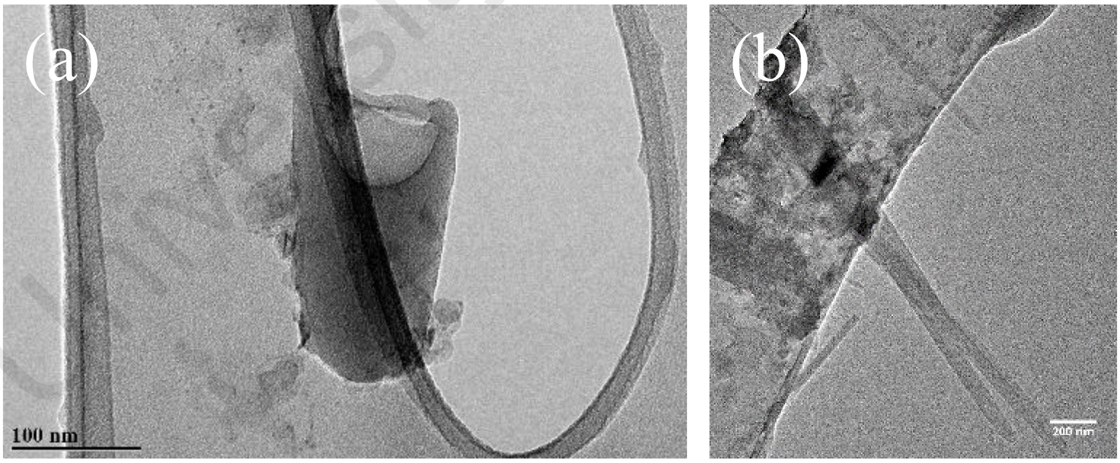

Figure 4.9: HRTEM images of (a) 15 mg/ml PCDTBT nanotubes and (b) PCDTBT nanoflowers.

The hollow nanotubes of 15 mg/ml is confirmed by TEM image shown in Figure 4.9(a), where a meniscus is occurred at the end of the flow. TEM image of individual nanoflowers in Figure 4.9(b) has supported the solid structure of sharp-end petal (Figure 4.7(f)), with a diameter less than 100 nm.

Based on the observed formed nanostructures, PCDTBT solution was unlikely to infiltrate through the porous template that having a 60 μm in thickness. This postulation is made based on the obtained length of individual nanotube, nanorod and nanoflower. The main contribution to the imperfect infiltration is the existing of stronger adhesive force (between the template wall and PCDTBT solution) than the cohesive force (Kokonou et al., 2013). Imperfect infiltration can also contribute by the high spin coating rate. A high spin coating rate could increase the solvent evaporation rate and adhesive force.

The proposed formation of nanorods, nanotubes and nanoflowers are presented in Figure 4.10(a), (b) & (c), respectively. High surface tension of alumina template enables the PCDTBT solution to wet its surface and form the nanotubes, nanorods or nanoflowers depend on the parameter involved. The stronger adhesive force between the template's surface and PCDTBT solution assisted the flow of PCDTBT solution inside the alumina template's pore. High spin coating rate promotes the PCDTBT solution to flow faster and become comparable to the adhesive force of the template's surface. This phenomenon contributes to the formation of the solid structure (nanorod and nanoflowers) instead of hollow structure. Meanwhile, for the hollow structure (nanotubes), the wetting and complete filling of the template's pore walls occurs consecutively where wetting of pore walls occurs prior to the complete filling due to the stronger adhesive forces between PCDTBT molecules and pore wall surface. Intermolecular attractive force (cohesive force) between the PCDTBT molecule, has caused most of the nanostructure to meet up at the tip instead of aligned themselves vertically as illustrated in Figure 4.10(a) & (b). Unlike other nanostructures, nanoflowers use a high concentration of 15 mg/ml PCDTBT solution with high spin coating rate of 3000 rpm, which has enhanced stress at the basal instead at the tip. Viscosity separation in a very small channel also influences the stronger intermolecular forces at basal. This explained the outward pointing of nanoflowers instead of meeting up at the tip as shown in Figure 4.10(c).

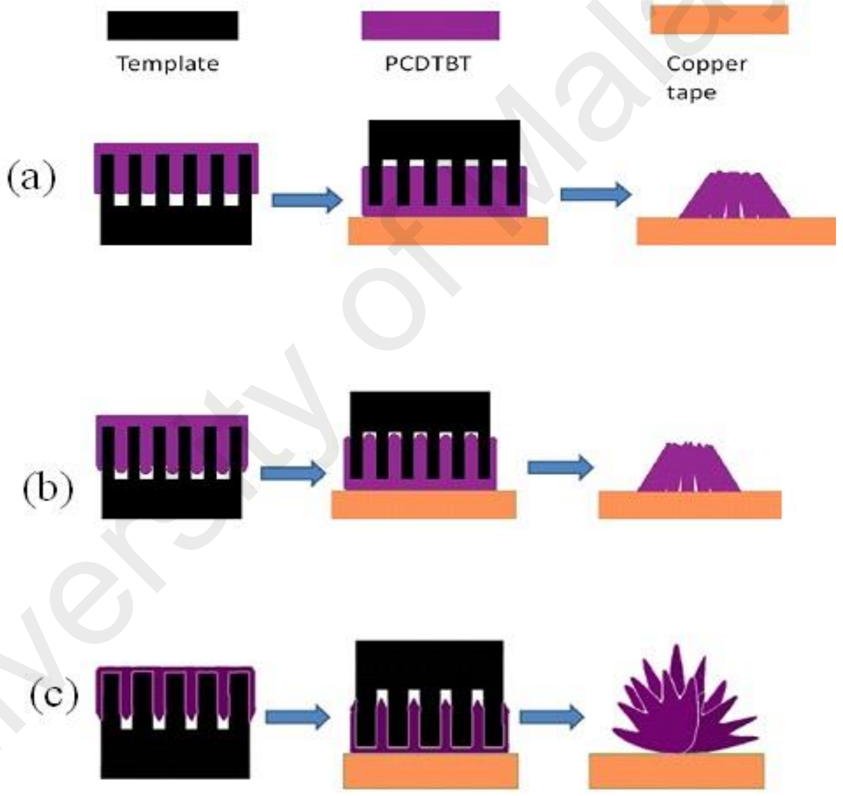

Figure 4.10: Schematic illustration of the formation of (a) PCDTBT nanorods, (b) nanotubes and (c) nanoflowers.

4.1.1.2 Optical Properties

The UV–vis absorption spectra of 5 mg/ml PCDTBT nanostructures of different spinning rates (1000, 2000 and 3000 rpm) are shown in Figure 4.11(a). The UV-vis absorption spectra clearly shown the two absorption bands at UV and visible region which represent the donor carbazole (Cz) and acceptor dithienylbenzothiadiazole (DTBT), respectively (Jha et al., 2013). It shows that 1000 rpm give a significant red shift and wider absorption range compared to 2000 and 3000 rpm where its dominant peak at 570 nm exceed the dominant absorption peaks for 2000 and 3000 rpm located at 563 nm by 7 nm. Even 2000 and 3000 rpm have the similar maximum peak at 563 nm, 2000 rpm shown a wider absorption range as compared to 3000 rpm. A significant red shift is portrayed by 1000 rpm owing to the further aggregated configuration in the polymer backbone. The π–π^* interaction between carbazole (Cz) units and conjugated main chains for 1000 rpm are centred at 396 nm and 570 nm respectively which is seen to be dominant compared to the other spin rate.

UV-vis spectra of 10 mg/ml PCDTBT nanostructures of 1000, 2000 and 3000 rpm are shown in Figure 4.11(b). Most significant red shifted spectra of 10 mg/ml could be observed for 1000 rpm as compared to 2000 and 3000 rpm. Both Cz and DTBT region absorb the highest intensity at 398 nm and 574 nm, respectively, compared to 396 nm for 2000 and 3000 rpm, while 561 nm for 2000 rpm and 560 nm for 3000 rpm. 1000 rpm of 5 mg/ml also showed a wider absorption range as compared to the other spinning rates. The similar pattern could be observed for 15 mg/ml (Figure 4.11(c)), where 1000 rpm absorb light at a longer wavelength (583 nm) compared to 2000 rpm (580 nm) and 3000 rpm (581 nm).

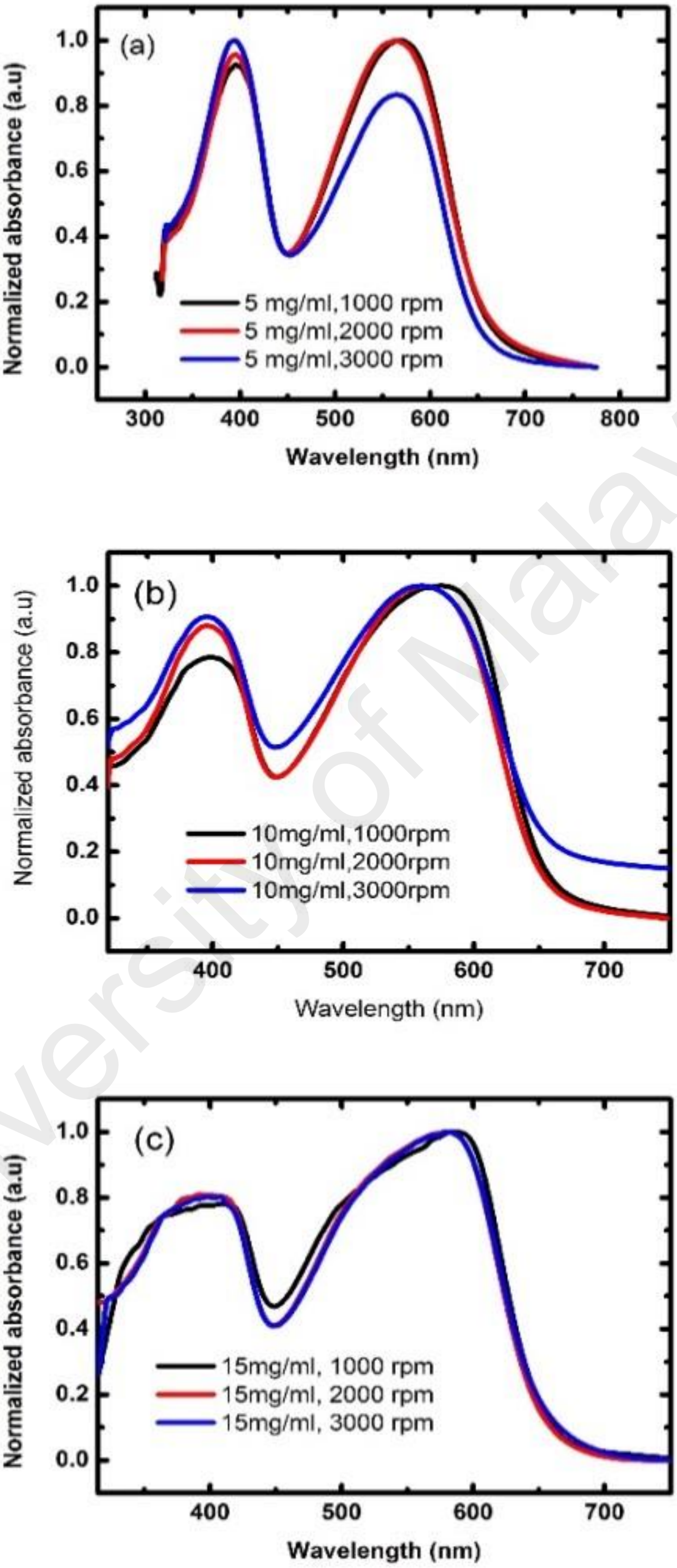

Figure 4.11: UV-vis absorption spectra of PCDTBT nanostructures of (a) 5 mg/ml, (b) 10 mg/ml (c) and 15 mg/ml produced from different spinning rate of 1000, 2000 and 3000 rpm.

The photoluminescence (PL) spectra of PCDTBT nanostructures synthesised at different spinning rate of different concentration are shown in Figure 4.12. The emission of Cz segment that usually lies between 400 to 500 nm is completely quenched for all spectra with the dominance of emissions are due to the DTBT unit, indicating an efficient energy transfer from Cz segment to the DTBT. Higher degree of quenching is shown by 1000 rpm for all concentrations followed by 2000 and 3000 rpm. The quenching of PL intensity lowered the luminescence quantum yield and increased the photon absorption, which useful in enhancing the optical devices performances.

Low spinning rate efficaciously produced nanostructures that are better in their optical properties as compared to the higher spinning rate. This could be due to the rapid evaporation of the volatile chloroform solvent at higher spinning rate (2000 and 3000 rpm), which tends to favour retention of the tightly coiled chains. There is simply too little time for chain–chain or substrate–chain interactions to cause the polymer to extend its conformation before the solvent has evaporated (Nguyen et al., 1999). When 1000 rpm from each concentration is compared (Figure 4.13), 15 mg/ml shown better optical properties which showing a significant red shifted of UV-vis spectra with maximum absorption is at 583 nm compared to 574 and 570 nm for 10 and 5 mg/ml, respectively.

These UV-vis absorptions are well correlated with the red shift emission patterned shown in the PL spectra (Figure 4.12). This indicates that the solution concentration plays a vital role in manipulating the photo physics of the nanostructured formation. Solution concentration of polymer imposed a strong influence on the aggregation behaviour and significantly related to the red-shifted of UV-vis absorption peak.

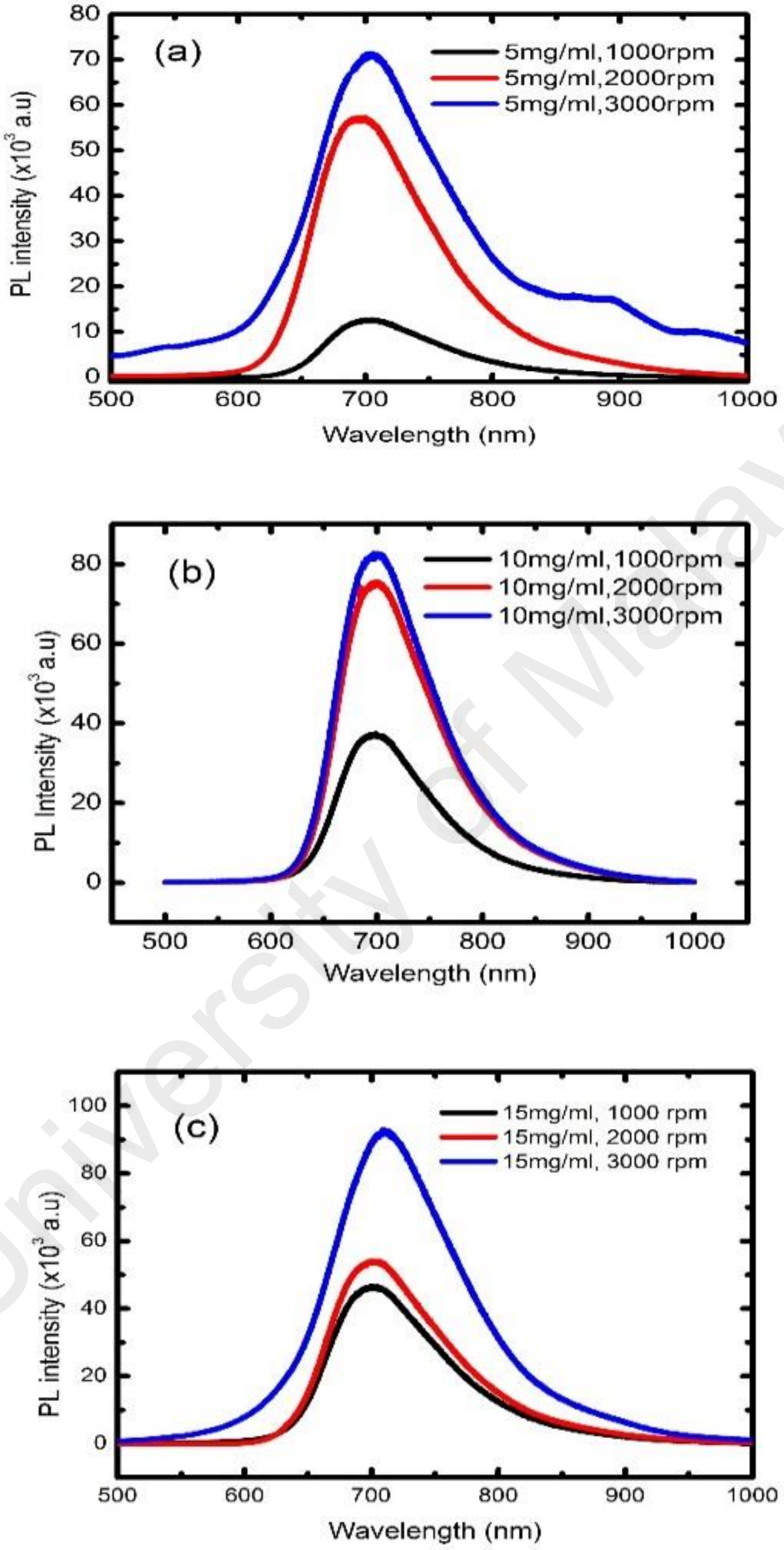

Figure 4.12: Photoluminescence spectra of PCDTBT nanostructures of (a) 5 mg/ml, (b) 10 mg/ml and (c) 15 mg/ml produced from different spinning rate of 1000, 2000 and 3000 rpm.

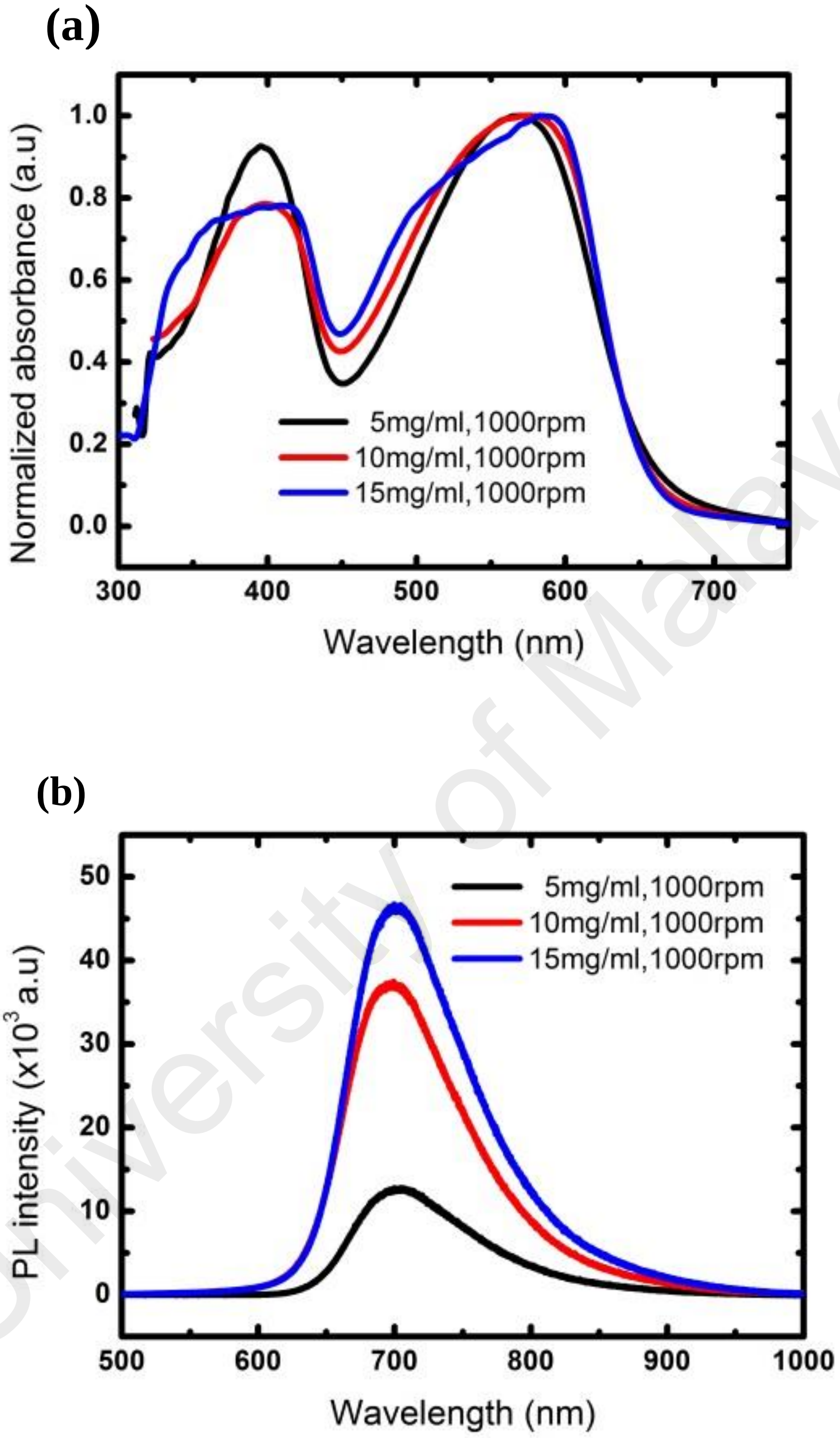

Figure 4.13: (a) UV-vis and (b) Photoluminescence spectra of 1000 rpm for 5, 10 and 15 mg/ml.

According to the previous research (Nguyen et al., 2000), degree of aggregation is higher at the higher polymer concentration**.** Polymer aggregates occurred when two or more chain segments come together and share their π-electron density. High concentration solution will provide a greater number of chains segments available for interaction and increased the extent of aggregation between adjacent polymer chains as illustrated in the 4.14.

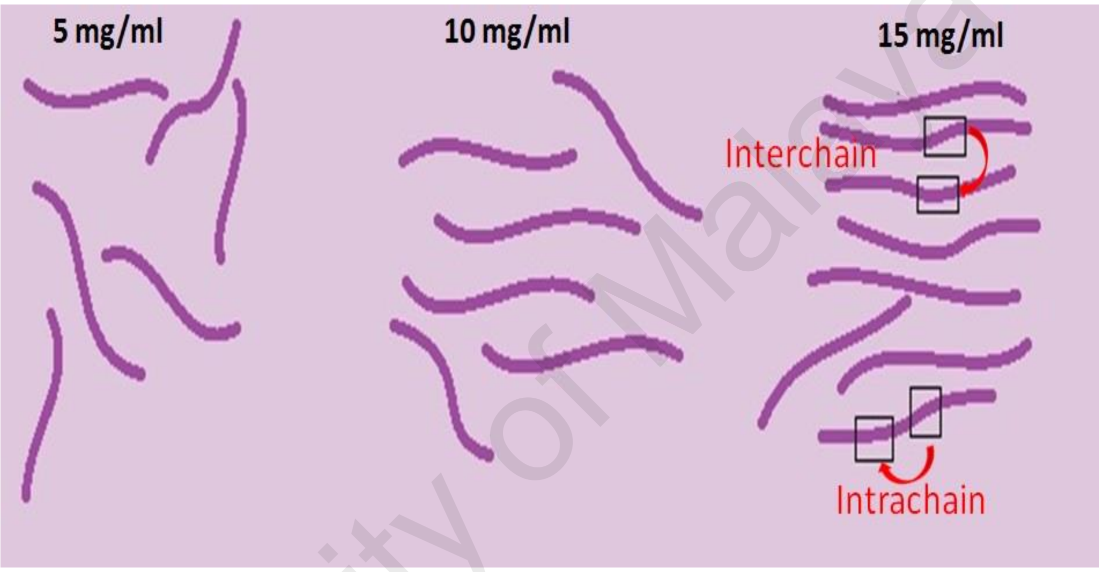

Figure 4.14: Schematic illustration on how polymer chain aggregated in different solution concentration of (a) 5 mg/ml, (b) 10 mg/ml and (c) 15 mg/ml.

4.1.1.3 Structural Properties

To further clarify the impact of spin coating technique of different concentration on the produced nanostructures, only the best sample from each concentration is selected for Raman analysis. Raman spectra and Raman peak position of PCDTBT nanostructures of 5, 10 and 15 mg/ml that spin coated at 1000 rpm are shown in Figure 4.15 and Table 4.2, respectively.

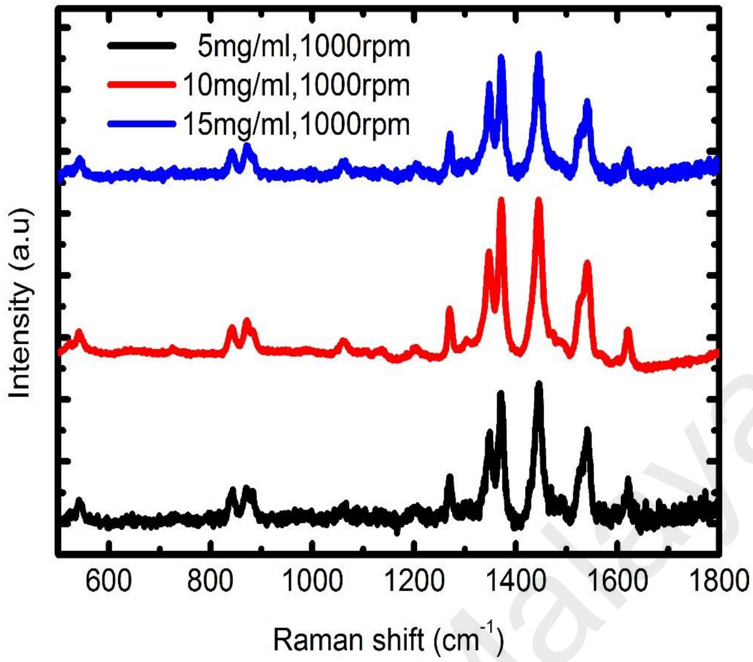

Figure 4.15: Raman spectra of PCDTBT nanostructures of 5, 10 and 15 mg/ml that spin coated at 1000 rpm.

Table 4.2: Raman peak position of PCDTBT nanostructures of 5, 10 and 15 mg/ml that spin coated at 1000 rpm

Raman shift (cm^{-1})			
5 mg/ml	**10 mg/ml**	**15 mg/ml**	**Assignments**
844	842	843	Sym C-S stretch
870	871	871	Asym C-S stretch
1066	1062	1062	L: Th CH ip δ+$V_{C=C}$
1270	1270	1271	D: BT δ +$V_{C=C}$ + C-H ip δ, Cz+Th CH ip δ+$V_{C=C}$
1349	1347	1348	D: BT+Th CH δ, Cz+BT $V_{C=C}$
1371	1372	1371	BT+Th+Cz $V_{C=C}$ +,CH in plane δ,CZ V_{C-N}
1446	1444	1446	L:Cz Th $V_{C=C}$ + CH ip δ, Cz VC-N
1541	1541	1541	L:BT+Th sym $V_{C=C}$, CH ip δ
1621	1621	1622	L:Cz $V_{C=C}$ +CH ip δ
Sym, symmetric; asym, asymmetric; L, localized; Th, thiophene; ip,in plane; Va-b, stretch of a-b bond; δ, bend; D, delocalized; BT, benzothiadiazole; Cz, carbazole			

There is a downward shift of about 2 cm^{-1} as the concentration increases from 5 to 10 mg/ml, which then drop by 1 cm^{-1} for 15 mg/ml that assign for symmetric C-S stretch. Meanwhile, asymmetric C-S stretch has shown a little upward shift of 1 cm^{-1} as the concentration increases from 5 to 10 and 15 mg/ml. A significant downward shift of about 4 cm^{-1} could be observed for localized Thiophene (Th) of C-H in plane bending and C=C stretch as the concentration increases from 5 (1066 cm^{-1}) to 10 (1062 cm^{-1}) and 15 mg/ml (1062 cm^{-1}). No significant change for delocalized BT of C=C stretch and C-H bending as well as Cz+Th of C-H bending and its C=C stretch between these three concentrations of 5,10 and 15 mg/ml except 1 cm^{-1} upward shift for 15 mg/ml located at 1271 cm^{-1}. Downward (1347 cm^{-1}) and upward (1348 cm^{-1}) shifts of 2 and 1 cm^{-1} could be observed for 10 and 15 mg/ml, respectively, represents C-H bending and C=C stretch of delocalized Th & Cz+BT. Upward and downward shifts of 1 cm^{-1} are recorded for BT, Th & Cz of C=C stretch, C-H in plane bending and C-N stretch of Cz segment. Whereas, C-H in plane bending, C=C and C-N stretch of localized Cz and Th shown 2 cm^{-1} downward to 1444 cm^{-1} and upward shift to 1446 cm^{-1} for 10 and 15 mg/ml, respectively. Similar Raman peak position is observed at 1541 cm^{-1} for all concentrations denotes symmetric C=C stretch and C-H in plane bending of localized BT and Th. Only 15 mg/ml shows a small shift of about 1 cm^{-1} for Cz C=C stretch and C-H bending.

Localized Thiophene (Th) of C-H in plane bending & C=C stretch, C-H bending & C=C stretch of delocalized Th & Cz+BT and C=C & C-N stretch of localized Cz and Th show a significant higher upward shift for 5 mg/ml as compared to 10 and 15 mg/ml. This significant upward shift of 5 mg/ml (1000 rpm) could be due to the decrease in its effective bond length. Decrease in the effective bond length of 5 mg/ml (1000 rpm) samples is highly correlated with its blue shift UV-vis spectra (Botelho et al., 2014; Schaffer et al., 1991).

4.2 Part II: Immersion Technique

4.2.1 Results & Discussion

4.2.1.1 Morphological Properties

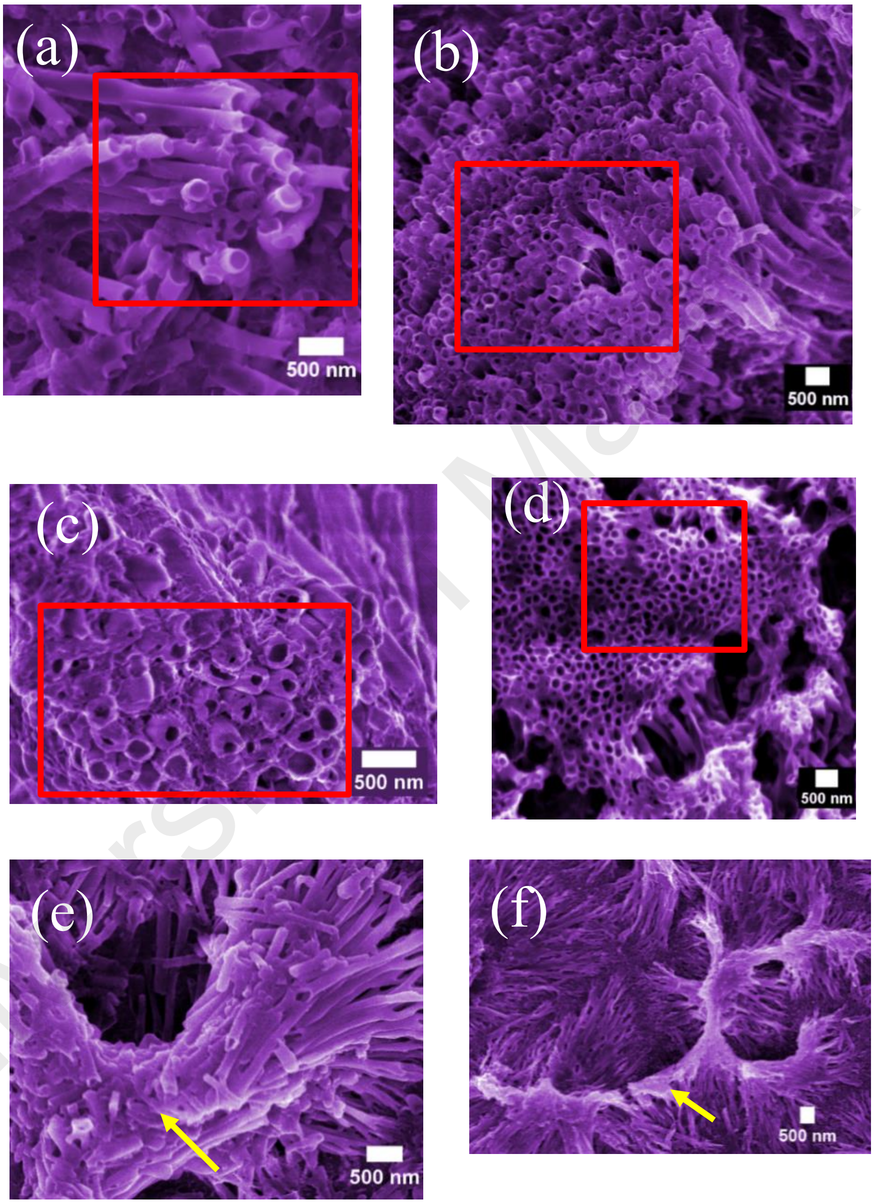

Figure 4.16: FESEM images of 5 mg/ml (a&b) nanostructures produced from 2, (c&d) 12 & (e&f) 24 hours immersion time annealed at 50 and 150 °C, respectively.

Figure 4.16 shows FESEM images of 5 mg/ml nanostructures produced from 50 and 150 °C annealing temperature that immersed for 2, 12 and 24 hours prior to annealing. Red box in Figure 4.16(a), (b), (c) & (d) show a better alignment of 2 and 12 hours immersion time for both annealing temperatures of 50 and 150 °C compared to 24 hours. Collapsed structures are observed in 24 hours immersion time for both annealing temperatures (50 and 150 °C) compared to 2 and 12 hours immersion time as can be seen in Figure 4.16(e) & (f). The collapsed structure can be clearly seen by looking at the top of the nanotubes where they possess smaller island tip as indicated by yellow arrow (collapsing part). This could be due to the longer immersion time of 24 hours which allow the PCDTBT solution to penetrate deeper and become high in aspect ratio, this high aspect ratio nanostructure reduces its stability during dissolution process and tends to collapse and forms a bundle which also contributed by the intermolecular force between the nanotubes.

Figure 4.17 shows FESEM images of 10 mg/ml PCDTBT nanostructures produced from (a) & (b) 2, (c) & (d) 12 & (e) & (f) 24 hours immersion time of 50 and 150 °C annealing temperature, respectively. PCDTBT nanostructures of 10 mg/ml showed the similar pattern as 5 mg/ml where 2 and 12 hours of both annealing temperatures (50 and 150 °C) possess a better alignment of lesser collapsing and agglomerating as shown in the red box of Figure 4.17(a), (b), (c) & (d) if compared to 24 hours immersion time (Figure 4.17(e) & (f)). Yellow arrow in Figure 4.17(e) & (f) shows a smaller tip bundle that agglomerated and collapsed when immersed in 10 mg/ml of PCDTBT solution for 24 hours at 50 and 150 °C.

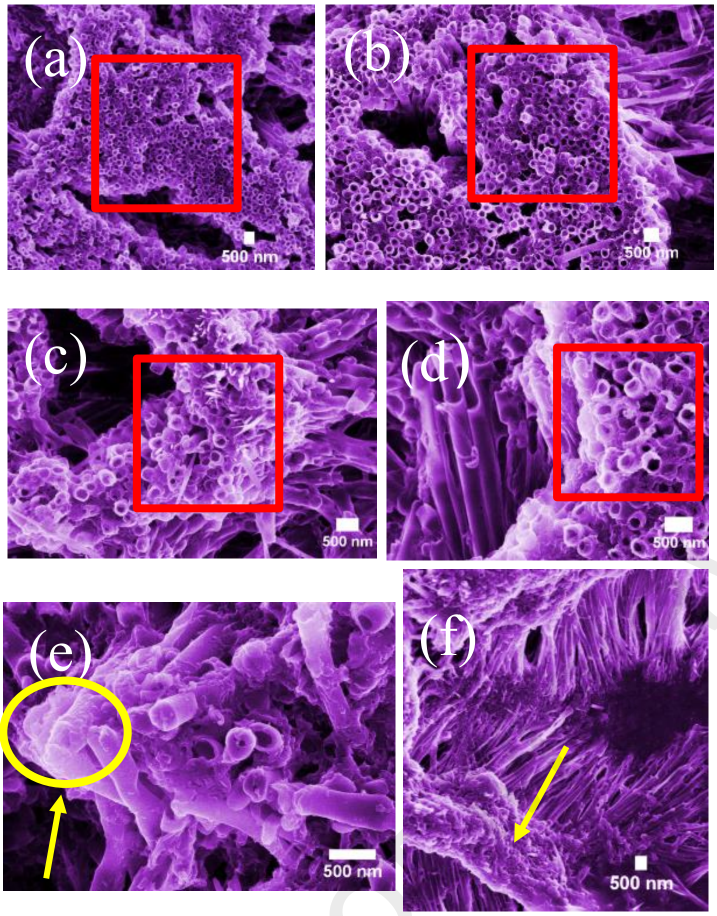

Figure 4.17: FESEM images of 10 mg/ml PCDTBT nanostructures produced from (a&b) 2, (c&d) 12 & (e&f) 24 hours immersion time at 50 and 150 °C annealing temperature, respectively.

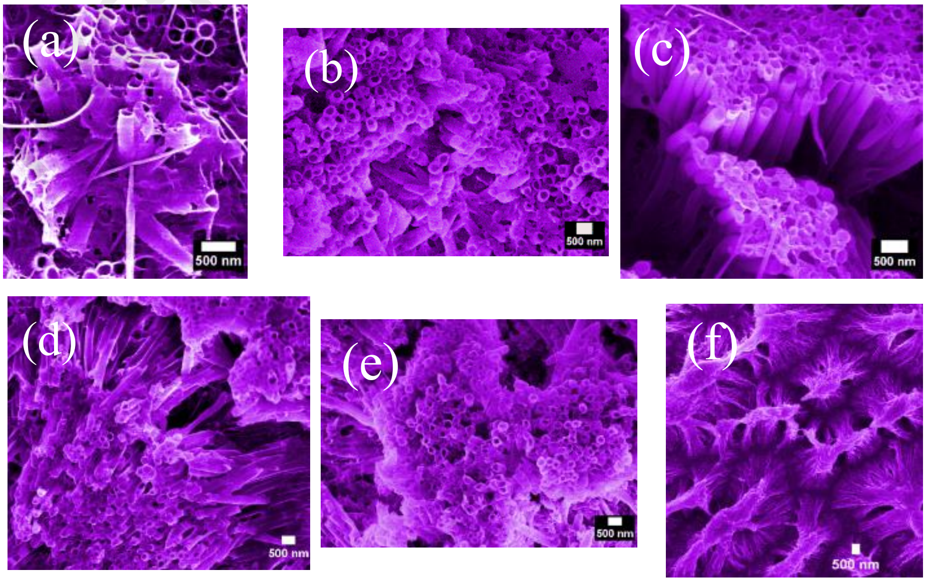

Figure 4.18: FESEM images of 15 mg/ml PCDTBT nanostructures produced from (a,b&c) 50 and (d,e&f) 150 °C annealing temperature of 2, 12 and 24 hours immersion time, respectively.

Figure 4.18 shows FESEM images of 15 mg/ml PCDTBT nanostructures produced from 50 ((a), (b) & (c)) and 150 °C ((d), (e) & (f)) annealing temperatures that immersed in 2, 12 and 24 hours immersion time. 15 mg/ml designate a different mechanism at lower annealing temperature (50 °C) where the alignment getting better as the immersion time is increased from 2, 12 and 24 hours as shown in Figure 4.18(a), (b) & (c), respectively. Nanotubes of 24 hours immersion time exhibited the longest among the other immersion times. However, for the higher concentration (15 mg/ml) at low annealing temperature (50 °C), the alignment increases as the densification increases. The denser nanotubes of low annealing temperature (50 °C) could be observed for 24 hours immersion time of 15 mg/ml PCDTBT solution as shown in Figure 4.18(c) which is aligned and no collapsing of nanostructures are observed. Low wettability at higher concentration due to the increase in the cohesive forces (intermolecular forces) between the PCDTBT molecules prevents the PCDTBT solution to penetrate deeper and reduce the aspect ratio of the produced nanotubes. Higher concentration of 15 mg/ml is able to produce a thicker nanotubes wall, which is more stable. However, as the annealing temperature increases (150 °C), the cohesive force getting weaker and stronger adhesive force will increase the wetting action and allow the PCDTBT solution to infiltrate deeper and produce high aspect ratio nanotubes that confined inside the template. This high aspect ratio nanotube tends to collapse and agglomerate during dissolution process as previously mentioned. This could be the reason for the aligned nanotubes of 24 hours annealed at 50 °C, but not for the collapsed nanotubes annealed at 150 °C for the similar concentration of 15 mg/ml.

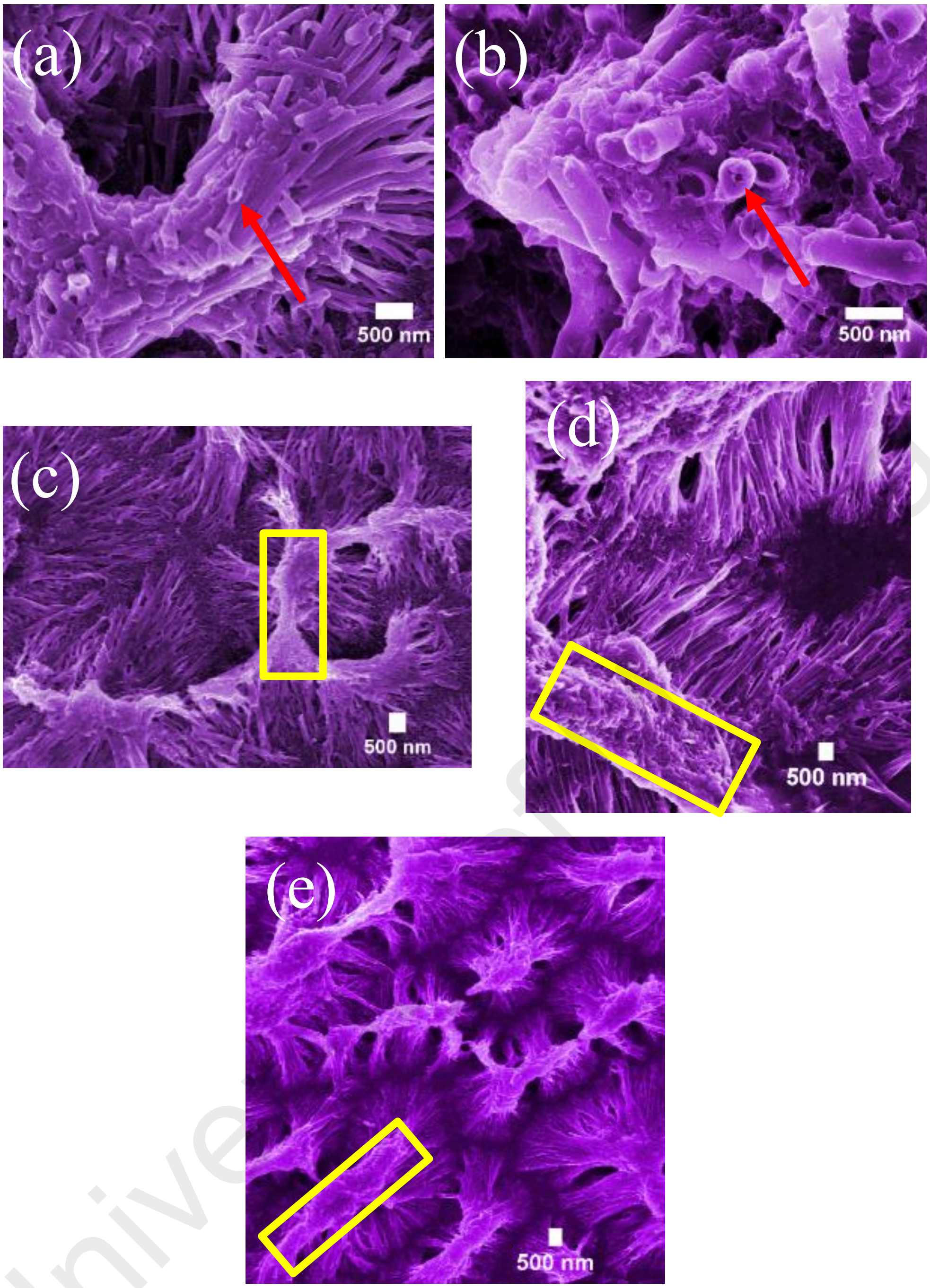

Figure 4.19: FESEM images of PCDTBT nanostructures produced from (a) 5 and (b) 10 mg/ml of 50 °C and (c) 5, (d) 10 and (e) 15 mg/ml of 150 °C annealing temperature of 24 hours immersion time.

One significant observation of each concentration is the effect of annealing temperature on the wettability of the PCDTBT solution. As discussed previously, 24 hours immersion time produced the collapse structures, which turn into a bundle (smaller island at the top part) of every concentration and annealing time. However, the degree of agglomeration is different between the low (50 °C) and high (150 °C) annealing temperature. As shown in Figure 4.19, nanotubes that produced from 150 °C annealing temperature have more agglomeration at the tip. Red arrow in Figure 4.19(a) & (b) indicate a hollow part of the nanotubes that can be clearly seen for all nanotubes of low annealing temperature (50 °C). However, this hollow cannot be seen from the top surface of nanotubes that annealed at 150 °C (Figure 4.19(c), (d) & (e)) due to the extreme agglomeration. The molecules in PCDTBT solution are bound together by the attractive intermolecular forces (e.g. van der walls forces). The increase in the temperature causes the kinetic or thermal energy to increase while these attractive intermolecular forces become weaker. The weak intermolecular force will reduce the surface tension and increase the wetting properties of the PCDTBT solution. The increase in the wetting properties allows the solution to coat the alumina surface deeper and produce longer nanotubes. This longer nanotube will be unstable, collapse and agglomerate during the dissolution process.

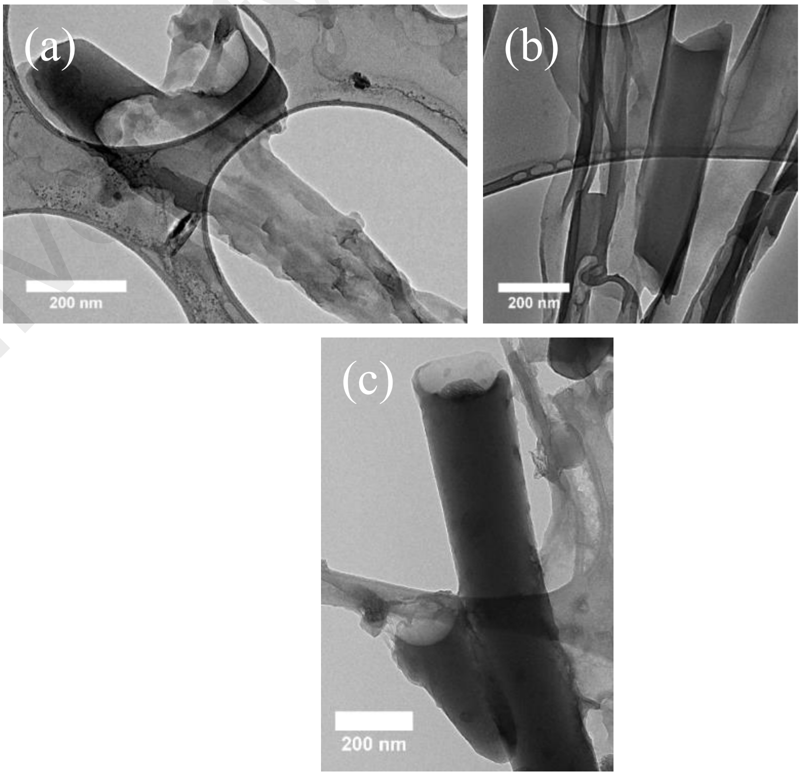

Figure 4.20: HRTEM images of (a) 5, (b) 10 and (c) 15 mg/ml nanotubes produced from immersion technique.

Figure 4.20(a), (b) & (c) shows the HRTEM images for 5, 10 and 15 mg/ml nanotubes that produced from the immersion technique, respectively. Formations of nanotubes are confirmed through the broken structures where a hollow part of the tubes is shown. The HRTEM images support the preceding observations which all of the nanostructures produced using this immersion technique are nanotubes. The diameter of approximately ~200 nm in FESEM images of all nanostructures is complying with the obtained HRTEM images.

Basic wetting mechanism of nanotubes formation has been explained in previous part (part I: Spin coating techniques). Better alignment of nanotubes occurred for 2 and 12 hours of immersion time compared to the 24 hours immersion time, which collapse for almost all parameters involved at 50 and 150 °C as shown in Figure 4.16-4.18. However, unique situation occurred for nanotubes produced from 15 mg/ml that have been immersed and annealed at 24 hours and 150^0 C, respectively. Nanotubes are aligned when immersed for 24 hours and annealed at 50 °C, but collapsed at 150 °C due to some reasons as mentioned previously.

4.2.1.2 Optical Properties

Optical properties of nanostructures can be generally analysed from the UV-vis and PL spectra. UV-vis and PL spectra can be correlated to each other to identify the favourable samples that suit with the specific applications. Figure 4.21(a) shows the UV-vis spectra of 5 mg/ml nanotubes that annealed at 50 °C and immersed for 2, 12, and 24 hours. For 12 hours immersion time, the UV-vis spectrum indicates a red shifted which accompanied by a significant shift to a longer wavelength for its PL spectra shown in Figure 4.21(b). Although PL spectra of 2 and 24 hours immersion time display a slightly better quenching compared to 12 hours, the 12 hours immersion time showed a significant considerable red shifted of PL spectra.

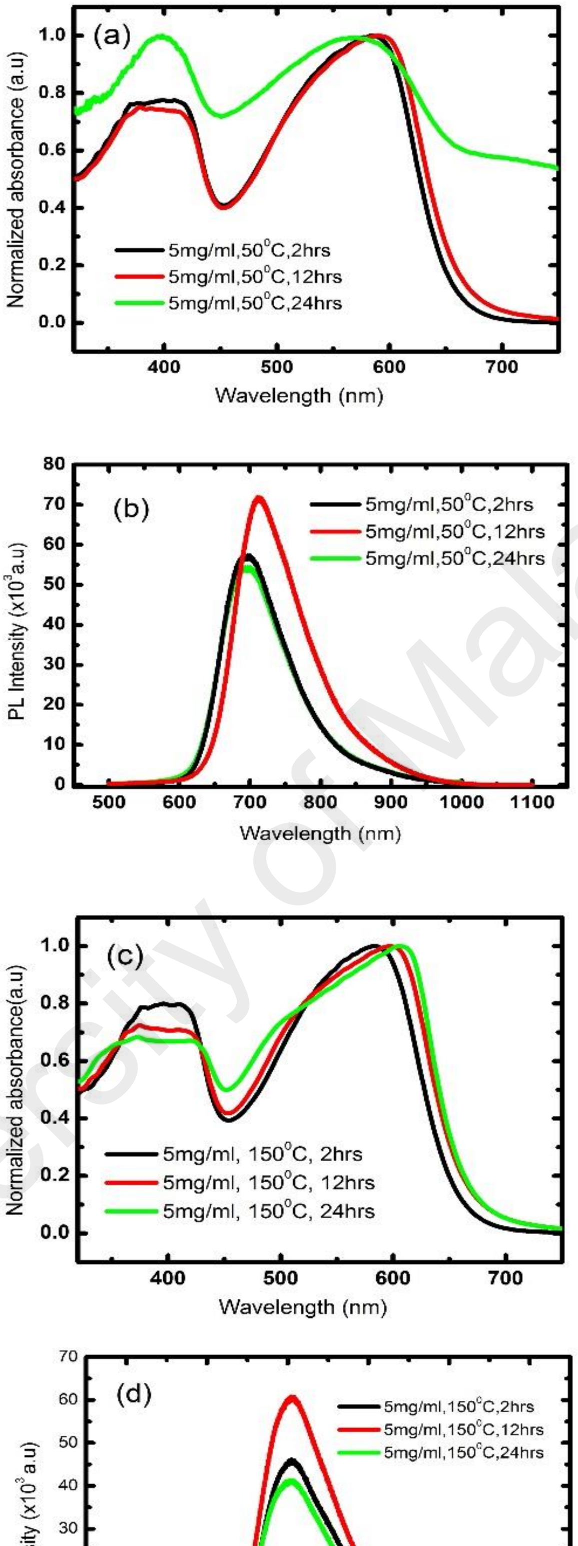

Figure 4.21: UV-vis absorption and photoluminescence spectra of 5 mg/ml PCDTBT nanotubes that annealed at (a&b) 50 °C and (c&d) 150 °C, respectively, which immersed for 2, 12, and 24 hours.

Red-shifted of PL spectra at 713 nm in 12 hours nanotubes system is due to the increased in the Stokes shift, which implies that the polymer chain become more rigid. The increase in rigidity is well associated with the better alignment state of polymer chains in the porous alumina template (Liu et al., 2008; Yang et al., 2008). When the degree of annealing increased to 150 °C, a remarkable patterned of UV-vis spectra could be seen where a longer immersion time of 24 hours shown the widest absorption range and having absorption at the longest wavelength followed by 12 and 2 hours immersion time as shown in Figure 4.21(c). Higher degree of PL quenching occurred for 24 hours immersed nanotubes compared to the other immersion times of 2 and 12 hours. This is well correlated with the UV-vis spectrum of 24 hours immersion time which having the widest and longest absorption range.

Figure 4.22(a) shows the UV-vis spectra of 10 mg/ml annealed at 50 °C for 2, 12 and 24 hours immersion time. Uncommon pattern could be seen where 2 hours immersion time show better optical properties in term of the wideness and red-shiftiness of light absorption. This pattern made a very good correlation with the PL spectra shown in Figure 4.22(b), with 2 hours immersion time exhibit the most quenched PL intensity followed by 12 and 24 hours. However, 24 hours immersion time of 10 mg/ml still retained the similar optical properties as of 5 mg/ml, when the annealing temperature is increased to 150 °C. Figure 4.22(c) shows the widest absorption range for 24 hours compared to 2 and 12 hours immersion time and it is in good correlation with its PL quenching (Figure 4.22(d)).

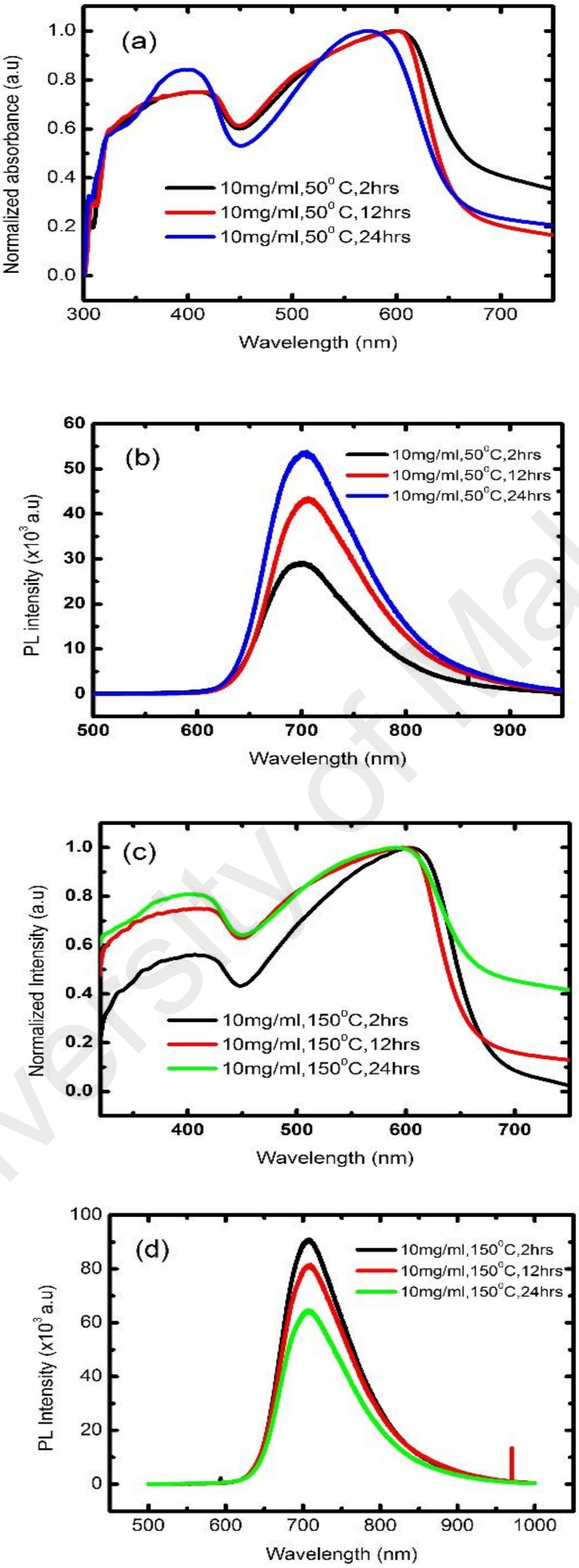

Figure 4.22: UV-vis absorption and photoluminescence spectra of 10 mg/ml PCDTBT nanotubes that annealed at (a&b) 50 °C and (c&d) 150 °C, respectively, which immersed for 2, 12, and 24 hours.

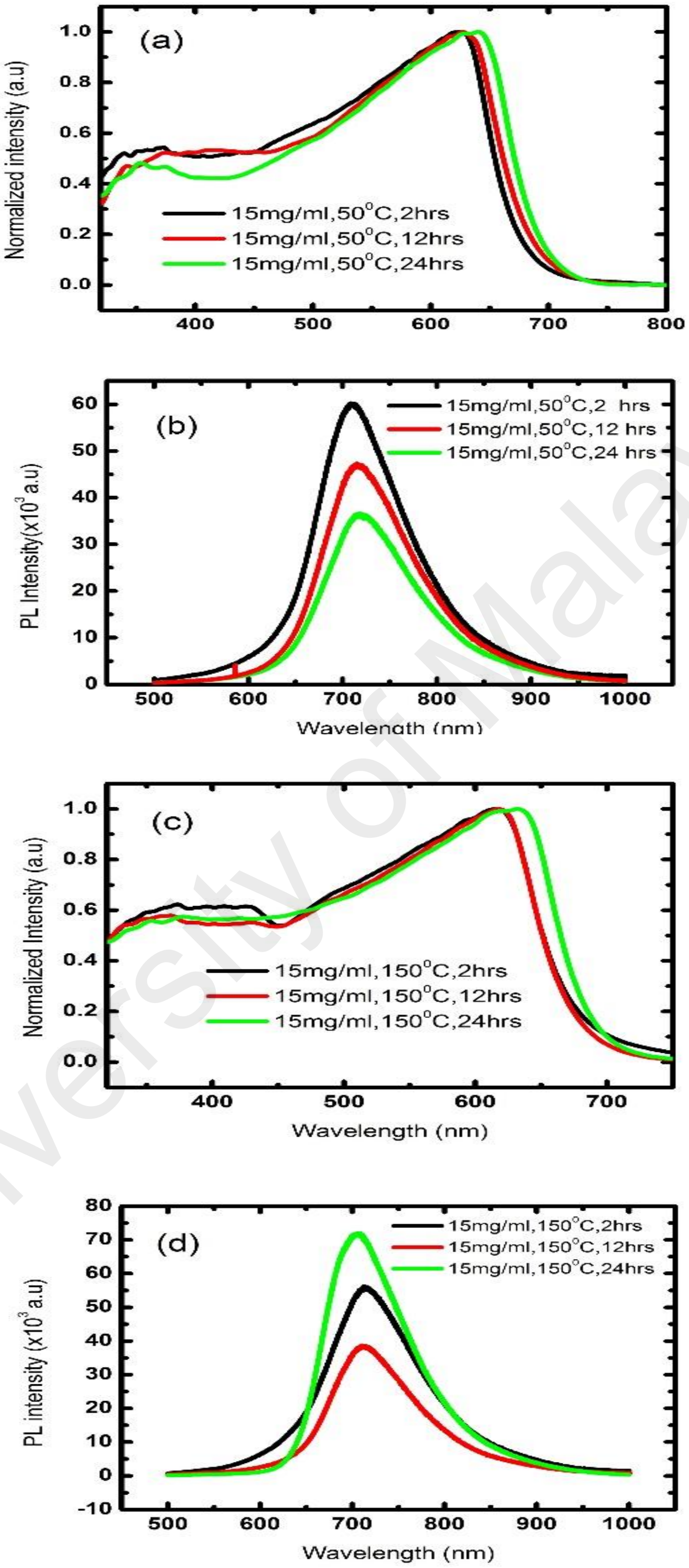

Figure 4.23: UV-vis absorption and photoluminescence spectra of 15 mg/ml PCDTBT nanotubes that annealed at (a&b) 50 °C and (c&d) 150 °C, respectively, which immersed for 2, 12, and 24 hours.

UV-vis and PL spectra of 15 mg/ml nanostructures annealed at 50 °C and 150 °C for 2, 12 and 24 hours immersion times are shown in Figure 4.23. Nanostructures that immersed for 24 hours and annealed at 50 °C shows a substantial red shift when compared to the other immersion time of 2 and 12 hours (Figure 4.23(a)). Higher degree of quenching also could be seen for its (24 hours) PL intensity as compared to 2 and 12 hours (Figure 4.23(b)). At 150 °C, the longer immersion time of 24 hours also show the most prominent optical properties as 50 °C with its UV-vis spectrum exhibits the maximum red-shifting as compared to 2 and 12 hours immersion time (Figure 4.23(c)). However, the PL emission of 24 hours (15 mg/ml, 150 °C) is more intense (Figure 4.23 (d)) as compared to 2 and 12 hours which might be contributed by the deeper infiltration of PCDTBT solution (thicker film) due to the longer immersion time (24 hours) at higher degree annealing temperature of 150 °C. With increase in thickness, photons are more likely to be absorbed and less photons is converted into charge carrier collection because the thickness of layer is larger than the exciton diffusion length (Islam et al., 2013).

Looking back at the FESEM images of 50 °C annealing temperature in Figure 4.16(c) (12 hours), Figure 4.17(a) (2 hours) & Figure 4.18(c) (24 hours) for concentration of 5, 10 and 15 mg/ml, respectively, all of these images shown a better morphology which are denser and aligned than other samples that annealed at 50^0 C. Good alignment of nanotubes could be one of the factor that contributes to the better optical properties of these samples since it can reduce the light scattering effect (Fakir et al., 2014a). Conversely, 24 hours immersion time is the most prominent parameters for 150 °C annealing temperature of all concentrations (5, 10 and 15 mg/ml). Although there is an exhibition of agglomerated structure, annealing at higher temperature (150

°C) could provide a better polymer chain alignment (Chuang et al., 2009) which enhanced the optical properties of these nanostructures.

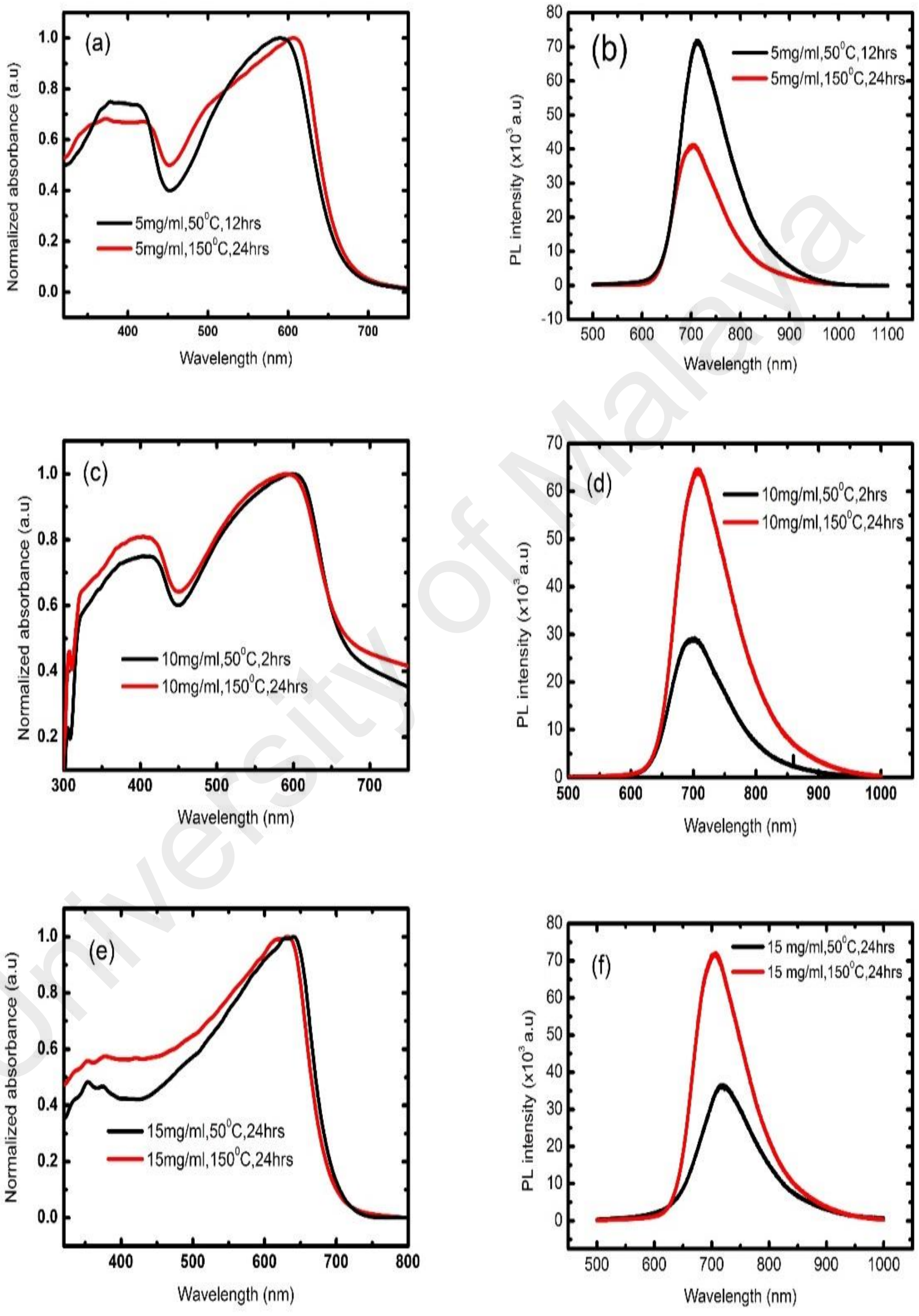

Figure 4.24: UV-vis absorption and photoluminescence spectra of (a&b) 5, (c&d) 10 and (e&f) 15 mg/ml PCDTBT nanotubes that annealed at 50 °C and 150 °C with immersion time of 12 & 24, 2 & 24 and 24 & 24 hours.

Figure 4.24 shows the comparison spectra made towards the most promising samples of each solution concentration and annealing temperature. At low concentration (5 mg/ml), as discussed earlier, 12 and 24 hours immersion time show the better optical properties at 50 and 150 °C, respectively. When these two samples are compared, higher degree annealing temperature of 150 °C show the significant shift towards longer wavelength where the maximum absorption at 606 nm exceed the low annealing temperature (50 °C) by 16 nm (Figure 4.24(a)). PL spectrum of 150 °C (24 hours) is significantly quenched if compared to 50 °C (12 hours) annealing temperature (Figure 4.24(b)). Figure 4.24(c) & (d) show the UV-vis and PL spectra of 10 mg/ml concentration nanostructures that annealed at 50 and 150 °C for 2 and 24 hours immersion time, respectively. Low annealing temperature (50 °C) at shorter immersion time of 2 hours indicated better optical properties for both UV-vis (red shift) and PL spectra (quenched) compared to 150 °C (24 hours). However, as the concentration increases to 15 mg/ml, longer immersion time of 24 hours give better optical properties for both annealing temperatures of 50 and 150 °C. Figure 4.24(e) & (f) show the UV-vis and PL spectra of 15 mg/ml, respectively. There is a red shift for nanotubes annealed at 50 °C as well as quenched in its PL spectra. It can be deduced that, as the concentration increases to 10 and 15 mg/ml, 50 °C presented the enhanced optical properties instead of 150 °C. Back to the FESEM images in Figure 4.17(a) & (f) and 4.18(c) & (f) of 10 and 15 mg/ml, respectively, 50 °C possess promising morphological properties with denser and aligned structures if compared to the 150 °C.

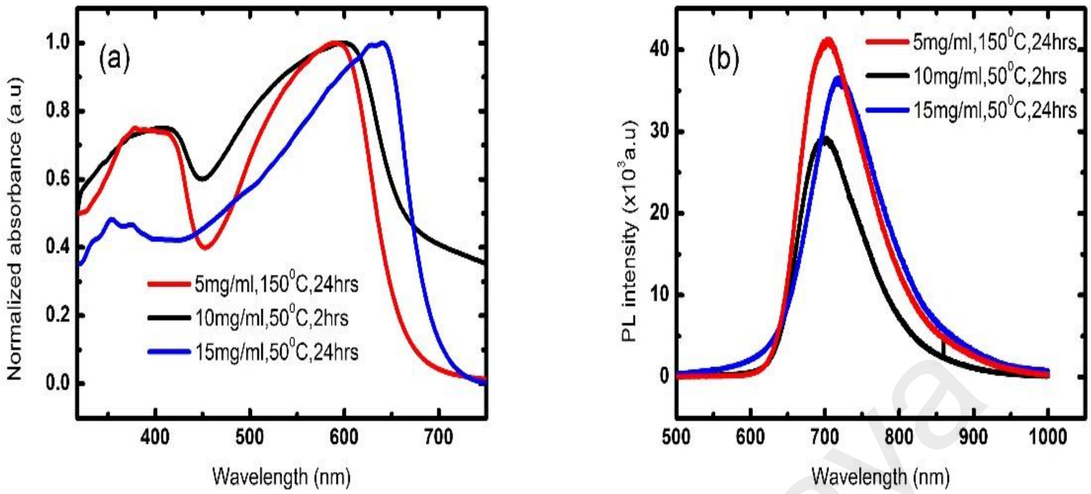

Figure 4.25: (a) UV-vis absorption spectra and (b) photoluminescence spectra of the best samples selected from concentration of 5 (150 °C, 24 hours), 10 (50 °C, 2 hours) and 15 (50 °C, 24 hours) mg/ml.

When the best samples that selected from each concentration are compared, 15 mg/ml shows the most prominent optical properties with the maximum red shift in UV-vis spectrum followed by 10 and 5 mg/ml (Figure 4.25(a)). 15 mg/ml also exhibit the reddest shift for its PL spectrum compared to 5 and 10 mg/ml as shown in the Figure 4.25(b). Even PL spectrum of 5 mg/ml shown a slightly red shift when compared to 10 mg/ml, 10 mg/ml however own a significant quenched of PL spectrum. This pattern indicated enhancement in the optical properties as the concentration is increased from 5, 10 and 15 mg/ml. Higher solution concentration nanostructures are reported to have better optical properties in term of enhancement in light absorption and lower energy gap as well as good molecular arrangement (Fakir et al., 2016). PCDTBT *p*-type nanostructures produced from the concentration of 15 mg/ml with the combination of 24 hours immersion time and annealed at 50 °C is chosen to be the optimum nanostructures. One of the other justification that can be made is the combination between parameters plays a vital role in the wetting process. The parameters can be chosen preferably to suit the selected applications.

4.2.1.3 Structural Properties

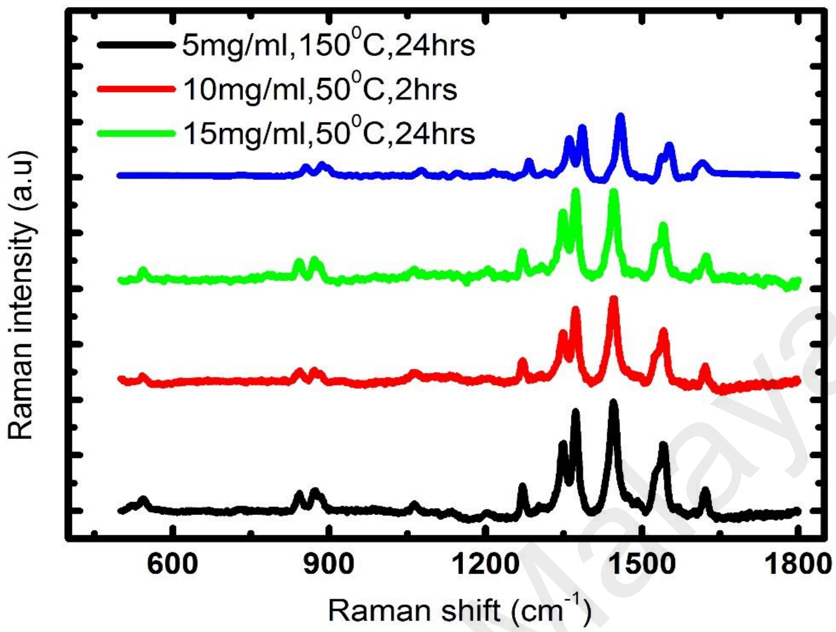

Figure 4.26: Raman spectra of PCDTBT nanostructures of 5 (150 °C, 24 hours), 10 (50 °C, 2 hours) and 15 (50 °C, 24 hours) mg/ml.

Table 4.3: Raman peaks position of PCDTBT nanostructures of 5 (150 °C, 24 hours), 10 (50 °C, 2 hours) and 15 (50 °C, 24 hours) mg/ml.

Raman shift (cm^{-1})			
5 mg/ml (150 °C, 24 hours)	**10 mg/ml (50 °C, 2 hours)**	**15 mg/ml (50 °C, 24 hours)**	**Assignments**
843	844	856	Sym C-S stretch
874	872	886	Asym C-S stretch
1066	1065	1076	L:Cz $V_{C=C}$ + CH ip δ
1271	1271	1284	L: Th CH ip δ + $V_{C=C}$
1350	1348	1361	D: BT δ + $V_{C=C}$ + C-H ip δ, Cz+Th CH ip δ + $V_{C=C}$
1373	1373	1386	D: BT + Th CH δ, Cz + BT $V_{C=C}$
1445	1444	1460	BT + Th + Cz Vc=c +, CH in plane δ, CZ V_{C-N}
1540	1542	1553	L:Cz Th $V_{C=C}$ + CH ip δ, Cz V_{C-N}
1622	1622	1623	L: BT + Th sym $V_{C=C}$, CH ip δ

Sym, symmetric; asym, asymmetric; L, localized; Th, thiophene; ip,in plane; Va-b, stretch of a-b bond; δ, bend; D, delocalized; BT, benzothiadiazole; Cz, carbazole

A difference in Raman spectra and Raman peaks position for the best-selected samples of immersion technique is shown in Figure 4.26 and Table 4.3, respectively. For this part, the best-selected samples will be denoted as A, B and C which represents nanostructures immersed for 24 hours & annealed at 150 °C (A), 2 hours & annealed at 50 °C (B) and 24 hours & annealed at 50 °C (C) of 5, 10 and 15 mg/ml, respectively. There are several shifts detected in Raman peak positions due to certain assignment as tabulated, which is caused by the parameter involved during the formation of the nanostructures such as the annealing temperature, concentration and immersion time.

Symmetric C-S stretch shows 1 cm^{-1} upward shift for sample B as compared to A which then significantly upward shift by 12 cm^{-1} for sample C. Whereas, asymmetric C-S stretch of sample C shown a remarkable upward shift of 12 and 14 cm^{-1} from sample A and B, respectively. Localized Carbazole (Cz) of C=C stretch and C-H in plane bending shows a decrease of 1 cm^{-1} from sample A to B while a notable upward shift by 10 cm $^{-1}$ could be seen from 1066 to 1076 cm^{-1} for sample C. C=C stretch and C-H in plane bending of Benzothiadiazole (BT) as well as C=C stretch of Cz + Thiophene (Th) segment indicated a downward and upward shit of about 2 and 13 cm^{-1} for sample A (1350 cm^{-1}), B (1348 cm^{-1}) and C (1361 cm^{-1}). C-H bending, C-N and C=C stretch of Th and Cz possess a upward shift of 2 cm^{-1} for sample B as compared to sample A and upward shift by 11 cm^{-1} for sample C compared to sample B.

Another peak arise are assigned to C-H bending, C=C stretch, C-N stretch of several delocalized and localized modes of Cz, Th and BT as well as combination between them shown no significant difference between samples A and B. However, when it goes to samples C, prominent upward shift occurred for all the mentioned assignment located at 1284, 1386, 1460 and 1623 cm^{-1} as tabulated in the Table 4.3.

In the previous section of morphological and optical properties, sample C possesses the most auspicious characteristics compared to the other samples, which are strongly supported by its Raman spectra characteristic. Raman peaks position for sample C shows the most significant upward shift for all dominant peaks as compared to samples A and B. This could be due to the enhancement in the molecular arrangement of the PCDTBT polymer system in sample C (Coppedè et al., 2010; Kamarundzaman et al., 2013).

4.3 Part III: Combination of Drop Casting & Annealing Technique (Above PCDTBT Melting Point)

4.3.1 Results & Discussion

The results and discussion for drop casting & annealing combination techniques (above PCDTBT melting point) have been divided into three separate sections, as follows:

4.3.1.1 Morphological Properties

Solution drop casting on the porous alumina template through template-assisted method is a common approach to produce nanostructured materials. Nanostructures of PT5, PT10, and PT15 with concentrations of 5, 10 and 15 mg/ml were synthesised using solution drop casting on the template and were subjected to annealing at several temperatures. The morphology of neat (solution wetting) and annealed (polymer melt wetting) samples was investigated by FESEM, and is presented in Figure 4.27 and Figure 4.28, respectively. Micrographs shown in Figure 4.27 reveal the formation of nanorods from neat samples of PT5, PT10 and PT15. Figure 4.27(a) and (b) show nanorods produced by PT5 for a concentration of 5 mg/ml. Formation of nanorods is assumed to originate from PCDTBT itself. This assumption is due to the observation of PCDTBT nanorods that are confined inside the template. Most of the PCDTBT nanorods of PT5 seem intact but are shorter in length and have smaller diameter. The small size of these nanorods might be owing to less infiltration of solution through the template due to low viscosity and high rate of solvent evaporation. Nanorods are formed not only due to solvent evaporation but also because of adhesive properties of PCDTBT (Bakar et al., 2015). The formation of nanorods to some extent also verified the infiltration of solution through the template. Moreover, elongated nanorods are observed in the micrographs of PT10 in Figure 4.27(c) and (d). As can be seen, these nanorods have grown larger in size, become denser and have aligned them in a regular pattern. The reason behind the formation of such long, dense and regular shaped nanorods could be the maximum infiltration of solution through porous template cavities. Sufficient polymer supply that does not evaporate at the beginning of nanorods formation process, could contribute to the longer (higher aspect ratio) nanorods development. Appearance of Y-shape branched nanostructures might be due to the existing branched structures of the commercial porous alumina used in this study, as previously reported in the literature (Fakir et al., 2014a). Furthermore, the large distance from the top to the Y-branched structure indicates the improved infiltration (Bakar et al., 2015; Fakir et al., 2014a). Well-aligned nanorods with minimised collapsing might be due to the high density of nanorods and the little space created between them. The optimum concentration of solution also could avoid the collapsing or agglomeration of produced nanostructures which is a significant evidence of successful synthesis of PCDTBT nanorods at the concentration of 10 mg/ml. Size increment of nanorods was witnessed only up to a certain level of concentration, beyond which, the nanorods could no longer sustain stability and collapsed into much smaller sized nanorods. However, higher solution concentration should give further higher infiltration and aspect ratio and hence, longer and denser nanorods should have been obtained. But in the present case, the obtained results were quite different from our expectations. Broken nanorods were achieved, which showed the formation of longer unstable nanorods at initial stage. The longer nanorods broke in order to attain stability. The broken nanorods for the concentration of 15 mg/ml (PT15) are revealed by the FESEM images of Figure 4.27(e) and (f). The increase in the solution concentration after 10 mg/ml resulted in small-sized nanorods, even smaller than the nanorods obtained from PT5, owing to the fact that the nanorods grew very large in size and became more fragile and vulnerable, which then, collapsed in the middle after attaining optimum size and scattered in non-aligned form. The collapsed PCDTBT nanorods of PT15 might be attributed to the fact that the solvent near the substrate contains more volume fraction as compared to the regions away from the substrate due to which the nanorods fall down and fracture in the areas of less volume fraction (Kong et al., 2008). It can be postulated that the size of nanorods is very much dependent on the concentration of PCDTBT solution. PCDTBT concentration of 10 mg/ml (PT10) demonstrated the best concentration for producing long, dense and well-arranged PCDTBT nanorods. PCDTBT results in the formation of nanorods that are confined inside the template (Bakar et al., 2015).

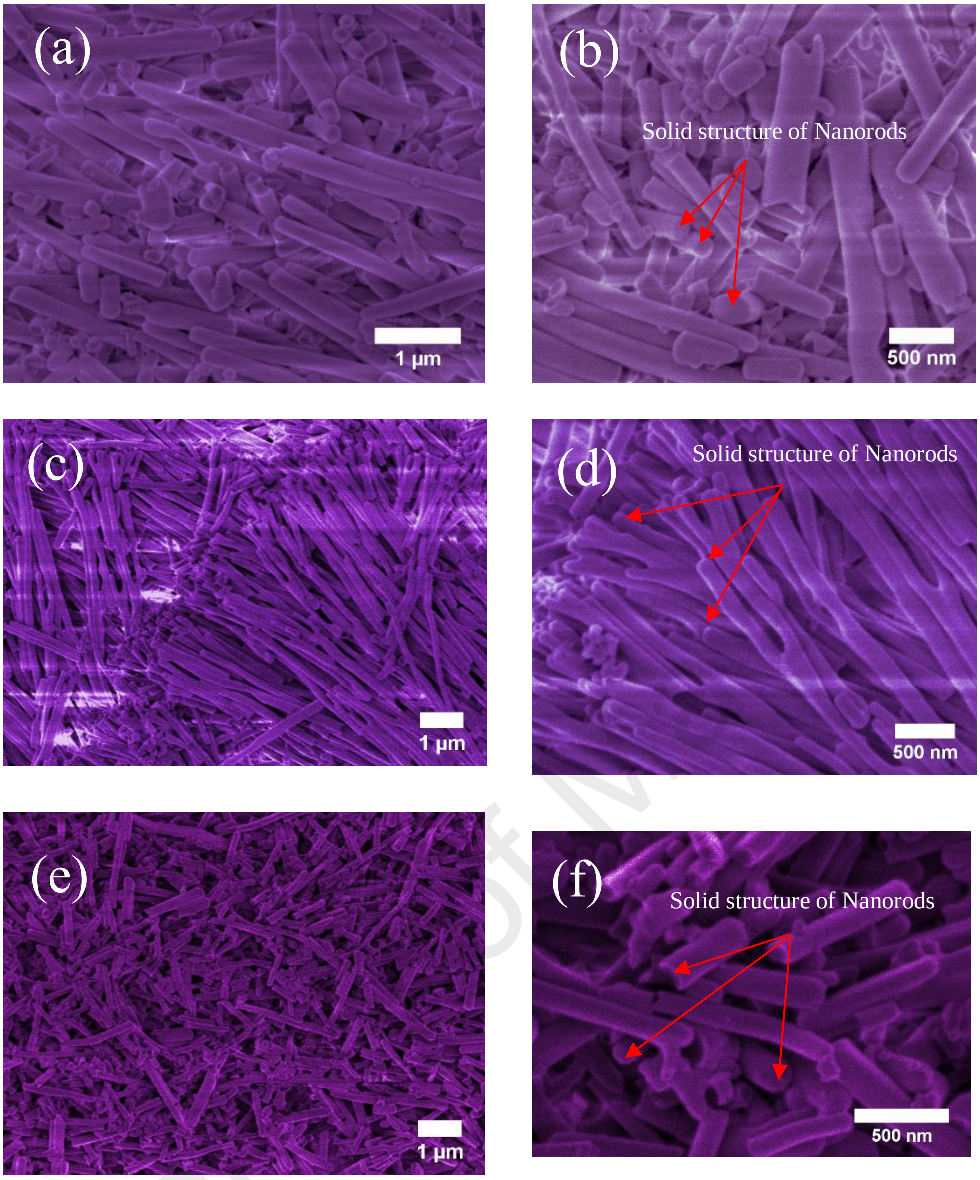

Figure 4.27: FESEM micrographs of PCDTBT nanorods of (a&b) PT5, (c&d) PT10 and (e&f) PT15.

After some analysis are done (shown in the later section (optical properties)) on the neat samples (PT5, PT10 and PT15), PT5 and PT10 were chosen in order to study the effect of melt wetting process on the PCDTBT neat samples. The annealed samples (PT5-1, PT5-2, PT5-3, PT10-1, PT10-2 and PT10-3) were further investigated by FESEM. FESEM micrographs of all annealed nanostructures are presented in Figure 4.28. Morphological study of the samples that annealed at temperature above the melting point of PCDTBT, revealed the formation of nanotubes. FESEM image of PT5-1 in Figure 4.28(a) suggests that the nanotubes have just started to form. A complete formation of nanotubes might not be successful due to insufficient polymer solution and uneven adherence of solution to the walls of the template. However, PT10-1 in Figure 4.28(b) demonstrates that the PCDTBT nanotubes have not only been produced but are also elongated and well arranged. The well-aligned nanotubes are obtained at the temperature of 300 °C. The formation of nanotubes confirms the stronger adhesive properties of PCDTBT to the template to form nanostructures. However, the nanotubes are prone to deformation above 300 °C, which can be well understood from the images of Figure 4.28(c) through (f). The deformation of nanotubes above 300 ^{o}C might be ascribed to the instability of materials. Very less number of open nanotubes can be found in PT5-2, however, melting and misalignment is observed in nanotubes of PT10-2. The nanotubes not only close at the top tubular end but also tend to misalign in PT5-3. Some evacuation is also observed in the same image. PT10-3 portrays melting and breaking of the nanotubes. The results indicate that nanotubes are sufficiently stable at 300 ^{o}C, which tend to melt and deform above 300 ^{o}C. The micrographs depict that the nanotubes with 10 mg/ml solution concentration and annealed at 300 °C are elongated and well aligned. Nonetheless, temperatures beyond 300 °C (i.e. 350 and 400 °C) are not suitable for sustainability of the nanotubes due to misalignment, fracturing and deformation. Annealing temperature plays a vital role in the formation and alignment of the nanotubes. Transformation of PCDTBT nanorods into nanotubes at high temperature might be due to the, strong adhesiveness to the template walls, melting of solution and rapid evaporation of solvent inhibiting the polymer solution to completely fill core region of the template-pores which result in nanotubes instead of nanorods (Steinhart et al., 2002). Another possible reason for the produced nanotubes might be that, fundamentally, the polymer melt bears lower surface energy as compared to the porous alumina template surface, which possesses inherited higher surface energy (Bakar et al., 2014a). Accordingly, when the polymer melts are treated at temperatures higher than the melting point, the melts swiftly wet and flow in nanochannels (Ali et al., 2015). Hence, the PCDTBT melt with lower surface energy can favourably wet and permeate into the template by virtue of wetting. The results suggest lengthening, densification, alignment and morphological distribution of PCDTBT nanotubes that is dependent on the concentration of PCDTBT solution as well as heat treatment.

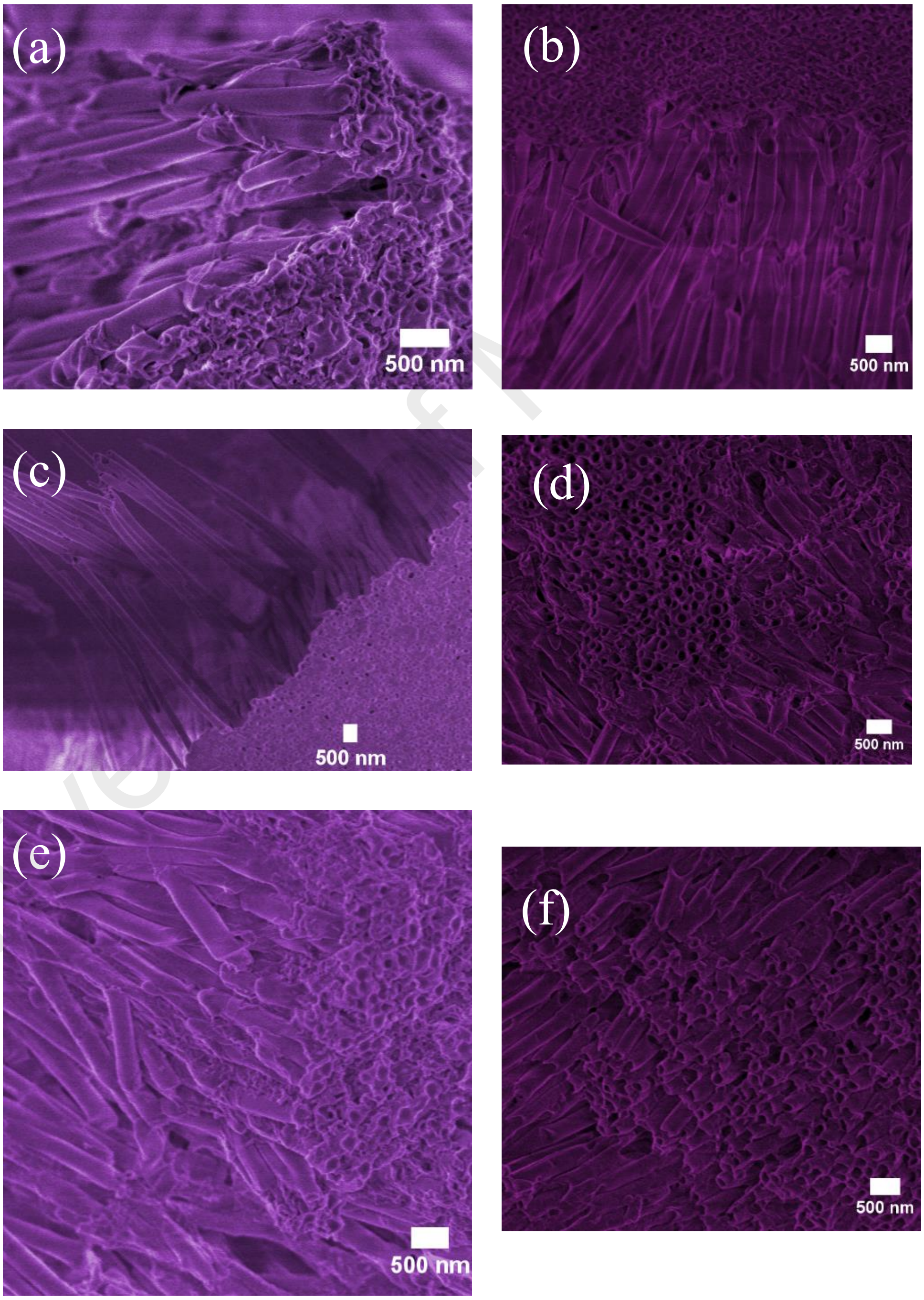

Figure 4.28: FESEM micrographs of annealed PCDTBT nanotubes; (a) PT5-1, (b) PT10-1, (c) PT5-2, (d) PT10-2, (e) PT5-3 and (f) PT10-3.

TEM images of PCDTBT nanotubes for two different concentrations, 5 and 10 mg/ml annealed at 300 °C (PT5-1 and PT10-1) are shown in Figure 4.29. The images suggest that the nanotubes are not completely grown for PT5-1 as shown in Figure 4.29(a). However, Figure 4.29(b) shows lucid formation of PCDTBT nanotubes of PT10-1. The diameter of PCDTBT nanotubes observed for PT10-1 (~230 nm) is greater as compared to that of PT5-1 (~170 nm). The nanotubes obtained at 10 mg/ml concentration and 300 °C annealing temperature exhibit longer and wider nanostructure as compared to the ones formed at lower concentration (5 mg/ml).

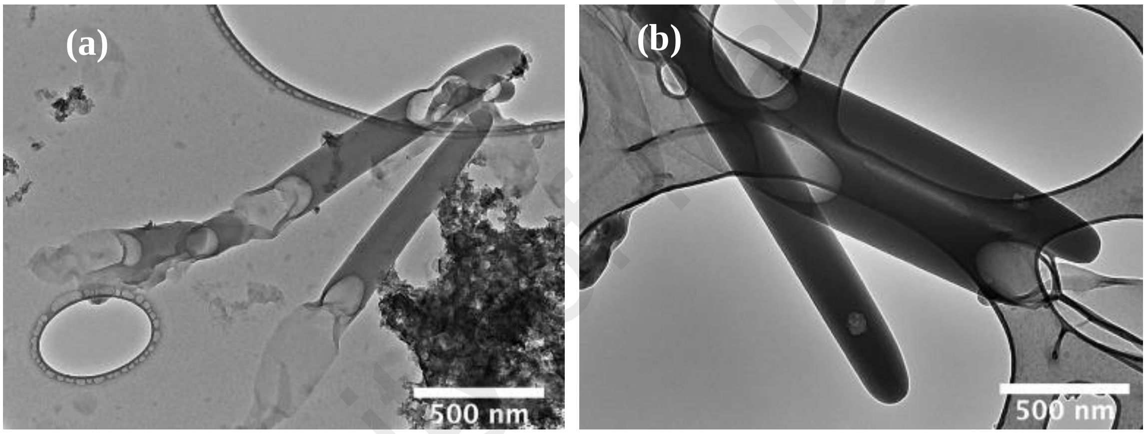

Figure 4.29: TEM images of PCDTBT nanotubes for (a) PT5-1 and (b) PT10-1.

Figure 4.30(a) and (b) illustrate two-stage growth mechanism of PCDTBT nanorods and their transition into nanotubes. The fabrication mechanism of nanorods in Figure 4.30(a) demonstrates that the confined PCDTBT nanorods are formed by immediately placing a template over the substrate with drop-casted solution. The solution infiltrates through the deep-hole template-pores to form nanorods of various sizes and morphologies. The size and morphology of the nanorods depend on the concentration of the solution. The higher the concentration of PCDTBT, the longer, denser and regularly aligned the nanorods and vice versa. The reason behind the longer and well-arranged nanorods could be the maximum infiltration through the cavities of the template. When the solution is brought into contact with the substrate of high surface energy, the solution spreads and forms a thin film. Once the template is immersed in the solution, it infiltrates and fills the nanochannels of the template to a certain extent. The formation of nanorods might be ascribed to the rapid filling of nanochannels with solution by capillary forces (Cepak & Martin, 1999; Chu et al., 2015). The lowest concentration results in small-sized PCDTBT nanorods due to low solution density and inadequate permeation. The relatively higher concentration leads to elongated PCDTBT nanorods due to sufficient infiltration through the template. Concentration above a critical value, produces broken and fractured nanorods owing to higher solution density and higher dilation stress, which is directly proportional to the volume fraction (Liu et al., 2004). The solvent levels in the higher density regions (near the substrate) are higher than the levels at the far end. In other words, there remains some solvent in higher density regions while solvent in lower density regions disappears. Consequently, PCDTBT nanorods stand straight near the substrate where there still rests some solvent while they collapse and fall down at the region away from the substrate with less or almost no solvent (Kong et al., 2008).

The morphology of the fabricated nanostructures can be very much influenced by thermal annealing as reported elsewhere (Chen et al., 2007; Schlitt et al., 2008). Figure 4.30(b) presents the proposed formation of PCDTBT nanotubes by thermal annealing process. The nanorods are transformed into nanotubes by annealing them at higher temperatures. At such elevated temperatures, the nanorods start to melt and completely permeate core regions of the nanochannels of the template by rapid evaporation of solvent, which was initially inhibited at lower temperatures. The polymer melt bears lower surface energy as compared to the porous alumina template (which inherently possesses higher surface energy) (Bakar et al., 2014a). Hence, the polymer melts, when treated at higher temperatures, swiftly wet and flow in nanochannels (Ali et al., 2015).

The transition of nanorods into nanotubes might be attributed to two phenomena: (i) evaporation of the bound solvent molecules at temperatures above PCDTBT melting point and (ii) flow of the polymer melt through the nanochannels due to the difference in surface energies of the template and polymer. At temperatures near or above the melting point of PCDTBT, the nanorods start to melt and the bound solvent rapidly evaporates, thereby, allowing the polymer solution to completely fill the template-pores, thus, giving rise to PCDTBT nanotubes (Steinhart et al., 2002). At critical temperature and lower concentration, the nanotubes just begin to form owing to maximum drying of the solvent from low-density solution introduced during nanorods fabrication. At the optimum higher concentration with higher volume fraction, and of course critical temperature, the melt permeates into the template to a maximum depth leading to the growth of elongated nanotubes. The temperature above the critical value results in deformation of the nanotubes in the form of choking and breaking of the nanotubes and evacuation due to almost complete melting and evaporation of PCDTBT, respectively. Varying the solution concentration can alter the size, density and alignment of the nanorods. However, the size and morphology of the nanotubes can be significantly controlled by, both, the annealing temperature and solution concentration.

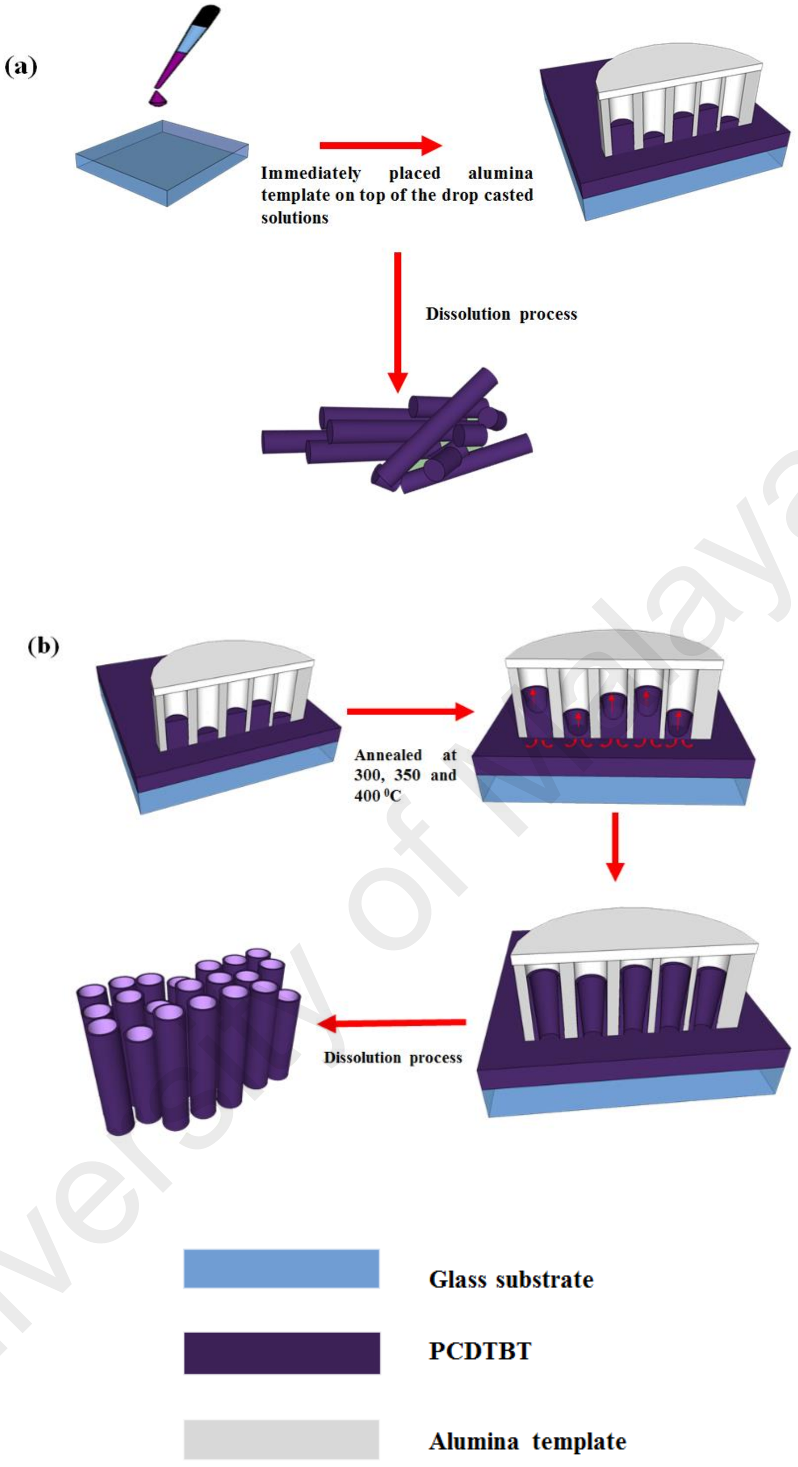

Figure 4.30: Schematic illustration of two-stage growth mechanism of (a) PCDTBT nanorods and their transition into (b) PCDTBT nanotubes.

4.3.1.2 Optical Properties

A two-fold study, solution wetting followed by melt wetting, has been carried out on PCDTBT nanostructures in terms of varied concentrations undergoing different annealing temperatures. The UV-vis absorption spectra of all samples of PCDTBT nanostructures in Figure 4.31 clearly indicate two absorption bands at 390 and 557 nm, in the UV and visible spectral regions, respectively, as reported in literatures (Murugesan et al., 2015; Zafar et al., 2016). The peak at 390 nm corresponds to the donor carbazole (Cz), which is assigned to π-π* transition. However, the absorption peak at 557 nm is attributed to acceptor dithienyl-benzothiadiazole (DTBT), with n-π* transition. A broad valley also appears in the range of 400-500 nm (Bakar et al., 2015; Jha et al., 2013). All PCDTBT nanostructures, when compared with PCDTBT thin film, exhibit a red shift at ~600 nm, although, the peak at 390 nm undergoes a significant change and gets broadened in the range of 380-440 nm. A close examination of solution wet samples, PT5, PT10 and PT15, in Figure 4.31(a), reveal that the nanorods of PT10 have augmented absorption intensity and wider band over the entire (UV and visible) spectral range with a red shift of ~20 nm, as compared to the nanorods of PT5 and PT15. On the contrary, PT15 exhibits reduced intensity which might be due to the deformation and fracturing of PCDTBT nanorods shown in the micrographs of PT15 in Figure 4.27(e) and (f). It can be deduced, here, that the solution concentration has demonstrated an important part in elucidating distinct features of optical absorption.

To investigate the effect of melt wetting process, only two samples (PT5 and PT10) were selected. The samples were thermal annealed at three different temperatures of 300, 350 and 400 °C. PT15, due to its vulnerability to deformation, misalignment and fracturing (as shown in Figure 4.27(e) and (f)), has been omitted for optical studies. The absorption spectra of PT5-1, PT5-2, PT5-3, PT10-1, PT10-2 and PT10-3 nanotubes are presented in Figure 4.31. The nanotubes of PT5-1 exhibit a broad range with reduced intensity in the visible region. PT5-1 also demonstrates a small red shift of ~10 nm. However, PT5-2 and PT5-3 in Figure 4.31(b) show optical properties similar to that of PCDTBT thin film with a valley at 450 nm. Moreover, the nanostructures of PT5-2 and PT5-3 display blue shift (as compared to nanorods). The nanotubes of PT10-1 (annealed at 300 ºC) in Figure 4.31(c) reap better optical properties in terms of light absorption as compared to the nanorods and nanotubes fabricated at lower concentration. It can be observed from Figure 4.31(c), that the optical spectral range of PT10-1 nanotubes has broadened further with augmented intensity especially in the visible domain as compared to the nanotubes of PT10-2 and PT10-3. Moreover, the nanotubes of PT10-1 also show a pronounced red shift of ~45 nm while PT10-2 and PT10-3 exhibit a slight blue shift which is consistent with the results of FESEM illustrated in Figure 4.28(d) and (f). A comparison of optical spectra of PT5-1 and PT10-1 in Figure 4.31(d), explicitly demonstrates that PT10-1 outcasts all other concentrations and annealing temperatures in many respects which include broadened spectral range, heightened absorption intensity over the entire spectral coverage and remarkable red shift of ~50 nm towards longer wavelength.

The red shift illustrates a strong influence on the aggregation behaviour of PCDTBT nanorods manifesting better conjugation length and chain segment. Elongated and well-aligned PCDTBT nanotubes at 300 °C might be due to pronounced shift (~50 nm) towards longer wavelengths. Moreover, blue shift displayed by the nanotubes suggests deformation due to melt wetting at temperatures greater than the optimum temperature. The downturn in the optical properties for the nanotubes annealed beyond 300 °C (350 and 400 °C) might be owing to the triggering of melting process, which leads to deformation, misalignment and breaking of the nanotubes at temperatures higher than 300 °C. The optical results obtained, here, are consistent with the morphological investigations carried out for the prepared nanostructures.

Here, we can draw certain conclusions: (1) the PCDTBT nanorods prepared at concentrations higher than 10 mg/ml lead to lower absorption intensities and introduction of distinct valleys (similar to thin films) implying deformation of the nanorods; and (2) the PCDTBT nanotubes annealed at temperatures higher than 300 ºC lead to attenuated optical absorption. It can be conjectured that the solution concentration and annealing temperatures have evoked a strong influence on the aggregation behaviour of the nanostructures, which are related to the red shift (absorption edge transition) of the optical absorption spectra. It is known that the red shift leads to highly aggregated configuration, which helps polymer chains to align themselves and increase in conjugation length (Schwartz et al., 2001). Aligned polymer chains give rise to efficient path for charge transfer (π to π*) between the conjugated main chains and carbazole units. It can be postulated that modification in the molecular structure of nanotubes e.g. aggregation, better conjugation length and chain alignment might be the cause of improved optical properties due to enhanced interchain interaction (Bakar et al., 2014a). A broad optical spectrum with incremented light absorption can harvest maximum light, which is beneficial for the fabrication of state-of-the-art photovoltaic devices.

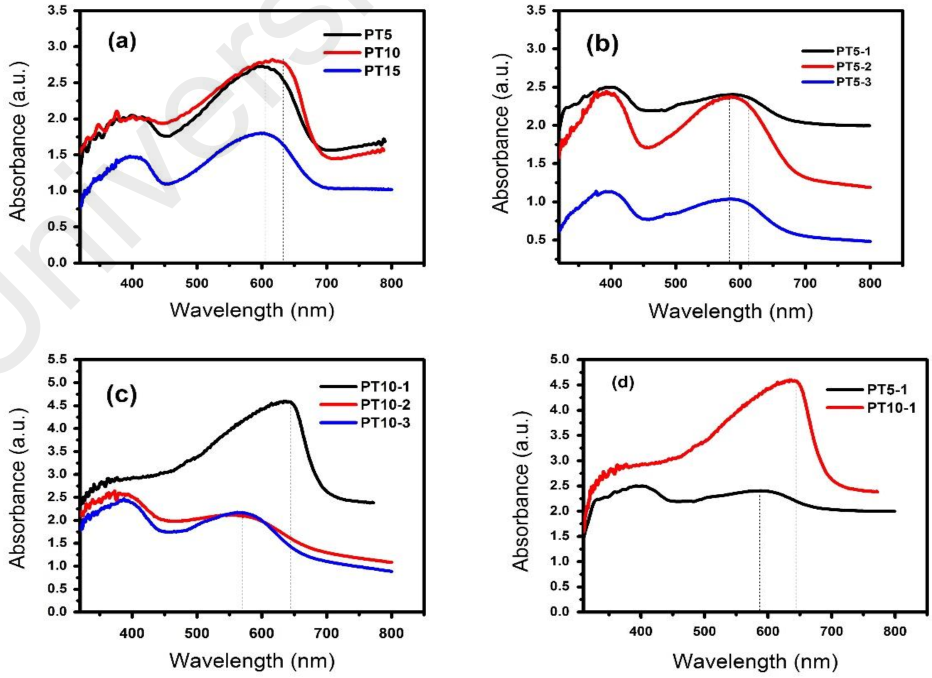

Figure 4.31: Absorption spectra of PCDTBT nanostructures; (a) nanorods of PT5, PT10 and PT15, (b) nanotubes of PT5-1, PT5-2 and PT5-3, (c) nanotubes of PT10-1, PT10-2 and PT10-3 and (d) comparison of nanotubes of PT5-1 and PT10-1.

The effect of solution concentration and thermal annealing is also analysed by photoluminescence (PL) spectroscope. Figure 4.32 shows the PL spectra of PCDTBT nanostructures. PL spectra for all nanorods and nanotubes of PCDTBT recorded an intense peak at 700 nm, which demonstrates the dominance of emission due to the DTBT unit and the absence of Cz segment, thus, indicating that Cz segment has been completely quenched by efficient energy transfer to the DTBT unit (Liu et al., 2008). PL spectra of PCDTBT nanorods of PT5, PT10 and PT15 in Figure 4.32(a), exhibit almost similar PL pattern with a slight quenching of PT10 nanorods. Moreover, the nanorods of PT5 and PT10 are significantly red shifted. The red shift in the PL emission of PT10, which is well matched with the red shift of its UV-vis absorption, suggests dense, aligned and longer nanorods.

Figure 4.32(b) and (c) show PL spectra of PT5-1, PT5-2, PT5-3, PT10-1, PT10-2 and PT10-3 nanotubes. PL spectrum of PT5-1 in Figure 4.32(b) shows appreciable quenching as compared to PT5-2 and PT5-3. It can also be seen that when the nanorods of PT10 are annealed at 300 °C to form nanotubes (PT10-1 in Figure 4.32(c)), the characteristic peak of PCDTBT shifts to longer wavelengths and quench appreciably. A close examination of PT10-2 and PT10-3 indicate that their PL is blue shifted to lower wavelengths. A comparison of PT5-1 and PT10-1 in Figure 4.32(d) reveals that the PL of the nanotubes of PT10-1 is sufficiently quenched and red shifted. Quenching of the PL band is due to annealing of the nanorods as the luminescence quantum yield is lowered (Reddy et al., 2010) by annealing the nanorods at optimal temperatures to form nanotubes. Also, quenching leads to increased photon absorption resulting in enhanced optical device performance owing to better conjugation length and improved chain alignment (Fakir et al., 2014b; Schwartz, 2003). The red-shift emission of PL spectra can be associated with delocalization of electrons between conjugated segments in PCDTBT. The red-shift has caused improvement in the degree of aggregation which is in compliance with the previous reported work (Pasquali et al., 2010). This indicates that the solution concentration and annealing temperatures essentially contribute in manipulating the photophysics of nanostructures formed. It can further indicate that the energy transfer between carbazole segments and DTBT unit is either via intra- or intermolecular mechanism (Bakar et al., 2014b). Hence, it can be postulated that significant quenching has been observed for PCDTBT nanotubes as compared to nanorods, which is consistent with the reported literature (Bakar et al., 2015).

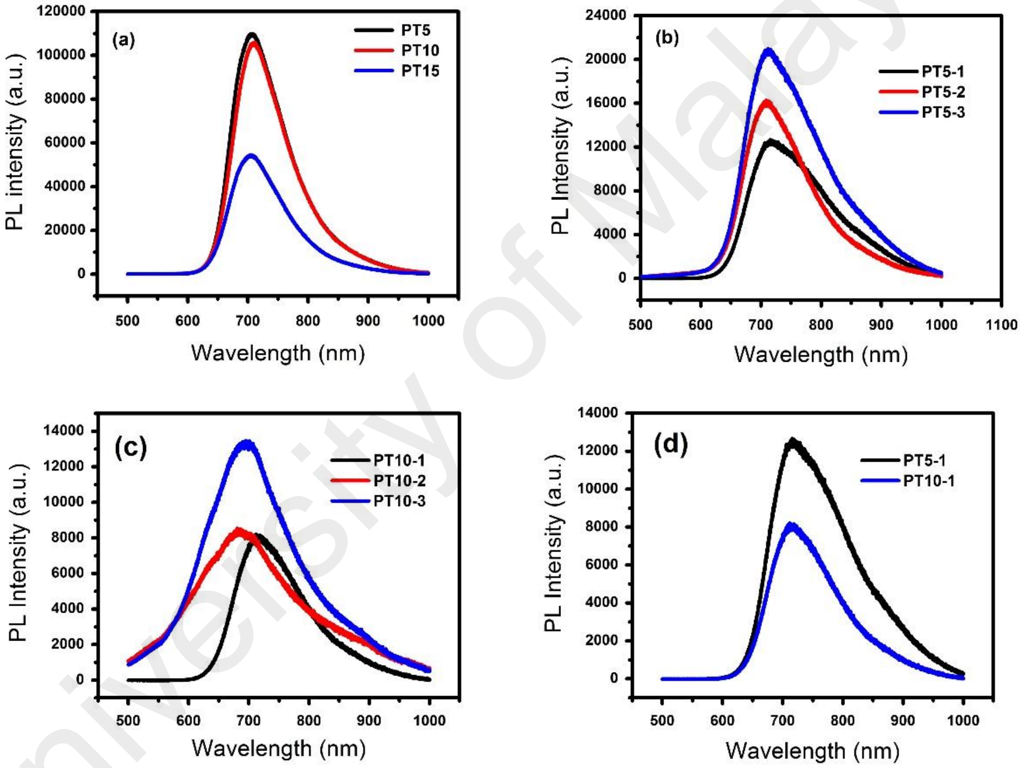

Figure 4.32: Photoluminescence spectra of PCDTBT nanostructures; (a) nanorods of PT5, PT10 and PT15, (b) nanotubes of PT5-1, PT5-2 and PT5-3, (c) nanotubes of PT10-1, PT10-2 and PT10-3 and (d) comparison of nanotubes of PT5-1 and PT10-1.

4.3.1.3 Structural Properties

To further unfold the impact of melt wetting on the solution wet produced nanorods, only two best samples, PT10 from the neat samples and PT10-1 out of the annealed samples, were selected for Raman analysis. Raman spectra and Raman peak position of

PCDTBT nanorods of PT10 and nanotubes of PT10-1 are shown in Figure 4.33 and Table 4.4. Raman peaks appearing at 841, 871, 1063, 1270, 1349, 1371, 1446, 1541 and 1621 cm^{-1} arise due to PCDTBT molecular motion which are in agreement with previous reports (Bakar et al., 2014a; Bakar et al., 2014b; Bakar et al., 2015). The peak at 542 corresponds to S–S stretching, while the peaks at 841 and 871 cm^{-1} are assigned to symmetric and asymmetric C–S stretching. The band at 1063 cm^{-1} corresponds to a localized mode characterised by C–H in-plane bending together with C=C stretching at the thiophene ring. The absorption peak observed at 1270 cm^{-1} represents C–H in-plane bending and C=C stretch bending of the benzothiadiazole in delocalized mode. C–H in-plane bending with C=C stretching for both the carbazole and thiophene units are also ascribed to the same mode. The delocalized motion involving the benzothiadiazole, thiophene and carbazole unit is observed at 1349 cm^{-1}. Peak associated with 1371 cm^{-1} corresponds to C=C stretching together with C–H in-plane bending for benzothiadiazole, thiophene and carbazole units and C–N stretching for carbazole unit only. The band appearing at 1446 cm^{-1} is ascribed to the localized motion involving carbazole, thiophene and localized motion involving carbazole unit only. Peak appearing at 1541 cm^{-1} is assigned to symmetric C=C stretching together with C–H in-plane bending for benzothiadiazole, thiophene in localized mode. Band at 1621 cm^{-1} refers to localized motion involving the carbazole unit which is related to the C–H in-plane bending together with C=C stretching.

When the nanorods and nanotubes were compared, similar peaks located at 542, 1063, 1349, 1446, 1541 and 1621 cm^{-1} were observed. PCDTBT nanotubes of PT10-1 at the band 842 and 873 cm^{-1}, assigned to symmetric and asymmetric C–S stretch, respectively, experience an upward shift of 1 and 2 cm^{-1}. The Raman shift of delocalized motion involving the benzothiadiazole, thiophene and carbazole unit for the nanotubes at 1271 cm^{-1} shows an apparent upward shift of about 1 cm^{-1} as compared to nanorods. The upward shift of 2 cm^{-1} of nanotubes can also be seen at 1373 cm^{-1} associated with localized motion involving benzothiadiazole, carbazole and thiophene. These upward shifts support the enhanced molecular arrangement of PCDTBT nanotubes.

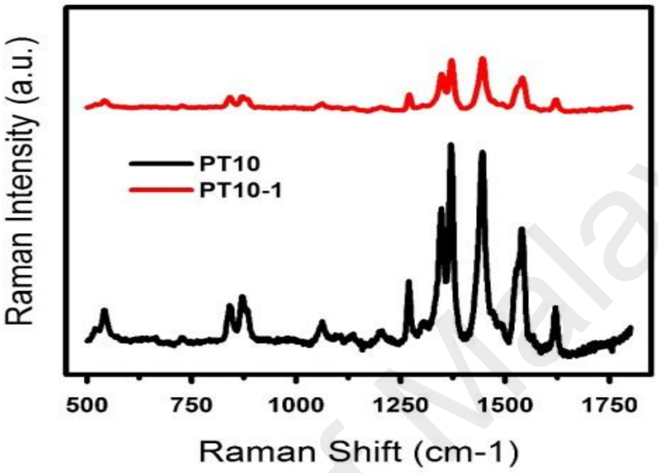

Figure 4.33: Raman spectra of PCDTBT nanorods of PT10 and nanotubes of PT10-1.

Table 4.4: Raman peak position of PCDTBT nanorods and nanotubes produced by solution plus melt wetting process. [a]

Solution Wetting (PT10)	Solution plus Melt Wetting (PT10-1)	Assignments
542	542	S–S stretch
841	842	Sym C–S stretch
871	873	Asym C–S stretch
1063	1063	L: Th CH ip δ+ $V_{C=C}$
1270	1271	D: BT δ + $V_{C=C}$ + CH ip δ, Cz + Th CH ip δ + $V_{C=C}$
1349	1349	D: BT + Th CH δ, Cz + BT $V_{C=C}$
1371	1373	BT + Th + Cz $V_{C=C}$ + CH ip δ, Cz V_{C-N}
1446	1446	L: Cz Th $V_{C=C}$ + CH ip δ, Cz V_{C-N}
1541	1541	L: BT + Th sym $V_{C=C}$, CH ip δ
1621	1621	L: Cz $V_{C=C}$ + CH ip δ

[a] Sym, symmetric; asym, asymmetric; L, localized; Th, thiophene; ip, in-plane; V_{a-b}, stretch of the a–b bond; δ, bend; D, delocalized; BT, benzothiadiazole; Cz, carbazole.

CHAPTER 5: FORMATION OF PCDTBT:$PC_{71}BM$ COMPOSITE NANOSTRUCTURES VIA TEMPLATING METHOD

The synthesis of polymer composite at the nanoscale has received numerous attentions. Polymer composites that composed of both *p*- and *n*-type materials have a potential to enhance the charge carrier separation, charge carrier transfer and light absorption due to the formation of *p*-*n* junction (Ahmad Makinudin et al., 2015; Clarke et al., 2012; Kannappan et al., 2012; Yan et al., 2013). The beneficial features of the *p*-type and *n*-type materials also could be merged in a composite to enhance the properties of some other devices such as humidity sensor (Azmer et al., 2016). Template-assisted method is one of the considerable methods in fabricating the innumerable polymer composite architectures due to its mass production capabilities with minimal investment in cost and time (Al-Kaysi et al., 2009; Bakar et al., 2014b; Fakir et al., 2014b; Martín et al., 2012). The most common techniques used in templating method are immersion (template wetting) and spin coating (Ahmad Makinudin et al., 2015; Bakar et al., 2014b; Supangat et al., 2014; Wei et al., 2013). A spin coating technique has been widely used in fabricating the bulk heterojunction based devices such as OPV, OLED and sensors by blending the *p*- and *n*-type materials (Chu et al., 2011; Clarke et al., 2012; Ng et al., 2008; Sekine et al., 2014). By blending these materials, the interpenetrating structures are later produced, thus creating the bulk heterojunction system. Researchers have alternatively incorporated the conjugated polymer (*p*-type) and fullerenes (*n*-type), in order to provide charge transfer within the blends (Gu et al., 2012; Kannappan et al., 2012; Tsoi et al., 2011). Practically, fullerenes such as [6,6]-phenyl C_{71}-butyric acid methyl ester ($PC_{71}BM$) and [6,6]- phenyl C_{61}-butyric acid methyl ester ($PC_{61}BM$) have an energetic deep lying LUMO which bestows the molecule with a high electron affinity relative to the various potential organic donors thus making it as an ideal *n*-type materials (Yadav & Kumar, 2008).

To the author best knowledge, studies involving one dimensional nanostructures of PCDTBT:fullerene junction composite have not been reported. Template-assisted method is useful in producing heterostructured composite via a simple layer by layer approach (two different materials incorporated together at a different time) such as composite nanotubes and nanorods (Ahmad Makinudin et al., 2015; Supangat et al., 2014; Yan et al., 2013). Since the charge separation of excitons is taking place at the interface between the *p*- and *n*- type, an intimate contact of both materials is required for the efficient splitting of the photogenerated excitons. To fulfil the vigorous charge carrier splitting, the large interfacial areas are highly needed, which in turns yielding the higher charge generation rates. Intimate contact at the nanoscale could be realised from the formation of *p*-*n* junction composite nanostructure. On the other hand, bulk heterojunction has been limited by its charge percolation within the intermixed phases.

The use of templating method to synthesise the *p*-*n* junction composite of poly [N-90-hepta-decanyl-2, 7-carbazole-alt-5, 5-(40, 70-di-2-thie-nyl 20, 10,30benzothiadiazole)] (PCDTBT): [6, 6]-phenyl C_{71}-butyric acid methyl ester ($PC_{71}BM$) is reported in this chapter. Selected PCDTBT nanostructures of each concentration and each technique from the previous chapter will be used to incorporate with the $PC_{71}BM$ for the fabrication of PCDTBT:$PC_{71}BM$ composite nanostructures. PCDTBT nanostructures were first produced followed by the infiltration of $PC_{71}BM$. Formation of PCDTBT:$PC_{71}BM$ composite was elaborated in which its morphological, optical and structural properties were compared over its *p*-type counterparts from each of previously mentioned technique which have been studied through FESEM, HRTEM, UV-vis, PL and Raman spectroscope.

5.1 Results & Discussion

The results and discussion of composite section have been divided into three separate sections, as follows:

5.1.1 Morphological Properties

Figure 5.1 shows the FESEM images of (a) PCDTBT nanostructures and (b) PCDTBT: $PC_{71}BM$ *p-n* junction composite of 5 mg/ml solution concentration at spin coating rate of 1000 rpm. As can be seen from the images, the infiltration of $PC_{71}BM$ into the infiltrated template has changed the morphological properties of the original *p*-type (PCDTBT) nanostructures. There are some significant differences between the PCDTBT nanostructures (Figure 5.1(a)) and its *p-n* junction composite nanostructures (Figure 5.1(b)), where entangled and collapsed structures can only be seen for PCDTBT nanostructures (Figure 5.1(a)) but not for its PCDTBT:$PC_{71}BM$ composite structures. Conversely, meniscus end-cap was formed for its PCDTBT:$PC_{71}BM$ composite structure as shown by the red circle in Figure 5.1(b). This could be due to the thicker nanotube's wall after the infiltration of the $PC_{71}BM$ solution into the infiltrated PCDTBT. Composite structures of PCDTBT:$PC_{71}BM$ clearly shown an open-end of hollow structures compared to the PCDTBT nanostructures (*p*-type) which hollow structures could not be seen from the top due to the extreme agglomeration.

As the concentration increases to 10 mg/ml, the PCDTBT nanostructures getting more stable causing less collapsing and agglomerating (Figure 5.2(a)) due to the reasons mentioned in the previous chapter (Chapter 4). Not much difference could be seen between PCDTBT nanostructures and their composites (Figure 5.2(b)) except for the meniscus formation after the infiltration of $PC_{71}BM$ into the infiltrated PCDTBT as shown by the red arrows.

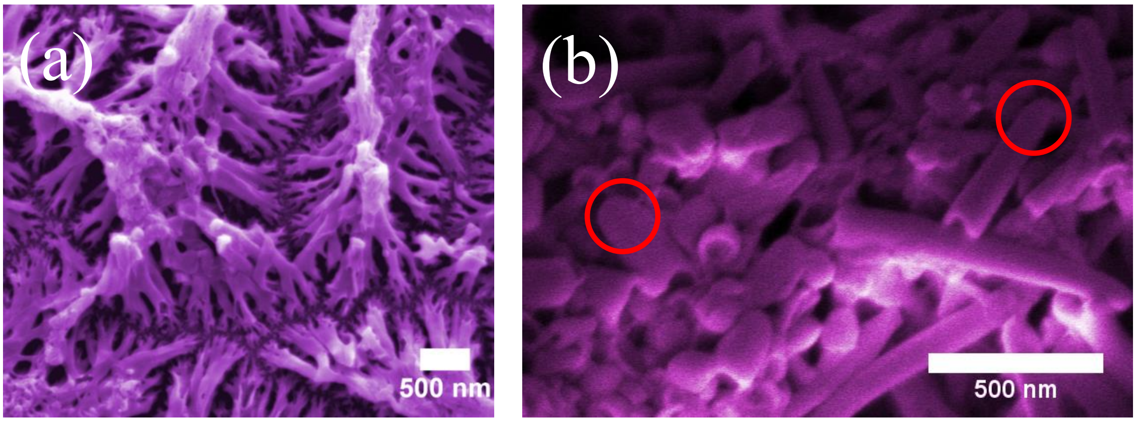

Figure 5.1: FESEM images of (a) PCDTBT nanostructures and (b) PCDTBT:PC$_{71}$BM p-n junction composite of 5 mg/ml solution concentration at spin coating rate of 1000 rpm.

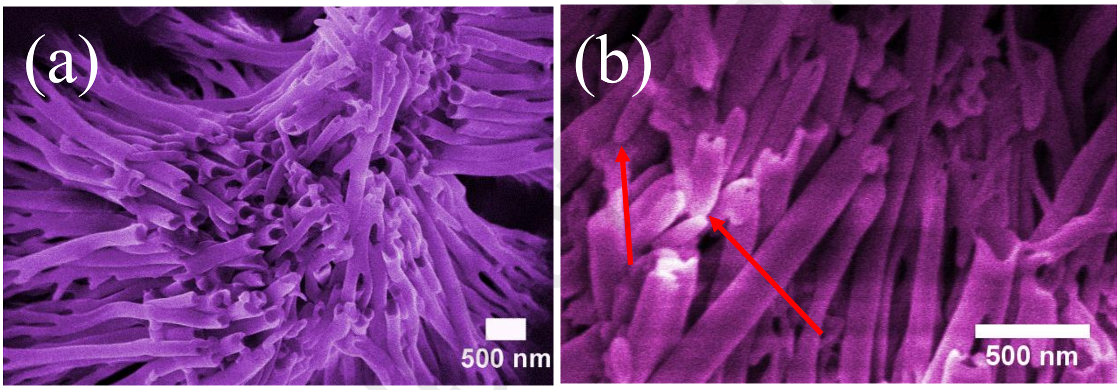

Figure 5.2: FESEM images of (a) PCDTBT nanostructures and (b) PCDTBT:PC$_{71}$BM p-n junction composite of 10 mg/ml solution concentration at spin coating rate of 1000 rpm.

Figure 5.3(a) & (b) show the difference in morphological properties between PCDTBT nanostructures and *p-n* junction composite (PCDTBT:PC$_{71}$BM) of 15 mg/ml solution concentration at spin coating rate of 1000 rpm. The infiltration of PC$_{71}$BM into the infiltrated PCDTBT has made some changes just like the other concentrations (5 and 10 mg/ml), which reduced the degree of collapsing and agglomerating. Figure 5.3(b) shows the formation of end-meniscus, which this observation (red arrow) is similar to the lower concentration. Most of the composite structures of 5, 10 and 15 mg/ml observed to be broken into shorter 1-D structures if compared to the non-composite (*p*-type only) structures. This could be due to the disruption cause by the infiltration of

$PC_{71}BM$ into the infiltrated PCDTBT as illustrated in Figure 5.4. The flow of $PC_{71}BM$ solution into the confined PCDTBT nanostructures has caused some of the PCDTBT tube's wall to be disrupted and become extremely thin or vanished in some area while some area become thicker. These thinned and vanished tube's walls tend to break after the dissolution process, in which produced the shorter and broken nanotubes.

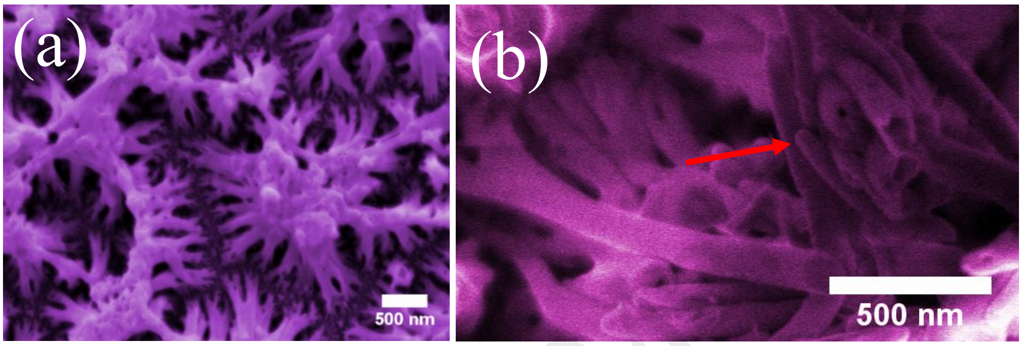

Figure 5.3: FESEM images of (a) PCDTBT nanostructures and (b)PCDTBT:$PC_{71}BM$ p-n junction composite of 15 mg/ml solution concentration at spin coating rate of 1000 rpm.

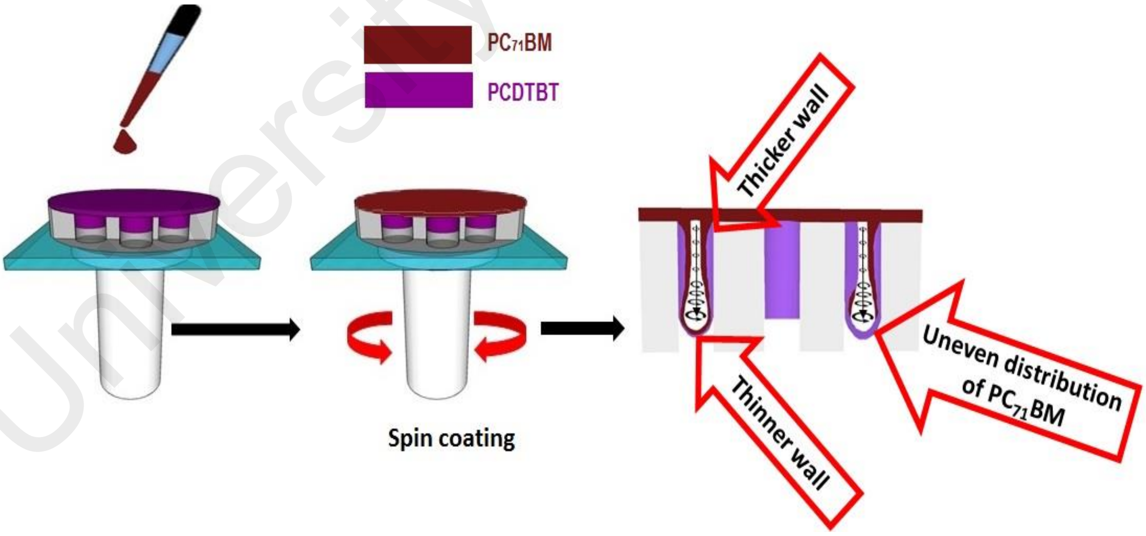

Figure 5.4: The infiltration of PCBM into the confined PCDTBT nanostructures.

As mentioned in the previous chapter, the agglomeration of 5 mg/ml PCDTBT nanostructures produced by the immersion technique (24 hours) that annealed at 150 °C as shown in Figure 5.5(a) is caused by the low concentration and high degree of annealing temperature that associated with the very thin nanotubes' wall. After the infiltration of $PC_{71}BM$ into the *p*-type infiltrated PCDTBT, the agglomeration is reduced due to the thickening of the nanotubes' wall caused by the formation of another layer of $PC_{71}BM$. However, some of the nanostructures have been cut into the shorter part (Figure 5.5(b)) influenced by the flow of the $PC_{71}BM$ through the infiltrated PCDTBT. Meanwhile, 10 mg/ml PCDTBT *p*-type nanostructures do not shown any agglomeration due to the thicker and shorter nanotubes (Figure 5.5(c)). Thicker wall is hardly affected by the infiltration of $PC_{71}BM$ solution as can be seen in Figure 5.5(d), where the condition after the infiltration is almost the same. The same goes for 15 mg/ml (Figure 5.5(e)) where thicker nanotubes wall prevent the occurrence of the agglomeration. However, the infiltration of $PC_{71}BM$ causes little disruption on the PCDTBT nanotubes surfaces as indicated by the lower inset of Figure 5.5(f). FESEM images in Figure 5.6(a) & (b) and Figure 5.6(c) & (d) show the nanostructures of 5 and 10 mg/ml annealed at 300 °C and its PCDTBT: $PC_{71}BM$ *p-n* junction composite, respectively. Several substantial morphological differences are observed with both 5 (Figure 5.6(a)) and 10 mg/ml (Figure 5.6(c)) PCDTBT nanotubes show a better alignment and smoother surface compared to its *p-n* junction composite. As seen in Figure 5.6(b) & (d), composite structures were breaking into the shorter segment and collapsed as well as less aligned. This could be due to the reasons explained earlier where the flow of $PC_{71}BM$ into the infiltrated PCDTBT has caused some disruption to the PCDTBT nanotube's wall. Some defects on the composite nanotubes' surface are seen with several holes are appeared as indicated by the red arrow.

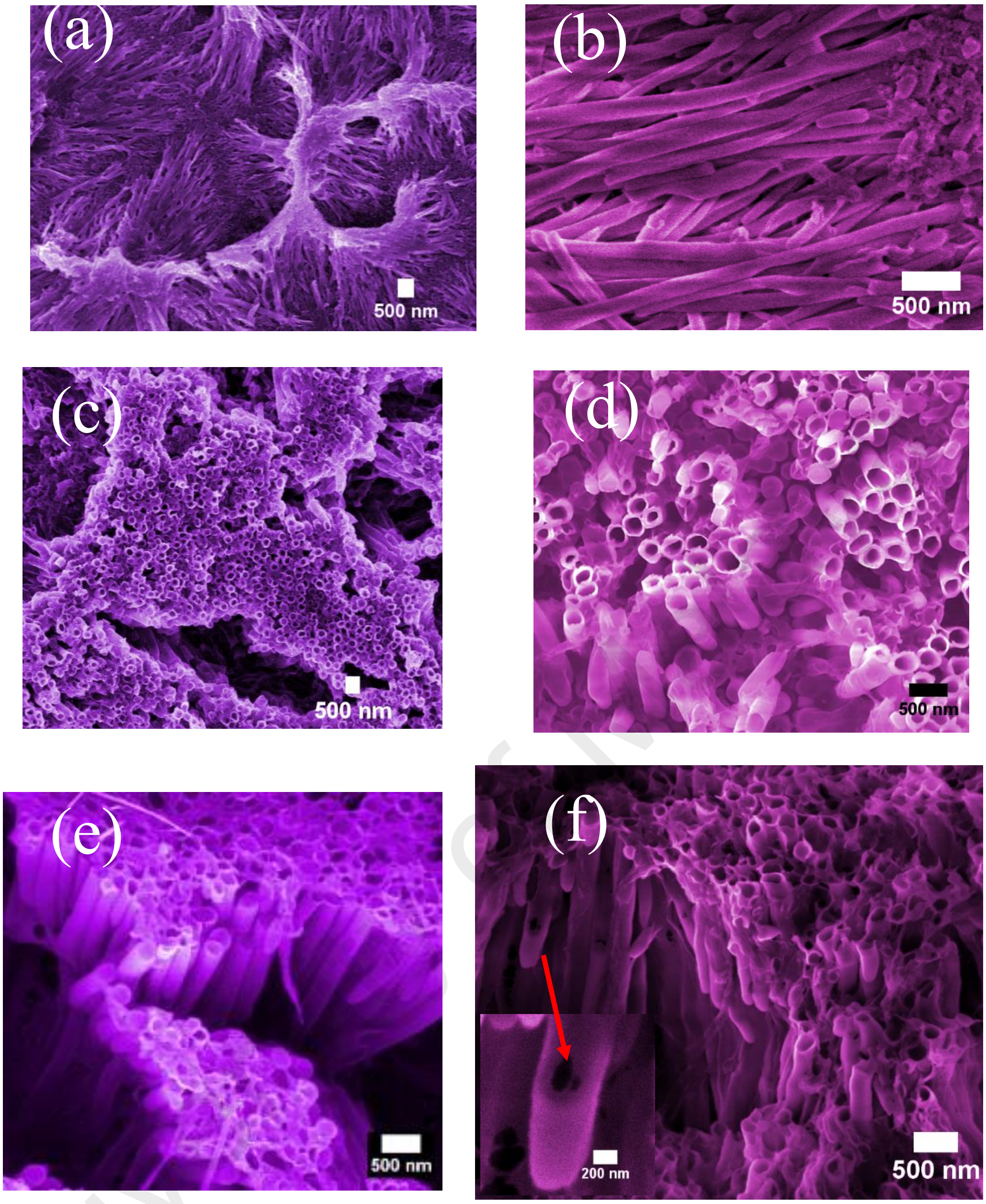

Figure 5.5: FESEM images of (a) 5 mg/ml PCDTBT nanostructures produced from 24 hours immersion time then annealed at 150 °C & (b) its PCDTBT:PC_{71}BM p-n junction composite, (c) 10 mg/ml PCDTBT nanostructures produced from 2 hours immersion time then annealed at 50 °C & (d) its PCDTBT:PC_{71}BM p-n junction composite and (e) 15 mg/ml PCDTBT nanostructures produced from 24 hours immersion time then annealed at 50 °C & (f) its PCDTBT:PC_{71}BM p-n junction composite.

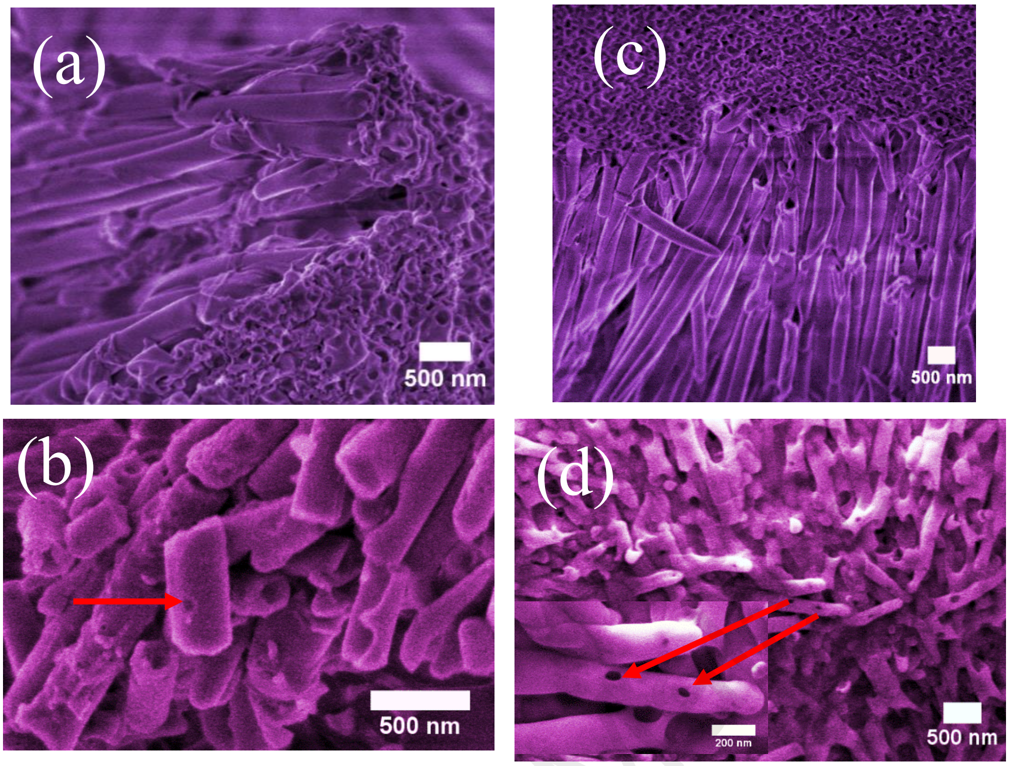

Figure 5.6: FESEM images of (a) 5 mg/ml PCDTBT nanostructures annealed at 300 °C and (b) its PCDTBT: $PC_{71}BM$ *p-n* junction composite and (c) 10 mg/ml PCDTBT nanostructures annealed at 300 °C and (d) its PCDTBT: $PC_{71}BM$ p-n junction composite.

5.1.2 Optical Properties

Figure 5.7(a) shows the UV-vis spectra of $PC_{71}BM$ thin film, PCDTBT thin film and PCDTBT:$PC_{71}BM$ bulk heterojunction of different solution concentrations and spin coating rates. PCDTBT thin film has portrayed the significant peaks absorption between 350-650 nm at UV and visible region, which represent the carbazole (Cz) donor and dithienylbenzothiadiazole (DTBT) acceptor, respectively. UV-vis spectrum of PCDTBT thin film portrayed a broad valley between 400-500 nm while the UV-vis spectrum of $PC_{71}BM$ thin film shows its main peak absorption between 450-500 nm. It can be observed that, the main peak of DTBT located at 580 nm decreased in intensity, while the middle valley (500 nm) showed an increased intensity after the incorporation of PCDTBT and $PC_{71}BM$ for both concentrations (5 and 15 mg/ml) which represent the mixed state of the two parent materials. By incorporating these two materials, a broader absorption peak at a visible region can be recognised. Solution concentration has played a vital role in giving the significant difference in term of optical properties (wider absorption band at a longer wavelength), in which 5 mg/ml of bulk heterojunction film shows a red-shifted and wider absorption if compared to 15 mg/ml which is in contrast with its PCDTBT nanostructures that absorb light at longer wavelength as the concentration increases from 5 to 15 mg/ml (Figure 5.7(b)). PCDTBT nanoflowers of 15 mg/ml show a red-shifted and wider absorption at its second peak whereas 5 mg/ml PCDTBT nanorods shows a red-shifted at its first peak. Absorption edge of PCDTBT nanotubes (10 mg/ml) is consistent with PCDTBT nanorods (5 mg/ml) and nanoflowers (15 mg/ml), which fall between these two concentrations. The solution concentration and polymer-fullerene ratio have enforced a strong influence on the aggregation behaviour of the blends that are related to the red shift (absorption edge transition) of the optical absorption spectra.

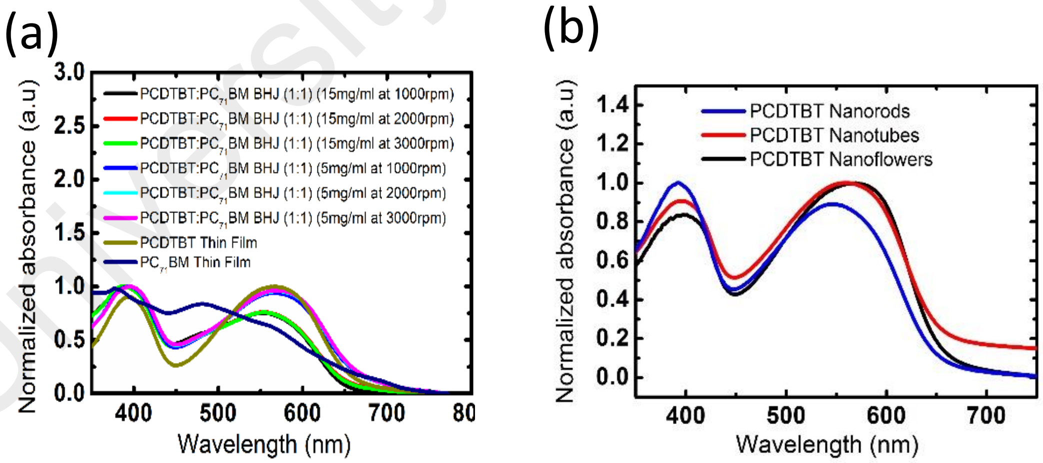

Figure 5.7: UV-vis absorption spectra of (a) PCDTBT thin film, $PC_{71}BM$ thin film and PCDTBT:$PC_{71}BM$ bulk heterojunction of 5 and 15 mg/ml of 1000, 2000 and 3000 rpm and (b) PCDTBT nanostructures of 5 (nanorods), 10 (nanotubes) and 15 (nanoflowers) mg/ml.

The UV–vis and PL spectra of PCDTBT: $PC_{71}BM$ *p-n* junction composite of spin coating technique is shown in Figure 5.8(a) & (b), respectively. It shows that UV-vis spectra of PCDTBT: $PC_{71}BM$ composite for 5, 10 and 15 mg/ml exhibit peaks at 558, 559 and 556 nm, respectively. 5 and 10 mg/ml of PCDTBT: $PC_{71}BM$ composites absorb light at a longer wavelength that exceeds the 15 mg/ml by 2 and 3 nm, respectively. PL spectra of 5 mg/ml quenched better compared to 10 and 15 mg/ml as can be seen in Figure 5.8(b). This is well correlated with its UV-vis spectra where low concentration of 5 and 10 mg/ml absorb light at the longer wavelength compared to 15 mg/ml PCDTBT: $PC_{71}BM$ composite. However, composite structure that formed through immersion technique of 15 mg/ml (24 hours, 50 °C) still retain as the most promising optical properties compared to the other parameters involved in that technique. UV-vis spectrum of 15 mg/ml shows the widest and reddest light absorption at 404 and 608nm for first and second peak, respectively, as well as its PL spectra (Figure 5.8(c) & (d)). By looking at the PL spectra of these samples, 10 and 15 mg/ml demonstrated a substantial red shifted of PL spectra compared to 5 mg/ml (Gieseking et al., 2012). Low concentration, with the same ratio of PCDTBT and $PC_{71}BM$ (1:1), do not give a significant change in PL spectra (unlike the 10 and 15 mg/ml). This could be the reason for the absence of second peak of PL spectra indicated in Figure 5.8(d). Different coating technique of PCDTBT (immersion) and $PC_{71}BM$ (spin coating) to the template's walls give an influence towards the observed of 5 mg/ml composite PL spectra. Immersion technique provides a thick coating of PCDTBT compared to a spin coating technique of $PC_{71}BM$.

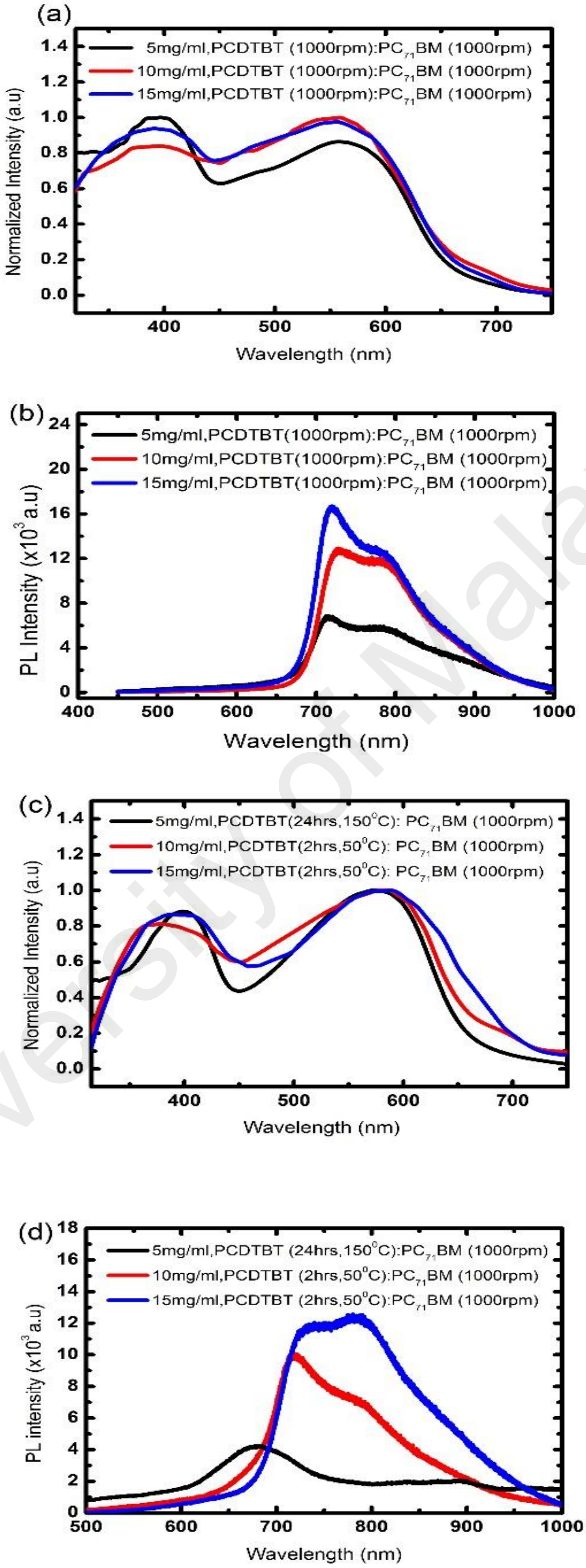

Figure 5.8: UV-vis and PL spectra of PCDTBT:PC$_{71}$BM p-n junction composite of (a&b) spin coating technique and (c&d) immersion technique, respectively.

Figure 5.9 shows the UV-vis and PL spectra of PCDTBT:PC$_{71}$BM p-n junction composite for 5 and 10 mg/ml of combination of drop casting & annealing (300 °C) techniques. As can be seen in Figure 5.9(a), unusual spectrum is observed for 5 mg/ml where low energy absorption peak represents the DTBT segment of PCDTBT is absent or diminished in intensity significantly. This could be due to the initial heating treatment (300 °C) of PCDTBT prior to the infiltration of PC$_{71}$BM, which in line with the previous report where the higher degree of annealing cause some part of the polymer to undergo thermal decomposition (Marin et al., 2013). Thermal decomposition will occur when the heat cause changes in a chemical species (Beyler & Hirschler, 2002; Witkowski et al., 2016). The significant decrease in lower energy absorption peak intensity only significantly affects the low concentration (5 mg/ml) PCDTBT nanostructures (Figure 5.9(a)) due to its low viscosity. 10 mg/ml possess a higher intensity of lower energy absorption peak as compared to 5 mg/ml. However, PC$_{71}$BM gives greater impacts towards 5 mg/ml compared to 10 mg/ml as can be seen through their UV-vis spectra where 5 mg/ml PCDTBT:PC$_{71}$BM composite closely resembles PC$_{71}$BM UV-vis absorption spectra (Figure 5.9(a)). The influence of the PC$_{71}$BM towards the PCDTBT infiltrated template (5 mg/ml, 300 °C) clearly showed by the composite UV-vis absorption spectra in the Figure 5.9(b) where the peak arise cause by the PC$_{71}$BM indicated by the green arrow (Figure 5.9(a)&(b)). Due to the effect of thermal decomposition, it is complicated to determine which sample are possessed better optical properties in UV-vis spectra. Therefore, further analysis on PL spectra is needed in order to understand and justify the optical properties of both 5 and 10 mg/ml composite structures. Figure 5.9(c) shows a PL spectra of 5 and 10 mg/ml PCDTBT:PC$_{71}$BM composite nanostructures. 5 mg/ml shows a better quenching in PL spectra as compared to 10 mg/ml which is in a good correlation with the previous claimed (Chapter 4, Part III), where 5 mg/ml concentration composite structures have better optical properties compared to 10 and 15 mg/ml. A comparison between *p*-type PCDTBT and *p-n* PCDTBT:PC$_{71}$BM composite nanostructures have been made where composite structure shows a significant quenched and slightly red shift in PL spectra compared to *p*-type only structure. By referring back to its morphological properties in Figure 5.6, composite structures possess a defective wall surface, which consists of several holes as compared to its PCDTBT *p*-type structure. This defective wall surface could be the reason of enhanced optical properties of *p-n* junction composite nanostructures of PCDTBT:P$_{71}$BM when compared to the PCDTBT *p*-type structure which is in consistent with the previous studies (Harrah & Swan, 2011; Singh et al., 2011). Defects in the nanostructures can significantly influence their electronic and optical properties (Anand et al., 2014).

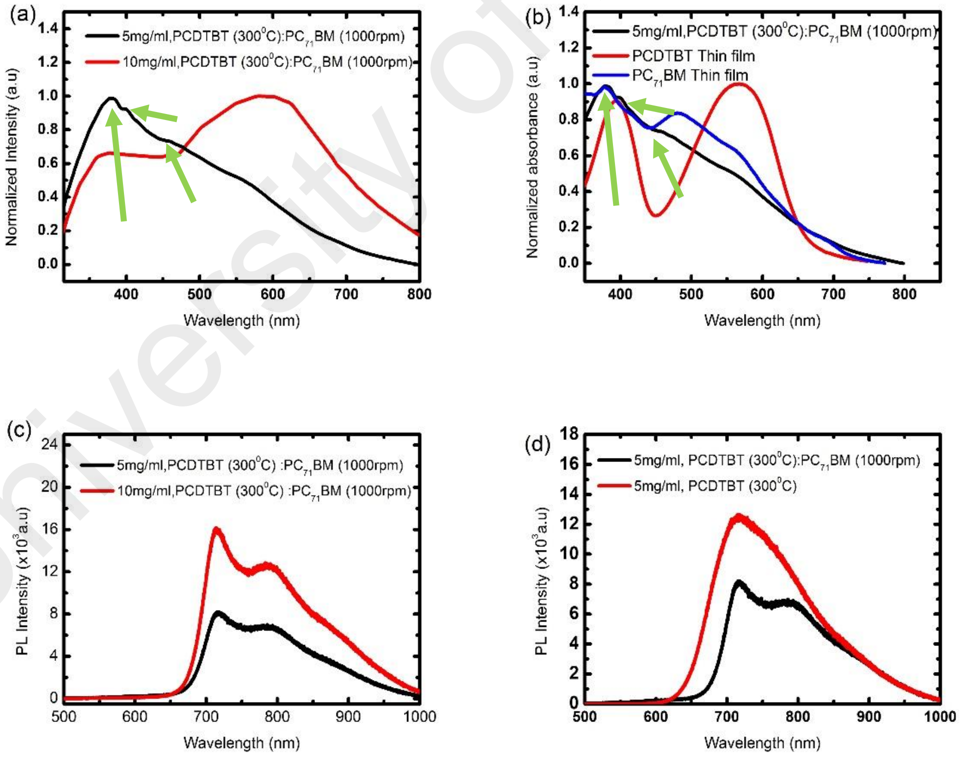

Figure 5.9: (a) UV-vis absorption spectra of PCDTBT:PC$_{71}$BM p-n junction composite for 5 and 10 mg/ml, (b) UV-vis absorption spectra of PCDTBT:PC$_{71}$BM p-n junction composite of 5 mg/ml, PCDTBT & PC$_{71}$BM thin film, (c) PL spectra of PCDTBT:PC$_{71}$BM p-n junction composite of 5 and 10 mg/ml and (d) PL spectra of PCDTBT:PC$_{71}$BM p-n junction composite of 5 mg/ml & PCDTBT nanostructures of 5 mg/ml for combination of drop casting & annealing (300 °C) techniques.

5.1.3 Structural Properties

To further understand the properties of PCDTBT:PC$_{71}$BM composite nanostructures, three samples were selected for Raman analysis. Figure 5.10 and Table 5.1 show the Raman spectra and Raman peak position of chosen PCDTBT:PC$_{71}$BM composite structures of 3 different techniques; spin coating, immersion and combination of drop casting & annealing techniques. 5 mg/ml solution concentration that spin coated at 1000 rpm was chosen for the spin coating technique (A), 15 mg/ml solution concentration with immersion time of 24 hours then annealed at 50 °C was chosen for the immersion technique (B) and 5 mg/ml solution concentration that annealed at 300 °C was chosen for the drop casting & annealing combination techniques (C). PC$_{71}$BM was infiltrated into this infiltrated *p*-type using the spin coating technique at 1000 rpm.

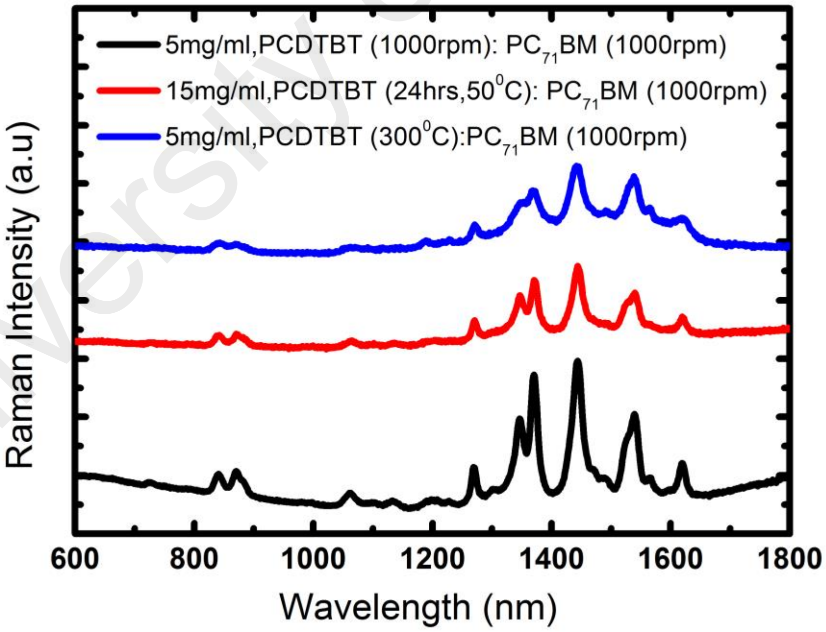

Figure 5.10: Raman spectra of PCDTBT:PC$_{71}$BM nanostructures of samples A (5 mg/ml, 1000 rpm), B (15 mg/ml, 24 hours, 50 °C) and C (5 mg/ml, 300 °C).

Table 5.1: Raman peaks position of PCDTBT:$PC_{71}BM$ nanostructures of samples A (5 mg/ml,1000 rpm), B (15 mg/ml, 24 hours, 50 °C) and C (5 mg/ml, 300 °C).

Raman shifts (cm^{-1})			
A	**B**	**C**	**Assignments**
841	842	842	Sym C-S stretch
870	871	871	Asym C-S stretch
1061	1063	1062	L: Th CH ip δ+ $V_{C=C}$
1269	1271	1271	D: BT δ + $V_{C=C}$ +C-H ip δ, Cz+Th CH ip δ+ $V_{C=C}$
1346	1346	1349	D: BT+Th CH δ,Cz+BT $V_{C=C}$
1371	1371	1373	BT+Th+Cz $V_{C=C}$ +, CH in plane δ, Cz V_{C-N}
1444	1444	1442	L:Cz Th $V_{C=C}$ + CH ip δ, Cz $V_{C=C}$
1539	1540	1538	L:BT+Th sym $V_{C=C}$, CH ip δ
1566	1566	1566	Antisymmetric stretch modes of the fullerene
1619	1620	1621	L:Cz $V_{C=C}$ + CH ip δ

[a] Sym, symmetric; asym, asymmetric; L, localized; Th, thiophene; ip, in-plane;
$V_{a–b}$, stretch of the a–b bond; *δ*, bend; D, delocalized; BT, benzothiadiazole; Cz, carbazole

Annealing causes some alteration towards molecular arrangement in the materials including enhanced the chain alignment and decreased the bond length (Kim et al., 2013) of the molecular system which result in an upward shift in its Raman peaks position. These can be observed for 1 cm^{-1} upward shift of sample B and C as compared to sample A which represents symmetric and asymmetric C-S stretch at 842 and 871 cm^{-1}, respectively, as well as in delocalised mode of some segments for its C=C stretch and C-H bending (1271 cm^{-1}). Whereas, annealing at higher degree of 300 °C (sample C) causing a upward shift by several cm^{-1} located at 1349 and 1373 cm^{-1} while sample A and B remain unchanged at 1346 and 1371 cm^{-1} which belong to different assignments. Localized mode of Cz segments for C=C stretch and C-H in plane bending also shown a upward shift by 1 cm^{-1} as the temperature increases from sample A (not annealed), to the sample B (50 °C) and C (300 °C) of different techniques at 1619, 1620 and 1621 cm^{-1}.

Some downward shift is also recorded for sample C for some of the assignments. 2 cm^{-1} downward shift is observed at 1442 cm^{-1} compared to sample A and B which is at 1444 cm^{-1} represent C-H bending, C=C and C-N stretch of Cz and Th due to the increase in length of the mentioned bonds (Schaffer et al., 1991). Localized BT, Th and Cz of C=C stretch and C-H in plane bending recorded an upward shift for sample B located at 1063 and 1540 cm^{-1} as compared to sample A and C. This could be due to the consequences of drastic changes in the electronic band structure. There is no difference in Raman shift between these three samples for antisymmetric stretch modes of the fullerenes located at 1566 cm^{-1}. However, all peaks arise for sample A shows a higher intensity as compared to samples B and C which could be related to the annealing effect that cause the amount of some elements in B and C to reduce (Su et al., 2012).

CHAPTER 6: UTILISATION OF PCDTBT:PC$_{71}$BM COMPOSITE NANOSTRUCTURES FOR THE CAPACITIVE HUMIDITY SENSOR

Due to the promising and fast developing nano-composite technology, various studies have been carried out in exploring the composite for humidity sensing applications (Azmer et al., 2016; Li et al., 2014; Sajid et al., 2016). The claim has been made where composites correspond to the existence of nanostructures as the active sensing layer. The exceptional properties of the high porosity and large surface to volume ratio promote enhancement in absorption mechanism of the composite sensing layer and thus adds towards higher sensitivity, faster response and smaller hysteresis gap for the fabricated sensor devices.

The incorporation of PCDTBT and PCBM composite has been first investigated by Blouin et al., which then applied in the solar cell application by Park and his group (Blouin et al., 2007; Park et al., 2009). 6 % power conversion efficiency of bulk heterojunction solar cells is reported in the study, which is the highest performance of any bulk heterojunction at that time. The nano-morphology of the composite could be easily altered by several parameters such as solution concentration, types of solvent, thermal annealing, blend ratio as well as molecular structure of the material involved. Meanwhile, analysis on morphological surface properties of the composite has been done by several researchers (Ahmad Makinudin et al., 2015; Bakar et al., 2015; Fakir et al., 2016; Supangat et al., 2014).

Among the reported literatures, it is indicate that modification in the structural morphology has shown to enhance optical properties of the composite (Ahmad Makinudin et al., 2015; Bakar et al., 2015; Supangat et al., 2014). Other than that, composite structures has also reported to possess a better electrical properties as compared to its individual component (Kumar et al., 2015). All these fascinating properties hold by the PCDTBT: PCBM composite structures has not been utilised yet in the humidity sensing applications, though the PCDTBT humidity sensor in the form of thin film sensing layer has been recently reported (Zafar & Sulaiman, 2016). Besides being very stable in air and high temperature due to its nature that stable against oxidation, the PCDTBT humidity sensors is reported to exhibit significantly higher sensitivity, narrow hysteresis as well as fast response and recovery time. PCDTBT has found to display the coarse and porous surface morphology which ensures the larger capacity towards humidity adsorption (Zafar et al., 2016).

Therefore, by considering all the intriguing properties of PCDTBT and PCDTBT:$PC_{71}BM$, comparative study into discovering the different surface morphology based on the composite sensing film towards the humidity sensing performance has been proposed. Problems that commonly associated with the humidity sensors performance such as hysteresis, response & recovery time and sensitivity can be simply modified by altering the surface morphological characteristics (Hayat et al.,2016) as shown in the previous chapter. Surface type humidity sensor (Al/PCDTBT:$PC_{71}BM$/Al) in planar configuration has been fabricated and the relationship between relative humidity and the electrical response has been studied. The capacitance has been measured at varied humidity level with the aim to produce higher sensing parameters of the humidity sensors than those previously reported in the literature. The humidity sensing characteristics of the sensor have been investigated by exposing the composite active layer to various wide range relative humidity levels (15-95 *%RH*) at room temperature. Exclusive morphological properties of each active layer have also been studied and relate to their humidity sensing characteristics. Different morphological properties exhibit by each of the nanostructures of different techniques contribute to different sensors ability. PCDTBT:$PC_{71}BM$ composite nanostructures produced from immersion technique shows significantly higher sensitivity of ~62.34

pF/%*RH* as compared to the spin coating (0.2 pF/%*RH*) and drop casting & annealing combination techniques (7.5 pF/%*RH*) .

6.1 Results & Discussion

Figure 6.3(a), (b) & (c) show the capacitance-relative humidity relationship of Al/PCDTBT:PC$_{71}$BM/Al humidity sensor of different PCDTBT infiltration techniques of spin coating (5 mg/ml, 1000 rpm), immersion (15 mg/ml, 50 °C, 24 hours) and drop casting & annealing combination techniques (5 mg/ml, 300 °C) which denoted here as samples A, B and C, respectively. The capacitance has been measured at different frequencies of 100 Hz, 1 kHz and 10 kHz for each of the proposed sensor of the AC test signal. As the humidity level increases from 20 to 95 %*RH*, the capacitance of all devices (A, B and C) has also increased. However, the variations in capacitance as a function of %*RH* are greatly influenced by the operational frequencies. For low operational frequency of 100 Hz, the capacitance has increased by about 2.7, 628 and 70 times in magnitudes for device A, B and C, respectively, with the rise of *RH* level from 20 to 95 %. On the other hand, capacitance variations at higher order operational frequencies (1 &10 kHz) have been estimated to be 1.35 & 1.16, 48 & 3.75 and 3.32 & 1.37 times for device A, B and C, respectively. It can be observed that at lower operational frequency (100 Hz), the influence of %*RH* on the capacitance is stronger than the higher operational frequencies (1&10 kHz). The sensitivities of the proposed sensor have been calculated by using Equation 6.1.

$$Sensitivity = \frac{C_{\max} - C_{\min}}{RH_{\max} - RH_{\min}} \tag{6.1}$$

$C_{\max}$ & $C_{\min}$ and $RH_{\max}$ & $RH_{\min}$ represent the maximum & minimum capacitance and relative humidity value, respectively. The sensitivities (within 20 % to 95 % bandwidth) at 100 Hz operational frequency have been estimated to be 0.2 (A), 62.34 (B) and 7.5

(C) pF/ %*RH*. Meanwhile, sensitivities of higher order frequencies (1 & 10 kHz) have been estimated to be 0.04 & 0.013, 4 & 0.2 and 0.87 & 0.08 pF/ %*RH* for devices A, B and C, respectively. The significantly higher sensitivities that has been observed at low frequency may be attributed to the rapid polarization of adsorbed water molecule as well as more water molecule is adsorbed on the surface of the sensor (Qi et al., 2008; Tripathy et al., 2014). On the other hand, the electric field changes its direction rapidly in high frequency range and causes the charge redistribution fails to follow the prompt changes. As a result, the capacitance values become smaller and independent of *RH*.

However, below the 20 %*RH*, the capacitance variation to *RH* changes is not significant indicating that capacitance is independent of humidity at low %*RH* levels. This could be attributed to the mode changes of water molecules adsorption in sensing surface where the coverage of humidity absorbed at low humidity level is low and restricted to immobile single layer. Meanwhile, as the humidity level increases, the mobile multilayers continue to build up on the pre-existing adsorbed water layer as a result of progressive increase in humidity adsorption (Aziz et al., 2012; Azmer et al., 2016). At this mobile multilayer stage, the capacitance of the sensor starts to increase significantly which represent the close relation between capacitance variation and the amount of adsorbed water molecules. This phenomenon is illustrated in Figure 6.4.

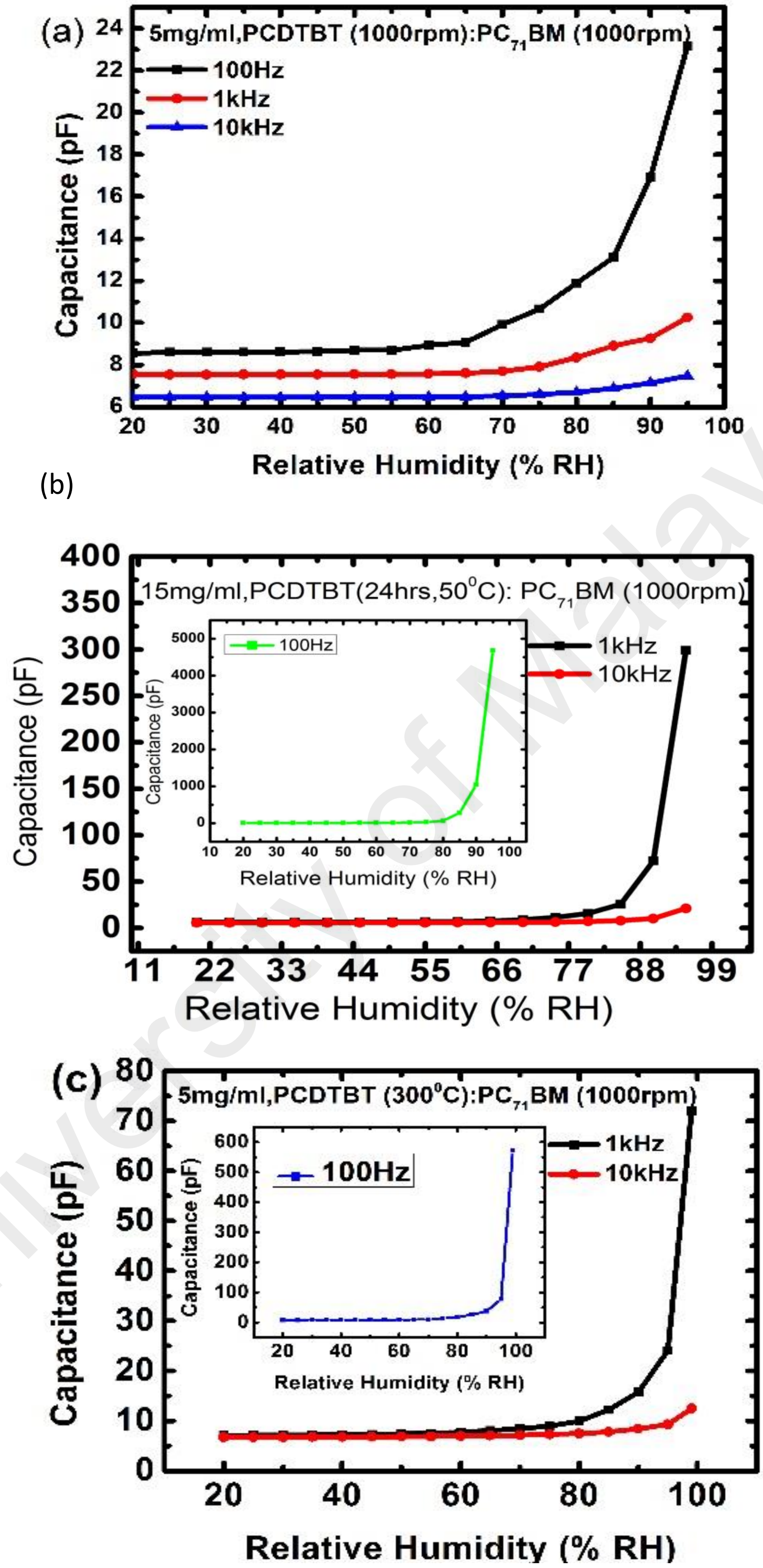

Figure 6.1: The capacitance-relative humidity relationship of Al/PCDTBT:$PC_{71}BM$/Al humidity sensor of (a) spin coating (5 mg/ml, 1000 rpm), (b) immersion (15 mg/ml, 50 °C, 24 hours) and (c) drop casting & annealing combination (5 mg/ml, 300 °C) techniques for 100Hz, 1kHz and 10kHz.

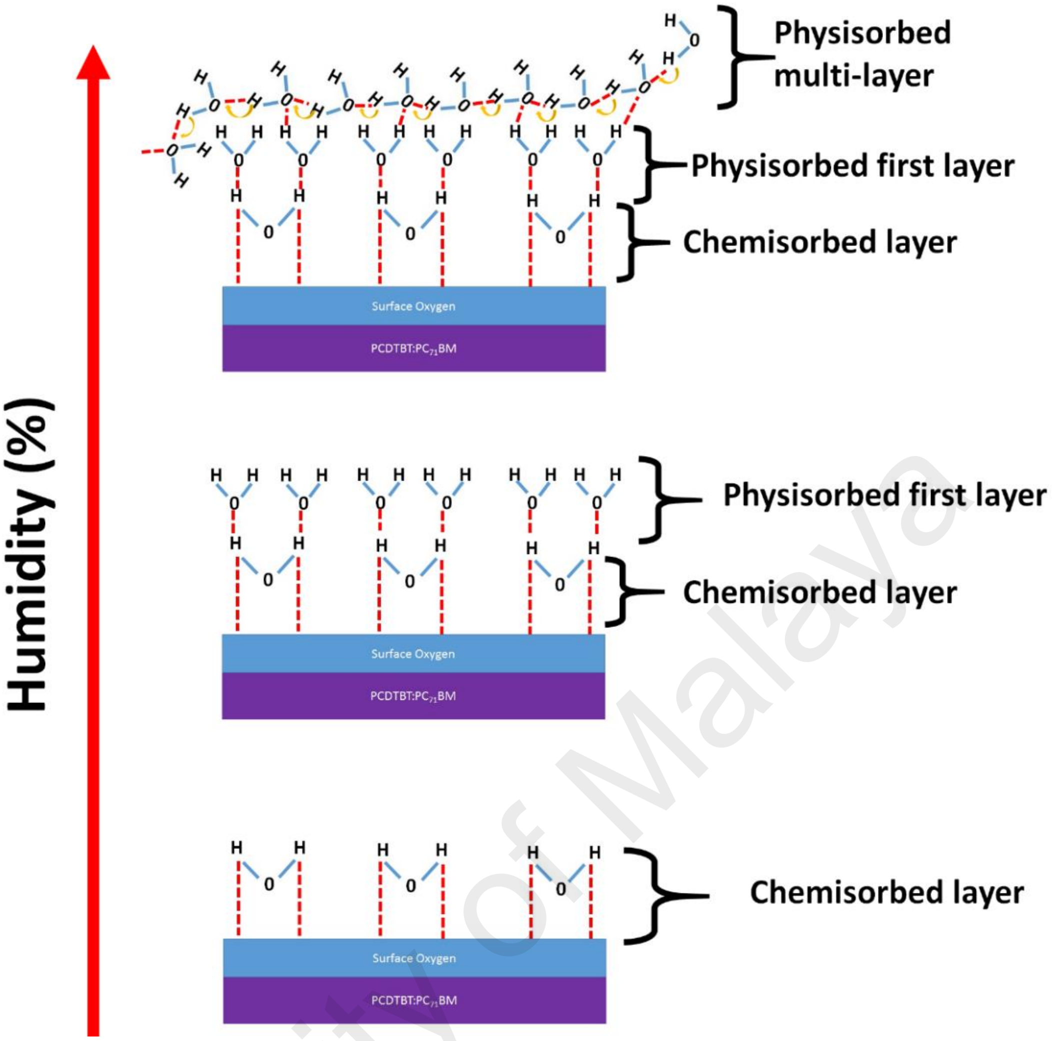

Figure 6.2: Schematic representation of the humidity sensing mechanism of PCDTBT:PC$_{71}$BM composite nanostructures at different humidity levels.

The operating conditions for the next subsequent electrical characterisations are kept at low frequency of 100 Hz since this low frequency gives the maximum sensitivity for all proposed devices of A, B and C. Further low order of operational frequency is usually avoided since it will cause disruption in the stability and repeatability of the electrical response (Zhang et al., 2014). Each device is stored for 3 months in ambient condition to monitor its lifetime where acceptable decrease in capacitance of approximately 1.4, 3 and 2.6 % at 100 Hz frequencies is observed for devices A, B and C, respectively.

Figure 6.5 shows capacitance-relative humidity relationship of devices A, B and C at low operational frequency of 100 Hz where the change in capacitance variations is highest for devices B followed by devices C and A. The sensitivity for devices A, B and C is 0.2, 62.34 and 7.5 pF /%*RH*, respectively, as previously mentioned. It can be seen that sensor B possesses the most significant sensitivity compared to the others two sensors (A and C).

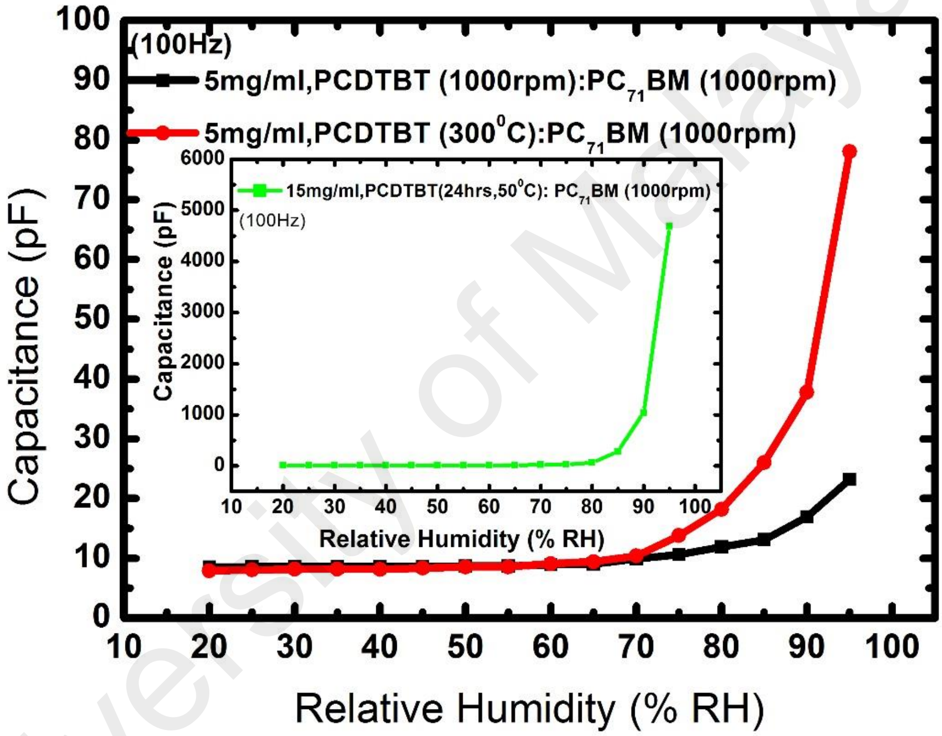

Figure 6.3: Capacitance-relative humidity relationship of devices A, B and C at low operational frequency of 100 Hz.

Since the degree of porosity on the surface of the sensing film is one of the crucial factor which can affect the performance of the sensor, the differences in sensitivity between these three devices are strongly related to their sensing layer morphological characteristics as shown in Figure 6.6(a) (device A), Figure 6.6(b) (device B) and Figure 6.6(c) (device C). The presence of pores is critical to trigger changes in both electrical and physical properties of the film efficiently as well as dimension, volume and pores distribution (Aziz et al., 2012). Sensing layer surface of device B shows a higher degree of porosity as compared to the other two sensors (A and C). Besides being more orderly distributed, nanotubes of sensing layer in device B are more aligned and denser. This will provide larger exposed internal surfaces area for adsorption of vapour molecules. Larger internal exposed surface area will help to facilitate the adhesion of vapour molecules to the sidewalls of nanotubes and accumulates it into mono/multilayers around the opening pores (Yeow & She, 2006). The type of porous structures in device B sensing layer will not only increase the expose surface area for vapour molecules adhesion, but also trigger the capillary condensation. Capillary condensation can boost the increase in capacitance significantly which strongly related to the sensitivity of the device. Several researches have shown that capillary condensation is one of the important factor in determining the sensitivity of a particular range of *RH* as well as improve the sensing capability of materials (Chen et al., 2009).

As the *RH* increases, proportion of vapour and water that exist in the mixture of the dielectric medium will also increase. The relative dielectric constant of liquid water is about 80, which is much higher than that of water vapour, which is 1. The capillary condensation of vapour to water will increase the effective dielectric constant substantively as well as capacitance value. As expressed in Equation 6.2, the capacitance is directly related to the surface area of the electrodes (A), dielectric constant of free space (ε_0), separation between the aluminium electrodes (d) and effective dielectric constant of the organic composite humidity sensing thin film (ε').

$$C = \frac{\varepsilon_0 \varepsilon' A}{d} \tag{6.2}$$

The capillary condensation phenomenon can be further explained by kelvin equation (Equation 6.3):

$$r_k = \frac{2M\gamma\cos\theta}{R\rho T\ln\frac{P_s}{P_o}} \tag{6.3}$$

where P_o is the water vapour pressure; P_s is the water vapour pressure at saturation; γ is the surface tension; R is the universal gas constant; T is the temperature in Kelvin; ρ and M are the density and molecular weight of water, respectively; and θ is the contact angle. Based on the equation, capillary condensation can take places in a radius of pores up to r_k at a particular *RH* and temperature.

As explained in the previous chapters, the parameter and technique involved could be the primary factors for the morphological characteristics hold by the nanostructures. Both nanostructures of devices A and C are prepared using 5 mg/ml with two different approaches of spin coating and drop casting & annealing combination techniques, respectively. Meanwhile, immersion technique of 15 mg/ml is used in preparing the sensing layer nanostructures in device B. The higher solution concentration of 15 mg/ml and immersion technique give a better stability to the nanostructures which improved nanotubes alignment and densification as well as offer higher porosity for better devices efficiency.

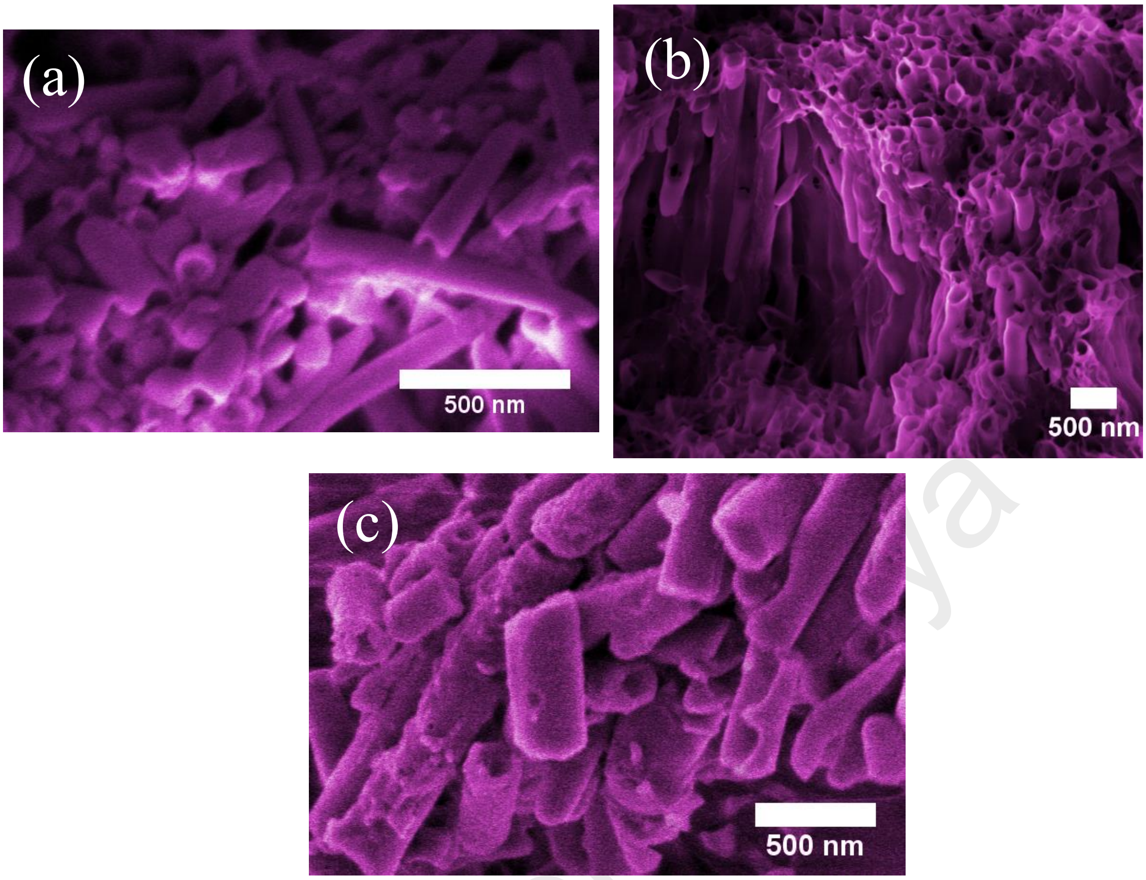

Figure 6.4: PCDTBT:PC$_{71}$BM composite nanostructures sensing layer of (a) devices A, (b) devices B and (c) devices C.

Response and recovery behaviour is one of the crucial factors in evaluating the performance of the humidity sensors particularly in determining the device's competency for practical purpose. Practically, the time taken by the sensor to achieve 90 % of the total change in its output is defined as the response time in the case of humidification cycle, meanwhile reset time is the duration required for a sensor to recover back to its initial value in the desiccation process (Tripathy et al., 2014). Figure 6.7(a), (b) and (c), illustrates the capacitive response of devices A, B and C, respectively. Two-repeated cycle of response-recovery curves have been obtained by alternately placing the sensor into humidity chambers with two distinctive *RH* levels of 15 and 65 *%RH*. The average response and recovery time for devices A, B and C have been evaluated to be 10 &10, 10 & 5 and 15 & 5 seconds, respectively. It shows that the time taken for devices A and B to respond is similar which is 10 seconds, while devices C took 5 second slower (15 seconds) than devices A and B. However, for recovery time, devices B and C show 5 second faster compared to devices A. It can be compute that devices B own a better combination of response and recovery time, which is faster, compared to devices A and C. This is also in a good correlation with the sensitivity own by each device stated earlier.

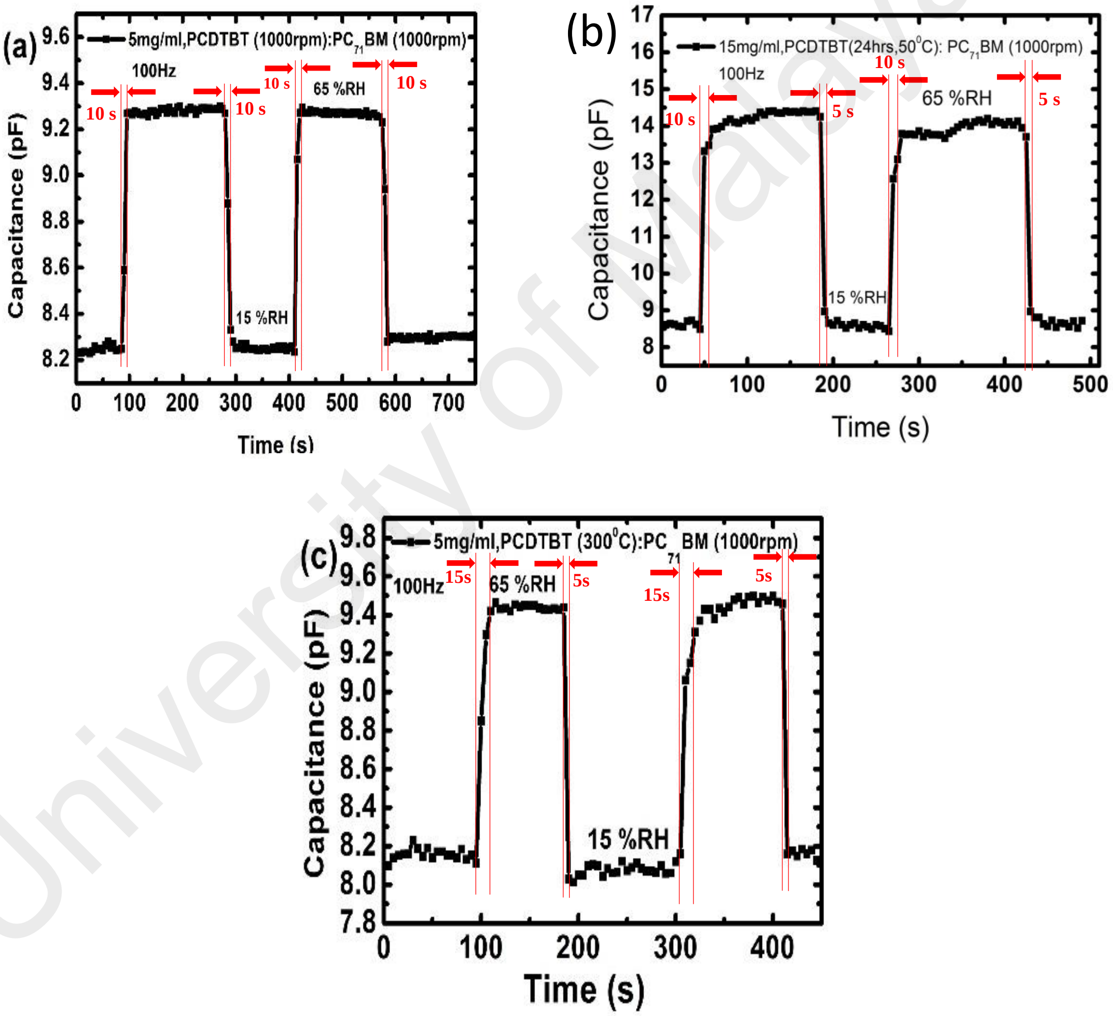

Figure 6.5: The capacitive response-recovery curves of devices A (a), B (b) and C (c).

Hysteresis is a well-known problem usually occurred in humidity sensor based on the principle of absorption/desorption of water molecules. By evaluating the humidity absorption and desorption curves, the hysteresis percentage can be obtained and studied among the proposed sensors. The graph shown in Figure 6.8(a), (b) and (c), depicts the formation of hysteresis gap in devices A, B and C, respectively, at 100 Hz operating frequency in response to the increasing and decreasing of surrounding *RH* levels. Average hysteresis value for each device A, B and C has been estimated to be in acceptable ranges, which are 9, 11 and 10 %, respectively. The hysteresis gap of device B looks small in graph (Figure 6.8(b)) due to the huge difference range of capacitance among devices as can be seen in inset of Figure 6.8(b). The hysteresis percentage of the proposed sensors has been calculated by using Equation 6.4.

$$Hysteresis\ percentage = Average\left[\frac{C_{Desorption} - C_{Absorption}}{C_{Absorption}}\right] \times 100\% \qquad (6.4)$$

$C_{Desorption}$ and $C_{Absorption}$ stands for capacitance value of desorption and absorption for each involved point, respectively. Device B recorded a fastest recovery time (5 s) but with a slightly higher hysteresis as compared to the devices A and C. This is because the response and recovery curves were obtained at 15 and 65 *%RH* which is lower range. However, hysteresis of device B is contributed by the higher range of %*RH* (Figure 6.8(b)) where capillary condensation occurred. Polymer-based humidity sensors typically have been found to exhibit hysteresis value up to 13 % (Chani et al., 2013; Lee et al., 2001). Improper diffusion out of water from the porous sensing layer could be one of the reason for the considerable hysteresis value (Fürjes et al., 2003). This phenomenon might cause by the higher thickness and rough surface structure of the device-sensing layer. However, the hysteresis percentage in polymer-based humidity sensor can be reduced using several approaches such as polymer crosslinking (Watt, 2006), varying the thickness of the sensing film (Kulwicki, 1991) and enlarging the porous structures (Björkqvist et al., 2006) to reduce capillary condensation effect.

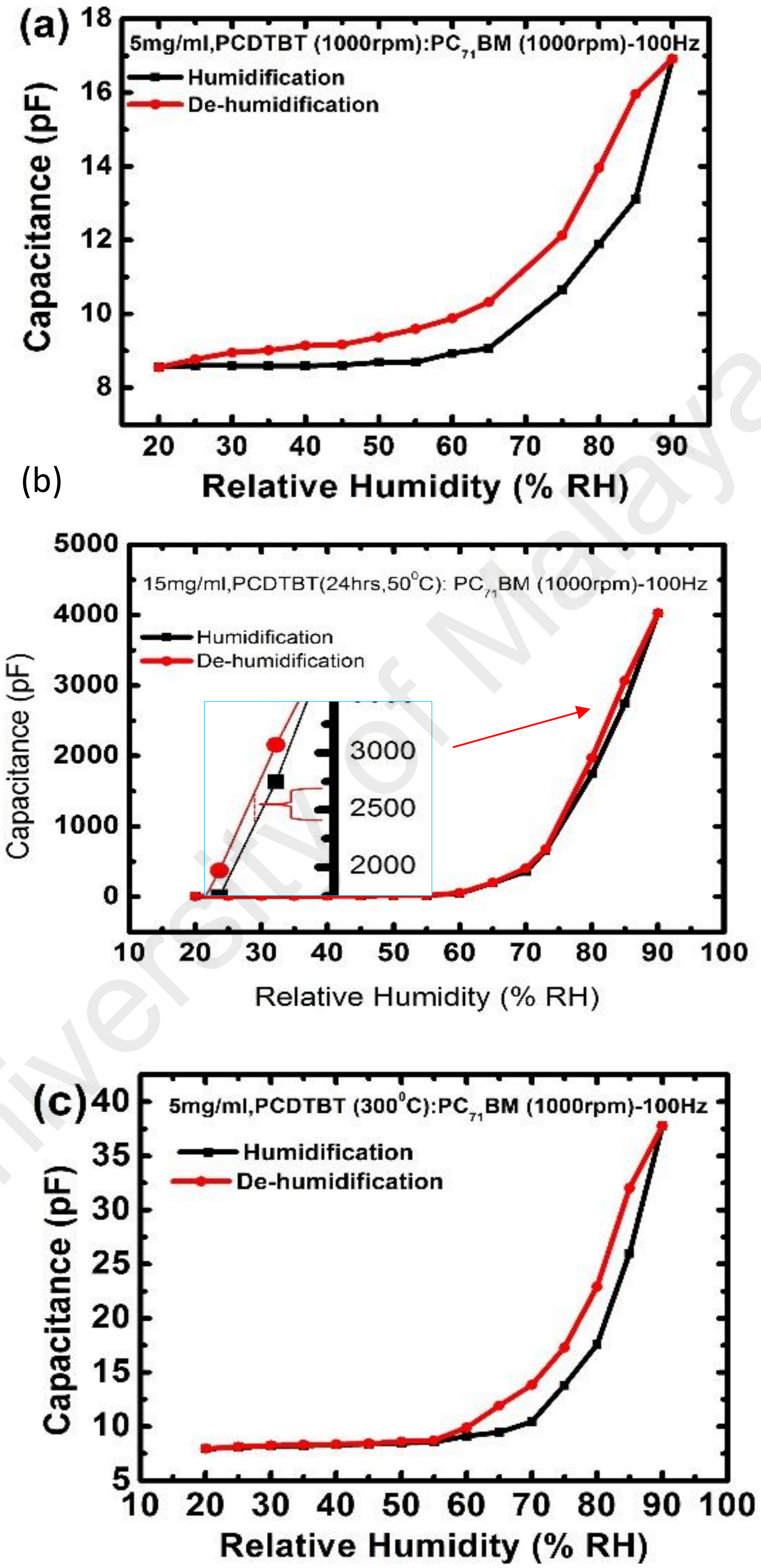

Figure 6.6: Hysteresis graph of devices (a) A, (b) B and (c) C.

As described in the Fig. 6.7(a), direct relation between capacitive outputs of the sensor to change in relative humidity (%*RH*) can be observed while Fig. 6.7(b) depicts inversely proportional response of both devices conductivity to RH level changes. Even though, capacitance slowly increase from 20 *%RH*, significant change of the capacitive output has been found particularly at points from 80 *%RH* leading up to 95 *%RH*. In comparison, resistive values were measured and revealed a better linearity of resistance output particularly at the lower range of 40 *%RH* to 90 *%RH*. This further confirmed the hypotheses proposed how the capacitive based humidity sensors mostly shows non-linear response in contrast to the resistive ones (Björkqvist et al., 2004; Rittersma, 2002)

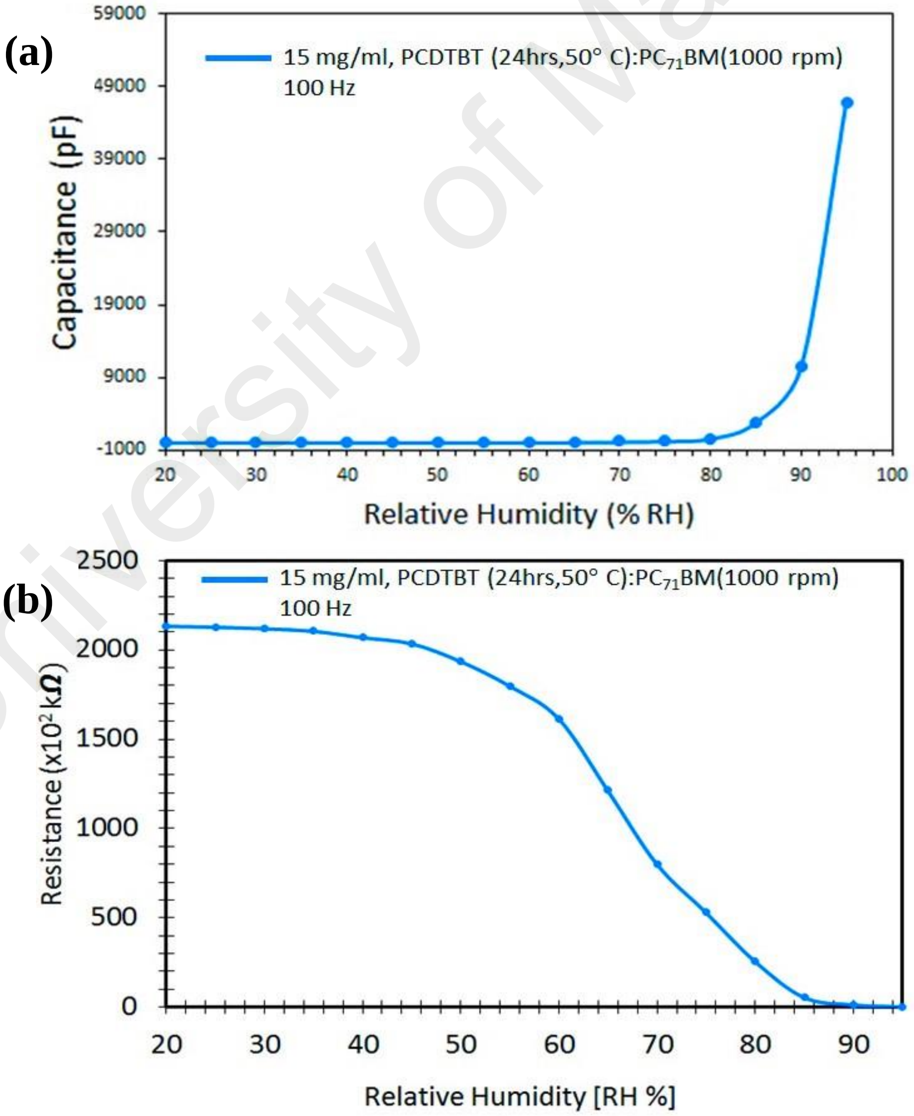

Figure 6.7: The capacitive (a) and resistive (b) responses for samples B (15 mg/ml, PCDTBT (24hrs,50° C):PC$_{71}$BM(1000 rpm)) at 100 Hz operational frequency.

Table 6.1 shows the comparison of sensing parameters between the proposed PCDTBT:PC$_{71}$BM based humidity sensors of devices A, B and C. It can be observed that the sensing performance of devices B is significantly higher compared to devices A and C.

Table 6.1: Comparison of the sensing parameters between the proposed PCDTBT:PC$_{71}$BM based humidity sensors of devices A, B and C.

Samples	**Sensitivity (@100Hz)**	**Response Recovery time**	**Hysteresis**
A	0.2 pF / %*RH*	~10 and 10 s	~9 %
B	62.34 pF / %*RH*	~10 and 5 s	~11%
C	7.5 pF / %*RH*	~15 and 5 s	~10 %

Figure 6.8(a), (b) and (c) show the capacitance-relative humidity relationship, hysteresis loop and capacitive response-recovery of alumina template-based devices, respectively. When the device B that has the most significant sensing performance is compared with the neat alumina template without any infiltrated polymer, device B shown a much higher sensitivity of 62.34 pF/%*RH* than the alumina template-based device, which recorded only 2.05 pF/%*RH*. Meanwhile, the other sensing parameters such as hysteresis and response & recovery are not varying in a substantial amount as recorded in Table 6.2. Sensing parameters of formerly reported devices are also being compared with the proposed sensors in Table 6.2. It can be well witnessed that the sensing behaviour of the proposed sensor is improved.

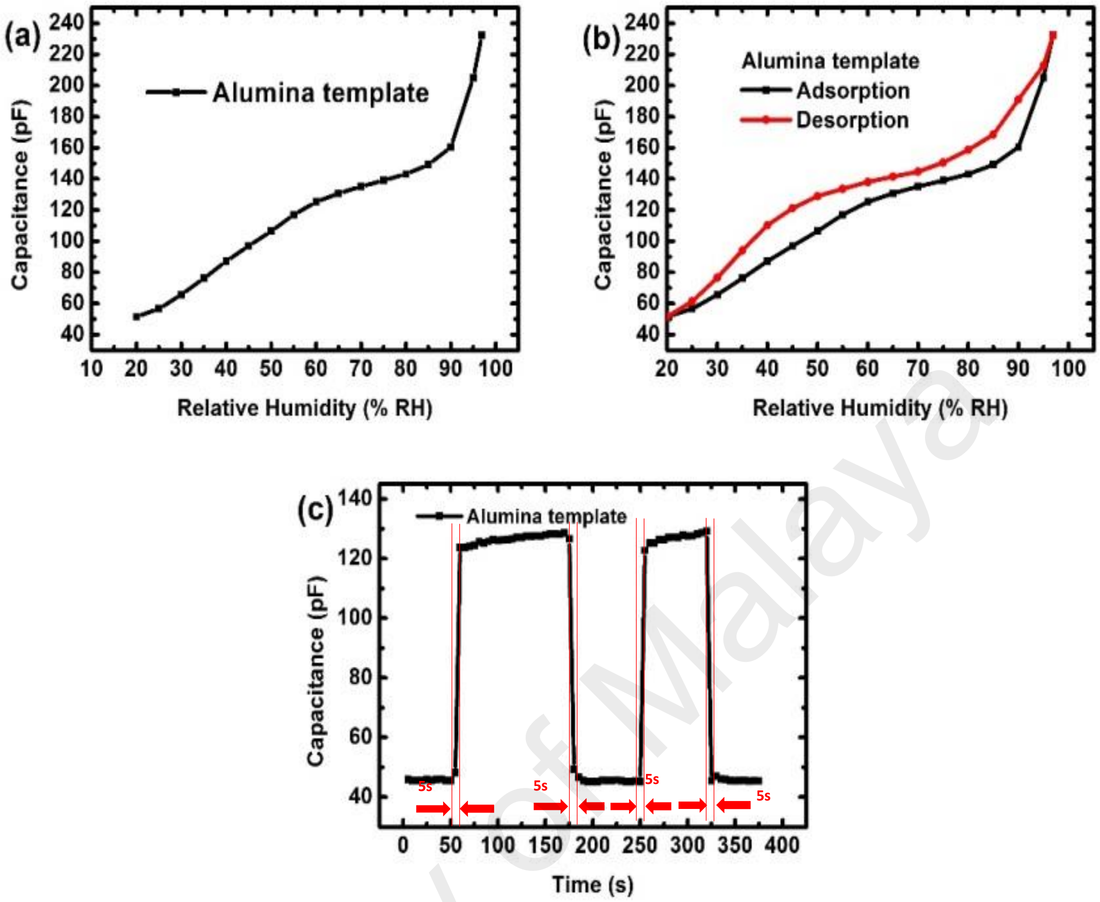

Figure 6.8: (a) Capacitance-relative humidity relationship, (b) hysteresis loop and (c) capacitive response-recovery of alumina template-based devices.

Table 6.2: Comparison of formerly reported sensors with the proposed sensors.

Samples	**Sensitivity (@100Hz)**	**Bandwidth**	**Response Recovery time**
Methyl-red (Ahmad et al., 2008)	16.92 pF/*%RH*	30-95 *%RH*	~10 s each
DMBHPET (Azmer et al., 2015)	0.007 pF / *%RH*	30–80 *%RH*	10, 15 s
Polyimide (Choi et al., 2014)	22.29 pF/*%RH*	20-90 *%RH*	25 s
PCDTBT (Zafar & Sulaiman, 2016)	39.73 pF/*%RH*	37-98 *%RH*	8, 14 s
PCDTBT:PC$_{71}$BM	62.34 pF/*%RH*	20-95 *%RH*	~10 and 5 s
Alumina template	2.05 pF/*%RH*	20-95 *%RH*	5 s each

CHAPTER 7: CONCLUSIONS AND FUTURE WORK

The works that have been presented in this thesis can be categorised mainly into three parts. Summary of each part is given below and followed by the recommended future works that can be potentially developed from the present study;

7.1 Conclusions

First section demonstrated the fabrication of PCDTBT nanostructures by using template-assisted method and its characterisation. The effect of different infiltration techniques (spin coating, immersion and drop casting & annealing combination techniques) on the morphological, structural and optical properties of produced PCDTBT nanostructures is reported. Different spinning rate (1000, 2000 and 3000 rpm) with the combination of different concentration of 5, 10 and 15 mg/ml has produced numerous types of 1D nanostructures, which are nanorods, nanotubes and nanoflowers. Low spinning rate (1000 rpm) and higher concentration (15 mg/ml) produced nanostructures that are better in the optical properties as compared to the higher spinning rates (2000 and 3000 rpm) and lower concentrations (5 and 10 mg/ml). The spinning rate, solution concentration and incorporation between two techniques play an important role in determining the final properties of the PCDTBT nanostructures. Meanwhile for immersion technique, nanotubes have been produced at all parameters. Better alignment of nanotubes occurred for 2 and 12 hours immersion time compared to the 24 hours immersion time with an exclusive situation occurred for 15 mg/ml that anneal at 50 °C where the alignment is improved as the immersion time is increased from 2, 12 to 24 hours. Enhancement in optical properties is recorded as the concentration is increased from 5, 10 to 15 mg/ml. A concentration of 15 mg/ml with the combination of 24 hours immersion time and annealed at 50 °C is chosen to be the best parameter for PCDTBT *p*-type nanostructure. For the drop casting & annealing combination techniques, the effective transformation of PCDTBT nanorods into nanotubes by wetting of porous templates with PCDTBT melts at controlled wetting temperature via facile melt wetting strategy is clearly shown. PCDTBT nanotubes fabricated at the optimum concentration of 10 mg/ml and annealed at 300 °C show enhancement in morphological and optical properties. These PCDTBT nanotubes are elongated, dense and well aligned as compared to the PCDTBT nanorods obtained at the same concentration. PCDTBT nanotubes portrayed promising morphological and optical properties as compared to the PCDTBT nanorods. In a nutshell, a combination between parameters plays a vital role in the wetting process. The parameters can be preferably chosen to suit the selected applications.

In the second section, PCDTBT:$PC_{71}BM$ composite nanostructures were synthesised by infiltrating the $PC_{71}BM$ solution into the infiltrated PCDTBT. The infiltration of $PC_{71}BM$ into the infiltrated template has changed the morphological, optical and structural properties of the original *p*-type (PCDTBT) nanostructures. In spin coating technique, low concentrations of 5 and 10 mg/ml PCDTBT: $PC_{71}BM$ composite absorb light at the longer wavelength compared to 15 mg/ml PCDTBT: $PC_{71}BM$ composite. However, composite structure that formed through immersion technique, indicates that 15 mg/ml (24 hours, 50 °C) as the most promising optical properties compared to the other parameters involved in this technique. In drop casting & annealing combination techniques, 5 mg/ml possesses better optical properties compared to 10 mg/ml. Composite structures has also shown a significant quenched and slightly red shift in PL spectra compared to *p*-type. The infiltration techniques and the parameters involved is compliment to each other in determining the outcome properties of the nanostructures.

In the third section, capacitive-type humidity sensing devices based on PCDTBT:PC$_{71}$BM composite nanostructures have been fabricated and evaluated. Upon exposure to humidity, an increase in electrical capacitance has been predominantly observed. The capacitance variation has been explained to be associated with the difference in dielectric permittivity of humid and desiccated organic sensing film. The experimental results indicate that the surface morphology of sensing layer plays an important role in determining the performances of the devices. Composite sensing layer that fabricated via immersion technique exhibited the highest porosity, better alignment and higher densification. This technique has produced the best devices performance with the highest sensitivity compared to the other devices produced from other infiltration techniques. Composite nanostructures-based humidity sensor also exhibits the improved sensitivity as compared to previous reported PCDTBT thin film-based humidity sensor. The reason of improved sensing parameters of the proposed humidity sensor is believed to be associated with the higher density of porosity and exceptional surface morphology of the organic composite nanostructures.

7.2 Future Work

The astonishing properties of PCDTBT and PCDTBT: PC$_{71}$BM composite nanostructures as well as the humidity sensor devices that have been explored in this thesis suggest the following research studies that should be considered in the future work:

- This study involved an investigation towards formation mechanism, morphological, structural and optical properties of PCDTBT and PCDTBT:PC$_{71}$BM composite nanostructures. Hence, wide variety of applications can be further explored based on the results obtained from this research such as optical or light harvesting-based devices. Furthermore, the charge transport can be enhanced by replacing the conventional disordered and discontinued D/A interface topology of bulk heterojunction (BHJ) blend with the nanostructured semiconductor-based devices, since nanostructures possesses high surface to volume ratio which could enhance the exciton dissociation efficiency due to increase in D/A interfacial area. The unique structure of 1-D nanostructures would also allow efficient absorption of the light. Other applications such as gas sensor and mechanical transducer shall also be considered.

- One of the advantages of organic polymer-based devices is their flexibility for performance enhancement through manipulated parameters. Further study on other optimising parameters can be proposed in much thoroughly way to overcome the issue arise from the present devices. For instance, in term of devices performances, the studies on discovering the parameters that would contributes to lower hysteresis value as well as improve the sensor linearity shall be considered.

REFERENCES

Abthagir, P. S., & Saraswathi, R. (2004). Charge transport and thermal properties of polyindole, polycarbazole and their derivatives. *Thermochimica Acta, 424*(1-2), 25-35.

Ahmad Makinudin, A. H., Fakir, M. S., & Supangat, A. (2015). Metal phthalocyanine: Fullerene composite nanotubes via templating method for enhanced properties. *Nanoscale Research Letters, 10*, 53.

Ahmad, Z., Sayyad, M. H., Saleem, M., Karimov, K. S., & Shah, M. (2008). Humidity-dependent characteristics of methyl-red thin film-based Ag/methyl-red/Ag surface-type cell. *Physica E: Low-dimensional Systems and Nanostructures, 41*(1), 18-22.

Ahmad, Z., Zafar, Q., Sulaiman, K., Akram, R., & Karimov, K. S. (2013). A humidity sensing organic-inorganic composite for environmental monitoring. *Sensors (Basel), 13*(3), 3615-3624.

Al-Kaysi, R. O., Ghaddar, T. H., & Guirado, G. (2009). Fabrication of one-dimensional organic nanostructures using anodic aluminum oxide templates. *Journal of Nanomaterials, 2009*, 1-14.

Al-Kaysi, R. O., Muller, A. M., Ahn, T. S., Lee, S., & Bardeen, C. J. (2005). Effects of sonication on the size and crystallinity of stable zwitterionic organic nanoparticles formed by reprecipitation in water. *Langmuir, 21*(17), 7990-7994.

Ali, S., Tian, W., Ali, N., Shi, L., Kong, J., & Ali, N. (2015). Polymer melt flow through nanochannels: From theory and fabrication to application. *RSC Advances, 5*(10), 7160-7172.

Anand, B., Krishnan, S., Podila, R., Sai, S. S. S., Rao, A. M., & Philip, R. (2014). The role of defects in the nonlinear optical absorption behavior of carbon and ZnO nanostructures. *Physical Chemistry Chemical Physics, 16*(18), 8168-8177.

Andrade, J., Gregonis, D., & Smith, L. (1985). Polymer surface dynamics. *Surface and interfacial aspects of biomedical polymers* (pp. 15-41): Springer.

Aziz, F., Sayyad, M. H., Sulaiman, K., Majlis, B. H., Karimov, K. S., Ahmad, Z., & Sugandi, G. (2012). Corrigendum: Influence of humidity conditions on the capacitive and resistive response of an Al/VOPc/Pt co-planar humidity sensor. *Measurement Science and Technology, 23*(6), 069501.

Azmer, M. I., Ahmad, Z., Sulaiman, K., & Al-Sehemi, A. G. (2015). Humidity dependent electrical properties of an organic material DMBHPET. *Measurement, 61*, 180-184.

Azmer, M. I., Zafar, Q., Ahmad, Z., & Sulaiman, K. (2016). Humidity sensor based on electrospun MEH-PPV:PVP microstructured composite. *RSC Advances, 6*(42), 35387-35393.

Bakar, N. A., Supangat, A., & Sulaiman, K. (2014a). Controlling the morphological, structural, and optical properties of one-dimensional PCDTBT nanotubes by template wetting. *Nanoscale Research Letters, 9*(1), 600.

Bakar, N. A., Supangat, A., & Sulaiman, K. (2014b). Elaboration of PCDTBT nanorods and nanoflowers for augmented morphological and optical properties. *Materials Letters, 131*, 27-30.

Bakar, N. A., Supangat, A., & Sulaiman, K. (2015). Formation of PCDTBT:PC71BM p-n junction composite nanotubes via a templating method. *RSC Advances, 5*(124), 102689-102699.

Banerjee, G., & Sengupta, K. (2002). Pore size optimisation of humidity sensor—A probabilistic approach. *Sensors and Actuators B: Chemical, 86*(1), 34-41.

Banerji, N., Gagnon, E., Morgantini, P.-Y., Valouch, S., Mohebbi, A. R., Seo, J.-H., . . . Heeger, A. J. (2012). Breaking down the problem: Optical transitions, electronic structure, and photoconductivity in conjugated polymer PCDTBT and in its separate building blocks. *The Journal of Physical Chemistry C, 116*(21), 11456-11469.

Baruah, S., & Dutta, J. (2009). Hydrothermal growth of ZnO nanostructures. *Science and Technology of Advanced Materials, 10*(1), 013001.

Bauskar, D., Kale, B., & Patil, P. (2012). Synthesis and humidity sensing properties of $ZnSnO_3$ cubic crystallites. *Sensors and Actuators B: Chemical, 161*(1), 396-400.

Bearden, S. D., Cannon, J. P., & Gold, S. A. (2011). Solvent effects on template wetting nanofabrication of MEH-PPV nanotubules. *Macromolecules, 44*(7), 2200-2205.

Beyler, C. L., & Hirschler, M. M. (2002). Thermal decomposition of polymers. *SFPE handbook of fire protection engineering 2* (pp. 111-131).

Björkqvist, M., Paski, J., Salonen, J., & Lehto, V. P. (2006). Studies on hysteresis reduction in thermally carbonized porous silicon humidity sensor. *IEEE Sensors Journal, 6*(3), 542-546.

Blouin, N., Michaud, A., & Leclerc, M. (2007). A low-bandgap poly(2,7-carbazole) derivative for use in high-performance solar cells. *Advanced Materials, 19*(17), 2295-2300.

Boland, P., Lee, K., & Namkoong, G. (2010). Device optimization in PCPDTBT:PCBM plastic solar cells. *Solar Energy Materials and Solar Cells, 94*(5), 915-920.

Bonn, D., Eggers, J., Indekeu, J., Meunier, J., & Rolley, E. (2009). Wetting and spreading. *Reviews of Modern Physics, 81*(2), 739-805.

Botelho, A. L. S., Yongwoo, Liu, J., & Lin, X. (2014). Structure and optical bandgap relationship of π-conjugated systems. *PLoS ONE, 9*(1), 1-8.

Boudreault, P.-L. T., Beaupre, S., & Leclerc, M. (2010). Polycarbazoles for plastic electronics. *Polymer Chemistry, 1*(2), 127-136.

Bovill, E., Yi, H., Iraqi, A., & Lidzey, D. G. (2014). The fabrication of polyfluorene and polycarbazole-based photovoltaic devices using an air-stable process route. *Applied Physics Letters, 105*(22), 223302.

Boyle, J. (2005). *Lehninger principles of biochemistry: Nelson, D., and Cox, M.* New York: W.H. Freeman and Company.

Burda, C., Chen, X., Narayanan, R., & El-Sayed, M. A. (2005). Chemistry and properties of nanocrystals of different shapes. *Chemical Reviews, 105*(4), 1025-1102.

Burgues-Ceballos, I., Hermerschmidt, F., Akkuratov, A. V., Susarova, D. K., Troshin, P. A., & Choulis, S. A. (2015). High-performing polycarbazole derivatives for efficient solution-processing of organic solar cells in air. *ChemSusChem, 8*(24), 4209-4215.

Cai, X.-d., Huang, R., & Guo, Y.-n. (2013). Preparation and characterization of humidity sensor based on poly(3-alkyl)pyrrole containing phosphonic acid groups. *Chinese Journal of Polymer Science, 31*(10), 1443-1450.

Cepak, V. M., & Martin, C. R. (1999). Preparation of polymeric micro- and nanostructures using a template-based deposition method. *Chemistry of Materials, 11*(5), 1363-1367.

Chang, J. H., & Hunter, I. W. (2011). Characterization and control of the wettability of conducting polymer thin films. *MRS Proceedings, 1228*.

Chani, M. T. S., Asiri, A. M., Karimov, K., S. , Niaz, A. K., Khan, S. B., & Alamry, K., A. . (2013). Aluminium phthalocyanine chloride thin films for temperature sensing. *Chinese Physics B, 22*(11), 118101.

Chen, J.-T., Wei, T.-H., Chang, C.-W., Ko, H.-W., Chu, C.-W., Chi, M.-H., & Tsai, C.-C. (2014). Fabrication of polymer nanopeapods in the nanopores of anodic aluminum oxide templates using a double-solution wetting method. *Macromolecules, 47*(15), 5227-5235.

Chen, J.-T., Zhang, M., & Russell, T. P. (2007). Instabilities in nanoporous media. *Nano Letters, 7*(1), 183-187.

Chen, W. P., Zhao, Z. G., Liu, X. W., Zhang, Z. X., & Suo, C. G. (2009). A capacitive humidity sensor based on multi-wall carbon nanotubes (MWCNTs). *Sensors (Basel), 9*(9), 7431-7444.

Chen, Z., & Lu, C. (2005). Humidity sensors: A review of materials and mechanisms. *Sensor Letters, 3*(4), 274-295.

Cheng, Y.-J., Yang, S.-H., & Hsu, C.-S. (2009). Synthesis of conjugated polymers for organic solar cell applications. *Chemical Reviews, 109*(11), 5868-5923.

Chiang, C. K., Fincher, C. R., Park, Y. W., Heeger, A. J., Shirakawa, H., Louis, E. J., . . . MacDiarmid, A. G. (1977). Electrical conductivity in doped polyacetylene. *Physical Review Letters, 39*(17), 1098-1101.

Cho, S., Seo, J. H., Park, S. H., Beaupre, S., Leclerc, M., & Heeger, A. J. (2010). A thermally stable semiconducting polymer. *Advanced Materials, 22*(11), 1253-1257.

Choi, K. S., Kim, D. S., Yang, H. J., Ryu, M. S., & Chang, S. P. (2014). A highly sensitive humidity sensor with a novel hole array structure using a polyimide sensing layer. *RSC Advances, 4*(61), 32075.

Chou, K.-S., Lee, T.-K., & Liu, F.-J. (1999). Sensing mechanism of a porous ceramic as humidity sensor. *Sensors and Actuators B: Chemical, 56*(1–2), 106-111.

Chu, C.-W., Huang, Y.-C., Tsai, C.-C., & Chen, J.-T. (2015). Wetting in nanopores of cylindrical anodic aluminum oxide templates: Production of gradient polymer nanorod arrays on large-area curved surfaces. *European Polymer Journal, 63*, 141-148.

Chu, T.-Y., Alem, S., Tsang, S.-W., Tse, S.-C., Wakim, S., Lu, J., . . . Tao, Y. (2011). Morphology control in polycarbazole based bulk heterojunction solar cells and its impact on device performance. *Applied Physics Letters, 98*(25), 253301.

Chuang, S.-Y., Chen, H.-L., Lee, W.-H., Huang, Y.-C., Su, W.-F., Jen, W.-M., & Chen, C.-W. (2009). Regioregularity effects in the chain orientation and optical anisotropy of composite polymer/fullerene films for high-efficiency, large-area organic solar cells. *Journal of Materials Chemistry, 19*(31), 5554.

Clarke, T. M., Peet, J., Nattestad, A., Drolet, N., Dennler, G., Lungenschmied, C., . . . Mozer, A. J. (2012). Charge carrier mobility, bimolecular recombination and trapping in polycarbazole copolymer:Fullerene (PCDTBT:PCBM) bulk heterojunction solar cells. *Organic Electronics, 13*(11), 2639-2646.

Coppedè, N., Castriota, M., Cazzanelli, E., Forti, S., Tarabella, G., Toccoli, T., . . . Iannotta, S. (2010). Controlled polymorphism in titanyl phthalocyanine on mica by hyperthermal beams: A micro-raman analysis. *The Journal of Physical Chemistry C, 114*(15), 7038-7044.

Corti, C. W., Holliday, R. J., & Thompson, D. T. (2002). Developing new industrial applications for gold: Gold nanotechnology. *Gold Bulletin, 35*(4), 111-117.

D'apuzzo, M., Aronne, A., Esposito, S., & Pernice, P. (2000). Sol-gel synthesis of humidity-sensitive P_2O_5-SiO_2 amorphous films. *Journal of Sol-Gel Science and Technology, 17*(3), 247-254.

Darmanin, T., & Guittard, F. (2014). Wettability of conducting polymers: From superhydrophilicity to superoleophobicity. *Progress in Polymer Science, 39*(4), 656-682.

Dongfeng, Z., Walter, D., Jean-Marc, B., Reymond, C., & Johann, M. (2009). A high-sensitivity and quasi-linear capacitive sensor for nanomechanical testing applications. *Journal of Micromechanics and Microengineering, 19*(7), 075003.

Doris, M., Aziz, F., Alhummiany, H., Bawazeer, T., Alsenany, N., Mahmoud, A., . . . Supangat, A. (2017). Determining the effect of centrifugal force on the desired growth and properties of PCPDTBT as p-type nanowires. *Nanoscale Research Letters, 12*(1), 67.

Dougherty, S., & Liang, J. (2009a). Core–shell polymer nanorods by a two-step template wetting process. *Nanotechnology, 20*(29), 295301.

Dougherty, S., & Liang, J. (2009b). Fabrication of segmented nanofibers by template wetting of multilayered alternating polymer thin films. *Journal of Nanoparticle Research, 11*(3), 743-747.

Faia, P. M., Libardi, J., & Louro, C. S. (2016). Effect of V_2O_5 doping on *p*- to *n*-conduction type transition of TiO_2:WO_3 composite humidity sensors. *Sensors and Actuators B: Chemical, 222*, 952-964.

Fakir, M. S., Supangat, A., & Sulaiman, K. (2014a). Properties of y-shaped PFO-DBT nanotubes. *Journal of Nanomaterials, 2014*, 1-7.

Fakir, M. S., Supangat, A., & Sulaiman, K. (2014b). Templated growth of PFO-DBT nanorod bundles by spin coating: Effect of spin coating rate on the morphological, structural, and optical properties. *Nanoscale Research Letters, 9*(1), 225.

Fakir, M. S., Supangat, A., & Sulaiman, K. (2016). Fabrication of PFO-DBT:OXCBA nanostructured composite via hard template. *Journal of Applied Polymer Science, 133*, 44228.

Farahani, H., Wagiran, R., & Hamidon, M. N. (2014). Humidity sensors principle, mechanism, and fabrication technologies: A comprehensive review. *Sensors (Basel, Switzerland), 14*(5), 7881-7939.

Feng, X., Mei, S., & Jin, Z. (2011). Wettability transition induced transformation and entrapment of polymer nanostructures in cylindrical nanopores. *Langmuir, 27*(23), 14240-14247.

Fraunhofer, J. A. v. (2012). Adhesion and cohesion. *International Journal of Dentistry, 2012*.

Fu, Y., & Bo, Z. (2005). Synthesis, optical, and electrochemical properties of the high-molecular-weight conjugated polycarbazoles. *Macromolecular Rapid Communications, 26*(21), 1704-1710.

Fürjes, P., Kovács, A., Dücso, amp, x030B, Cs, . . . Mescheder, U. (2003). Porous silicon-based humidity sensor with interdigital electrodes and internal heaters. *Sensors and Actuators B: Chemical, 95*(1–3), 140-144.

Geoghegan, M., & Krausch, G. (2003). Wetting at polymer surfaces and interfaces. *Progress in Polymer Science, 28*(2), 261-302.

Gerard, M., Chaubey, A., & Malhotra, B. D. (2002). Application of conducting polymers to biosensors. *Biosensors and Bioelectronics, 17*(5), 345-359.

Gieseking, B., Jäck, B., Preis, E., Jung, S., Forster, M., Scherf, U., . . . Dyakonov, V. (2012). Excitation dynamics in low band gap donor-acceptor copolymers and blends. *Advanced Energy Materials, 2*(12), 1477-1482.

Gleiter, H. (2000). Nanostructured materials: Basic concepts and microstructure. *Acta Materialia, 48*(1), 1-29.

Gu, Y., Wang, C., & Russell, T. P. (2012). Multi-length-scale morphologies in PCPDTBT/PCBM bulk-heterojunction solar cells. *Advanced Energy Materials, 2*(6), 683-690.

Gusmano, G., Montesperelli, G., Traversa, E., & Mattogno, G. (1993). Microstructure and electrical properties of $MgAl_2O_4$ thin films for humidity sensing. *Journal of the American Ceramic Society, 76*(3), 743-750.

Hare, J. P., Kroto, H. W., & Taylor, R. (1991). Preparation and UV/visible spectra of fullerenes C60 and C70. *Chemical Physics Letters*, *177*(4-5), 394-398.

Harrah, D. M., & Swan, A. K. (2011). The role of length and defects on optical quantum efficiency and exciton decay dynamics in single-walled carbon nanotubes. *ACS Nano, 5*(1), 647-655.

Hayat, K., Niaz, F., Ali, S., Iqbal, M. J., Ajmal, M., Ali, M., Iqbal, Y. (2016). Thermoelectric performance and humidity sensing of La_2CuO_4 nanofibers. Sensors and Actuators B: Chemical, 231, 102-109.

Holm, R., & Storp, S. (1980). Surface and interface analysis in polymer technology: A review. *Surface and Interface Analysis, 2*(3), 96-106.

Holzinger, M., Le Goff, A., & Cosnier, S. (2014). Nanomaterials for biosensing applications: A review. *Frontiers in Chemistry, 2*, 63.

Hong-Tao, S., Ming-Tang, W., Ping, L., & Xi, Y. (1989). Porosity control of humidity-sensitive ceramics and theoretical model of humidity-sensitive characteristics. *Sensors and Actuators, 19*(1), 61-70.

Hu, X., Gong, J., Zhang, L., & Yu, J. C. (2008). Continuous size tuning of monodisperse ZnO colloidal nanocrystal clusters by a microwave-polyol process and their application for humidity sensing. *Advanced Materials, 20*(24), 4845-4850.

Huang, F., Chen, K. S., Yip, H.-L., Hau, S. K., Acton, O., Zhang, Y., . . . Jen, A. K. Y. (2009). Development of new conjugated polymers with donor–π-bridge–acceptor side chains for high performance solar cells. *Journal of the American Chemical Society, 131*(39), 13886-13887.

Huang, J., Virji, S., Weiller, B. H., & Kaner, R. B. (2003). Polyaniline nanofibers: Facile synthesis and chemical sensors. *Journal of the American Chemical Society, 125*(2), 314-315.

Huh, C., & Mason, S. G. (1977). Effects of surface roughness on wetting (theoretical). *Journal of Colloid Interface Science, 60*(1), 11-38.

Islam, M. S., Islam, M. E., Ismail, A. B. M., & Baerwolff, H. (2013). Influence of thickness and annealing temperature on the optical properties of spin-coated photoactive P3HT: PCBM blend. *Optics and Photonics Journal, 3*(08), 28.

Jacobasch, H. J. (1993). Surface phenomena at polymers. *Makromolekulare Chemie. Macromolecular Symposia, 75*(1), 99-113.

Jain, M. K., Bhatnagar, M. C., & Sharma, G. L. (1999). Effect of Li+ doping on ZrO_2–TiO_2 humidity sensor. *Sensors and Actuators B: Chemical, 55*(2–3), 180-185.

Jha, P., Koiry, S. P., Saxena, V., Veerender, P., Gusain, A., Chauhan, A. K., . . . Gupta, S. K. (2013). Air-stability and bending properties of flexible organic field-effect transistors based on poly[n-9′-heptadecanyl-2,7-carbazole-alt-5,5-(4′,7′-di-2-thienyl-2′,1′,3′-benzothiadiazole)]. *Organic Electronics, 14*(10), 2635-2644.

Jie, S., Li-lai, L., Rui-ming, Y., & Peng-xiang, Z. (2008). Anodic aluminum oxide template with large area and small holes prepared by gradual voltage-rising method. *Nanotechnology and Precision Engineering, 5*, 004.

Jingbo, L., Wenchao, L., Yanxi, Z., & Zhimin, W. (2001). Preparation and characterization of Li^+-modified $Ca_xPb_{1-x}TiO_3$ film for humidity sensor. *Sensors and Actuators B: Chemical, 75*(1), 11-17.

Jusman, Y., Ng, S. C., & Abu Osman, N. A. (2014). Investigation of CPD and HMDS sample preparation techniques for cervical cells in developing computer-aided screening system based on FE-SEM/EDX. *The Scientific World Journal, 2014*, 11.

Kai, L., Du Kai, C. J., Lan, Z., Lin, Z., & Yu, F. (2010). Fabrication of high quality ordered porous anodic aluminum oxide templates. *High Power Laser and Particle Beams, 7*, 025.

Kamarundzaman, A., Fakir, M. S., Supangat, A., Sulaiman, K., & Zulfiqar, H. (2013). Morphological and optical properties of hierarchical tubular VOPcPhO nanoflowers. *Materials Letters, 111*, 13-16.

Kannappan, S., Palanisamy, K., Tatsugi, J., Shin, P.-K., & Ochiai, S. (2012). Fabrication and characterizations of PCDTBT: $PC_{71}BM$ bulk heterojunction solar cell using air brush coating method. *Journal of Materials Science, 48*(6), 2308-2317.

Kaur, G., Adhikari, R., Cass, P., Bown, M., & Gunatillake, P. (2015). Electrically conductive polymers and composites for biomedical applications. *RSC Advances, 5*(47), 37553-37567.

Khanna, V. K., & Nahar, R. K. (1986). Carrier-transfer mechanisms and Al_2O_3 sensors for low and high humidities. *Journal of Physics D: Applied Physics, 19*(7), L141.

Kim, B., Yeom, H. R., Yun, M. H., Kim, J. Y., & Yang, C. (2012). A selenophene analogue of PCDTBT: Selective fine-tuning of lumo to lower of the bandgap for efficient polymer solar cells. *Macromolecules, 45*(21), 8658-8664.

Kim, J.-H., Park, J. B., Shin, S. A., Hyun, M. H., & Hwang, D.-H. (2014). Low-bandgap copolymers consisting of 2,1,3-benzoselenadiazole and carbazole derivatives with thiophene or selenophene π-bridges. *Polymer, 55*(16), 3605-3613.

Kim, M. S., Lee, S.-h., Yoon, H., Jung, J. H., & Leem, J.-Y. (2013). Effects of post-annealing on structural and optical properties of a-axis oriented ZnO nanorods. *Journal of Nanoscience and Nanotechnology, 13*(9), 6236-6239.

Kim, T., Yang, S. J., Kim, S. K., Choi, H. S., & Park, C. R. (2014). Preparation of PCDTBT nanofibers with a diameter of 20 nm and their application to air-processed organic solar cells. *Nanoscale*, *6*(5), 2847-2854.

Kokonou, M., Ioannou, G., Rebholz, C., & Doumanidis, C. C. (2013). Polymeric nanowires and nanopillars fabricated by template wetting. *Journal of Nanoparticle Research*, 1552-1564.

Kong, J., Yung, K. L., Xu, Y., He, L., Lau, K., & Chan, C. (2008). Self-organized micropatterns of high aspect ratio polymer nanofibers by wetting of nanopores. *Journal of Polymer Science Part B: Polymer Physics, 46*(12), 1280-1289.

Korotcenkov, G. (2016). *Porous silicon: From formation to application: Biomedical and sensor applications, volume two: Biomedical and sensor applications*: CRC Press.

Kraus, E., Orf, L., Heilig, M., Baudrit, B., Starostina, I., & Stoyanov, O. (2017). Characterization of polymer surfaces by the use of different wetting theories regarding acid-base properties. *International Journal of Polymer Science, 2017*, 7.

Kronholm, D., & Hummelen, J. C. (2007). Fullerene-based n-type semiconductors in organic electronics. *Material Matters, 2*, 16-20.

Kulwicki, B. M. (1991). Humidity sensors. *Journal of the American Ceramic Society, 74*(4), 697-708.

Kumar, P., Kumar, A., Fernandes, T., & Ayoko, G. A. (2014). Nanomaterials and the environment. *Journal of Nanomaterials, 2014*, 4.

Kumar, R., Singh, S., & Yadav, B. C. (2015). Conducting polymers: Synthesis, properties and applications. *International Advanced Research Journal in Science, Engineering and Technology, 2*(11), 110-124.

Lee, C. W., Rhee, H. W., & Gong, M.-S. (2001). Humidity sensor using epoxy resin containing quaternary ammonium salts. *Sensors and Actuators B: Chemical, 73*(2–3), 124-129.

Lee, M. H. (1998). In-situ measurement of surface tension during electrochemical doping of polypyrrole films. *Molecular Crystals and Liquid Crystals Science and Technology. Section A. Molecular Crystals and Liquid Crystals, 316*(1), 329-332.

Lee, W., & Park, S. J. (2014). Porous anodic aluminum oxide: Anodization and templated synthesis of functional nanostructures. *Chemical Reviews, 114*(15), 7487-7556.

Leonard, F., & Talin, A. A. (2011). Electrical contacts to one- and two-dimensional nanomaterials. *Nature Nanotechnology*, *6*(12), 773-783.

Li, T., Li, L., Sun, H., Xu, Y., Wang, X., Luo, H., . . . Zhang, T. (2017). Porous ionic membrane based flexible humidity sensor and its multifunctional applications. *Advanced Science*, 1600404-n/a.

Li, Y., Wu, T., & Yang, M. (2014). Humidity sensors based on the composite of multi-walled carbon nanotubes and crosslinked polyelectrolyte with good sensitivity and capability of detecting low humidity. *Sensors and Actuators B: Chemical, 203*, 63-70.

Li, Z.-F., Blum, F. D., Bertino, M. F., Kim, C. S., & Pillalamarri, S. K. (2008). One-step fabrication of a polyaniline nanofiber vapor sensor. *Sensors and Actuators B: Chemical, 134*(1), 31-35.

Liu, H., Li, S., Zhai, J., Li, H., Zheng, Q., Jiang, L., & Zhu, D. (2004). Self-assembly of large-scale micropatterns on aligned carbon nanotube films. *Angewandte Chemie International Edition, 43*(9), 1146-1149.

Liu, H., Li, Y., Xiao, S., Gan, H., Jiu, T., Li, H., . . . Chen, Y. (2003). Synthesis of organic one-dimensional nanomaterials by solid-phase reaction. *Journal of the American Chemical Society, 125*(36), 10794-10795.

Liu, R. S., Zeng, W. J., Du, B., Yang, W., Hou, Q., Shi, W., . . . Cao, Y. (2008). Novel red light-emitting polymers based on 2,7-carbazole and thiophene derivatives *Chinese Journal of Polymer Science, 26*(2), 231-240.

Lu, X., Hlaing, H., Germack, D. S., Peet, J., Jo, W. H., Andrienko, D., . . . Ocko, B. M. (2012). Bilayer order in a polycarbazole-conjugated polymer. *Nature Communications, 3,* 795.

Lu, X., Wang, C., & Wei, Y. (2009). One-dimensional composite nanomaterials: Synthesis by electrospinning and their applications. *Small, 5*(21), 2349-2370.

Luanphaisarnnont, T. (2009). *Intermolecular forces: Van der waals interaction*. Evans Group Meeting.

MacDiarmid, A. G. (2001). “Synthetic metals”: A novel role for organic polymers (nobel lecture). *Angewandte Chemie International Edition, 40*(14), 2581-2590.

Mahboob, M. R., Zargar, Z. H., & Islam, T. (2016). A sensitive and highly linear capacitive thin film sensor for trace moisture measurement in gases. *Sensors and Actuators B: Chemical, 228*, 658-664.

Marin, L., Penxten, H., Van Mierloo, S., Carleer, R., Lutsen, L., Vanderzande, D., & Maes, W. (2013). In situ monitoring the thermal degradation of PCPDTBT low band gap polymers with varying alkyl side-chain patterns. *Journal of Polymer Science Part A: Polymer Chemistry, 51*(22), 4912-4922.

Martín, J., Maiz, J., Sacristan, J., & Mijangos, C. (2012). Tailored polymer-based nanorods and nanotubes by "template synthesis": From preparation to applications. *Polymer, 53*(6), 1149-1166.

Mi, D., Kim, J. H., Kim, H. U., Xu, F., & Hwang, D. H. (2014). Fullerene derivatives as electron acceptors for organic photovoltaic cells. *Journal of Nanoscience and Nanotechnology, 14*(2), 1064-1084.

Michinobu, T., Osako, H., & Shigehara, K. (2009). Synthesis and properties of conjugated poly(1,8-carbazole)s. *Macromolecules*(2), 8172-8180.

Montesperelli, G., Pumo, A., Traversa, E., Bearzotti, A., Montenero, A., & Gnappi, G. (1995). Sol—gel processed TiO_2-based thin films as innovative humidity sensors. *Sensors and Actuators B: Chemical, 25*(1-3), 705-709.

Moon, J. S., Jo, J., & Heeger, A. J. (2012). Nanomorphology of PCDTBT:$PC_{70}BM$ bulk heterojunction solar cells. *Advanced Energy Materials*, *2*(3), 304-308.

Morin, J.-F., Leclerc, M., Adès, D., & Siove, A. (2005). Polycarbazoles: 25 years of progress. *Macromolecular Rapid Communications, 26*(10), 761-778.

Murugesan, V. S., Ono, S., Tsuda, N., Yamada, J., Shin, P.-K., & Ochiai, S. (2015). Characterization of organic thin film solar cells of PCDTBT: $PC_{71}BM$ prepared by different mixing ratio and effect of hole transport layer. *International Journal of Photoenergy, 2015*, 1.

Nalwa, H. S. (1997). *Handbook of organic conductive molecules and polymers, volume 4, conductive polymers: Transport, photophysics and applications*: John Wiley & Sons Ltd: Baffins Lane, Chichester, West Sussex PO19 IUD, England.

Navascues, G. (1979). Liquid surfaces: Theory of surface tension. *Reports on Progress in Physics, 42*(7), 1131.

Neo, W. T., Ong, K. H., Lin, T. T., Chua, S.-J., & Xu, J. (2015). Effects of fluorination on the electrochromic performance of benzothiadiazole-based donor-acceptor copolymers. *Journal of Materials Chemistry C, 3*(21), 5589-5597.

Ng, T. N., Wong, W. S., Chabinyc, M. L., Sambandan, S., & Street, R. A. (2008). Flexible image sensor array with bulk heterojunction organic photodiode. *Applied Physics Letters, 92*(21), 213303.

Nguyen, T.-Q., Doan, V., & Schwartz, B. J. (1999). Conjugated polymer aggregates in solution: Control of interchain interactions. *The Journal of Chemical Physics, 110*(8), 4068-4078.

Nguyen, T.-Q., Martini, I. B., Liu, J., & Schwartz, B. J. (2000). Controlling interchain interactions in conjugated polymers: The effects of chain morphology on exciton-exciton annihilation and aggregation in MEH-PPV films. *Journal of the Chemical Society, 104*, 237-255.

Nitta, T., & Hayakawa, S. (1980). Ceramic humidity sensors. *IEEE Transactions on Components, Hybrids, and Manufacturing Technology, 3*(2), 237-243.

Park, S. H., Roy, A., Beaupré, S., Cho, S., Coates, N., Moon, J. S., . . . Heeger, A. J. (2009). Bulk heterojunction solar cells with internal quantum efficiency approaching 100 %. *Nature Photonics, 3*(5), 297-302.

Parkhutik, V. P., & Shershulsky, V. I. (1992). Theoretical modelling of porous oxide growth on aluminium. *Journal of Physics D: Applied Physics, 25*(8), 1258.

Pasquali, M., Liang, J., & Shivkumar, S. (2010). Role of template and infiltration technique on resulting morphology of polymer nanostructures. *Materials Letters, 64*(18), 1943-1946.

Pasquali, M., Liang, J., & Shivkumar, S. (2011). Role of AAO template filling process parameters in controlling the structure of one-dimensional polymer nanoparticles. *Nanotechnology, 22*(37), 375605.

Peters, C. H., Sachs-Quintana, I. T., Kastrop, J. P., Beaupré, S., Leclerc, M., & McGehee, M. D. (2011). High efficiency polymer solar cells with long operating lifetimes. *Advanced Energy Materials, 1*(4), 491-494.

Pethrick, R. A. (1994). Conjugated polymers and related materials. The interconnection of chemical and electronic structure, edited by W. R. Salaneck, I. Lundstöm and B. Rånby. Oxford university press, oxford, 1993. *Polymer International, 35*(1), 105-105.

Prabhu, K. N., Fernades, P., & Kumar, G. (2009). Effect of substrate surface roughness on wetting behaviour of vegetable oils. *Materials & Design, 30*(2), 297-305.

Provencher, F., Berube, N., Parker, A. W., Greetham, G. M., Towrie, M., Hellmann, C., . . . Hayes, S. C. (2014). Direct observation of ultrafast long-range charge separation at polymer-fullerene heterojunctions. *Nature Communications, 5*, 4288.

Qi, Q., Zhang, T., Yu, Q., Wang, R., Zeng, Y., Liu, L., & Yang, H. (2008). Properties of humidity sensing ZnO nanorods-base sensor fabricated by screen-printing. *Sensors and Actuators B: Chemical, 133*(2), 638-643.

Raj, S., Jose, S., Sumod, U. S., & Sabitha, M. (2012). Nanotechnology in cosmetics: Opportunities and challenges. *Journal of Pharmacy & Bioallied Sciences, 4*(3), 186-193.

Raj, V., Madheswari, D., & Mubarak Ali, M. (2010). Chemical formation, characterization and properties of polycarbazole. *Journal of Applied Polymer Science*, *116*(1), 147-154.

Reddy, K. R., Jeong, H. M., Lee, Y., & Raghu, A. V. (2010). Synthesis of MWCNTs-core/thiophene polymer-sheath composite nanocables by a cationic surfactant-assisted chemical oxidative polymerization and their structural properties. *Journal of Polymer Science Part A: Polymer Chemistry, 48*(7), 1477-1484.

Rezlescu, N., Rezlescu, E., Sava, C. L., Tudorache, F., & Popa, P. D. (2004). On the effects of Ga^{3+} and La^{3+} ions in MgCu ferrite: Humidity-sensitive electrical conduction. *Crystal Research and Technology, 39*(6), 548-557.

Rittersma, Z. (2002). Recent achievements in miniaturised humidity sensors—a review of transduction techniques. *Sensors and Actuators A: Physi7*assembly of aromatic rod building blocks. *Chemical Communications (Camb)*(9), 1043-1054.

Sajid, M., Aziz, S., Kim, G. B., Kim, S. W., Jo, J., & Choi, K. H. (2016). Bio-compatible organic humidity sensor transferred to arbitrary surfaces fabricated using single-cell-thick onion membrane as both the substrate and sensing layer. *Scientifics Reports, 6*, 30065.

Sakai, Y., Sadaoka, Y., & Matsuguchi, M. (1996). Humidity sensors based on polymer thin films. *Sensors and Actuators B: Chemical, 35*(1), 85-90.

Salehi, A., & Jamshidi Kalantari, D. (2007). Characteristics of highly sensitive au/porous-gaas schottky junctions as selective CO and NO gas sensors. *Sensors and Actuators B: Chemical, 122*(1), 69-74."

Saritha, S., Neogi, P., & Wang, J. C. (2006). Wetting by polymer solutions. *Polymer, 47*(18), 6263-6266.

Schaffer, H. E., Chance, R. R., Silbey, R. J., Knoll, K., & Schrock, R. R. (1991). Conjugation length dependence of raman scattering in a series of linear polyenes: Implications for polyacetylene. *The Journal of Chemical Physics, 94*(6), 4161-4170.

Schlitt, S., Greiner, A., & Wendorff, J. H. (2008). Cylindrical polymer nanostructures by solution template wetting. *Macromolecules, 41*(9), 3228-3234.

Schmidt, H. K. (2013). Nanostructured fluid sampling device: Google Patents.

Schwartz, B. J. (2003). Conjugated polymers as molecular materials: How chain conformation and film morphology influence energy transfer and interchain interactions. *Annual Review of Physical Chemistry, 54*(1), 141-172.

Schwartz, B. J., Nguyen, T.-Q., Wu, J., & Tolbert, S. H. (2001). Interchain and intrachain exciton transport in conjugated polymers: Ultrafast studies of energy migration in aligned MEH-PPV/mesoporous silica composites. *Synthetic Metals, 116*(1), 35-40.

Sekine, C., Tsubata, Y., Yamada, T., Kitano, M., & Doi, S. (2014). Recent progress of high performance polymer OLED and OPV materials for organic printed electronics. *Science and Technology of Advanced Materials, 15*(3), 034203.

Shirakawa, H., Louis, E. J., MacDiarmid, A. G., Chiang, C. K., & Heeger, A. J. (1977). Synthesis of electrically conducting organic polymers: Halogen derivatives of polyacetylene,$(CH)_X$. *Journal of the Chemical Society, Chemical Communications*, 16, 578-580.

Singh, D. K., Giri, P. K., & Iyer, P. K. (2011). Evidence for defect-enhanced photoluminescence quenching of fluorescein by carbon nanotubes. *The Journal of Physical Chemistry C, 115*(49), 24067-24072.

Skotheim, T. A., & Reynolds, J. (2006). *Conjugated polymers: Theory, synthesis, properties, and characterization*. Boca Raton CRC Press.

Smit, H., Kivi, R., Vömel, H., & Paukkunen, A. (2013). Thin film capacitive sensors. *Monitoring Atmospheric Water Vapour*, 11-38.

Sohn, E. H., Ahn, J., Kim, B. G., & Lee, J.-C. (2011). Effect of n-alkyl and sulfonyl groups on the wetting properties of comblike poly(oxyethylene)s and stick−slip behavior. *Langmuir, 27*(5), 1811-1820.

Souharce, B., Kudla, C. J., Forster, M., Steiger, J., Anselmann, R., Thiem, H., & Scherf, U. (2009). Amorphous carbazole-based (co) polymers for OFET application. *Macromolecular Rapid Communications, 30*(14), 1258-1262.

Stegamat, R., & So, F. (2004). Conducting polymer for electronic devices: Google Patents.

Steinhart, M., Wehrspohn, R. B., Gösele, U., & Wendorff, J. H. (2004). Nanotubes by template wetting: A modular assembly system. *Angewandte Chemie International Edition, 43*(11), 1334-1344.

Steinhart, M., Wendorff, J., Greiner, A., Wehrspohn, R., Nielsch, K., Schilling, J., . . . Gösele, U. (2002). Polymer nanotubes by wetting of ordered porous templates. *Science, 296*(5575), 1997.

Steinhart, M., Wendorff, J. H., & Wehrspohn, R. B. (2003). Nanotubes à la carte: Wetting of porous templates. *ChemPhysChem, 4*(11), 1171-1176.

Stępniowski, W. J., & Salerno, M. (2014). Fabrication of nanowires and nanotubes by anodic alumina template-assisted electrodeposition (pp. 321-357): One Central Press: Manchester, UK.

Stępniowski, W. J., Zasada, D., & Bojar, Z. (2011). First step of anodization influences the final nanopore arrangement in anodized alumina. *Surface and Coatings Technology, 206*(6), 1416-1422.

Su, P.-G., & Tsai, W.-Y. (2004). Humidity sensing and electrical properties of a composite material of nano-sized SiO_2 and poly(2-acrylamido-2-methylpropane sulfonate). *Sensors and Actuators B: Chemical, 100*(3), 417-422.

Su, Y., Zhang, T., Zhang, P., Jiang, J., Xiao, Z., Li, S., . . . Jiang, Y. (2012). Effects of annealing temperature on raman scattering and electrical properties of te-doped nanostructured black silicon. *Journal of Materials Science Research, 2*(1), 34.

Supangat, A., Kamarundzaman, A., Bakar, N. A., Sulaiman, K., & Zulfiqar, H. (2014). P3HT:VOPcPhO composite nanorods arrays fabricated via template–assisted method: Enhancement on the structural and optical properties. *Materials Letters, 118*, 103-106.

Szilágyi, I. M., & Nagy, D. (2014). Review on one-dimensional nanostructures prepared by electrospinning and atomic layer deposition. *Journal of Physics: Conference Series, 559*, 012010.

Tan, S. E., & Sarjadi, M. S. (2016). A review of the modification of PCDTBT structure used in the polymeric solar cells. *Research & Reviews: Journal of Chemistry, 5*(4), 1-15.

Tran, H. D., Li, D., & Kaner, R. B. (2009). One-dimensional conducting polymer nanostructures: Bulk synthesis and applications. *Advanced Materials, 21*(14-15), 1487-1499.

Tripathy, A., Pramanik, S., Cho, J., Santhosh, J., & Osman, N. A. (2014). Role of morphological structure, doping, and coating of different materials in the sensing characteristics of humidity sensors. *Sensors (Basel), 14*(9), 16343-16422.

Tripathy, A., Pramanik, S., Manna, A., Bhuyan, S., Azrin Shah, N. F., Radzi, Z., & Abu Osman, N. A. (2016). Design and development for capacitive humidity sensor applications of lead-free Ca,Mg,fe,Ti-oxides-based electro-ceramics with improved sensing properties via physisorption. *Sensors (Basel), 16*(7).

Tsoi, W. C., James, D. T., Kim, J. S., Nicholson, P. G., Murphy, C. E., Bradley, D. D., . . . Kim, J. S. (2011). The nature of in-plane skeleton raman modes of P3HT and their correlation to the degree of molecular order in P3HT:PCBM blend thin films. *Journal of the American Chemical Society, 133*(25), 9834-9843.

Upadhyay, S. (2008). Humidity-sensitive characteristic of Ba0.99La0.01SnO3. *Physica Status Solidi (a), 205*(5), 1113-1119.

Wang, D. H., Kim, J. K., Seo, J. H., Park, O. O., & Park, J. H. (2012). Stability comparison: A PCDTBT/PC_{71}BM bulk-heterojunction versus a P3HT/PC_{71}BM bulk-heterojunction. *Solar Energy Materials and Solar Cells, 101*, 249-255.

Wang, W., & Virkar, A. V. (2004). A conductimetric humidity sensor based on proton conducting perovskite oxides. *Sensors and Actuators B: Chemical, 98*(2), 282-290.

Wang, X., Ederth, T., & Inganäs, O. (2006). In situ wilhelmy balance surface energy determination of poly(3-hexylthiophene) and poly(3,4-ethylenedioxythiophene) during electrochemical doping−dedoping. *Langmuir, 22*(22), 9287-9294.

Wang, Y., & Michinobu, T. (2016). Benzothiadiazole and its π-extended, heteroannulated derivatives: Useful acceptor building blocks for high-performance donor-acceptor polymers in organic electronics. *Journal of Materials Chemistry C, 4*(26), 6200-6214.

Watt, I. C. (2006). Adsorption-desorption hysteresis in polymers. *Journal of Macromolecular Science: Part A - Chemistry, 14*(2), 245-255.

Wei, T. H., Chi, M. H., Tsai, C. C., Ko, H. W., & Chen, J. T. (2013). Porous polymer nanostructures fabricated by the surface-induced phase separation of polymer solutions in anodic aluminum oxide templates. *Langmuir, 29*(32), 9972-9978.

Witkowski, A., Stec, A. A., & Hull, T. R. (2016). Thermal decomposition of polymeric materials. In M. J. Hurley, D. T. Gottuk, J. R. Hall Jr, K. Harada, E. D. Kuligowski, M. Puchovsky, J. L. Torero, J. M. Watts Jr, & C. J. Wieczorek (Eds.), *SFPE handbook of fire protection engineering* (pp. 167-254). New York, NY: Springer New York.

Xia, Y., Wiesinger, J. M., MacDiarmid, A. G., & Epstein, A. J. (1995). Camphorsulfonic acid fully doped polyaniline emeraldine salt: Conformations in different solvents studied by an ultraviolet/visible/near-infrared spectroscopic method. *Chemistry of Materials, 7*(3), 443-445.

Xia, Y., Yang, P., Sun, Y., Wu, Y., Mayers, B., Gates, B., . . . Yan, H. (2003). One-dimensional nanostructures: Synthesis, characterization, and applications. *Advanced Materials, 15*(5), 353-389.

Xie, Y., Kocaefe, D., Chen, C., & Kocaefe, Y. (2016). Review of research on template methods in preparation of nanomaterials. *Journal of Nanomaterials, 2016*, 1-10.

Xu, H., Shirvanyants, D., Beers, K., Matyjaszewski, K., Rubinstein, M., & Sheiko, S. S. (2004). Molecular motion in a spreading precursor film. *Physical Review Letters, 93*(20), 206103.

Yadav, B. C., & Kumar, R. (2008). Structure, properties and applications of fullerenes. *International Journal of Nanotechnology and Applications, 2*(1), 15–24.

Yan, J., Ye, Q., Han, X., & Zhou, F. (2013). Step-by-step build-up of ordered p-n heterojunctions at nanoscale for efficient light harvesting. *RSC Advances, 3*(1), 166-171.

Yang, R., Tian, R., Hou, Q., Yang, W., & Cao, Y. (2008). Synthesis and optical and electroluminescent properties of novel conjugated copolymers derived from fluorene and benzoselenadiazole. *Macromolecules, 41*(22), 8951-8951.

Yang, S.-P., Kong, W.-G., Liu, B.-Y., Zheng, W.-Y., Li, B.-M., Liu, X.-H., & Fu, G.-S. (2011). Highly efficient PCDTBT:$PC_{71}BM$ based photovoltaic devices without thermal annealing treatment. *Chinese Physics Letters, 28*(12), 128401.

Yasutani, Y., Honsho, Y., Saeki, A., & Seki, S. (2012). Polycarbazoles: Relationship between intra- and intermolecular charge carrier transports. *Synthetic Metals, 162*(17), 1713-1721.

Yeow, J. T. W., & She, J. P. M. (2006). Carbon nanotube-enhanced capillary condensation for a capacitive humidity sensor. *Nanotechnology, 17*(21), 5441-5448.

Yu, G., Gao, J., Hummelen, J. C., Wudl, F., & Heeger, A. J. (1995). Polymer photovoltaic cells: Enhanced efficiencies via a network of internal donor-acceptor heterojunctions. *Science, 270*(5243), 1789.

Yuan, Y., & Lee, T. R. (2013). Contact angle and wetting properties. *Surface Science Techniques, 51*, 3-34.

Yung, K.-L., Kong, J., & Xu, Y. (2007). Studies on flow behaviors of polymer melts in nanochannels by wetting actions. *Polymer, 48*(26), 7645-7652.

Zafar, Q., Aziz, F., & Sulaiman, K. (2016). Eco-benign visible wavelength photodetector based on phthalocyanine-low bandgap copolymer composite blend. *RSC Advances, 6*(16), 13101-13109.

Zafar, Q., & Sulaiman, K. (2016). Utility of PCDTBT polymer for the superior sensing parameters of electrical response based relative humidity sensor. *Reactive and Functional Polymers, 105*, 45-51.

Zang, L. (2011). *Energy efficiency and renewable energy through nanotechnology*: Springer London.

Zha, J., Lu, X., & Xin, Z. (2015). Hydrogen bonding effect on wettability of polysiloxane coatings. *The Journal of Physical Chemistry C, 119*(1), 420-425.

Zhang, D., Ward, R. S., Shen, Y. R., & Somorjai, G. A. (1997). Environment-induced surface structural changes of a polymer: An in situ IR + visible sum-frequency spectroscopic study. *The Journal of Physical Chemistry B, 101*(44), 9060-9064.

Zhang, M., Dobriyal, P., Chen, J.-T., Russell, T. P., Olmo, J., & Merry, A. (2006). Wetting transition in cylindrical alumina nanopores with polymer melts. *Nano Letters, 6*(5), 1075-1079.

Zhang, Q., Uchaker, E., Candelaria, S. L., & Cao, G. (2013). Nanomaterials for energy conversion and storage. *Chemical Society Reviews, 42*(7), 3127-3171.

Zhang, Y., Wu, J., Zhang, Y., Guo, W., & Ruan, S. (2014). Characterization and humidity sensing properties of the sensor based on $Na_2Ti_3O_7$ nanotubes. *Journal of Nanoscience and Nanotechnology, 14*(6), 4303-4307.

Zheng, W., Wang, C. C., Wang, S. P., & Ko, C. L. (2009). Surface wettability of rubbed polyimide thin films. *Molecular Crystals and Liquid Crystals, 512*(1), 81-90.

Zhu, Y., Yuan, H., Xu, J., Xu, P., & Pan, Q. (2010). Highly stable and sensitive humidity sensors based on quartz crystal microbalance coated with hexagonal lamelliform monodisperse mesoporous silica SBA-15 thin film. *Sensors and Actuators B: Chemical, 144*(1), 164-169.

LIST OF PUBLICATIONS

1. **Bakar, N. A.**, Supangat, A., & Sulaiman, K. (2014). Elaboration of PCDTBT nanorods and nanoflowers for augmented morphological and optical properties. *Materials Letters, 131*, 27-30.

2. **Bakar, N. A.**, Supangat, A., & Sulaiman, K. (2014). Controlling the morphological, structural, and optical properties of one-dimensional PCDTBT nanotubes by template wetting. *Nanoscale Research Letters*, *9*(1), 600.

3. **Bakar, N. A.**, Supangat, A., & Sulaiman, K. (2015). Formation of PCDTBT:PC$_{71}$BM *p-n* junction composite nanotubes via a templating method. *RSC Advances*, *5*(124), 102689-102699.

4. Aziz, F., **Bakar, N. A.**, Bashir, S., Alhummiany, H., Bawazeer, T., Alsenany, N., Mahmoud, A., Supangat, A., Sulaiman, K. (2017). Effective transformation of PCDTBT nanorods into nanotubes by polymer melts wetting approach. *Journal of Saudi Chemical Society*.